Article-based doctoral Thesis

Doctoral Program Aerospace Science and Technology

Contributions to real-time monitoring of ionosphere using GNSS signals

Cristhian Timoté

Advisors
Dr. Guillermo González-Casado
Dr. Miquel Escudero-Royo

Research group of Astronomy and Geomatics
Department of Mathematics
Universitat Politècnica de Catalunya

This page intentionally left blank.

Abstract

UNESCO Codes: 1203.21, 2501.18, 2504.03, 2504.07

This document presents the collection of four manuscripts published during my Doctoral academic formation, which main goal has been the real-time implementation of tools to monitor the ionosphere using Global Navigation Satellite System (GNSS) signals. Despite the fact that there is a vast literature on ionospheric modelling, the state-of-the-art becomes narrow when referring to real-time developments, especially fulfilling precise requirements on accuracy, performance, coverage, and confidence in the generated products. The main contribution of this work to the scientific community is the deployment of ionospheric-related products to monitor in real-time the state of the ionosphere.

The first and second publications targeted the implementation of a novel strategy based on a definition of a GNSS Solar Flare (SF) monitor to automatically confirm Solar Flare Effects (Sfe) in geomagnetism. In the first scientific article, it is inspected the methodology used to fine-tune (adapt) a SF monitor, working with an eleven years period of data to statistically correlate detected SF using GNSS signals with respect to SFe. The results demonstrated that the proposed GNSS Solar Flare monitor can confirm Sfe events when traditional Sfe detectors are not able to respond categorically. The second publication details the methodological approach for defining the proposed GNSS Solar Flare monitor, focusing on the theoretical formulation of the Slant Total Electron Content (STEC) obtained.

The third contribution used GNSS signals to detect the presence of Medium Scale Travelling Ionospheric Disturbance (MSTID) within a network of permanent GNSS stations that provide the high-accuracy positioning service known as Network-Real-Time Kinematics (NRTK). The effects of a MSTID are characterized in terms of fluctuations in the electron density in the ionosphere, experienced differently by each one of the GNSS stations used as reference receivers within the NRTK, and resulting in a degradation of the positioning of any user of the service. The $\texttt{MSTID}_{\texttt{idx}}$ index is proposed to warn users of the presence of a MSTID, implementing a novel methodology for assessing the errors in positioning based on fixing carrier-phase ambiguities in undifferenced measurements. The adoption of the proposed $\texttt{MSTID}_{\texttt{idx}}$ index proves to be efficient to reduce the errors on the user positioning by excluding measurements polluted by the MSTID effects, reaching accuracy levels within the overall network similar to the ones achieved by users located close to reference stations (and therefore, less affected by MSTID effects).

The fourth publication is the core of my doctoral thesis and presents the real-time implementation of a model to generate ionospheric corrections suitable to fulfill the Galileo HAS. The analyzed ionospheric correction system is based on the Fast Precise Point Positioning (FPPP) technique, in which it is highlighted the benefits of integer ambiguity resolution to obtain unambiguous carrier phase measurements as input to compute the FPPP ionospheric model. Additionally, this contribution underlines the benefit of the implemented strategy, in terms of the geometric model used by the ionospheric modelling and the dataset implemented. In terms of assessing the errors of the FPPP ionospheric corrections, the 99% of the Global Positioning

System (GPS) and Galileo errors in well-sounded areas and in mid-latitude stations are below one total electron content unit, which is in line according to the required ionospheric accuracy for the Galileo HAS. Furthermore, alongside the ionospheric corrections, it is presented some additional products generated by the FPPP Central Processing Facility (CPF), produced in real-time and with accuracy levels suitable to any HAS application.

This document is organized as follows: chapter 1 presents a basic introduction of concepts and definitions related to the subject of study of this thesis. In chapter 2 the main results obtained in each publication are described and some comments are given regarding their potential future research. Next, chapter 3 displays the metrics used to reference the scientific quality and impact of the Journals used to publish. The main conclusions of this dissertation are presented in chapter 4. Finally, chapter 5 presents the collection of articles.

Resumen

Códigos UNESCO para clasificación del conocimiento: 1203.21, 2501.18, 2504.03, 2504.07

Este documento es la colección de artículos científicos publicados durante mi formación académica como estudiante de doctorado, y que se centran en la implementación de herramientas para monitorizar la ionosfera terrestre por medio del uso de señales GNSS. Si bien se puede encontrar una literatura bastante amplia sobre el modelado de la ionosfera, son reducidos los trabajos y desarrollos relacionados con aplicaciones en tiempo real, particularmente si se busca cumplir con requerimientos especifícos vínculados con la precisión, el rendimiento, el cubrimiento y la certidumbre de los productos generados. En este sentido, la principal contribución de esta tesis doctoral es la generación en tiempo real de productos para monitorizar el estado de la ionosfera.

Las primeras dos publicaciones presentadas se centran en el desarrollo de una nueva metodología fundamentada en un detector de Fulguraciones Solares (SF) basado en mediciones GNSS para la confirmación de los efectos de un SF (SFe) detectados por sensores geomagnéticos. En el primer artículo científico, se expone el procedimiento para el diseño y ajuste del detector GNSS de SF (GNSS-SF), empleando para ello un periodo de once años de datos con los cuales correlacionar estadísticamente SF detectados por medio del detector GNSS y los eventos SFe detectados en magnetismo. Los resultados demuestan que el detector GNSS-SF es capaz de confirmar eventos SFe cuando estos últimos no son categóricamente validados por los instrumentos magnéticos. La segunda publicación detalla el efoque metodológico desarrollado para definir el detector GNSS-SF que se propone en el artículo, prestando atención especialmente a la formulación teorica de cómo es calculado el principal dato de entrada del detector (llamado, en inglés Slant Total Electron Content (STEC)).

La tercera publicación emplea señales GNSS para detectar la presencia de perturbaciones de escala media que se desplazan en la ionosfera (MSTID, por sus siglas en inglés) en una red de estaciones GNSS fijas que brindan servicios de posicionamiento muy preciso, conocido como NRTK. Los efectos de una MSTID pueden ser caracterizados por medio de la fluctuación en la densidad de electrones en la ionosfera, experimentado de manera diferente por cada una de las esaciones GNSS usadas como referencia dentro del servicio NRTK, ocasionando una degradación en el posicionamiento de cualquier usuario del servicio. Se propone entonces el índice $\texttt{MSTID}_{\texttt{idx}}$ con el objetivo de advertir a los usuarios del servicio NRTK de la presencia de efectos ocasionados por MSTID, implementando para ello una nueva metodología basada en la determinación de ambigüedades en observaciones sin diferenciar basadas en la fase de la portadora de la señal GNSS. Los resultados tras la implementación del índice $\texttt{MSTID}_{\texttt{idx}}$ demuestran ser eficientes en terminos de reducir los errores en el posicionamiento de los usuarios, descartando observaciones GNSS afectadas por los efectos de MSTID. Los niveles de precisión que se logran en toda la red NRTK por medio de esta estrategia son similares a los obtenidos por un usuario ubicado muy cerca de una estación de referencia (y por tanto, afectada muy poco por los efectos de la MSTID).

Por último, la cuarta publicación que se presenta en este documento representa el contenido central de mi tesis doctoral, fundamentado en la implementación en tiempo real de un sistema de correcciones para la ionosfera basado en la técnica de rápido posicionamiento preciso (FPPP, por sus siglas en inglés), adecuado para satisfacer los requerimientos HAS del sistema de navegación por satélite Galileo. El sistema de correcciones ionosféricas expuesto en el artículo se destacan las caracterítiscas de la técnica FPPP, tales como la fijación en números enteros de las ambigüedades en la fase de la portadora de la señal GNSS para obtener mediciones sin ambigüedad, de manera que puedan servir como dato de entrada para la generación de las correcciones ionosféricas obtenidas por el modelo FPPP. Adicionalmente, este artículo resalta las características tanto del modelo geométrico implementado como del conjunto de datos usado. En terminos de evaluar los errres de las correcciones ionosféricas generadas, el 99% los errores en GPS y Galileo estan por debajo de un TECU, en zonas de notable densidad de estaciones GNSS localizadas en media latitud. Estos resultados se corresonden con los requerimientos exigidos por el servicio HAS de Galielo para correcciones de ionósfera. De igual forma, se presentan algunos porductos adicionales generados por la misma Unidad de Procesamiento de Central (Central Processing Facility (CPF), por sus siglas en inglés) que genera las correcciones ionósfericas, calculados en tiempo real y con niveles de precisión apropiados para cualquier aplicacion HAS.

Este documento está organizado de la siguiente manera: el capítulo 1 presenta una introducción básica a los conceptos y definiciones relacionados con el tema de estudio de esta tesis doctoral. En el capítulo 2 se describen los principales resultados obtenidos en cada publicación y se dan algunos comentarios sobre el potencial trabajo a futuro que se puede desarrollar. A continuación, el capítulo 3 muestra las métricas utilizadas para referenciar la calidad científica y el impacto de las revistas utilizadas para publicar cada uno de los artículo científicos. Las principales conclusiones de esta tesís doctoral se presentan en el capítulo 4. Finalmente, el capítulo 5 presenta la colección de artículos.

Acknowledgements

This written document marks the end of one of the sweetest chapters of my life, made possible only thanks to Prof. Dr. Jaume Sanz and Prof. Dr. Miguel Juan. For the confidence they always placed in me and the continuous (academic and personal) support during all these years, I have nothing but my deepest and eternal gratitude.

Thanks to Dr. Guillermo González and Dr. Miquel Escudero for tutoring this thesis, constantly encouraging me to achieve the targeted goals. Thank you also for dealing not only with technical aspects but also for handling all the bureaucratic procedures required to submit this document.

I would also like to acknowledge the important role every friend and colleague at the UPC played during my doctoral formation. Especially, to Adrià Rovira, always friendly open to questions, and with a very useful and wise advice for every situation. Thanks also to Deimos Ibáñez, a.k.a. `AwkMan`, for rescuing me every time computers conspire against me.

In a more personal way, I would like to express my gratitude to all my family and friends, who invariably were present every day in our lives during these years. Despite being separated by the sea, we have never felt the distance.

To Prof. Ovidio Simbaqueva, the scientist who started it all, the friend who showed me the way. ¡Gracias profe!

To my dear wife, Paola. For her conviction in my dreams (even more than myself), the blind faith in a shining future by my side, and the love that never stops growing. Thanks to you we did it!

And of course, this modest achievement is dedicated to you *Mr. Bojangitols*.

This page intentionally left blank.

Contents

List of Figures

This page intentionally left blank.

List of Tables

This page intentionally left blank.

Chapter 1
GNSS principles, ionosphere and research overview

It has been more than 65 years since the U.S. Navy achieved the first position fix of one of its submarines in January 1964, using radio ranging techniques between beacons deployed in space (artificial satellites) and users on earth. This new global satellite positioning and, therefore, global satellite navigation technique was called to revolt the world, providing a user located anywhere in the world means to determine its own location with a meter-level accuracy. It is more than evident that since then, the Global Navigation Satellite System (GNSS) has been shaping human life from marine, air, and terrestrial navigation to geodesy and land-survey activities.

The research presented in this document is one of these many applications, feasible thanks to the interaction of the GNSS signals with the earth's atmosphere and the capability of working with data collected in real-time from GNSS stations located around the globe. The essential contribution of this thesis is to implement tools operative in real-time to provide information about the status of the ionosphere.

The reader will find in the present chapter four different sections devoted to introducing the theoretical concepts and the methodology followed to accomplish the research objectives. First, Section one gives a general view of any GNSS, from the architecture of the system up to the GNSS signal design and modeling of the observables. Section two introduces the main field of study: the ionosphere and its impact on GNSS signals. The proposed objectives and the methodology carried out during the research are presented in sections three and four, respectively.

1.1 Global Navigation Satellite System

The main objective of a GNSS is to provide accurate estimates of the position, velocity and time of a user, on a global scale and almost instantaneously. The basic operational principle uses radio signals transmitted from a set of n-satellites (denominated as *Constellation*), with known positions $(x_1^s, y_1^s, z_1^s), ..., (x_n^s, y_n^s, z_n^s)$, received by a user with unknown position (x_u, y_u, z_u) (as seen in Figure 1.1). By comparing the incoming signal with a locally generated replica at the receiver, the user can compute the travel time spent by the signal from the satellite to the

receiver antenna, and then compute its geometrical distance R to each satellite. A minimum number of 4 satellites are needed to determine the receiver position and time.

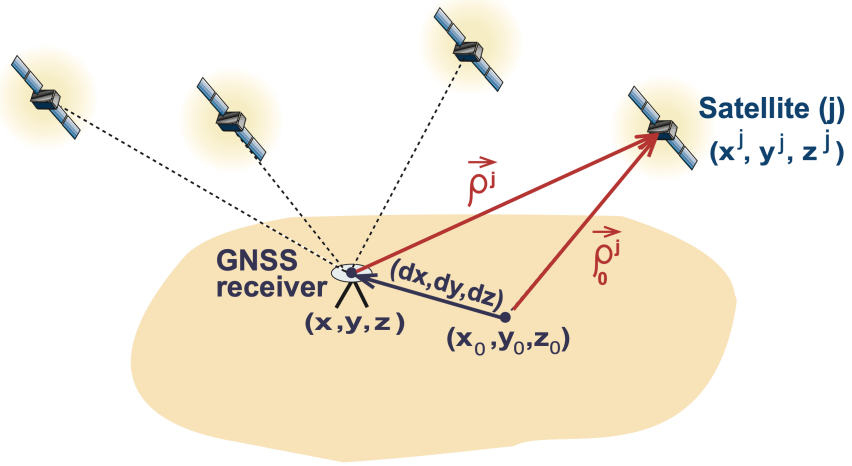

Figure 1.1: GNSS geometric operational principle. [Sanz et al., 2013]

Currently, there are four GNSS constellations able to provide worldwide coverage in a continuous manner: the Global Positioning System (GPS) developed by the U.S.A. and in a stable Full Operation Capability (FOC) since 1994, the Russian *Global'naya Navigatsionnaya Sputnikovaya Sistema* (GLONASS), operative in FOC mode since 1996 and again in 2011, after losing several satellites at the beginning of the 2000s. Finally, the most recent GNSS, the European Galileo and Chinese BEIDOU systems. Any of these before mentioned GNSS is a complex system generally represented in three major segments: The space, control, and user segment.

1.1.1 GNSS segments definition

Space segment

The space segment of a GNSS comprises satellites around the earth in a well-predefined orbit, with the main goal of generating and transmitting the GNSS signals [Sanz et al., 2013]. Any GNSS is a one-way ranging system, meaning that the GNSS signals are broadcasted only by the satellites. Table 1.1 summarizes the main orbital characteristics for each different constellation.

Table 1.1: GNSS orbital constellation main features.

Constellation	Current number of satellites[1]	Satellite height (km)	Orbit inclination and eccentricity	Orbital period	Orbital planes
GPS	31	20200	55° less than 0.02	11 hours 58 minutes	6
GLONASS	22	19100	64.8° 0.072	11 hours 15 minutes	3
GALILEO	25	23222	56° 0.002	14 hours 4 minutes	3

Control segment

The tasks of the control segment are mainly to monitor the status of the space segment, keep the GNSS time scale, and upload the navigation data to the satellites. The elements of the

[1] As of February 27, 2023. Visit the current status at https://www.navcen.uscg.gov/gps-constellation for GPS, https://www.glonass-iac.ru/glonass/sostavOG/ for GLONASS, https://www.gsc-europa.eu/system-service-status/constellation-information for GALILEO

control segment are typically a Master Control Station (MCS), Monitoring Stations (MS), and Ground Antennas (GA). The MSs are continuously tracking satellites in view to transmit their observations (raw data and navigation messages) back to the MCS. The MCS uses these observations to compute satellite positions and satellite clock errors. The MCS then uploads this information to all satellites through the Ground Antennas using an S-Band radio frequency link.

User segment

This segment encompasses any device that is capable of receiving GNSS signals. This includes single-frequency, double-frequency, and multi-frequency receivers, as well as static and moving receivers. These receiver devices can be used and categorized according to an expanding variety of applications, such as safety-of-life, mass market, and others. The main function of this segment is to receive GNSS signals, determine pseudoranges, and solve the navigation equations to provide accurate coordinates and time[Sanz et al., 2013].

1.1.2 GNSS signals

Satellites in space can be seen as very sophisticated beacons transmitting radio frequency signals (carrier) conveying useful information (called data signal) to the receiver to compute the satellite position (orbit ephemerides), apply corrections from modeled errors such as clock bias parameter and ionospheric modeling, and finally determine the traveled time spent by the electromagnetic wave along its path from the satellite to the receiver antenna (binary Pseudo Random Noise (PRN) code)[Sanz et al., 2013]. The combination of the carrier, code and data signal are depicted in Figure 1.2:

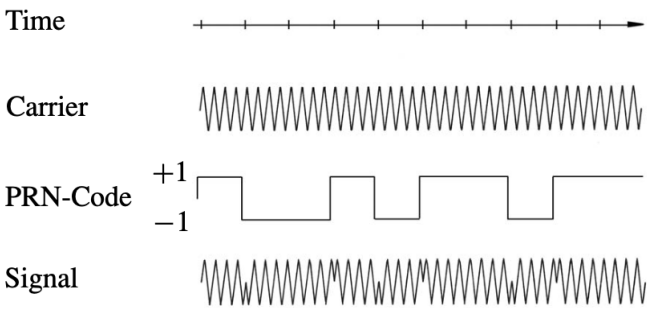

Figure 1.2: Structure of GPS satellite signals [Seeber, 2008].

The broadcasting frequencies of the GNSS satellites are allocated in the L-Band, from 1 up to 2 GHz [IEE, 2003]. Within this spectrum, there are allocated dedicated bands for specific applications, such as the Radionavigation Satellite Service (RNSS) and the Aeronautical Radio Navigation Service (ARNS). This is in order to prevent interference or jamming from any other radio-frequency emitter. Satellites of the GPS implement three frequencies: L1, L2 and L5 at 1575.42, 1227.60 and 1176.45 MHz, correspondingly (see [Gurtner and Estey, 2007] for detailed information on the definition of these standards). Galileo satellites' frequency allocation is as follows: E1 at 1575.42 MHz, E5a at 1176.45 MHz, E5b at 1207.140 MHz (and the resulting E8 at 1191.795 MHz), and finally E6 at 1278.75 MHz. Chinese BEIDOU satellites transmit in three main bands, B1, B2 and B3, different frequencies: in B1 there is the B1-2 frequency at 1561.098 MHz and the B1 frequency at 1575.42 MHz. In band B2 there is B2a at 1176.45 MHz, B2b at 1207.140 MHz and the resulting B2 (B2a+B2b) at 1191.795 MHz. Finally, B3 is allocated

for signal frequency transmission at 1268.52 MHz. In the case of GLONASS, there is not a unique dedicated frequency for the entire satellite constellation. This is due to the fact that, in order to allow receivers to track each different satellite from the signals arriving at the same time, GLONASS implements the Frequency Division Multiple Access (FDMA) technique, in which the G1, G2 and G3 bands are split and allocated to satellites according to a k factor that identifies each satellite. Figure 1.3 presents the full frequency allocation map.

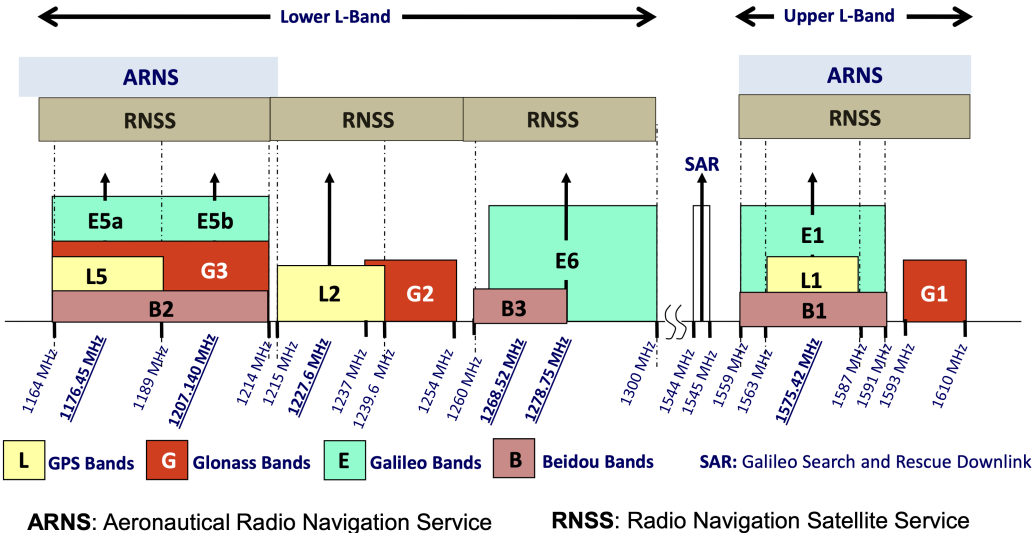

Figure 1.3: GPS, GLONASS, Galileo and BEIDOU frequency allocation [Sanz et al., 2013].

1.1.3 GNSS measurements and modeling

Once the receiver tracks and acquires the transmitted signal, it is then possible to determine its distance to the satellite. As it was mentioned previously, the basic observable of any GNSS is the travel time spent by the signal, Δt. If the receiver is able to recover this information from the signal, for instance by comparing the incoming PRN code with a locally generated replica, the apparent geometrical distance can be computed such as $R = \Delta t \cdot c$, where c is the speed of light in vacuum. However, this model is not entirely achievable, since there is no knowledge about the receiver time offset with respect to the GNSS reference time. This is also true for the satellites' clocks. Nevertheless, the satellite clock bias scale, δt^s, is fewer (compared to the receiver time offset δt_u) due to the very stable atomic oscillators onboard. Then, our expression for the geometrical distance becomes:

$$R = [t_u(T_2) - t^s(T_1)] \cdot c \tag{1.1}$$

where $t_u(T_2)$ is the time in which the signal is received, in the time scale of the receiver, and $t^s(T_1)$ is the transmission time of the signal, in the time scale of the onboard atomic clock. Additionally, there are other factors that affect the signal travel time and need to be included in Equation 1.1, such as the effects caused by the atmosphere, instrumental delays, multipath and receiver noise. The consequence of all these added errors is that, instead of determining the geometrical range between the user and the satellite, what it is computed is a *pseudorange*, defined as [Sanz et al., 2013]:

$$R_{P_f} = \rho + c(\delta t_u - \delta t^s) + T_r + \alpha_f STEC + K_{P_{f,u}} - K^s_{P_f} + \mu_{P_f} + \epsilon_{P_f} \tag{1.2}$$

where ρ is the actual geometric range from the satellite to the receiver antenna phase centers (APCs) at emission time. δt_u and δt^s are the receiver and satellite clock offsets, including the relativistic satellite clock correction. T_r is the tropospheric delay. $\alpha_f STEC$ is a frequency-dependent ionospheric delay term, where α_f is a conversion factor ($\frac{40.3}{f^2} 10^{16} m/(10^{16} e^-/m2)$,). $K_{P_{f,u}}$, $K^s_{P_f}$, are the receiver and satellite instrumental delays for code measurements, respectively. Finally, μ_{P_f} accounts for multipath effects.

GNSS receivers can also use the phase of the carrier signal to determine the signal travel time. Once again, the essential idea of this concept is to compare the locally generated carrier phase with respect to the incoming one. The difference will be then a fractional part of a full cycle, which provides a finer resolution (1 cycle in L1 is approximately 19 cm) compared to the code measurements previously explained. Unfortunately, the total number of prior cycles in the incoming carrier phase signal is not known. This ambiguous feature on the carrier phase measurements is called *integer ambiguity*, commonly denoted in the literature as N. Consequently, the formulation for the carrier phase measurement at a given frequency f is as follows:

$$\Phi_{L_f} = \rho + c(\delta t_u - \delta t^s) + T_r - \alpha_f STEC + K_{L_{f,u}} - K^s_{L_f} + \lambda_{L_f} N_{L_f} + \lambda_{L_f} w + \epsilon_{L_f} \tag{1.3}$$

where the additional terms (with respect to Equation 1.2) are the integer ambiguity $\lambda_{L_f} N_{L_f}$ and the wind-up effect, $\lambda_{L_f} w$, due to relative variations in the satellite and/or receiver antenna orientation, which can introduce false changes in the range determination.
Notice also that in Equation 1.3, the ionospheric delay is negative. This is a direct result of the behavior of the ionosphere as a dispersive medium for microwaves [Seeber, 2008]. Then, there is a delay experienced by the code measurements and an advance experienced by the carrier phase measurement [Misra and Enge, 2006].

The different errors affecting the GNSS observables (depicted and dimensioned in magnitude in Figure 1.4) can be modeled and corrected until obtaining accuracies according to needed requirements in either Standard Point Positioning (SPP) or high-accuracy positioning services (HAS). This latter scenario, which demands centimetric accuracy, is achieved by different techniques such as Precise Point Positioning (PPP), Real-Time Kinematics (RTK) or Network-Real-Time Kinematics (NRTK). For example, the clock modeling in SPP mode comprises applying a correction contained within the navigation message (a set of coefficients to be filled into a polynomial). This correction is computed by the Ground Segment, uploaded to the satellites and then broadcast to the users. In the other case, HAS requires the use of precise clock products computed by dedicated centres, such as the International GNSS Service (IGS) or the Center for Orbit Determination in Europe (CODE), operated by the Astronomical Institute of the University of Bern (AIUB). The quality of these products is directly proportional to the time taken to compute it (as seen in table Table 1.2), being the most precisely the final products available after two weeks, followed by rapid products, published after 18 hours approximately, and lastly the ultra-rapid products, available every 6 hours. This proposes a challenge for real-time applications, for which the level of quality of the broadcast products is sometimes not sufficient. The difference between using SPP or, for instance, the classical PPP clock corrections is at the order of 4.9 ns ($\approx$1.5 m).

Another different and resourceful approach to reduce errors or to extract valuable information of specific effects in the GNSS observables is to combine the different GNSS observables (Equation 1.2 and Equation 1.3). For instance, the following linear combinations can be defined for dual-frequency receivers [Sanz et al., 2013]:

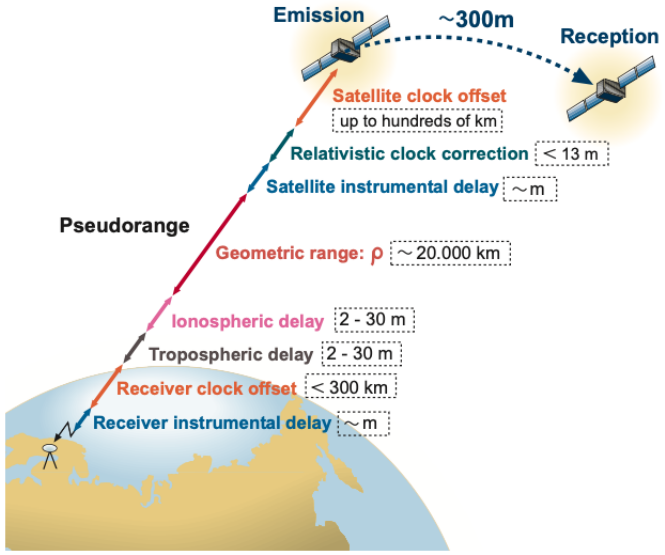

Figure 1.4: Pseudorange measurement contents and magnitude of errors budget [Sanz et al., 2013]

Table 1.2: IGS GPS orbits and clock products [Sanz et al., 2013]

Products	Broadcast	Ultra-rapid		Rapid	Final
		Predicted	Observed		
(delay)	(real-time)	(real-time)	(3–9 h)	(17–41 h)	(12–18 d)
Orbit GPS	100 cm	5 cm	3 cm	2.5cm	2.5 cm
(sampling)	(2 h)	(15 min)	(15 min)	(15 min)	(15 min)
Clock GPS	5ns	3ns	150ps	75ps	75ps
(sampling)	(daily)	(15 min)	(15 min)	(5 min)	(30 s)

Ionosphere-free (IF) combination, useful to reduce up to 99.9% the first-order effect of the ionosphere.

$$\Phi_{IF} = \frac{f_1^2\Phi_1 - f_2^2\Phi_2}{f_1^2 - f_2^2} \quad , \quad R_{IF} = \frac{f_1^2 R_1 - f_2^2 R_2}{f_1^2 - f_2^2} \tag{1.4}$$

Geometry-free (GF) combination, which eliminates the geometrical component of the measurements, leaving the frequency-dependent effects (this is the reason why it is also known as *ionospheric combination*).

$$\Phi_{GF} = L_1 - L_2 \quad , \quad R_{GF} = P_2 - P_1 \tag{1.5}$$

Wide-laning and *Narrow-laning combinations*, implemented to generate a resulting measurement with a wider or narrower wavelength, respectively.

$$\begin{aligned} \Phi_W &= \frac{f_1\Phi_1 - f_2\Phi_2}{f_1 - f_2} \quad , \quad R_W = \frac{f_1 R_1 - f_2 R_2}{f_1 - f_2} \\ \Phi_N &= \frac{f_1\Phi_1 + f_2\Phi_2}{f_1 + f_2} \quad , \quad R_N = \frac{f_1 R_1 + f_2 R_2}{f_1 + f_2} \end{aligned} \tag{1.6}$$

Dual-frequency receivers can directly implement the IF combination to correct from the ionospheric effects, having the trade-off of a resulting larger noise (about three times in contrast to individual signals) in the case of working with carrier-phase measurements[Seeber, 2008]. In

contrast, single-frequency receivers are not capable to build the IF combination, being forced to apply an external ionosphere modeling, each offering different performances. For instance, in GPS the Klobuchar's model [Klobuchar, 1987a] reduces the ionospheric range error by about 50% [Sanz et al., 2013] by transmitting a set of parameters within the navigation message, independently from the user receiver's position, considering the ionosphere as a thin layer concentrated 350 km. Another example of an ionospheric model for single-frequency GNSS users is the NeQuick model [Radicella, 2009], implemented by the Galileo system, which provides the electron density according to 5 different defined regions (Northen, Northern Midlle, Equatorial, Southern Middle and Southern) and time.

1.2 Ionosphere

The ionosphere, a layer commonly defined from a 50 km height up to 2000 km [Bilitza et al., 2022], relates to the portion of the earth's atmosphere in which there is a sufficient quantity of electrons and ions to affect electromagnetic waves. The electron density (N_e) on the ionosphere is not uniform, being driven mainly by the solar X- and Extreme UltraViolet (EUV) rays in the solar radiation and the incidence of charged particles [Sanz et al., 2013][Teunissen and Kleusberg, 2012]. When this radiation interacts with the ionosphere two processes can be identified: ionization, when the energy of the incoming radiation is sufficient to remove an electron from a neutral gas atom or molecule, and the contrary scenario, denominated recombination, in which a free electron is captured.

Most of the trajectory traveled by GNSS signals occurs in vacuum conditions, where it can be considered electromagnetic signals experience no affectation. However, this consideration is not longer valid when passing through earth's atmosphere, where the change in the media in which the GNSS signals travel results in a variation in the propagation speed [Sanz et al., 2013][Misra and Enge, 2006], as seen in Figure 1.5.

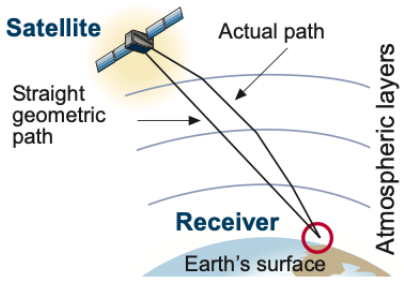

Figure 1.5: Bending effect of a GNSS signal travelling through atmosphere [Sanz et al., 2013]

This bending effect on the GNSS signal is not constant and unique across the atmosphere. For instance, the delay on the GNSS signals caused by the troposphere depends on the layer temperature, pressure and humidity. When considering the ionosphere (a layer defined by the electron content in the atmosphere) the delay of the GNSS signals depends on rather more complex factors.

1.2.1 Ionosphere definition and modeling

Generally, the electron content distribution varies following some repeated patterns: from day to night, seasonally, according to the 11 years of solar-cycle activity and depending on the

geographical location of the user receiver. The maximum electron density is found at the top of the bottomside ionosphere (Figure 1.6), which in turn is divided into several regions [Jursa, 1985]. Sporadic short-term fluctuations also have occurrence at the ionosphere. For instance, strong disturbances in the earth's magnetosphere can yield into the so-called ionospheric storms, increasing the ionization process [Buonsanto, 1999]. Another interesting example are the Solar Flares (SF), referred to sudden enhancement in solar irradiance, spanning time scales from minutes to hours, in both the EUV and the X bands[Curto et al., 2019]. All these short-time ionospheric effects may bring difficulties to the GNSS signal acquisition process, producing not desired effects, such as loss in the carrier-phase tracking (known as cycle-slips).

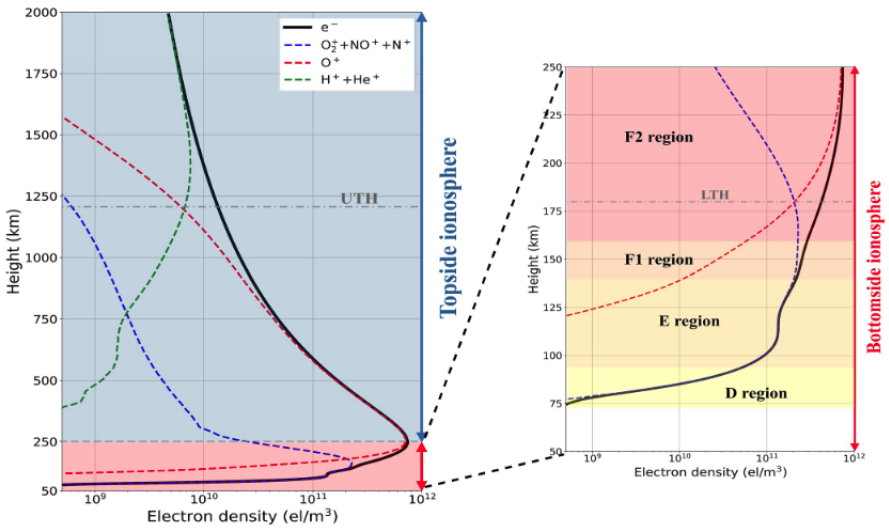

Figure 1.6: Vertical electron density profile and a zoom at the D, E, F1 and F2 layers [Bilitza et al., 2022]

TEC computation

The effect of the electron density (Ne) on a GNSS receiver, u, can be expressed as the Total Electron Content (TEC) integrated over the GNSS signal travel path, l, up to the satellite, s, in such a way that:

$$\mathtt{TEC} = \int_{\mathtt{u}}^{\mathtt{s}} \mathtt{Ne}(\mathtt{l})\, \mathtt{dl} \tag{1.7}$$

In other words, as defined in [Misra and Enge, 2006], TEC is the number of electrons in a tube of 1 m^2 cross-section extending from the receiver to satellite, expressed in Total Electron Content Units (TECU), where 1 TECU is equivalent to $10^{16}\mathtt{e}^-/\mathtt{m}^2$. This electron density produces different delays in electromagnetic wave propagation according to its frequency. For instance, in L1/E1 GNSS band the resulting delay caused by 1 TECU is 16.2 cm, whereas for L2 band is 26.7 cm.

From a user receiver located over the earth's surface, the traveled GNSS signal path length is not the same for a satellite directly over the user receiver's zenith than for a satellite at a low elevation over the horizon. These two different scenarios lead to a more precise definition of TEC: the Vertical Total Electron Content (VTEC), defined as if the satellite was directly at the receiver's zenith, and the Slant Total Electron Content (STEC) in any other case. The relationship between both re-definitions is given by the following expression [Misra and Enge, 2006]:

$$\mathtt{STEC} = \mathtt{VTEC} \cdot \mathtt{M}(\epsilon) \tag{1.8}$$

where it is assumed a concentrated and thin layer for the ionosphere at height $\mathtt{h_{ion}}$, the *mapping function* ($\mathtt{M}$) is a function depending on the satellite elevation angle (ϵ) and is defined by:

$$\mathtt{M}(\epsilon) = \frac{1}{\cos\chi} \tag{1.9}$$

where χ is the zenith angle between the signal path and a horizontal plane in the mean altitude $\mathtt{h_{ion}}$([Seeber, 2008]). This relation is valid at the intersection between the ionospheric layer and the line-of-sight path from the user receiver to the satellite in view, as a single point denominated Ionospheric Pierce Point (IPP).

The delays experienced by the GNSS signal due to the ionospheric effects can be used to detect sudden increases of STEC. In this sense, it is possible to use the GF combination for a given receiver "i" and a GNSS satellite "j", such as:

$$\Delta\mathtt{STEC}_i^j(t) = (\mathtt{L_{GF}}_i^j(t) - \mathtt{L_{GF}}_i^j(t-\tau)) \tag{1.10}$$

where τ is selected in such a way $\Delta\mathtt{STEC}_i^j(t)$ is sensitive enough to detect unexpected increments.

1.3 Research objectives and state of the art

The proposed initial research plan covers the complete objectives achieved during the development and course of the doctoral formation, being fundamentally:

- Propose a real-time implementation methodology for the ionospheric indexes AATR, MSTID, and SF.
- Implementation of an ionospheric corrections tool in real-time.
- Assessing the results of the ionospheric corrections tool in real-time.

The definition of the AATR and MSTID indexes were introduced to the scientific community in [Juan et al., 2018] and [Hernández-Pajares et al., 2006], respectively. In the AATR index case, numerous indicators are available to characterize ionospheric activity (see for instance [Pi et al., 1997], [Jakowski et al., 2006], [Gulyaeva and Stanislawska, 2008], [Cherniak et al., 2018] and [Wilken, Volker et al., 2018]), each with different performance, suitability, and applications. However, the AATR index stands out thanks to its sensitivity to regional ionospheric behavior, being able to identify specific effects on GNSS users, making it a reliable and valuable tool for identifying conditions such as degraded availability on SBAS systems. In the other case, since the first studies detecting MSTID events using GNSS signals [Afraimovich et al., 1998][Saito et al., 1998][Calais et al., 2003][Tsugawa et al., 2007], there has been a growing number of studies exploring various applications and datasets in terms of their spatial and temporal coverage. The MSTID index emerges as one of these new implementations, which aims to serve as a tool for alerting NRTK users from using GNSS measurements impacted by the MSTID effects. This document is a contribution to the related literature, presenting the real-time implementation of the before mentioned indexes, operating in a continuous and automatic manner within the real-time identification and tracking system for travelling ionospheric disturbances, which was developed as part of the European Commission project “TechTIDE”.

Additionally, a solar flare detector based on GNSS measurements performing in real-time is incorporated next to the computation of the AATR and MSTID indexes. This set of tools can be used to monitor space weather effects revealed by GNSS signals operating in real-time. While different types of GNSS detectors of solar flares have been defined in several publications [Afraimovich, 2000][Afraimovich et al., 2001] [Liu et al., 2004][García-Rigo et al., 2007][Hernández-Pajares et al., 2012], the literature lacks contributions regarding the definition of a GNSS solar flare detector that can operate as a complementary tool to confirm solar flare effects reported by magnetic sensors. Publications 1 and 2 presented in this document make a major achievement by demonstrating the capability of mixing measurements obtained from different sensor to provide a robust detection system. The derived GNSS solar flare detector is implemented in real-time alongside the AATR and MSTID indexes.

Regarding objectives two and three, important contributions have been made to ionospheric modelling (see for instance [Klobuchar, 1987b], [Bilitza, 2001] or [**?**], as well as the capability of computing such products in real-time mode [Coster et al., 1992][Roma-Dollase et al., 2018][Nie et al., 2019], reporting products accuracies of several TECUs. In the case of ionospheric corrections targeting high-precision applications, several works have been published informing the advantages of implementing unambiguous carrier phase measurements and the FPPP model to produce accurate ionospheric corrections in short times (see [Juan et al., 2012][Rovira-Garcia et al., 2015][Rovira-Garcia et al., 2016a][Rovira-Garcia et al., 2019]). These valuable contributions represent the foundations for the research presented in the fourth publication, which the major achievement is the deployment a tool to compute real-time ionospheric corrections on a systematic way, using data collected from GNSS stations worldwide distributed with reported results of ionospheric corrections with that meet the requirements established by the new Galileo service for high-accuracy positioning.

1.4 Methodology

The principal input data used in the development of this thesis are GNSS observation files in Receiver INdependent EXchange Format (RINEX) format. This data is transmitted in real-time by every receiver presented as a blue dot in Figure 1.7, using the Networked Transport of RTCM via Internet Protocol (NTRIP), defined specifically to stream GNSS data over the Internet. The real-time collection of these data streams is done in a daily basis using the third-party software BKG Ntrip Client (BNC) [Weber and Mervart, 2007]. BNC allows the selection of the output format file (RINEX version 3), and the data rate sampling (5 seconds). This configuration allows for a daily results-based data archive, which is a common and standard practice in most GNSS-related data centers.

Once the RINEX data is available, it is executed a series of sequential algorithms written in *Bash*, *Perl* and *Fortran* programming languages, to compute all the output files. The selection of these programming languages is based on their computational load and speed performances, key assets in real-time implementations.
A modular approach has been implemented, in which programs are executed sequentially, from the treatment of the GNSS observation data up to the ionospheric correction generation. This step-by-step methodology brings some useful advantages to the proposed implementation, such as being able (as operator of the tool) to supervise the entire program status by checking

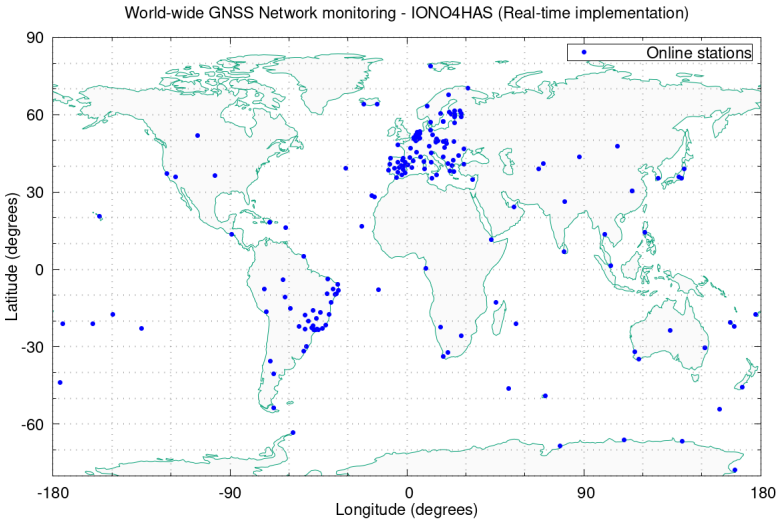

Figure 1.7: Implemented Global network of GNSS receivers. A list with the complete information is given in Appendix A

the generated control files at each stage, and the computational simplicity and speed experienced by the machine running the software by generating one single data flow.

The operative validation of the entire tool has been assessed using reference data for each product. In the case of publications one and two, in which a Solar Flare detector based on GNSS data was developed, the assessment of the performance was conducted with external and independent data from the GOES X-ray mission used to track solar activity and solar flares. The methodology and therefore the results obtained in the third publication were validated using a novel methodology for assessing the errors in positioning based on fixing carrier-phase ambiguities in the undifferenced measurements. Finally, the last publication techniques and results are validated using as reference ionospheric values derived from unambiguous, unbiased and undifferenced carrier-phase measurements.

The presented results are obtained under the frame of the following scientific projects:

1. European Union's Horizon 2020 research and innovation programme under grant agreement 776011 (TechTIDE project).
2. European Space Agency (ESA) contract IONO4HAS 4000128823/19/NL/AS.
3. Spanish Ministry of Science, Innovation and Universities RETOS RTI2018-094295-B-I00 (Programa Estatal de I + D + i Orientada a los Retos de la Sociedad).

The data, resources and additional products used to achieve the research objectives were taken from:

1. The National Oceanic and Atmospheric Administration (NOAA) for the satellite system which collects valuable information regarding solar radiation and for publishing these data.
2. INTERMAGNET and all the collaborating observatories which provide high-quality magnetic data.

3. The International Service of Rapid Magnetic Variations and their collaborating observatories.
4. CATNET NRTK service from the Cartographic and Geologic Institute of Catalonia, Spain (Institut Cartogràfic i Geològic de Catalunya – ICGC)
5. International GNSS Service (IGS).
6. Centre for Orbit Determination in Europe (CODE) Analysis center.
7. Bundesamt für Kartographie und Geodäsie (BKG).
8. The Crustal Dynamics Data Information System (CDDIS).
9. GNSS real-time data from *Rede Brasileira de Monitoramento Continuo belonging to Instituto Brasileiro de Geografia e Estatística* (IBGE).
10. GNSS real-time data from the EUREF Permanent GNSS Network.
11. GNSS real-time data from the Geoscience Australia AUSCORS.

Chapter 2
Results

This chapter presents the real-time deployment and implementation of techniques to detect and mitigate the effects of a disturbed ionosphere on the user positioning, and subsequently, the real-time implementation of the ionospheric corrections system applied to HAS.

2.1 Monitoring ionosphere disturbances using GNSS signals

The first stage of my research was devoted to the accomplishment of a real-time tool to compute the so-called *prefit residuals* from the GNSS observations. The *"prefit residuals"* denomination is given in this document to refer to the first modeling stage of GNSS measurements (code and carrier phase), in which known effects are corrected, such as the code and phase leap milliseconds, satellite and clock correction, satellite and receiver Antenna Phase Center (APC) and detection of cycle-slips.

2.1.1 GNSS signals as a tool to confirm Sfe in geomagnetism

The main goal of this task was to build an automatic and reliable tool based on GNSS observations to confirm Solar Flares Effects (Sfe) reported by magnetometers. A statistical study was conducted over the postulated GNSS SF detection parameters and threshold values were determined, to be compared with the Sfe detected by geomagnetism and crosscheck its effectiveness.

Definition of detection parameters

In subsection 1.2.1 of this document, it was brought to the light of this discussion the capability of GNSS measurements to detect enhancements on the STEC, similar to those observed in the presence of a SF. Therefore, the implemented real-time technique uses the double difference of $\mathtt{STEC}$ with respect to time (denoted as $\Delta^2\mathtt{STEC}$) at the Sub Solar Point (SSP), and the cosine of the angular distance (χ) between the Sub Solar Point and the IPP of the measurement.

The selection of these parameters is based on [Wan et al., 2002][Hernández-Pajares et al., 2012][Curto et al., 2019], where it was presented the linear dependency between $\Delta\mathtt{STEC}$ and $\cos(\chi)$. In [Curto et al., 2019], $\Delta^2\mathtt{STEC}$ demonstrated to have a more clear (better) correlation than $\Delta\mathtt{STEC}$. Therefore, the correlation coefficient (ρ), in combination with $\Delta^2\mathtt{STEC}$, were selected as good indicators of the presence of a SF, as depicted in Figure 2.1.

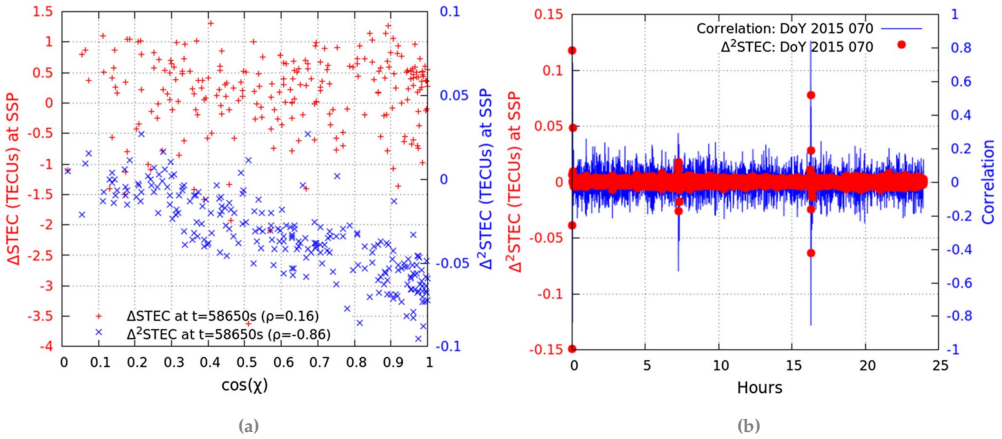

(a) (b)

Figure 2.1: (a) $\Delta\mathrm{STEC}$ (red) and $\Delta^2\mathrm{STEC}_i^j$ (blue) as a function of the cosine of the angular distance between the SSP and the IPP, at 58650 s of March 11, 2015. (b) $\Delta^2\mathrm{STEC}_i^j$ at the SSP (red points) and the corresponding correlation coefficient of the fittings (blue line) for March 11, 2015.

Selection of detection threshold values

A period of 11 years (2008-2018) was used to statistically characterize the selected GNSS parameters ($\Delta^2\mathrm{STEC}$ and $\cos(\chi)$). Consequently, statistical contingency tables were built to analyze the correlation between $\Delta^2\mathrm{STEC}$ and $\cos(\chi)$, implementing the Youden Index to determine the optimal threshold values. The selected values, $\Delta^2\mathrm{STEC} >= 0.01$ (in TECU) and $\rho >= 0.25$, proved to guarantee a satisfactory trade-off between reducing the false positive cases and increasing the true positive rates, maintaining a convenient number of SF candidates.

Results and future work

The developed SF detector based on GNSS measurements was tested over one solar cycle and currently operates continuously in real-time. During this period, it has been observed some unique advantageous features and some other limiting factors:

- The implementation of $\Delta^2\mathrm{STEC}$ rather than $\Delta\mathrm{STEC}$ provides two main advantages: a much clearer correlation coefficient ρ and a reduction on the typical ionospheric daily variations, which in the case of using $\Delta\mathrm{STEC}$, tends to bury the TEC enhancement resulting from a SF.
- The statistical study reveals a Gaussian distribution for the correlation coefficient ρ, which can be exploited as a self-consistent way of measuring the confidence level of SF detections.
- The extended global location of used GNSS receivers (Figure 1.7) provides a consistent coverage where magnetic observatories experience "blind" zones.
- The detection rate of SF lasting few minutes is very high (near 100%). However, the use of $\Delta^2\mathrm{STEC}$ almost restricts the SF detector to focus on these short TEC enhancements. This is a potentially improvable drawback it has been reported difficulties for the proposed SF detector to identify long flares with a gradual rise.

2.1.2 Medium-Scale traveling ionospheric disturbances: impact on user positioning

The developed research first characterizes the impact of Medium Scale Travelling Ionospheric Disturbance (MSTID) on the precise positioning technique denominated Network-Real-Time Kinematics (NRTK), assessing the degradation on the positioning of a user of the service working with single-frequency measurements. Additionally, it is proposed an index as a tool to alert users about the presence of MSTID effects on the GNSS measurements.

The research was conducted using one year of data (from the day of the year 200 in 2017 up to the day of the year 200 in 2018), using selected stations belonging to the CATNET NRTK service of the Cartographic and Geologic Institute of Catalonia, in Spain. The implementation of this index is currently executed in real-time, using the complete network of GNSS stations presented in Figure 1.7.

Assessing the impact of MSTID on the GNSS measurements

The first step was to define and generate reference measurements to be compared with respect to measurements affected by the MSTID effects. The traditional approach in NRTK is to generate double differences of the carrier-phase and code measurements (Equation 1.3 and Equation 1.2, respectively) with respect to a reference receiver and a reference satellite. In [Timoté et al., 2020], a novel method was implemented in which carrier-phase ambiguities are fixed before proceeding to generate the double differences, generating undifferenced and unambiguous STEC values. This process is presented in Figure 2.2, where it is evident the advantage of the proposed approach: the identification of the MSTID effects on the GNSS measurements.

Obtaining a reference navigation solution

The next step was to define a reference solution for user navigation, in such a way the effects of the MSTID can be determined when comparing both reference and non-reference navigation solutions. Using the defined reference measurements, the IF combination was built, removing the degradation of the differential ionospheric correction affecting the performance of RTK and NRTK techniques when the baseline between the user and receiver increases.

Linking the degradation in user's position with MSTID

The TEC fluctuations produced by a MSTID can be detected using the $\Delta^2\mathtt{STEC}$, finely tuned (τ) to detect ionospheric perturbations with periods at the order of 10 min. In this way, an indicator of the MSTID activity can be defined as:

$$\mathtt{MSTID}^2_{\mathtt{IDX}}(t) = \frac{1}{20} \sum_{i=t-2\tau}^{t} (m(\epsilon) \cdot \Delta^2\mathtt{STEC}(i))^2 \tag{2.1}$$

Therefore, it is possible to verify that MSTID not only affects the user's measurements, but also the ionospheric corrections provided by reference stations, and therefore, the final user positioning. This is due to the fact that NRTK assumes ionospheric linear behavior between reference receivers and rover receivers, something that was shown to be not true when a MSTID affects GNSS measurements [Timoté et al., 2020].

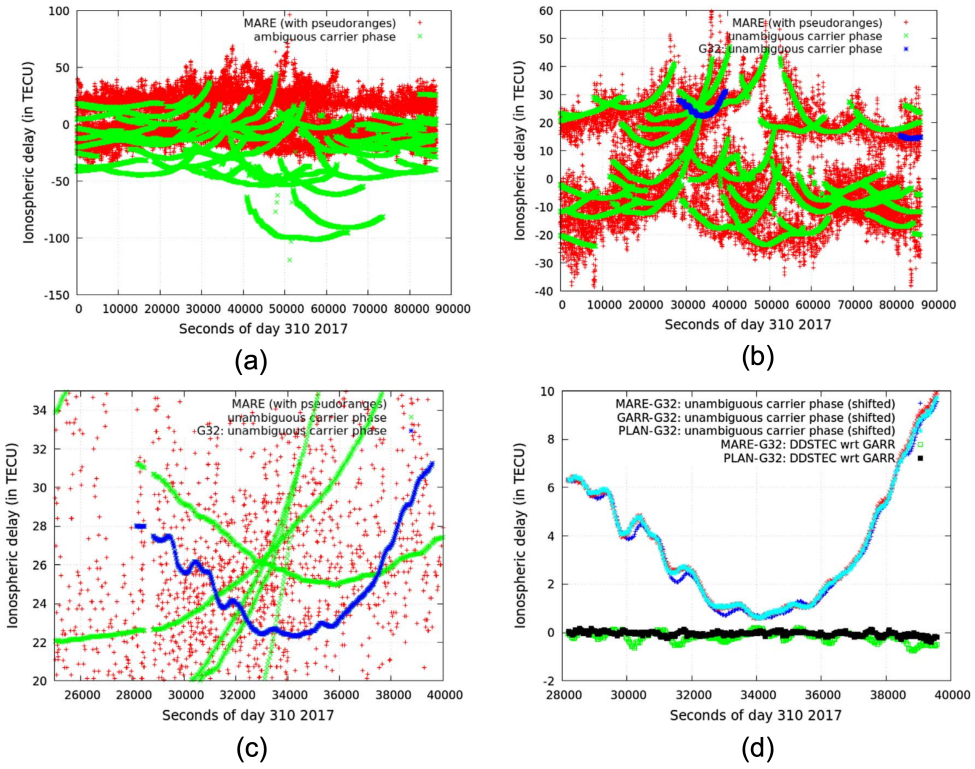

Figure 2.2: Obtaining reference measurements process: Top left panel (a) are *raw measurements* implementing the GF combination using carrier phases (green) and pseudoranges (red). The top right panel (b) corresponds to the measurements where the carrier-phase ambiguities have already been fixed. The bottom left panel (c) is a zoomed picture of the MSTID event affecting satellite G32 highlighted in blue in panel (b). The bottom right panel (d) compares the implemented novel approach for satellite G32 measured by receivers MARE (blue), GARR (red), and PLAN (cyan). The ionospheric delays with respect to GARR are also depicted in green (MARE) and black (PLAN), obtained through the traditional NRTK double differencing method

.

Reducing user's position degradation caused by MSTID by means of the $MSTID_{IDX}$

Once MSTID can be detected and its magnitude can be quantified, the subsequent step was to statistically define thresholds values of the defined $\texttt{MSTID}_{\texttt{IDX}}$ associated to the entire set of stations in NRTK service. In this way it is possible to exclude observations presenting large $\texttt{MSTID}_{\texttt{IDX}}$ values, considerably reducing the degradation in the user positioning. This approach led to the definition of the following threshold values:

- Observations for which $\texttt{MSTID}_{\texttt{IDX}}$ values are greater than 0.15 TECU, are considered as having a MSTID strong/high effect.
- Observations for which $\texttt{MSTID}_{\texttt{IDX}}$ values are greater than 0.10 but less than 0.15 TECU, are considered as having a MSTID moderate/medium effect.
- Observations with $\texttt{MSTID}_{\texttt{IDX}}$ values less than 0.10 TECU, are considered as having a MSTID weak/low effect.

From the implementation of these thresholds definition, it follows a reduction in the position degradation for the user of the NRTK service. In the case of the implemented CATNET network, such a decrease is more evident in users located farther with respect to reference receivers (around 25% of the degradation is reduced).

Results and future work

The proposed $\texttt{MSTID}_{\texttt{IDX}}$ was developed under the frame of the Warning and Mitigation Technologies for Travelling Ionospheric Disturbances Effects (TechTIDE) project, funded from the European Union's Horizon 2020 research and innovation programme under grant agreement No 776011. TechTIDE project provides in real-time a collection of different TID-related products [TechTIDE, 2022], among them the $\texttt{MSTID}_{\texttt{IDX}}$, for the complete set of GNSS stations presented in Figure 1.7.

The use of $\texttt{MSTID}_{\texttt{IDX}}$ is suitable as a warning tool for single-frequency users of services such as NRTK, preventing the use of measurements affected by MSTID. However, this conservative approach has the cost of decreasing the number of observations.

The presented implementation can be extrapolated to any region with a NRTK service, in such a manner that single-frequency users in the service area can be noticed about the presence of MSTID impacting the GNSS measurements.

2.2 Generation of ionospheric corrections for High Accuracy Services

The heart of the current research document is the adaptation and real-time implementation of a prototype of 3D high precision ionospheric correction caster tool on a continental scale, suitable for the expected new's Galileo capability for HAS. This research has been conducted under the sponsorship of the European Space Agency (ESA) under contract No. 4000128823/19/NL/AS). The current real-time development is based on the work performed by [Juan et al., 2012][Rovira-Garcia et al., 2015][Rovira-Garcia et al., 2016b] and [Rovira-Garcia et al., 2019].

2.2.1 Requirements of the ionospheric corrections

Broadcasting HAS corrections is a capability currently developed and under deployment of the Galileo, providing a service with a horizontal and vertical accuracy less than 20 cm and 40 cm, at a convergence time inferior to 100 s. This service is intended to be broadcast according to the SSR standard, including parameters such as satellite orbit errors, satellite clock errors, satellite signal biases, ionospheric propagation delays, and tropospheric delays [Agency, 2021]. Once the full capacity operation is achieved, the Galileo HAS shall provide user performances of about 20 cm 95% horizontal accuracy, 40 cm 95% vertical accuracy, and a convergence time of 100 s [Agency, 2021]. Regarding this convergence time requirement, it was shown in [Rovira-Garcia et al., 2015] the implementation of an ionospheric model able to speed up the convergence time of PPP with an accuracy better than 1 TECU, developing the Fast Precise Point Positioning (FPPP) concept [Juan et al., 2012].

2.2.2 A general overview of IONO4HAS corrections

The development of the IONO4HAS tool and its implementation in real-time is done according to the Figure 2.3. The basic data input are GNSS observations in RINEX format collected simultaneously from the worldwide network presented in Figure 1.7.

In this way, it is possible to separate the operative functionalities of the IONO4HAS tool:

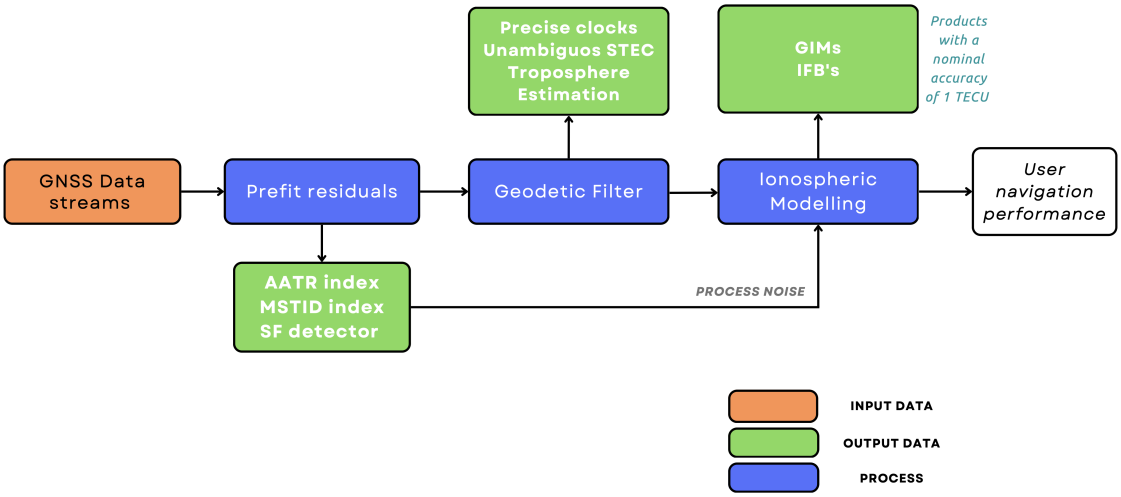

Figure 2.3: Schematic module representation of the real-time ionospheric corrections.

- Prefit residual generation, to correct the observations from well-known effects (geometry effects, relativistic and antenna phase corrections, cycle-slip detection, etc).
- Geodetic filter, where parameters linked to non-dispersive effects are estimated (clock biases, tropospheric effects and carrier-phase ambiguities).
- Ionospheric modeling, estimating the DCBs for satellites and receivers and the vertical electron content for a set of IGP´s distributed in two layers, accounting for the bottom side and topside ionosphere.

Prefit residuals generation

RINEX files are collected on a daily basis using third-party software (BKG Ntrip Client (BNC) [Weber and Mervart, 2007]), to then be converted into a plain text file and generate the *prefit residuals* (section 2.1). From this module, the SF detector (subsection 2.1.1), the MSTID index (subsection 2.1.2), and the Along Arc TEC Ratio (AATR) index are computed. This later product, the AATR, is a regional indicator of the ionosphere activity, used as the metric to characterize the ionosphere operational conditions in the frame of the European Space Agency activities on the European Geostationary Navigation Overlay System (EGNOS) and as a standard tool by the International Civil Aviation Organization (ICAO) for joint ionospheric studies in Satellite-Based Augmentation System (SBAS) [Juan et al., 2018].

The Geodetic Filter module

The performance and capabilities of the so-called Geodetic Filter are demonstrated in [Rovira-Garcia et al., 2015], where it has been shown the advantages of implementing the FPPP corrections:

- Satellite orbits with an error maintained at 3.9 centimeters compared to IGS Final Products.
- Precise satellite clocks accurate to two-tenths of a nanosecond with respect to IGS Rapid Products.
- Tropospheric delay (i.e., "wet" residual estimation after a first model and correction is applied to the measurements during the *prefit residuals* computation.)

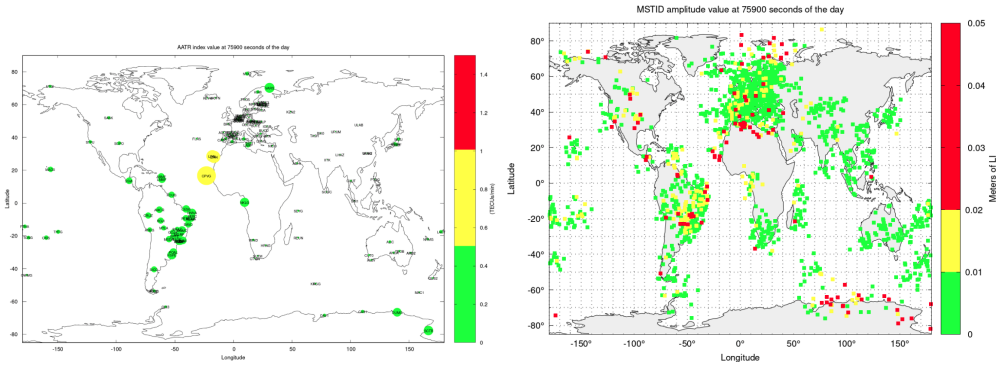

Figure 2.4: Real-time (A) $\texttt{AATR}_{\texttt{idx}}$ and (B) $\texttt{MSTID}_{\texttt{idx}}$ values at 75900 seconds of November 4, 2020, for the stations in Figure 1.7. The color scale indicates the type of activity: green for low/weak, yellow for medium/moderate, and red for high/strong.

- Unambiguous STEC data from the GF combination of carrier phases.

This module implements a pair of sub-filter modules for computing separately the beforementioned products. A Kalman Filter denominated "fast filter" generates satellite and receiver clock offsets with a higher rate than a second Kalman Filter implemented, denominated "geodetic filter" [Zhang et al., 2018], producing the remaining products (slow-varying parameters). The fast filter uses a reduced set of stations, depicted in Figure 2.5 and listed in Appendix A, to generate products with a higher update time (30 s).

The computation of ionospheric corrections

The proposed ionospheric modeling module takes in real-time the highly accurate STEC (GF combination) data computed by the Geodetic Filter to provide every 300 seconds the Vertical Total Electron Content (VTEC) for a set of IGPs distributed in two different layers accounting for the bottom side and topside ionosphere, alongside with estimates for the satellites and receivers DCB.
In this way, the proposed modeling of the ionospheric corrections exhibits the following characteristics:

- Model geometry: as mentioned earlier in this section, a two-layer model approach is implemented. Layer one is located at 270 km containing 7176 IGPs, and layer two is located at 1600 km and contains 1792 IGPs. The IGPs distribution is defined with respect to MODIP and Local Time (LT) coordinates.
- Ionospheric corrections interpolation: users estimate at each epoch the ionospheric delay over an IPP as a linear combination of the vertical electron content from eight IGPs (four at each layer).
- Process noise: both products, the electron content at the IGPs and the satellite and receiver DCBs are considered as random walk processes. The process noise modeling takes into account the region where the receiver is located.

Thanks to the undifferenced ambiguity fixing in the geodetic filter, a very accurate geometric free combination is obtained, producing very accurate estimates at the ionospheric model and reducing the convergence time of the PPP solution.

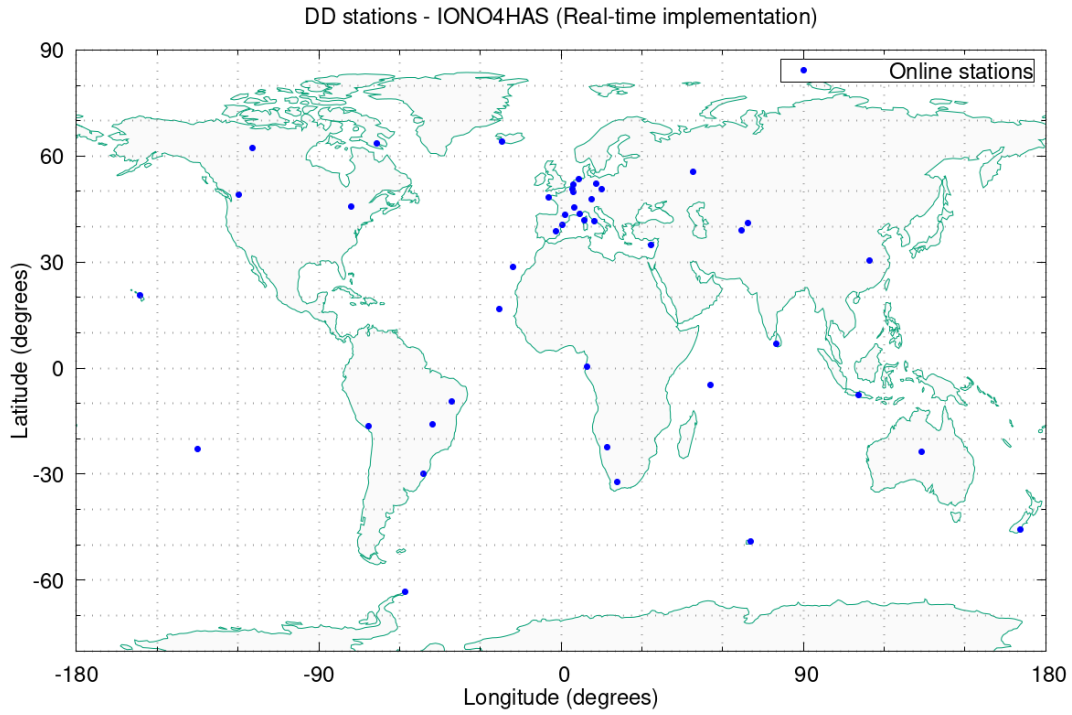

Figure 2.5: Near 40 GNSS stations are used by the "fast filter" within the Geodetic filter to compute satellite and receiver clock corrections.

Implementing a dual-layer model allows considering in the modeling of the different effects of the bottom side (main ionosphere content) and the topside (plasmasphere) layers of the ionosphere. From this design, the adopted grid in Local Time and MODIP coordinates represents a convenient synergy to achieve a reduction in the total number of IGPs implemented, reducing the computational load at the CPF as well as shortening the total data corresponding to ionospheric corrections to be broadcast in the HAS message. Additionally, the defined methodology enhances the performance of the ionospheric model providing higher density at low-latitude regions, where more ionospheric gradients are expected, improving precise navigation results in such locations.

2.2.3 Assessing the performance of the ionospheric model

The definition of an accurate and valid reference of the ionospheric delay is in general a very challenging task. In this research, the defined ionospheric model selected as a reference tailored for HAS is based on unambiguous, unbiased, and undifferenced carrier-phase measurements defined in [Rovira-Garcia et al., 2016b], which provides errors at the level of a tenth of a TECU. In addition to the performance of this ionospheric model, there is also the advantage of reducing the number of parameters to estimate, by about two orders of magnitude, when compared to other cited models. Moreover, in order to analyze and contextualize the results obtained, the test applied to the proposed real-time ionospheric model is also carried out over the rapid combined GIM of the IGS, termed IGRG.

The data set of the test comprises two different weeks in 2019 and 2021, for which the ionospheric activity has been characterized using the $\texttt{AATR}_{\texttt{idx}}$. The number of total GNSS stations included is about 180, distributed worldwide. From this network, seven stations were profiled as rover receivers (or users of the HAS), separated from the closest reference receiver in ranges from 100

up to 1000 km.

2.2.4 Results and future work

The main result of the research is the validation of the proposed ionospheric modeling as suitable for high-accuracy positioning services (HAS), allowing users of the service to correct from the ionospheric delay with an accuracy level of one TECU in well-sounded regions. This result was confirmed using 7 rover receivers within a network of around 180 reference stations distributed worldwide, focusing over Europe towards a potential implementation on the new's Galileo capability for broadcasting HAS corrections. The generated ionospheric corrections contain a prediction of the error, allowing HAS users to avoid degrading the already obtained accuracy and convergence time, provided by the solution based on the IF combination. Those results are currently being achieved on a daily basis in the real-time mode under the ESA project IONO4HAS.

The presented results can be validated by performing a real-time campaign over a larger period of time, focusing on the user navigation obtained by means of the ionospheric corrections. This future research is interesting because of the different scenarios and features that can be considered:

- Regions in Europe for which the number of GNSS stations is limited or the distribution is not profitable (especially in eastern Europe).
- The impact of having different observations from different GNSS constellations.
- Different user locations, for instance, the challenging low-latitude regions, especially near the South Atlantic Anomaly (where large and wide-ranging networks of GNSS stations in south America are transmitting observations in real-time).
- The generation of a metric based on statistics to characterize, over the full period of time, the performance of the user navigation. Especially, it is interesting to examine means to define error protection levels, in such a way the ionospheric model can also be assessed in terms of confidence of the results.

At the time of writing this document, the implementation of real-time ionospheric corrections has been in continuous operation for nearly a year. The collected results are currently being used to prepare a technical report that will be submitted as a scientific article to inform about the experienced performance of the ionospheric corrections in terms of operation and positioning, as seen by a user of the service.

This page intentionally left blank.

Chapter 3
Quality Indexes

This chapter provides the main information of the articles which composed this thesis document and presents some representative indicators to contextualize the relevance of the scientific journals in which the papers are published. In this sense, the contributions have demonstrated an appreciable relevance in related subjects and applications.
Additionally, it is presented additional research and academic contributions performed during my doctoral formation, such as the supervision of a master thesis.

3.1 Peer-reviewed Journals

The Table 3.1 provides the list of publications presented in this thesis and their corresponding journal. The Table 3.2 provides the relevance in the academic community of each journal in Table 3.1, using the latest Impact Factor (IF) and quartile data available, according to [Cla, 2021].

Table 3.1: Articles published in peer-reviewed journals

Journal Name	Publication Title	Year of the publication
Journal of Space Weather and Space Climate (**JSWSC**)	Confirming geomagnetic Sfe by means of a solar flare detector based on GNSS	2019
Journal of Space Weather and Space Climate (**JSWSC**)	Answer to the comments on "Confirming geomagnetic Sfe by means of a solar flare detector based on GNSS"	2020
Journal of Space Weather and Space Climate (**JSWSC**)	Impact of medium-scale traveling ionospheric disturbances on network real-time kinematic services: CATNET study case	2020
Journal of Geodesy (**JOGE**)	Ionospheric corrections tailored to the Galileo High Accuracy Service	2021

Table 3.2: Journals information and ranking in its category based on the impact factor.

Journal Name	ISSN	Impact Factor 2021	Impact Factor 5 Years	Quartile 2021
JSWSC	2115-7251	2.942	3.333	(40/87) Q2
JOGE	0949-7714	4.809	5.154	(13/34) Q2

3.1.1 Not incorporated Peer-reviewed Journals

During the doctoral research, there has been one additional publication not included in the collection of papers presented in Chapter 2, but worth to mention because it is in line with the main scope of this thesis. The main reason for not adding this scientific article is the large number of authors who contributed to writing it (14 professionals from 9 different organizations).

The paper *"An overview of methodologies for real-time detection, characterization and tracking of traveling ionospheric disturbances developed in the TechTIDE project"* [Belehaki, Anna et al., 2020] was published in 2020 in the Journal of Space Weather and Space Climate (**JSWSC**), presenting and defining the main techniques and results obtained in the *"TechTIDE"* project. The contribution in this paper was the presentation of the real-time implementation of two ionospheric indexes based on GNSS measurements: the Along Arc TEC Ratio (AATR) index, and the MSTID index.

3.1.2 Other scientific contributions

The development of a stable real-time tool producing different ionospheric-related products enabled the opportunity to detect unexpected phenomena in the ionosphere, fascinating and interesting enough to undertake the parallel task of proposing it as a main topic of a master thesis. The Erasmus student Giuseppe Troilo, Master in Space and Aeronautical Engineering, presented his final master dissertation *"Analysis of Ionospheric Disruptions in GNSS signals from Tonga eruption"* in July of 2022.

The master thesis main objective was the study of effects at the ionosphere detected by GNSS stations caused by the eruption of the volcano located in the Polynesian country of Tonga, on January 15, 2022. The real-time ionospheric tool presented in my doctoral thesis was operative during that day, allowing the master student to perform independently his own detailed analysis examining the real-time data as well as post-processed data. The results of this research identified and characterized the main features of the disturbances in the ionosphere due to the Volcano explosion.

Chapter 4: Conclusions

It is important to remark that the following conclusions respond directly to the objectives of the doctoral research: to deploy a real-time tool to first, generate ionospheric indexes and secondly, to produce ionospheric corrections.

It has been demonstrated the capability of the developed tool to perform in real-time, producing the expected products with the foreseen quality. This real-time capacity provides the operator with a tool with a more seamless and intuitive user experience, as operators can interact with the tool and see the results of their actions immediately. The achievement of this real-time feature is evidenced in all the publications:

- Despite the fact the main objective of the developed Solar Flare detector based on GNSS was to be used as a tool to confirm Solar Flare effects on the geomagnetism (a post-processed task), this detector is currently operative in real-time and performs efficiently under the mentioned circumstances (see subsection Figure 2.1.1).
- The implementation of the $\texttt{MSTID}_{\texttt{IDX}}$ within a NRTK service could help to reduce the degradation impact on users positioning caused by a MSTID, detected in real-time. In fact, this same approach can be translated to the other real-time deployed ionospheric index, the $\texttt{AATR}_{\texttt{IDX}}$, used by the ionospheric modeling module (see Figure Figure 2.3) to model internally the process noise variable. In [Belehaki, Anna et al., 2020], it is presented the format in which both indexes are provided to the interested scientific community as a continuous 24/7 service.
- In general terms, all the different products generated by the Central Processing Facility that computes the ionospheric corrections are available to be implemented by any user of the service with a latency of a maximum of around 30 s. This is, from the moment the observation data enters the tool up to the moment an ionospheric correction is produced, a time no longer than 30 seconds can be expected.

In terms of representing the current condition of the ionosphere, it has been shown that each scientific article is focused in developing methods to provide different information to account for the ionospheric effects. In this regard, the main findings of each publication are summarized as follows:

- A Solar Flare detector based on GNSS observations is built to confirm a list of Solar Flare Effects observed in geomagnetism. It was shown that the proposed Solar Flare detector is

defined to be optimum when its tuning parameters are set as $\mathrm{D^2STEC} \geq 0.01$ and $\rho \geq 0.25$. As seen in Table 4 of [Curto et al., 2019], these threshold values provide a very low rate of false positive cases with a very sufficient rate of true positive cases. Additionally to these satisfactory figures, there is also a compromise in decreasing the computational load, an issue achieved by reducing the number of potential candidates (around a 23% reduction).

- A definition and characterization of an index to detect and measure MSTID, denoted as $\mathrm{MSTID_{IDX}}$, shows to be of great benefit when implemented in positioning services such as the NRTK, reducing the degradation impact experienced by any user of the NRTK service by means of removing the GNSS observations polluted by the effects of the MSTID.

- An ionospheric corrections tool has been developed and deployed in real-time, with products assessed in post-process mode coherent to the requirements of the Galileo High Accuracy Service (see section subsection 2.2.1). This tool is able to provide ionospheric corrections with global coverage, according to the input GNSS data.
  The proposed tool operates with a modular and sequential approach design, meaning each module is in charge of producing a dedicated product, which in turn is used for the next module up to the final ionospheric correction is generated. This allows controlling the complete data process and computational flow.
  The FPPP model implemented has the ability to deliver ionospheric corrections with the required ionospheric accuracy, as well as realistic confidence bounds, for the Galileo HAS. In this regard, in well-surveyed areas and at mid-latitude stations, the majority (99%) of GPS and Galileo errors are less than 1 TECU, with the complementary capability of constraining large errors through the error prediction of the FPPP model.

Chapter 5: Publications

This chapter presents the collection of scientific publications accomplished during my doctoral research and formation. The section 5.1 provides a brief explanation regarding the thematic coherence joining all the presented publications, and the doctoral research itself. Then, section 5.2 presents the complete bibliographic information of the peer-reviewed journal articles and a copy of the original manuscripts.

5.1 Thematic justification

GNSS signals have been used in a wide and extensive range of applications, one of them being the possibility to analyse the status of the ionosphere. In this way, [Curto et al., 2019] and [Curto, Juan José et al., 2020] present the methodology and procedure to build and deploy a solar flare detector using the observations collected by GNSS receivers, which are sensitive to notice changes in the electron density at the ionosphere caused by solar flares. This detector is set as an automatized novelty tool to confirm Solar Flare effects detected by magnetic sensors.

Moreover, there are fluctuations on the ionospheric electron density which corresponds to travelling disturbances, with wavelengths of around tens of kilometers. This kind of disturbances are a degrading factor in high-accuracy positioning services, particularly in NRTK. The research on [Timoté et al., 2020] analyses these effects, and provides an index to warn NRTK users to dispose of GNSS measurements altered by the ionospheric travelling disturbance.

A complex model of the ionosphere is provided in [Rovira-Garcia et al., 2021], where the ultimate goal is to provide a high-accuracy correction of the ionosphere adapted specifically for Galileo users, improving their convergence time to fix a positioning. The definition of this correction system includes a series of key developments to guarantee the corrections provided by the model are in line with the expected Galileo High Accuracy Service requirements.

Finally, all these contributions have been deployed in real-time, being operative for almost one year, producing results in line with those mentioned in every respective publication.

5.2 List of articles in peer-reviewed journals

1. Curto JJ, Juan JM, Timote CC (2019) "Confirming geomagnetic Sfe by means of a solar flare detector based on GNSS" Journal of Space Weather and Space Climate 9:A42:1-15. DOI 10.1051/swsc/2019040
2. Curto JJ, Juan JM, Timote CC (2020) "Answer to the comments on “Confirming geomagnetic Sfe by means of a solar flare detector based on GNSS" Journal of Space Weather and Space Climate 10:A16:1-5. DOI 10.1051/swsc/2020016
3. Timoté CC, Juan JM, Sanz J, González-Casado G, Rovira-Garcia A, Escudero M (2020) "Impact of medium-scale traveling ionospheric disturbances on network real-time kinematic services: CATNET study case" Journal of Space Weather Space Climate 10:A29:1-13. DOI 10.1051/swsc/2020030
4. Rovira-Garcia A, Timoté CC, Juan JM, Sanz J, Gonzalez-Casado G, Fernández-Hernández I, Orus R, Blonski D (2021) "Ionospheric corrections tailored to the Galileo High Accuracy Service" Journal of Geodesy 95(12):A130:1-14. DOI 10.1007/s00190-021-01581-x

Articles not considered in the collection of publications to submit the doctoral thesis but developed during the doctoral research:

1. Belehaki A, Tsagouri I, Altadill D, Borries C, Buresova D, Chum J, Galkin I, Juan JM, Segarra A, Timote CC, Blanch E (2020) "An overview of methodologies for real-time detection, characterisation and tracking of traveling ionospheric disturbances developed in the TechTIDE project" Journal of Space Weather and Space Climate 10:A42:1-18. DOI 10.1051/swsc/2020043

J. Space Weather Space Clim. 2020, **9**, A42

https://doi.org/10.1051/swsc/2019040

JSWSC

Available online at:
www.swsc-journal.org

Topical Issue: Scientific Advances from the European Commission H2020 projects on Space Weather

RESEARCH ARTICLE OPEN ACCESS

Confirming geomagnetic Sfe by means of a solar flare detector based on GNSS

Juan José Curto[1,*], José Miguel Juan[2], and Cristhian Camilo Timoté[2]

[1] Observatorio del Ebro, (OE) CSIC – Universitat Ramon Llull (URL), 43520 Roquetes, Spain
[2] Research Group of Astronomy and Geomatics (gAGE) Universitat Politècnica de Catalunya (UPC) Jordi Girona 1–3, 08034 Barcelona, Spain

Received 25 July 2019 / Accepted 6 November 2019

Abstract – Solar Flares (SF) refer to sudden increases of electromagnetic radiation from the Sun lasting from minutes to hours. Irradiance in the Extremely Ultra-Violet (EUV) or X band is enhanced and it can produce a sudden over-ionization in the ionosphere, which can be tracked by several techniques. On the one hand, this over-ionization increases the ionospheric delays of GNSS signals in such a way as can be monitored using measurements collected by dual-frequency GNSS receivers. On the other hand, this over-ionization of the ionosphere is the origin of electrical currents which, in turn, induce magnetic fields which can be monitored with ground magnetometers. In this work we propose the use of a GNSS Solar Flare Monitor (GNSS-SF) for its utility to confirm the presence of ionospheric ionization which is able to produce Solar Flare Effects (Sfe) in geomagnetism. A period of 11 years (2008–2018) has been analyzed and contingency tables are shown. Although most of the GNSS-SF detections coincide with SF and most of the Sfe have a detected origin in the ionosphere, there are some paradoxes: sometimes small flares produce disturbances which are clearly detected by both methods while other disturbances, originated by powerful flares, go by virtually unnoticed. We analyzed some of these cases and proposed some explanations. We found that suddenness in the variation is a key factor for detection. Threshold values of the velocity of change to remove the background noise and the use of the acceleration of change instead of the velocity of change as the key performance detector are other topics we deal with in this paper. We conclude that the GNSS-SF detector could provide warnings of ionization disturbances from SF covering the time when the Sfe detectors are "blind", and can help to confirm Sfe events when Sfe detectors are not able to give a categorical answer.

Keywords: Sfe detection / GNSS-SF / rise time / solar flares / ionospheric disturbances

1 Introduction

1.1 Solar flares

The Extremely Ultra-Violet (EUV) photons ionize the atmosphere creating free electrons and ions, which form the ionosphere. Solar EUV irradiance varies by as much as an order of magnitude on time scales of minutes to hours (solar flares), days to months (solar rotation), and years to decades (solar cycle). Solar Flares (SF) are a sudden enhancement in solar irradiance in both the EUV and the X band.

This sudden increase of the energy emitted by the Sun produces an over-ionization of the Earth's ionosphere that can be measured using several techniques (Mitra, 1974). In particular, enhancements of the ionospheric Total Electron Content (TEC) can be measured by the effect of the ionospheric delays experienced by the Global Navigation Satellite Systems (GNSS) measurements. In fact, using a global network of GNSS dual frequency receivers, Afraimovich (2000) showed that it is possible to monitor the ionospheric response to solar flares. Analyzing in more detail the SF effects on the GNSS signals, Wan et al. (2002) showed that these effects depend on the angular distance (χ) between the Sub-Solar Point (SSP) and the Ionospheric Pierce Point (IPP) of the measurement. More recently, Hernández-Pajares et al. (2012) applied a similar model for analyzing the SFs which occurred during a period of several years. In their work, they defined a detector and an indicator of SF activity. The detector, the Sunlit Ionosphere Sudden TEC Enhancement Detector(SISTED), was based on the second difference of the Slant TEC (STEC) measurements and was able to detect 93% of the X-class SFs during a half solar cycle. The indicator, GNSS Solar Flare Activity Indicator (GSFLAI), was

*Corresponding author: jjcurto@obsebre.es

based on the linear fitting of the STEC rates of the satellite-receiver pairs with cos(χ). Using this indicator over a whole solar cycle, they found good correlations between their indicator and the photon flux rate measured by the Solar and Heliospheric Observatory (SOHO) satellite in the EUV band (26–34 nm).

As mentioned before, several proposals to construct a flare detector from GNSS data can be found in the bibliography (Afraimovich, 2000; García-Rigo et al., 2007; Hernández-Pajares et al., 2012; Syrovatskiy et al., 2019). In our case, we also use the relationship between sudden increases of STEC and cos(χ) to define two parameters for detecting SF activity. Details about these two indicators and their comparisons with similar detectors can be found in Sections 2.1 and 2.2.

1.2 Solar Flare Effects (Sfe) lists

The sudden perturbation in geomagnetic elements that follows the eruption of a solar flare, designated as Solar Flare Effects (Sfe) or a geomagnetic crochet, is a geophysical event that constitutes one of the most conspicuous Sudden Ionospheric Disturbances (SID). They are confined mostly to the sunlit hemisphere and are associated with currents that flow primarily in the ionosphere. They are caused by the extra ionization produced by X-ray and EUV flare radiation (Curto et al., 1994a, 1994b). They are reported in the International Association of Geomagnetism and Aeronomy (IAGA) bulletins according to the classification established by the International Service of Rapid Magnetic Variations, SRMV, located at the Ebro Observatory, and published by the International Service of Geomagnetic Indices, ISGI (http://isgi.unistra.fr/). The lists of Sfe elaborated by the SRMV refer to events detected primarily on the basis of magnetic observations and, later, confirmed by simultaneous observation of solar activity (flares). Detection is not an easy task because many factors are present in the origins of Sfe (Curto et al., 2016). Suddenness in Sfe is very variable, ranging from a few tenths of nT/min to 10 nT/min. Additional information of ionospheric disturbances helps to confirm if a movement in the magnetograms was down to a Sfe, although this confirmation is not absolutely essential. In the past, endorsement was also sought with the ionospheric activity of several SID (A3 method for absorption in D-layer, Sudden Enhancement/Decrease of Atmospherics [SEA/SDA], etc.). These disturbances were measured first-hand with instrumentation at the Ebro Observatory or other collaborating observatories, which promptly provided their data. Most of this auxiliary ionospheric data checking has disappeared and we would like to substitute it with other indices derived from automatic methods like that of the GNSS-SF detector.

The separation of Sfe events produced by ionizing flares from other magnetic perturbations produced by corpuscular ionizations (storms, substorms, etc.) caused by CME was carried out by the Service of Rapid Magnetic Variations whose results are the Sfe lists. In this paper, our study relies on these lists and no extra checking work has been done.

This article has two separate parts. In the first part, we will present the GNSS-SF detector algorithm and its ability to detect flares and, in the second part, we will specifically analyze the capability of this detector to track Sfe. We will compute the optimal parameters to achieve the best performance.

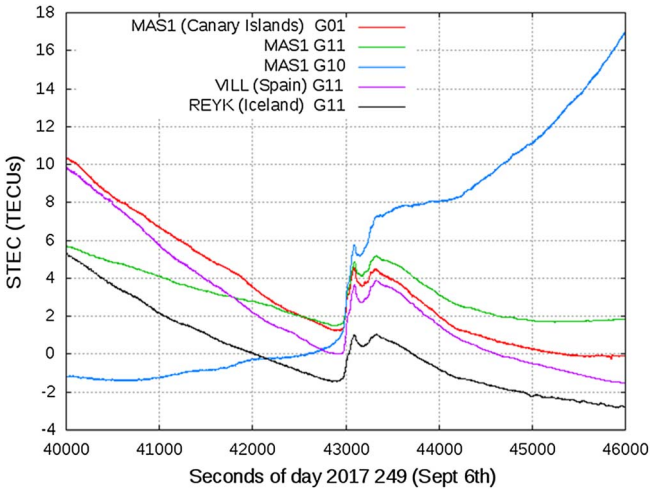

Fig. 1. STEC sudden increase at three different receivers for three GPS satellites.

2 GNSS-SF detector

2.1 Methodology

As commented on in the introduction, SFs produce sudden increases in the STEC measurements from GNSS receivers. Actually, for a given receiver "*i*" and a GNSS satellite "*j*", these increases in the STEC (ΔSTEC) can be measured with the well-known geometry-free ($L_{GF} = L_1 - L_2$) combination of carrier phases:

$$\Delta\mathrm{STEC}_i^j(t) = M(\varepsilon)\left(L_{\mathrm{GF}i}^j(t) - L_{\mathrm{GF}i}^j(t - 60\,\mathrm{s})\right)$$

where $M(\varepsilon)$ is an obliquity factor (or mapping function) that depends on the elevation (ε) and is used for mitigating the enhancement of STEC at low elevations.

For instance, Figure 1 depicts an example of these sudden increases in the ionospheric delay in observations gathered for different receivers (MAS1 in the Canary Islands, VILL in the centre of Spain, and REYK in Iceland). The example corresponds to the Solar Flare which occurred around noon of September 6, 2017 (the Day of Year [DoY] 249). As can be seen, all the observations increased their ionospheric delays by several TECUs at the time the Solar Flare occurred (around 12:00UT).

As was shown in Wan et al. (2002), for each $\Delta\mathrm{STEC}_i^j$, there should be a relationship with the angular distance (χ) between the SSP and the IPP, and, in particular, a linear relationship with cos(χ). Therefore, if we have a network of GNSS receivers, as that depicted in Figure 2, it is then possible to patrol the occurrence of an impact of a SF on the ionosphere by means of the relationship between $\Delta\mathrm{STEC}_i^j$ and χ.

For instance, Figure 3 depicts in red the values of $\Delta\mathrm{STEC}_i^j$ against cos(χ) for the example presented in Figure 1 at the instant when the SF occurred ($t \approx 43\,050$ s). In order to enhance the idea, we compare those $\Delta\mathrm{STEC}_i^j$ values with the same values 1 min before (t = 42 990 s, in blue). As can be seen, when the SF occurs, there is a clear dependency between $\Delta\mathrm{STEC}_i^j$ and cos(χ). This dependency can be fitted to a straight line which predicts a ΔSTEC close to 2 TECUs at the SSP (where cos(χ) = 1) (i.e., a TEC rate of 2 TECUs/min). Notice

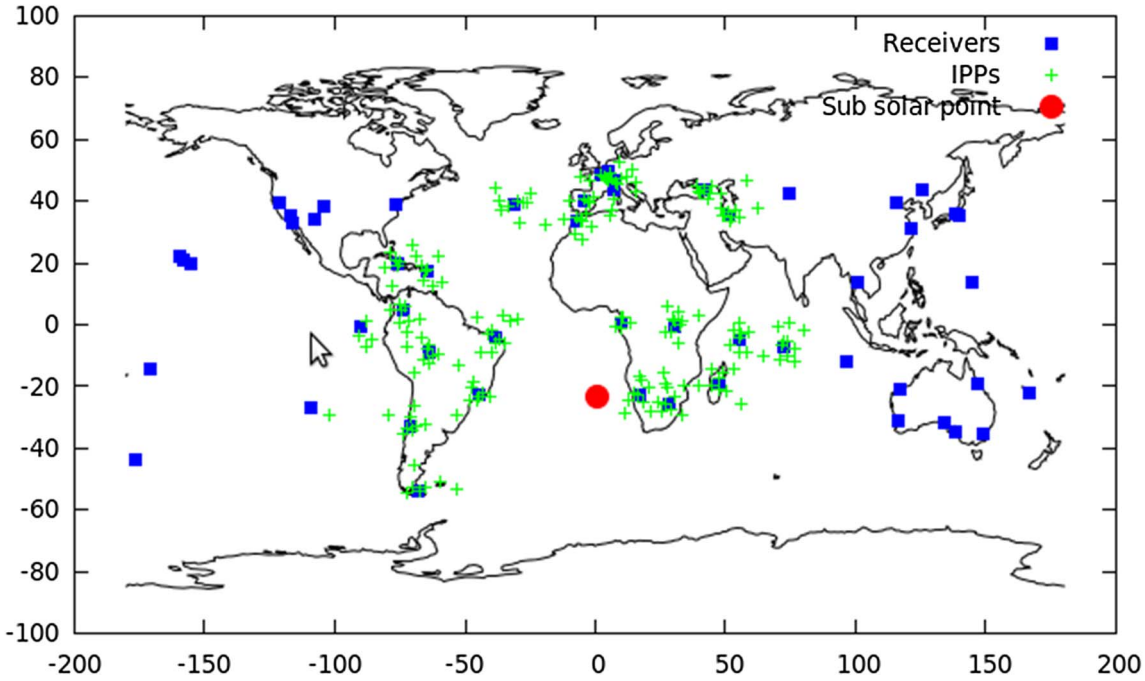

Fig. 2. An example of the network of IGS – GNSS receivers (blue squares) and the IPPs (green crosses). The SSP is also indicated with a red circle. The example corresponds to DoY 365 in 2009 at 12.

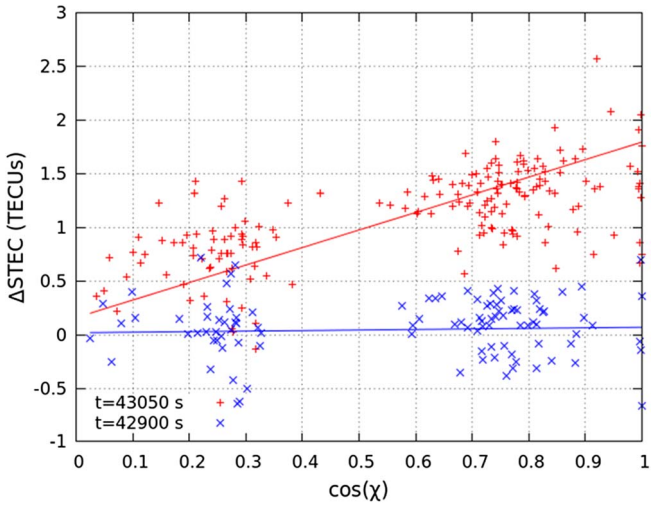

Fig. 3. ΔSTEC values as a function of the cosine of the angular distance between the SSP and the IPP at two different epochs (43 050 s of the day in red, 42 900 s of the day in blue) for the day 249 (September 6) of 2017.

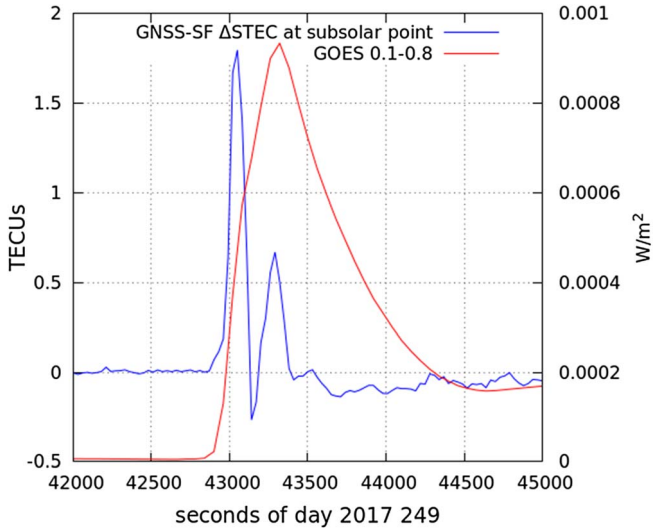

Fig. 4. ΔSTEC (blue line) detects the moment when the ionizing radiation (red line) has a sudden increase caused by the SF on September 6, 2017.

that, this is a similar approach to the GSFLAI detector in Hernández-Pajares et al. (2012). However, the GSFLAI measures the slope of the fitting instead of the value of ΔSTEC at the SSP.

Therefore, we can use the ΔSTEC prediction at the SSP as an indicator of the occurrence of an SF. For instance, Figure 4 depicts, for the same day, the predicted ΔSTEC value during a time interval where the peak at noon is clearly identified. In order to confirm the occurrence of an SF, the irradiance measured by the GOES satellite in the wavelength range of 0.1–0.8 nm is also depicted. Notice that, using the ΔSTEC prediction at the SSP as a SF indicator is equivalent to the GSFLAI index defined in Hernández-Pajares et al. (2012).

The example developed previously, i.e., the SF on September 6th in 2017, was one of the most powerful SFs which occurred in this solar cycle and it was an easy task to detect it from this fitting. However, this is not so easy to see for other SFs, especially if we aim to detect them in an automatic way.

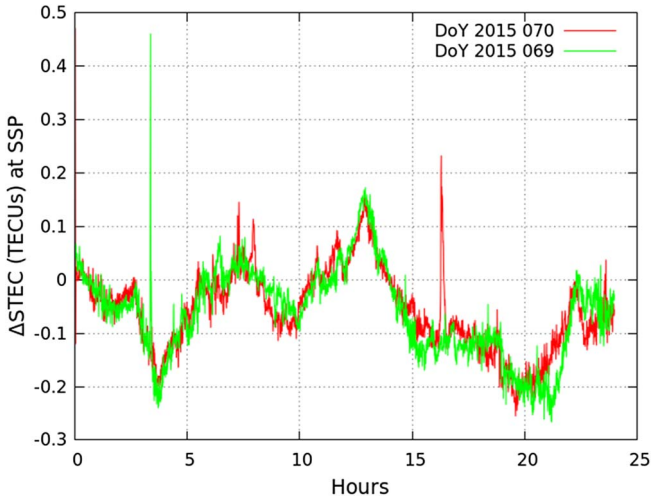

Fig. 5. ΔSTEC typical daily variations contrasted with two isolated peaks due to the occurrence of SFs, at around 04:00 and 16:00 hours UTC of the days 10 and 11 of March 2015, respectively.

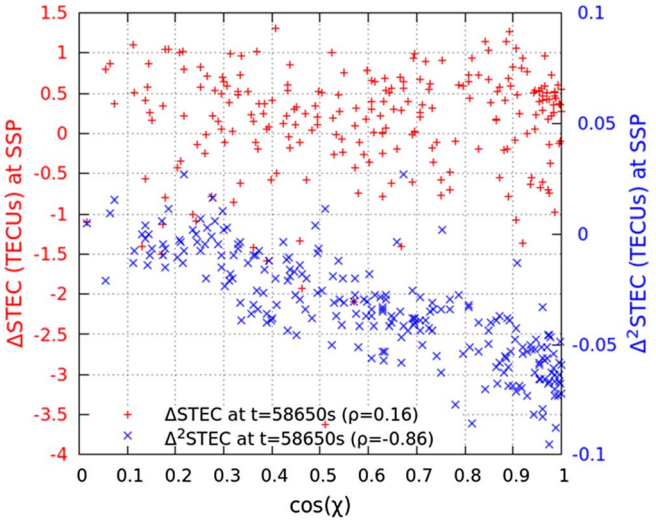

Fig. 6. $\Delta\mathrm{STEC}_i^j$ (red) and $\Delta^2\mathrm{STEC}_i^j$ (blue) as a function of the cosine of the angular distance between the SSP and the IPP at 58 650 s of March 11, 2015.

For example, if we depict the ΔSTEC prediction at the SSP for a whole day (for instance, March 11, DoY 070, 2015, Fig. 5), it can be seen that, besides the SF class X2.2 (i.e., 2.2×10^{-4} W m^{-2}) starting at 16:11UT, the ΔSTEC at the SSP also varies throughout the day, with these other variations of ΔSTEC having similar values to the sudden variations associated to the SF. Therefore, it is difficult to establish a threshold in order to distinguish the high values of ΔSTEC linked to SFs. These daily variations are related to the relative position of the Sun and the Earth's magnetic field. We depict the ΔSTEC at the SSP for the day before in order to confirm this.

Taking into account the time scales of SFs, an alternative way for establishing a detector is to focus on the peaks lasting just a few minutes, i.e., fast variations during short time intervals or, in other words, by taking into account not the ΔSTEC value but its difference with respect to the previous ones. However, this is, in some way, equivalent to considering the second difference of STEC ($\Delta^2\mathrm{STEC}_i^j$) instead of $\Delta\mathrm{STEC}_i^j$.

$$\Delta^2\mathrm{STEC}_i^j(t) = M(\varepsilon)\left[0.5 \cdot \left(L_{\mathrm{GF}i}^j(t) + L_{\mathrm{GF}i}^j(t-60\,\mathrm{s})\right) - L_{\mathrm{GF}i}^j(t-30\,\mathrm{s})\right]$$

Figure 6 depicts the values obtained of $\Delta^2\mathrm{STEC}_i^j$ for the same event presented before on March 11, 2015. As can be seen, the linear dependency between $\Delta^2\mathrm{STEC}_i^j$ and cos(χ) is maintained (correlation coefficient, $\rho = -0.86$) and it is even much clearer than that for the linear relationship with $\Delta\mathrm{STEC}_i^j$ ($\rho = 0.16$).

Figure 7 depicts the Δ^2STEC at SSP (red dots) during the whole day of March 11, 2015 (DoY 070), in a similar way as we did for ΔSTEC in Figure 5. As can be seen, now the large Δ^2STEC values can be easily observed and we can identify an initial SF around 00:00UT (M2.9), a second SF around 07:00 UT (M1.8), and a third one around 16:00UT (X2.2). Therefore, it will be easier to establish a threshold for the automatic detection of SF. In the same figure, we also depict

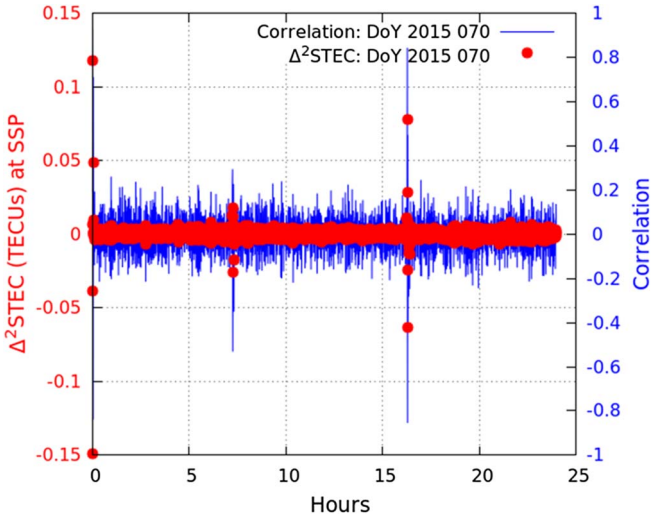

Fig. 7. Δ^2STEC at the SSP (red points) and the corresponding correlation coefficient of the fittings (blue line) for March 11, 2015.

the correlation coefficient (ρ) of the linear fitting (blue line) in order to show that both Δ^2STEC at SSP and ρ reach large values. In fact, both parameters could be used for detecting SF.

The reason for using 30 s as the time step for Δ^2STEC and 60 s for ΔSTEC is that we can also estimate, in an easy way, a value for ΔSTEC at the SSP by accumulating, from any instant t_o, the addition of two consecutive values of Δ^2STEC:

$$\Delta\mathrm{STEC}^*(t) = 2 \cdot \sum_{t_i=t_o}^{t} \left(\Delta^2\mathrm{STEC}(t_i) + \Delta^2\mathrm{STEC}(t_i - 30\,\mathrm{s})\right)$$

Notice that, the previous relationship is not obvious because ΔSTEC and Δ^2STEC are not extracted from direct measurements, but obtained by fitting the corresponding measurements and, thus, they can be affected by errors in the fitted model.

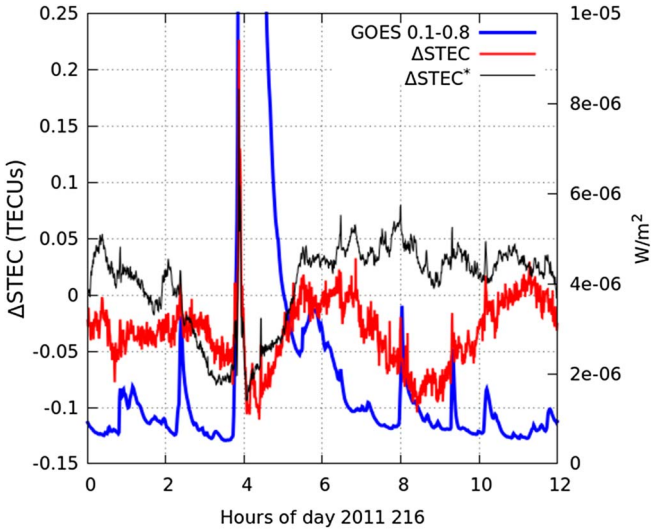

Fig. 8. NASA-GOES data (blue) and values of ΔSTEC and ΔSTEC* during an SF at 04:00 UTC. The case corresponds to the DoY 216 (August 8) in 2011.

Therefore, ΔSTEC and ΔSTEC* can present different variations. This is observed in Figure 8 which depicts, in blue, the Sun irradiance in the 0.1–0.8 nm band (measured by GOES satellite) during the DoY 216 in 2011. As can be seen, there is a SF class M around 04:00UT which is detected by both ΔSTEC and ΔSTEC*, in red and black respectively. However, there are other smaller class C solar flares that, because the noise, are more clearly distinguished in ΔSTEC*. In this sense, ΔSTEC* would be a less noisy indicator than ΔSTEC (or GSFLAI). However, we notice that the comparisons of ΔSTEC with ΔSTEC* can be done for short time intervals (hours), as misfits can introduce biases in Δ^2STEC that are revealed as drifts in ΔSTEC* for longer time intervals. Hence, once the detection is done using Δ^2STEC or ρ, we can use ΔSTEC* for quantifying the magnitude of the STEC increase at the SSP.

2.2 Data and thresholding

One of the most important issues for developing an automatic detector involves characterizing the confidence bounds of its detections, i.e., the probability of false detections (false positives). To establish such confidence bounds we have analyzed the statistical values of ΔSTEC and Δ^2STEC at the SSP and the corresponding correlation coefficient, ρ, during a solar cycle (from 2008 to 2018). With this, we manage to have a large number of small, medium and large (intense) flares. According to NOAA lists (https://www.ngdc.noaa.gov/stp/space-weather/), in this period more than 700 "intense" flares in X-ray (which include X and M type) were reported.

In order to carry out this study, we used a network of around 50 IGS receivers. This network of receivers has been changed from year to year to guarantee the number of receivers and the coverage of the network (see an example of the receiver distribution in the map in Fig. 2). In our receiver selection, we excluded those receivers that could be affected by fast variations of STEC, such as scintillation, that would increase the uncertainties of the SF detections. In this sense, following Juan et al. (2018), we excluded high latitude receivers and we used only the measurements from low latitude receivers gathered during the interval from 02:00LT to 18:00LT. For the computation of IPPs and the mapping function we used a single layer model for the ionosphere at 300 km of altitude.

In order to establish thresholds for the three detectors we computed their values during the whole solar cycle (i.e., around 1.1×10^7 estimates). Figure 9 depicts three plots with the complementary of the cumulative distribution functions for the absolute values of the three parameters ΔSTEC, Δ^2STEC, and the correlation coefficient, ρ, of the Δ^2STEC fittings.

For instance, the figure in the left panel represents the probability of having a ΔSTEC value larger than the value represented in the *X*-axis. Beside these probabilities (represented in red), we depict, in green, the complementary of the CDF during the year 2008 (a year without relevant SF) and also the complementary CDF for a Gaussian distribution (i.e., the complementary error function, erfc), in blue. The Gaussian distribution, which has been fitted with the smaller values, can be used for characterizing how Gaussian is the distribution and, if this is the case, what is the confidence level for a specific value to be different from a Gaussian error.

From Figure 9, it is clear that ΔSTEC (Fig. 9a) does not present a Gaussian behavior. Moreover, the difference between 2008 and the whole solar cycle reflects the fact that the values of ΔSTEC at the SSP depend on the solar flux. Then, the threshold for SF detections should be adapted to the solar flux. Therefore, a detector based on the ΔSTEC at the SSP does not seem to be adequate for automatic detections of SF.

On the contrary, the complementary CDF for Δ^2STEC (Fig. 9b) fits better to a Gaussian behavior, and a threshold value around 0.01TECU seems to guarantee a confident detection of SFs. Moreover, the results for 2008 seem to confirm this. This agrees with Hernández-Pajares et al. (2012), where a detector based on the individual $\Delta^2\text{STEC}_i^j$, SISTED, was used as an SF detector. However, unlike our detector, which is based on the predicted value at the SSP, SISTED was based on the percentage of measurements having a value of $\Delta^2\text{STEC}_i^j$ which were over a specific threshold. Therefore, the SISTED detection depends on the receiver distribution and the selected threshold. For instance, looking at Figure 6, one can see that a threshold of 0.07 TECUs (in absolute value) for $\Delta^2\text{STEC}_i^j$ will be overcome only if there are observations that verify the condition $\cos(\chi) > 0.75$.

Finally, the correlation coefficient of Δ^2STEC (ρ, Fig. 9c) can be assumed to be Gaussian and it can be used as an SF detector. In this sense, for instance, a value of 0.4 for ρ has a probability of 10^{-7} of being a Gaussian error rather than an SF, while for a value of 0.2 the probability is 10^{-2} (99th percentile or 3σ). In this way, looking at the results for 2008 (green points), it could be concluded that, during this year, no SFs occurred. This is confirmed by the GOES irradiance measurements with which only 20 weak C-class solar flares were reported in the band 0.1–0.8 nm. In conclusion, the value of ρ can be used as a measure of the confidence level for SF detection. This is a novelty with respect to previous SF detectors based on GNSS measurements, because it represents a self-consistent way for providing confidence to the SF detections.

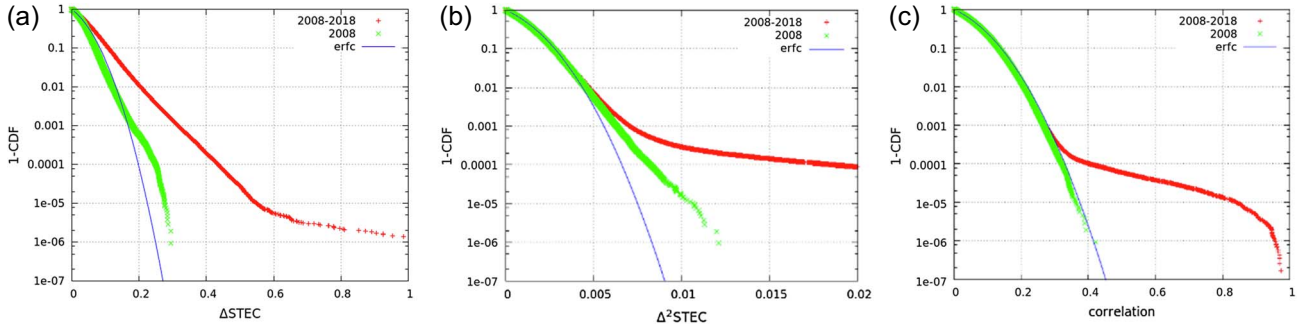

Fig. 9. Complementary of distribution functions for (a) ΔSTEC, (b) Δ^2STEC and (c) the correlation coefficient of the Δ^2STEC.

2.3 Grouping

In order to compare SF detections from different techniques we have to take into account that these techniques measure different physical properties that evolve with different time scales. For instance, in the SF depicted in Figures 1 and 4 it is clear that there are two fulgurations from the point of view of GNSS, while, from the point of view of GOES, there is a single SF. Therefore, in order to facilitate the automatic cross-checking of SF detections, using different techniques, we have to develop an algorithm to determine when two fulgurations can be considered as part of the same SF (grouping). This is particularly the case for GNSS detections where the detections typically last fewer minutes than the others. According to the definition of Δ^2STEC, one needs to compare STEC measurements taken during an interval of 1 min. Therefore, also taking into account that the recombination processes can have some influence, one should wait for several minutes with low values of Δ^2STEC before concluding that the SF has ended. In this grouping process of the SF detections with GNSS we have considered 5 min (300 s), as the minimum time interval for considering two SF detections as different fulgurations. This is in line with the 4 min found for the median of the rising times of Sfe (Curto et al., 1994a).

From the previous section, we find that we can use the Δ^2STEC and/or ρ values in order to establish thresholds for SF detections and their confidence levels can be extracted from the CDF for the correlation parameter. Therefore, a list of SFs detected by GNSS can be elaborated which will depend on the selected thresholds.

In order to make such a list, we proceed in the following way:

(i) For a given pair of thresholds, we can declare a new SF at time t_0 (beginning of the SF) when a new determination exceeds the aforementioned thresholds, and the instant at which it occurs is 300 s or more after the end of the previous SF.
(ii) Once the SF is detected (and t_0 established), during the next 5 min we check if the thresholds are exceeded again. If this does not happen, we define $t_1 = t_0$ as the final instant of this new SF. If it does occur, we update t_1 with the instant when the threshold is overcome.
(iii) If t_1 differs from t_0, we can also define t_m as the time where Δ^2STEC reaches its maximum value.

For instance, with a threshold of 0.01TECUs for Δ^2STEC and 0.25 for ρ (i.e., according to the CDF for ρ, a confidence level 99.9th) we are able to detect 1184 SFs. Table 1 shows a part of the complete list.

3 GNSS_SF indicator as Sfe tracker

3.1 Analysis

As commented in the previous section, using these criteria for the period of years 2008–2018, we obtained different candidate lists when imposing different conditions on the parameters. Our next task was to choose the more appropriate thresholds for Sfe detection. For the same period, the SRMV reported 134 Sfe events (http://www.obsebre.es/en/rapid).

3.1.2 Optimization

At this point, we need to find which values of the two parameters (Δ^2STEC and correlation, ρ) are the most suitable to be used in Sfe detection. First, let us define the basic concepts for computing the Youden index as the optimization parameter to be able to choose the best parameter configuration to align GNSS_SF candidates to Sfe events (Youden, 1950), as follows:

TP (True Positive) = true Sfe detected by *GNSS-SF* detector,
FN (False Negative) = true Sfe not detected by *GNSS-SF* detector = Total Sfe – TP,
FP (False Positive) = candidates indicated by *SNSS-SF* as Sfe, but which are not Sfe,
TN (True negative) = candidate dismissed by *GNSS-SF,* and which are not Sfe.

Then, we can compute the True Positive Rate (TPR), the True Negative Rate (TNR) and the False Positive Rate (FPR):

$$\text{Sensibility} = \text{TPR} = \text{TP}/(\text{TP} + \text{FN})$$

$$\text{Specificity} = \text{TNR} = \text{TN}/(\text{TN} + \text{FP})$$

$$1 - \text{Specificity} = \text{FPR} = \text{FP}/(\text{FP} + \text{TN})$$

The Sensitivity and the Specificity of a marker are usually used simultaneously as a joint measure of the behavior of the marker or test diagnostic. This is because they are complementary: in

Table 1. Sample of GNSS-SF candidates fulfilling the double condition.

Year	Month	Day	DoY_0	t_0	Δ^2STEC(t_0) TECUs	$\rho(t_0)$	DoY_1	t_1	Δ^2STEC(t_1) TECUs	$\rho(t_1)$	DoY_m	t_m	Δ^2STEC(t_m) TECUs	$\rho(t_m)$
2015	03	11	70	30	0.118	0.93	70	120	0.049	0.71	70	90	−0.149	−0.84
2015	03	11	70	26 070	0.018	0.29	70	26 310	−0.017	−0.35	70	26 100	−0.026	−0.53
2015	03	11	70	58 620	0.078	0.84	70	58 860	−0.013	−0.28	70	58 620	0.078	0.84
2015	03	12	71	12 120	0.018	0.40	71	12 150	−0.017	−0.35	71	12 120	0.018	0.40
2015	03	12	71	16 980	0.024	0.48	71	17 220	0.014	0.35	71	17 070	−0.095	−0.85

Table 2. Contingency table for several threshold values of the correlation parameter.

$\rho \geq$	TP	FN	TPR	GNSS_SF candidates	FP	TN	FPR	YI index
0.1	134 (100%)	0	1	100 429	100 295	11 348 885	0.00876002	0.99
0.2	126 (94%)	8	0.940298507	208 726	208 600	11 240 596	0.01821962	0.92
0.3	100 (75%)	34	0.746268657	8624	8524	11 440 724	0.0007445	0.75
0.4	83 (62%)	51	0.619402985	679	596	11 448 686	5.2056E-05	0.62
0.5	73 (54%)	61	0.544776119	356	283	11 449 019	2.4718E-05	0.54
0.6	57 (42%)	77	0.425373134	214	157	11 449 177	1.3713E-05	0.43
0.7	44 (32%)	90	0.328358209	144	100	11 449 260	8.7341E-06	0.33
0.8	35 (26%)	99	0.26119403	83	48	11 449 330	4.1924E-06	0.26
0.9	22 (16%)	112	0.164179104	37	15	11 449 389	1.3101E-06	0.16
1.0	0 (0%)	134	0	0	0	11 449 448	0	0.0

Abbreviations. FN, False Negative; FP, False Positive; TP, True Positive; TN, True Negative; TPR, True Positive Rate; FPR, False Positive Rate; YI, Youden Index.

general, if the fraction of true positives (TPR) increases, the fraction of true negatives (TNR) decreases. In this situation, an acceptable compromise must be reached. One of the proposed solutions is to select the cut-off point that maximizes the difference between the fractions of true positives and false positives. The maximum value of this amount is the Youden Index (YI) and the cut-off point – the point of the ROC curve corresponding to this index – is often selected as the optimal cut-off point of the marker (Fluss et al., 2005).

Thus, the Youden Index is

$$\mathrm{YI} = \mathrm{Sensibility} + \mathrm{Specificity} - 1$$

For the Sfe, we constructed the contingency tables (Table 2 and Table 3) and the calculation of the ROC curves (Fig. 10a and b) for each of the variables and then we calculated the Youden indexes in order to choose the best parameter or combination of parameters and to determine their optimal threshold values.

TN is very large. This means that flares with enough energy to produce an Sfe are very rare and our algorithms fortunately capture this aspect.

For the correlation parameter, it turns out that low values ($\rho \geq 0.1$ or 0.2) achieve the best performance (YI = 0.99–0.92). However, the number of candidates is non assumable (10^5) from a practical point of view. To revise this enormous amount of data would collapse the SRMV. And when the number of candidates reaches an assumable value – with orders of magnitude similar to the number of big Sfe detected for this period – which is achieved with $\rho \geq 0.4$, then the Youden index is very poor (0.62). Notice that $\rho \geq 0$ is not representative because the whole set of 1 149 448 samples accomplishes the condition and the grouping function sees this as a unique event. We conclude that ρ alone is not an appropriate condition.

For Δ^2STEC we repeated the process (Table 3). With a threshold of 0.01TECUs (grey row), we obtained more assumable figures: YI = 0.82, 82% coverage in the Sfe and 1.4×10^3 candidates.

The Receiver Operating Characteristic, ROC, curves are two-dimensional graphs in which the True Positives Fraction (TPF) is represented on the *Y*-axis and the Fraction of False Positives (FPF) is represented on the *X*-axis. It shows the relative compensations between the benefits (true positives) and costs (false positives).

ROC curves (Fig. 10) show that Δ^2STEC has a slightly better performance at the inflection point. Any point in the ROC space is better than another one if this (the former) is to the northwest (high fraction of true positives, low fraction of false positives, or both) of the latter (Fawcett, 2006).

Then we explored the double combination of the correlation and Δ^2STEC. We took the threshold of Δ^2STEC to be equal to or greater than 0.01 as our fixed condition because this condition achieved the best compromise of a high YI index and an assumable number of candidates (Table 3). And then, we simultaneously imposed a threshold of correlation in a (0.2–0.25–0.3–0.35–0.4) rank because, as seen in Table 2, in this rank this condition achieved the best results. Effectively, this combination produced a significant reduction of candidates with respect to the Δ^2STEC condition alone without an obvious reduction in Sfe coverage (Table 4).

When fixing the first condition in $\Delta^2\mathrm{STEC} \geq 0.01$ and requiring a second condition $\rho \geq 0.25$ (grey row), the

Table 3. Contingency table for several threshold values of the Δ^2STEC parameter.

Δ^2STEC $\geq$	TP	FN	TPR	GNSS_SF candidates	FP	TN	FPR	YI index
0.005	134 (100%)	0	1	1	0	11 449 446	0	0.01
0.01	110 (82%)	24	0.82089552	1411	1301	11 447 927	1.14E-04	0.82
0.015	93 (69%)	41	0.69402985	673	580	11 448 682	5.07E-05	0.69
0.02	84 (67%)	50	0.62686567	423	339	11 448 941	2.96E-05	0.63
0.025	78 (58%)	56	0.58208955	300	222	11 449 070	1.94E-05	0.58
0.03	69 (51%)	65	0.51492537	226	157	11 449 153	1.37E-05	0.51
0.035	60 (45%)	74	0.44776119	179	119	11 449 209	1.04E-05	0.45
0.04	53 (40%)	81	0.39552239	148	95	11 449 247	8.30E-06	0.40
0.045	46 (34%)	88	0.34328358	120	74	11 449 282	6.46E-06	0.34
0.05	43 (32%)	91	0.32089552	107	64	11 449 298	5.59E-06	0.32
1.00	0 (0%)	134	0	0	0	11 449 448	0	0.0

Abbreviations. FN, False Negative; FP, False Positive; TP, True Positive; TN, True Negative; TPR, True Positive Rate; FPR, False Positive Rate; YI, Youden Index.

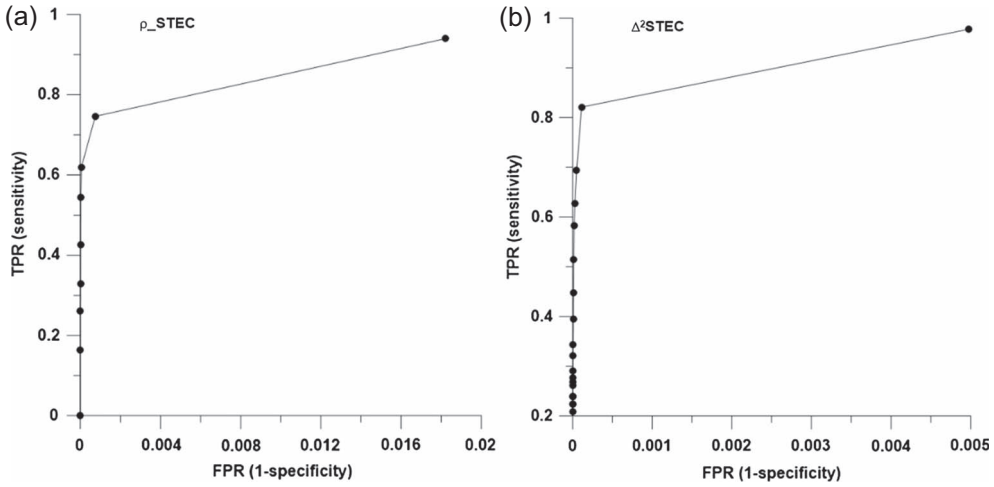

Fig. 10. (a) ROC curve for correlation and (b) ROC curve for Δ^2STEC. In both cases, we only show the left part of the curve to depict where the inflection point is achieved.

Table 4. Contingency table for several threshold values of correlation when the fix condition Δ^2STEC $\geq$ 0.01 is imposed simultaneously.

Δ^2STEC $\geq$ 0.01 & $\rho \geq$	TP/Relative reduction	FN	TPR	GNSS_SF candidates/ relative reduction	FP	TN	FPR	YI index
0.0	110 (0%)	24	0.820895522	1411 (0%)	1301	11 447 927	0.00011363	0.82
0.20	108 (2%)	26	0.805970149	1348 (8%)	1240	11 447 992	0.0001083	0.81
0.25	105 (4%)	29	0.78358209	1184 (23%)	1079	11 448 159	9.4242E-05	0.78
0.30	96 (12%)	38	0.71641791	935 (34%)	839	11 448 417	7.328E-05	0.72
0.35	89 (19%)	45	0.664179104	675 (52%)	586	11 448 684	5.1182E-05	0.66
0.40	81 (26%)	53	0.604477612	521 (63%)	440	11 448 846	3.843E-05	0.6
1	0 (100%)	134	0	0 (100%)	0	11 449 448	0	0.0

Abbreviations. FN, False Negative; FP, False Positive; TP, True Positive; TN, True Negative; TPR, True Positive Rate; FPR, False Positive Rate; YI, Youden Index.

number of candidates was reduced relatively by 23% while the coverage of the Sfe was reduced relatively by only 4%. The YI index = 0.78 was still more than acceptable. It would be possible to go further in the reduction of candidates, for example, with $\rho \geq 0.4$. However, in this case the candidates are reduced by 63% but the coverage of the Sfe is reduced by 26% and YI = 0.6 is no longer very satisfactory.

In summary, the double condition (Δ^2STEC $\geq$ 0.01) and ($\rho \geq 0.25$) is the best option for the detection of Sfe.

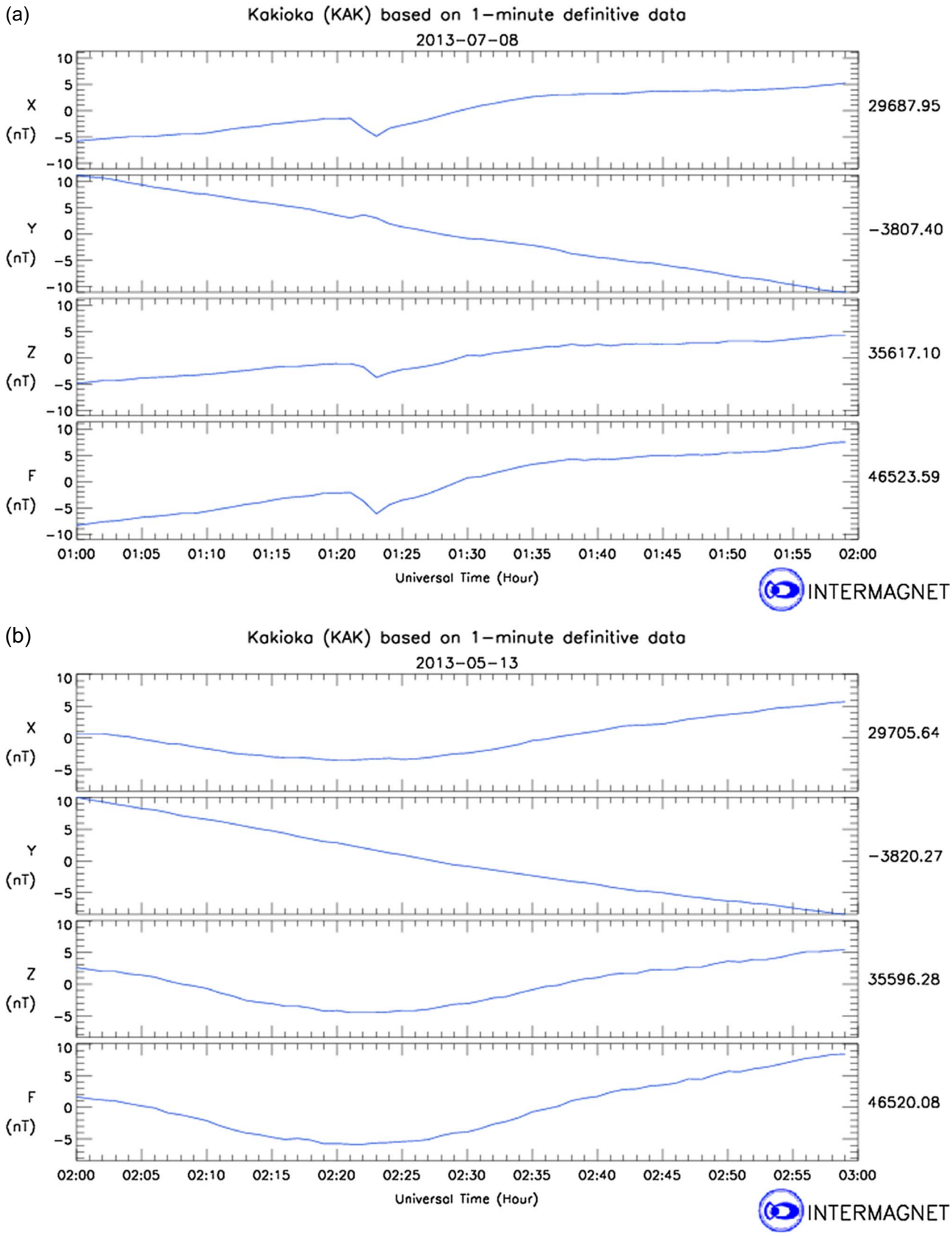

Fig. 11. (a) Sfe at KAK produced by a C9.7 flare (July 8, 2013, at 01:21 UT). The variation ΔB was 7 nT but with a duration, Δt, of 10 min. (b) Sfe at KAK produced by a X2.2 flare (May 13, 2013, at 01:57 UT). The variation ΔB was 15 nT but with a duration, Δt, of 35 min.

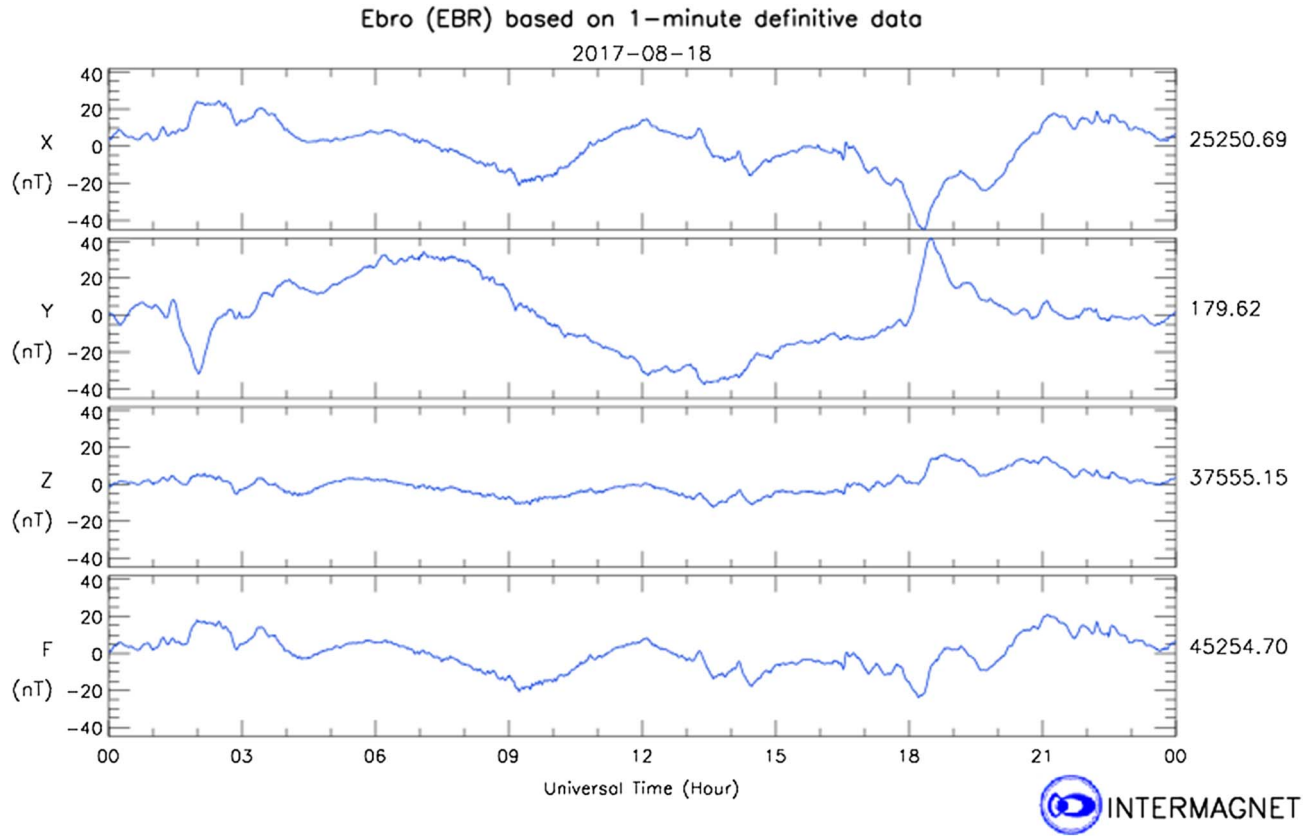

Fig. 12. Ebro magnetogram corresponding to August 18, 2017. Magnetospheric disturbances prevented observers from detecting Sfe effects.

4 Discussion: limiting factors

Even with these lax conditions, these GNSS candidate lists include 110 events (about 80% coverage of the Sfe reported by the SVMR) which is really a successful endeavor. But, what happened to the other 20%? Furthermore, there is a large number of cases (1079) detected by GNSS-SF that are not included in the Sfe lists. These facts reveal that both methods have their own limitations. We will study such limitations in this section.

Moreover, according to our experience, sometimes, powerful flares (M-type and even some X-type), go by virtually unnoticed. This is the case depicted in Figure 11a. A big X2.2 flare happened on May 13, 2013, at 01:57 UT. The magnetogram of KAK, an observatory well located to see an Sfe, only presented a magnetic variation, ΔB, of 15 nT but with a duration, Δt, of 35 min. However, paradoxically other small flares produce disturbances which were clearly detected by both methods (Sfe, GNSS-SF) which means the ionosphere and the geomagnetic field could be sensitive to small additional amounts of energy. Thus, it is not rare to have Sfe events which can be related to C-type X-ray flares. Figure 11b depicts an Sfe seen at the same observatory, KAK, and produced by a C9.7 flare on July 8, 2013, at 01:21 UT. The magnetic variation, ΔB, was 7 nT but with a duration, Δt, of 10 min.

Hence, in the detection process, apart from the intensity of the X-ray ionizing radiation, there are other factors just as important as the intensity of the flare that influence the imprinting in the ionosphere and in terrestrial magnetism. Hereafter, we will consider some limiting factors whose presence implies a detriment of our detection capacity.

4.1 Natural noise. Blind temporal window

One of the most limiting factors in Sfe event detection is the noise produced by other natural variations with frequencies close to the frequencies of phenomena producing Sfe. Most of them have a magnetospheric origin (such as pulsations and substorms). They occur spontaneously, irregularly, and, very often, simultaneously to the effects of solar flares. This happens during more than a third of the time (Curto & Gaya-Pique, 2009b) and masks our view of Sfe partially or totally. So, the current methods of event detection (GNSS-SF, Sfe) are strongly conditioned by the need to separate our signal from these other natural noises with similar frequencies. Moreover, other variations with longer wavelengths such as the diurnal and semidiurnal variations should also be removed to analyze specific cases of Sfe (Curto et al., 1994a) more clearly. As an example, we present a case reported by GNSS-SF on August 18, 2017, at 21:00 UT. Only looking at magnetism, observers could not distinguish this event because it occurred in the middle of other disturbances of a magnetospheric origin (Fig. 12). It was the coherence of the Δ^2STEC signal with radial distance at SSP and diminishing amplitudes in the GNSS detector which revealed it.

As regards the GNSS-SF detector, a deep analysis of Sfe undetected by GNSS-SF reveals that in these cases, the Δ^2STEC

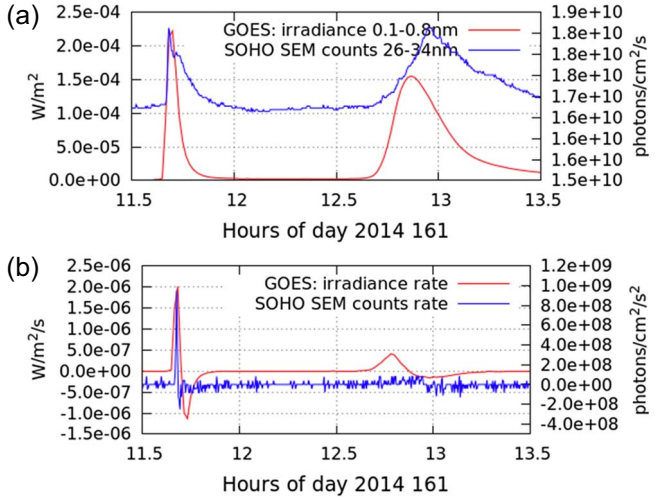

Fig. 13. (a) Irradiance measured by GOES (red) and photons counts measured by SOHO SEM (blue) during DoY 161 (June 10) in 2014. (b) Flux rates of the magnitudes in the top panel.

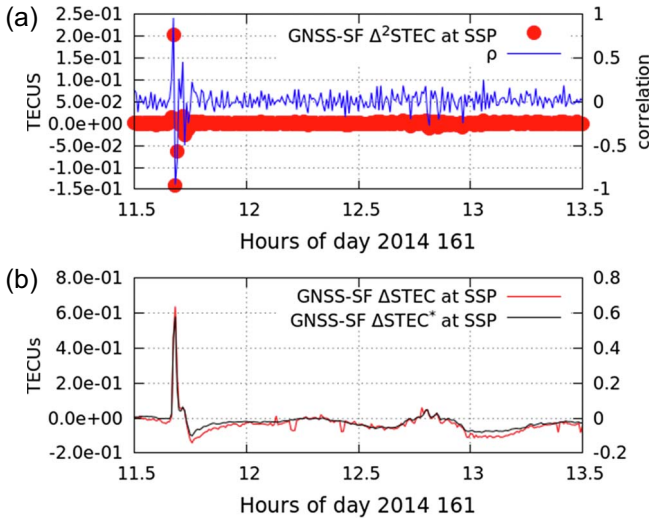

Fig. 14. STEC variations for DoY 161 (June 10) in 2014 from the same GNSS data as those of Figure 13. (a) $\Delta^2$2STEC (red) and ρ (blue) at the SSP. (b) ΔSTEC (red) and ΔSTEC* (integrated from $\Delta^2$2STEC) (black).

signal was very weak and could not overcome its threshold, and neither could the correlation coefficient. Hence, although small ionospheric variations were present at most of the observation points, the signal had the same order of magnitude as the noise. For example, in Figure 5 it is observed that the ΔSTEC at the subsolar point has a similar "pattern" in consecutive days, which could indicate that, in addition to the irradiance (which does not have to vary with the rotation of the Earth), the value of the ΔSTEC at the subsolar point depends on the coordinates of the subsolar point. The low values of the correlation coefficient are due to the fact that the STEC signals have a poor coherence among themselves. In some cases, the dependence between the signal and the distance to the subsolar point manifests itself very weakly. That is why the model applied, in which it is assumed that there is a linear dependence with the cos(χ), hardly works.

4.2 Suddenness and spectral balance

Additionally, we should remember that the lists of Sfe are elaborated on the basis of manual detection. Observers around the world produce checking lists after visual observation of the magnetic movements in the magnetograms. But they only detect them by observing contrast (suddenness) and, therefore, only sudden rises are appreciated by the human eye or even by algorithms. Therefore, the velocity in the change of radiation and, consequently, in the change of the magnetic field become elements that have the same level of importance as the absolute amplitude in terms of detection.

In the case of the GNSS-SF detector, suddenness is also a key parameter. We use the derivative as a filtering method for the separation of signal from the noise but it entails the difficulty of weakening the signal of valid ionospheric and/or magnetic variations, especially those of slow rise/fall times, making them undetectable in many cases. Using Δ^2STEC instead of ΔSTEC implies enhancing the events with greater acceleration even more, in detriment of those that have a more constant speed. In this sense, as was shown in Hernández-Pajares et al. (2012), solar flare detections with GNSS are more sensitive to

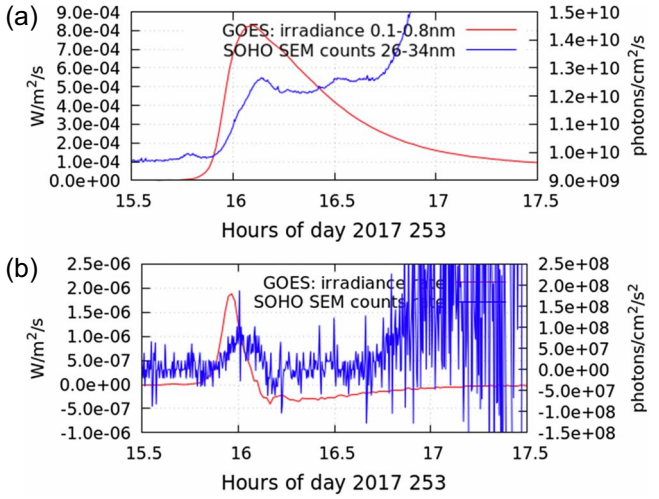

Fig. 15. (a) X-ray radiation for September 10, 2017 (DoY 253). A powerful flare happened in the afternoon with a starting time at 15:35, maximum at 16:06, and end time at 16:31. (b) Flux rates of the magnitudes in the top panel.

flux rates than to the flux itself. For instance, Figure 13 depicts the SFs which occurred on DoY 161 of 2014 (June 10). This case is interesting because GOES measurements detected two X-class SF (X2.2 and X1.5) in an interval of 2 h. The top panel of the figure depicts the irradiance measured by GOES and the photons flux measured by SOHO, while the bottom panel shows the rate of the fluxes depicted in the top panel.

As can be seen, the pattern of the fluxes differs from their rates, with the flux of the first SF being much clearer than the second one, which is practically not visible for the SOHO measurements. In order to compare the GNSS detections, Figure 14 depicts Δ^2STEC and ρ during the same 2-hour period in the top

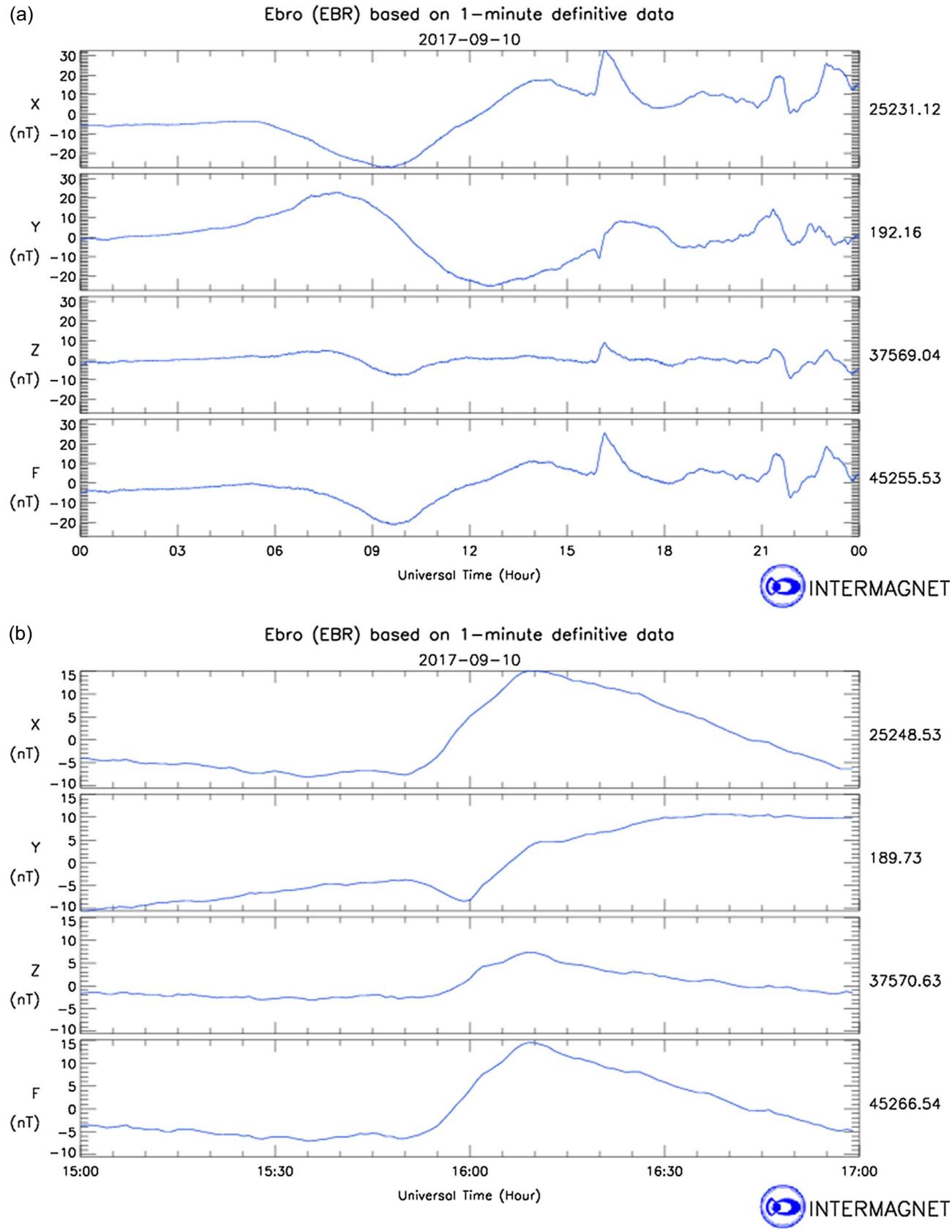

Fig. 16. (a) Ebro magnetogram corresponding to September 10, 2017, with Sfe at 15:51. (b) Detail of this magnetogram magnifying the time of this long-lasting Sfe.

panel, and the ΔSTEC in the bottom panel. From these two panels, it is possible to conclude that the ionospheric response to SF is more closely related to the flux rates.

In these cases, which have a small signal due to the slow temporal increase in ionization, the traditional method of detecting Sfe, based on manual observations, is more powerful than GNSS-SF because observers are able to re-scale the visual window to get a complete picture of the event which can last from a few minutes to more than an hour and can have a very mild slope (Curto et al., 1994a). However, GNSS-SF, on the other hand, operates with fixed narrow temporal windows which are not possible to change. To illustrate the difficulties that we identified in the detection process, we present an additional case study where the GNSS-SF detector failed. On September 10, 2017, a powerful X8.2 started at 15:35 and peaked at 16:06 (Fig. 15). The flare was located in the NOAA 2673 region. On this day, this group was in its declining epoch, having only a quarter of the sunspots it had had a few days before and was located in the limb of the Sun (S09W83) according to NOAA files. Looking at the SOHO SEM counts, the SF is also clear, but lasting for several minutes and before the arrival of relativistic electrons several minutes after the flare (Tsurutani et al., 2009).

Comparing the flux values with the values of the SFs in Figure 13a, we can observe different proportionalities between the GOES measurements (in the band 0.1–0.8 nm) and the SOHO measurements (in the band 26–34 nm). Indeed, in the example of Figure 13b, we can see that increases in the X-band irradiance at the level of 2×10^{-4} W m^{-2} correspond to increases in the photon flux of around 2×10^{9} photons cm^{-2} s^{-1}, which are similar to the case depicted in Figure 15. However, in these cases, the increase of the X-band irradiance is four times larger.

These different proportionalities were reported in Curto and Gaya-Pique (2009a) but, especially, in Le et al. (2011), justifying the different effectiveness of X-band SF in ionizing the ionosphere which is more closely linked to the EUV irradiance. Indeed, comparing X-ray and EUV emissions, Le et al. (2011) only found a correlation of around 0.5. That is, broadly speaking, only half of the EUV variation relates well to X variation. Or, in other words, there may be an important fulguration in X, but, it may not exist with regards to EUV and the final result in the ionosphere can be disappointing, and vice versa. The relationship between X-ray and EUV is affected by the distance of the fulguration from the center of the Sun. That is, the EUV emissions that occur in the solar corona would suffer a greater attenuation than the emissions in the X-band. Therefore, the effectiveness in ionization of an SF would also depend on the place in the Sun where the flare has occurred.

Regarding the flux rates, the rate in the GOES measurements is more similar to the rates in the first flare in Figure 13, i.e., around 2×10^{-6} W m^{-2} s^{-1}. However, for the photon counts, the rate is around 2×10^{8} photons cm^{-2} s^{-2}, which is more similar to the second flare in Figure 13.

In geomagnetism, this event was detected as an Sfe by the magnetic observatories network collaborating with the SVMR at 15:51 UT. This Sfe was seen all the way from the west coast of America to the western republics of the former USSR. Figure 16a depicts Ebro magnetograms for this day. Its effects lasted more than one hour but even during the rise time, the variation dB/dt was slow (about 1 nT/min) (Fig. 16b).

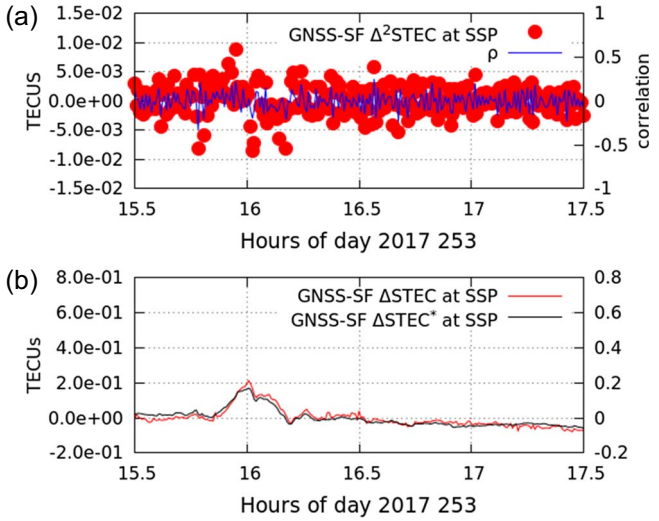

Fig. 17. (a) Δ^2STEC (red) and ρ (blue) at the SSP. (Panel b) from the GNSS data in the case of Figure 13. (b) ΔSTEC and ΔSTEC integrated from Δ^2STEC.

As regards the GNSS-SF detector, it could not detect this movement. This happened because, as can be seen in Figure 17, Δ^2STEC peaked at only 0.009 TECUs, which is under the threshold of detection. This weak detection can also be seen in ΔSTEC, which reflects only a slight increase of STEC at the SSP at the time the SF occurs. Such a small enhancement in ΔSTEC can be detected by a manual observation, as was done with geomagnetism in this case, but it is harder to be detected in an automatic mode.

This situation was repeated during other events. In general, we noted that events with $dB/dt < 1$ nT/min variation were not usually recovered by the GNSS-SF automatic detection.

Also, it is worth pointing out that for the double condition abs(Δ^2STEC) > 0.01 TECUs and abs(ρ) > 0.25 from 2585 detected points, after grouping there are 1184 candidates. This means that most of the events are so short that they last for only about a minute! Of course such small disturbances do not produce appreciable movements in the magnetograms and, hence, they are not reported as Sfe. These are not unusual cases; in fact, 596 candidates, i.e., 50% of the grouped candidates, last only 30 s ($t_0 = t_1$), thus they correspond to very weak SF and they are undetectable in the magnetograms.

4.3 Blind spatial zones

Another adverse element for Sfe detection is the uneven distribution of the magnetic observatories around the world. There are large "blind" zones (without observatories, or without observatories collaborating with the SRMV) which prevents detection in those UT time slots. That represents 50% of the useful space (Curto & Gaya-Pique, 2009b). On the contrary, the distribution of primary GNSS TEC signals is very extensive and covers the entire globe well. Hence, the number of Sfe reported by the SRMV will be necessarily lower than the number of ionospheric disturbances detected by GNSS-SF. Nevertheless, GNSS coverage is not perfect either and large areas of the oceans are poorly covered (Fig. 2). As the linear

adjust depends on the distribution of the IPPs, in these zones it will be difficult to achieve good correlations.

In general, most GNSS-SF candidates with a good correlation have significant Δ^2STEC. However, the opposite case is not true. Many candidates with large Δ^2STEC do not have a good correlation. Hence, there is a disproportion between the number of candidates depending on whether we take one parameter or the other.

5 Conclusions

In this study, we presented a GNSS-SF detector for solar flares and looked at its ability to confirm Sfe in geomagnetism. We consider there to be Sfe events when there are X-ray flares in the Sun, over-ionization in the ionosphere and magnetic variations on Earth, all of them coincident in time (we can say when they are "aligned"). These three event sets are similar, but not identical.

In this work, we have constructed a solar flare monitor to confirm the presence of ionospheric ionization which is able to produce Sfe in geomagnetism. We then imposed some conditions to adjust the GNSS-SF detector so as to produce a list of candidates that match the Sfe lists provided by SRMV.

A period of 11 years (2008–2018) has been analyzed and contingency tables have been produced. ROC curves and the Youden Index were used to find the optimal values of the threshold to minimize false positive rates and to maximize the true positive rates. Also, the number of candidates to be revised played an important role in our decision.

During this testing period, we have studied the performance of three parameters for detecting SF using GNSS: ΔSTEC, Δ^2STEC and the correlation coefficient, ρ. From the statistical analysis, we conclude that Δ^2STEC and ρ are the more adequate ones. In particular, we have shown that ρ has a Gaussian behavior and it can be used for measuring the confidence level of the detections.

The Δ^2STEC parameter proved to have a superior performance than the correlation coefficient for our aims. However, with a particular set of parameters (the double condition of $\Delta^2\text{STEC} \geq 0.01$ and $\rho \geq 0.25$) we achieved the best performance of our GNSS-SF detector to be used as a complement to confirm Sfe detection.

However, according to our statistics, the correspondence between the candidates from the Sfe and GNSS-SF lists is not perfect. Limitations of both methods were revised. Background noise, suddenness, temporal and spatial blind windows, or spectral unbalance conditioned the detection.

Despite these limitations, the two detection methods have their own strong points and they complement each other. In particular, the GNSS-SF detector could provide alerts of ionization disturbances from solar flares covering the whole day, principally during the time when the Sfe detectors are "blind". Also the spatial coverage of the GNSS-SF detector is global while Sfe observers only patrol half of the world. In addition, the GNSS-SF detector can help to confirm Sfe events when Sfe detectors are not able to give a categorical answer regarding some doubtful cases.

On the other hand, Sfe detections can help to produce more complete lists than those produced only with the GNSS-SF method because having an algorithm with fixed patterns and a limited scope of time segments means the GNSS-SF can barely detect long flares with a gradual rise. The "manual" detection of Sfe with magnetograms (analogue record bands containing a 24-hour chart) allows the observer to mentally zoom in on different areas of the graph, covering in each case both those movements of short duration and those of long duration, so that long flares (even those that last an hour) do not escape their gaze either and are detected.

Acknowledgements. This research has been partially supported by Spanish government projects CTM2014-52182-C3-1-P, PGC2018-096774-B-I00 and RTI2018-094295-B-I00 of MINECO and H2020 Grant agreement 776011 from the EU. The authors also wish to thank the NOAA for the satellite system which collects valuable information regarding solar radiation and for publishing these data. We acknowledge the CELIAS/SEM experiment on the Solar Heliospheric Observatory (SOHO) spacecraft (SOHO is a joint European Space Agency, United States National Aeronautics and Space Administration mission). We also thank INTERMAGNET and all the collaborating observatories which provide high-quality magnetic data. Finally, we thank the International Service of Rapid Magnetic Variations and their collaborating observatories. The editor thanks two anonymous referees for their assistance in evaluating this paper.

References

Afraimovich EL. 2000. GPS global detection of the ionospheric response to solar flares. *Radio Sci* **35(6)**: 417–1424.

Curto JJ, Alberca LF, Castell J. 2016. Dynamic aspects of the Solar flare effects and their impact in the detection procedures. *J Ind Geophys Union* **2**: 99–104.

Curto JJ, Amory-Mazaudier C, Cardús JO, Torta JM, Menvielle M. 1994a. Solar flare effects at Ebre: regular and reversed solar flare effects, statistical analysis (1953 to 1985), a global case study and a model of elliptical ionospheric currents. *J Geophys Res* **99(A3)**: 3945–3954.

Curto JJ, Amory-Mazaudier C, Cardús JO, Torta JM, Menvielle M. 1994b. Solar flare effects at Ebre: unidimensional physical, integrated model. *J Geophys Res* **99(A12)**: 23289–23296.

Curto JJ, Gaya-Pique LR. 2009a. Geoeffectiveness of solar flares in magnetic crochet (sfe) production: I – Dependence on their spectral nature and position on the solar disk. *J Atmos Solar-Terr Phys* **71**: 1695–1704.

Curto JJ, Gaya-Pique LR. 2009b. Geoeffectiveness of solar flares in magnetic crochet (sfe) production: II – Dependence on the detection method. *J Atmos Solar-Terr Phys* **71**: 1705–1710.

Fawcett T. 2006. An introduction to ROC analysis. *Pattern Recogn Lett* **27(8)**: 861–874.

Fluss R, Faraggi D, Reiser B. 2005. Estimation of the Youden Index and its Associated Cutoff Point. *Biom J* **47(4)**: 458–472.

García-Rigo A, Hernández-Pajares M, Juan JM, Sanz J. 2007. Solar flare detection system based on global positioning system data: first results. *Adv Space Res* **39**: 889–895.

Hernández-Pajares M, García-Rigo A, Juan JM, Sanz J, Monte E, Aragón-Àngel A. 2012. GNSS measurement of EUV photons flux

rate during strong and mid solar flares. *Space Weather* **10**: S12001. https://doi.org/10.1029/2012SW000826.

Juan JM, Sanz J, Rovira-Garcia A, González-Casado G, Ibáñez D, Orus Perez R. 2018. AATR an ionospheric activity indicator specifically based on GNSS measurements. *J Space Weather Space Clim* **8**: A14. https://doi.org/10.1051/swsc/2017044.

Le H, Liu L, He H, Wan W. 2011. Statistical analysis of solar EUV and X-ray flux enhancements induced by solar flares and its implication to upper atmosphere. *J Geophys Res* **116(A11)**: A11301. https://doi.org/10.1029/2011JA016704.11.

Mitra AP. 1974. *Ionospheric effects of solar flares*. D. Reidel, Norwell, MA.

Syrovatskiy SV, Yasyukevich YV, Edemskiy IK, Vesnin AM, Voeykov SV, Zhivetiev IV. 2019. Can we detect X/M/C-class solar flares from global navigation satellite system data? *Results Phys* **12**: 1004–1005.

Tsurutani BT, Verkhoglyadova OP, Mannucci AJ, Lakhina GS, Li G, Zank GP. 2009. A brief review of "solar flare effects" on the ionosphere. *Radio Sci* **44**: RS0A17. https://doi.org/10.1029/2008RS004029.

Wan W, Yuan H, Liu L, Ning B. 2002. The sudden increase in ionospheric total electron content caused by the very intense solar flare on July 14, 2000. *Sci China Ser A* **45(1)**: 142–147.

Youden WJ. 1950. Index for rating diagnostic tests. *Cancer* **3(1)**: 32–35.

Cite this article as: Curto JJ, Juan JM & Timoté CC, 2020. Confirming geomagnetic Sfe by means of a solar flare detector based on GNSS. *J. Space Weather Space Clim*. **9**, A42.

J. Space Weather Space Clim. 2020, **10**, 16

https://doi.org/10.1051/swsc/2020016

JSWSC

Available online at:
www.swsc-journal.org

Topical Issue - Scientific Advances from the European Commission H2020 projects on Space Weather

Reply on Comment

OPEN ACCESS

Answer to the comments on "Confirming geomagnetic Sfe by means of a solar flare detector based on GNSS"

Juan José Curto[1,*], Jose Miguel Juan[2], and Cristhian Camilo Timoté[2]

[1] Observatorio del Ebro, (OE) CSIC – Universitat Ramon Llull (URL), 43520 Roquetes, Spain
[2] Research group on Astronomy and Geomatics (gAGE), Universitat Politècnica de Catalunya (UPC), Jordi Girona, 1–3, 08034 Barcelona, Spain

Received 7 February 2020 / Accepted 11 March 2020

Abstract – Hernández-Pajares and García-Rigo have written a document criticizing our paper "Confirming geomagnetic Sfe by means of a solar flare detector based on GNSS. *J Space Weather Space Clim* **9**: A42. https://doi.org/10.1051/swsc/2019040" (Curto et al., 2019). The main goal of our paper was to define a methodology based on GNSS measurements that is able to detect solar flares (SF) in an automatic way. This methodology was used to confirm Sfe (SF effects) detected by geomagnetism in an unsupervised manner. In their document, Hernández-Pajares and García-Rigo posed two objections related to the correctness and the novelty of the methodology used in our paper. This document is a reply to these objections and concludes that they are not relevant.

Keywords: Sfe detection / GNSS-SF / rise time / solar flares / ionospheric disturbances

1 Introduction

The aim of the work presented in Curto et al. (2019) was to define a methodology based on GNSS measurements that is able to detect solar flares (SF) in an automatic way, to confirm solar flare effects (Sfe) detected by geomagnetism in an unsupervised manner.

The basic measurements used to define the SF detector presented in Curto et al. (2019) are the slant total electron content (STEC) variations, corrected by an obliquity factor (see below). This obliquity factor was introduced to reduce the increase in STEC variations at low elevations, i.e. to normalise such STEC variations.

Based on these corrected STEC values, denoted as $\Delta\mathrm{STEC}_i^j$, we analysed three candidates for this automatic detector during an entire solar cycle (see Curto et al., 2019 for more information):

1. ΔSTEC at the subsolar point (SSP).
2. Δ^2STEC at the subsolar point (SSP).
3. Correlation coefficient, ρ, of the Δ^2STEC fitting.

Our work concluded that the combined use of the Δ^2STEC and ρ detectors provides a successful ratio of Sfe confirmations.

*Corresponding author: jjcurto@obsebre.es

The comments received by Hernández-Pajares and García-Rigo (hereafter HP&GR) regarding our paper can be summarized as follows:

1. Mistakes in the methodology could invalidate our results.
2. The SF detectors used in our paper were already defined in their papers.

The present document aims to refute these objections.

2 Regarding the claim about mistakes in the methodology

It is clear that HP&GR assume a single-layer model for the ionosphere, where the obliquity factor is a factor that converts the vertical total electron content (VTEC) to the slant total electron content (STEC) in such a way that, for a satellite "j" and a receiver "i", the ionospheric delay can be written as:

$$\mathrm{STEC}_i^j = m(\varepsilon) \cdot \mathrm{VTEC}(A) \qquad (1)$$

where A is the ionospheric pierce point (IPP) (i.e. the intersection of the line of sight vector with the ionospheric layer) and $m(\varepsilon)$ is the so-called obliquity factor or mapping function, defined as:

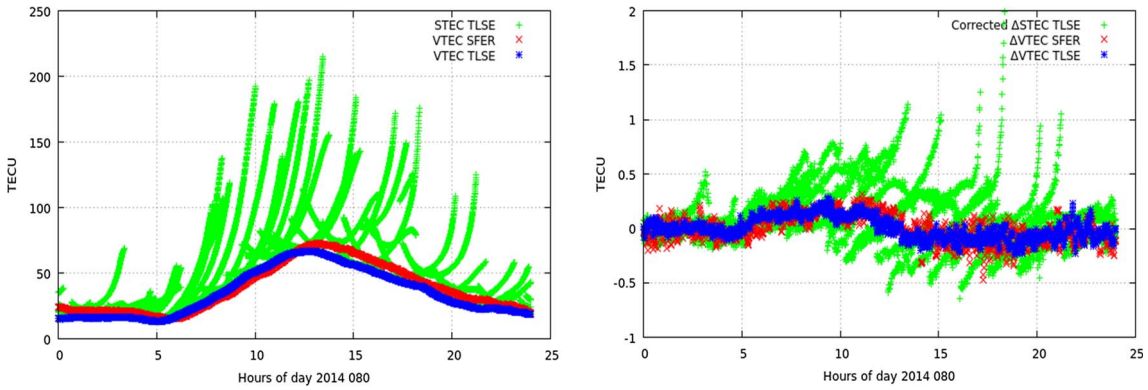

Fig. 1. Left panel: STEC values from the receiver TLSE (green), VTEC at TLSE (blue) and VTEC at SFER (red). Right panel: corrected variations of the STECs in the left panel (green) and variations of VTEC (blue and red).

$$m(\varepsilon) = \sqrt{\frac{1}{1 - \left(\frac{R_E \cdot \cos(\varepsilon)}{R_E + h_{ion}}\right)^2}}$$

where R_E is the Earth radius, ε is the satellite elevation angle, and h_{ion} is the height of the ionospheric layer.

In GNSS, one of the basic ionospheric measurements for extracting STEC in (1) is the well-known geometry-free combination of carrier-phase (L_{GF}), that shall be corrected from geometric effects such as antenna phase centres (of both satellite and receiver) and from the satellite wind-up. L_{GF} is related to the STEC by:

$$L_{GF_i}^j = \mathrm{STEC}_i^j + B_{GF_i}^j$$

where $B_{GF_i}^j$ is a constant per arc, which includes the so-called carrier phase ambiguities and instrumental biases (of both the satellite and the receiver).

If $B_{GF_i}^j$ is known, thence VTEC can be obtained from the L_{GF} measurements through:

$$\mathrm{VTEC(A)} = \frac{1}{m(\varepsilon)}\left(L_{GF_i}^j - B_{GF_i}^j\right).$$

Therefore, using the previous relationship one could relate an increase of VTEC at A with the occurrence of a SF.

However, the knowledge of $B_{GF_i}^j$ is not trivial. Therefore, it is common to cancel this term by taking differences on time of $L_{GF_i}^j$ along a continuous arc of data, where it is assumed that $B_{GF_i}^j$ is constant. Thus, this differences on time can be identified with differences of STEC_i^j:

$$L_{GF_i}^j(t_B) - L_{GF_i}^j(t_A) = \mathrm{STEC}_i^j(t_B) - \mathrm{STEC}_i^j(t_A)$$

where A and B are the IPPs at the times t_A and t_B, respectively.

Applying (1), the previous relationship can be written as:

$$L_{GF_i}^j(t_B) - L_{GF_i}^j(t_A) = m(\varepsilon_B) \cdot \mathrm{VTEC}(B) - m(\varepsilon_A) \cdot \mathrm{VTEC}(A).$$

Following the HP&GR reasoning this last expression could be approximated as:

$$L_{GF_i}^j(t_B) - L_{GF_i}^j(t_A) \approx m(\varepsilon_A) \cdot \Delta\mathrm{VTEC}(A).$$

Therefore, the increase of VTEC at the IPP can be approximated by:

$$\Delta\mathrm{VTEC}(A) \approx \frac{1}{m(\varepsilon_A)}\left(L_{GF_i}^j(t_B) - L_{GF_i}^j(t_A)\right). \qquad (2)$$

This is the expression that HP&GR are thinking on their first comment.

However, interpreting the right side of equation (2) as a VTEC variation is just an approximation that assumes that the STEC variations are linked to an increase of the VTEC at the IPP A. This assumption would be only true for a geostationary satellite, where both, A and B, are the same IPP. Nevertheless, in general, STEC variations depends also on the spatial gradients which, at low elevations, use to be, by far, the predominant component of the STEC variations.

In order to illustrate the dependency of the STEC variations on the spatial gradient, Figure 1 depicts, in the left panel, the STEC values for the receiver TLSE (South of France) during the day 080 in 2014. These STEC values, in green, are obtained after solving, for each arc, the constant $B_{GF_i}^j$. The solution for these constants are computed by means of a sophisticated process that includes worldwide carrier phase ambiguity fixing (see Rovira-Garcia et al., 2016 for more details). Beside these very accurate STEC values, the VTEC values for TLSE and SFER (South of Spain) are also depicted in the left panel. The VTEC values are obtained from these very accurate STECs and using a dual layer ionospheric model that, as it is shown in Rovira-Garcia et al. (2016) or in Rovira-Garcia et al. (2019), is several times more accurate than the standard single layer ionospheric models. In the right panel, the difference of these three magnitudes along 1 minute are depicted. As it can be seen, while the VTEC variations (computed from the ionospheric model) are less than 0.2 TECU (1 TECU = 10^{16} electrons/m^2), the STEC variations (computed directly using Eq. (2)) can be larger than 1 TECU (even if one puts and elevation mask of 20 degrees). These larger variations of the STECs cannot be attributed to the possible low latitude of the IPPs (this is the reason we depict also the VTEC for SFER). Thus, the variations in the right side of equation (2) are far from being a VTEC variation.

Therefore, in our paper, we interpreted the right side of equation (2) as it is: a STEC variation multiplied by an obliquity

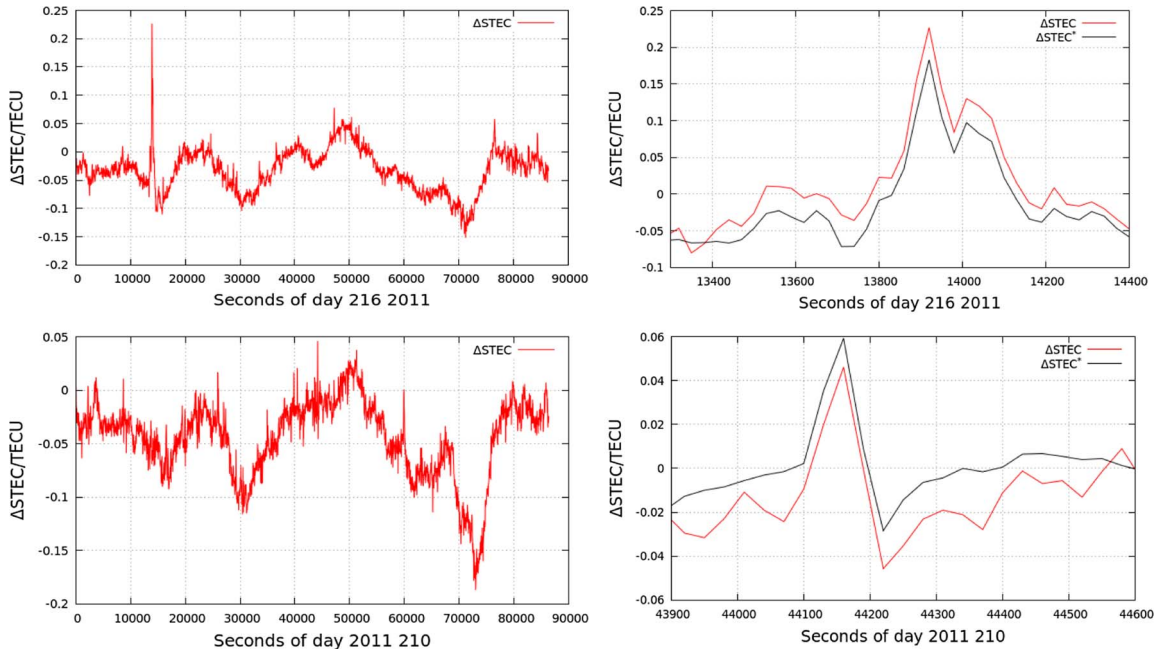

Fig. 2. Left column: ΔSTEC at the SSP during two days of 2011: day 216 at the top and day 210 at the bottom. Right column: in red, an enlarged view of the plots on the left side during the same time interval as in Hernández-Pajares et al. (2012). Additionally, ΔSTEC* is depicted in black.

factor $\left(M(\varepsilon_A) = \frac{1}{m(\varepsilon_A)}\right)$ which mitigates the large variations of STEC at low elevations. Thus, we define ΔSTEC_i^j as this corrected (normalised) STEC variation:

$$\Delta\text{STEC}_i^j = M(\varepsilon_A) \cdot \left(L_{\text{GF}i}^j(t_B) - L_{\text{GF}i}^j(t_A)\right). \qquad (3)$$

This is the definition done in Curto et al. (2019).

In our opinion this is a more general interpretation than considering this as a VTEC variation at a specific IPP. This different interpretation (in fact, just a different name) for the same measurement is the origin of the two supposed mistakes that HP&GR claim in their comments:

> *First mistake*: "The difference of ionospheric carrier phases in the same phase-continuous transmitter-receiver arc, provides directly the STEC variation, without the need of any mapping function term".
>
> *Answer*: In our paper, we clearly defined ΔSTEC_i^j as the STEC variations corrected by the obliquity factor. As we have explained, considering ΔSTEC_i^j as a VTEC variation at a given IPP is just a rough approach.
>
> *Second mistake*: "In GSFLAI the linear dependence is in terms of the Vertical TEC variation, not the Slant TEC one".
>
> *Answer*: This could have happened if we had defined ΔSTEC_i^j without correcting from the obliquity factor, but this not the case.

To sum up, there is no mistakes in our strategy and the disagreement regarding HP&GR is in how the STEC variations corrected by the obliquity factor are named/interpreted. In this point, we think that our interpretation is more adequate.

HP&GR also state that, due to these supposed mistakes, our results and conclusions could be erroneous. After having processed data from an entire solar cycle, we have been able to satisfactorily cross-check our results with those found in the literature: in our opinion, this task is mandatory in any scientific work. For instance, Figure 2 depicts two of the examples that can be found in Hernández-Pajares et al. (2012) and correspond to days 216 and 210 of 2011 (during those days, two weak SF occurred, as reported in Hernández-Pajares et al., 2012). Using the same time intervals as in Hernández-Pajares et al. (2012), the panels on the right side show that our ΔSTEC detector is able to reproduce similar results to those in Hernández-Pajares et al. (2012). Indeed, the amplitude of the peak reaches to 0.2 TECU. Additionally, the detection is better if we use ΔSTEC* (a parameter also defined in our paper) because the noise is reduced and the detection is clearer. However, this detection can be done only if short time intervals are exclusively considered, as it has been done in the panels on the right side of Figure 1. In contrast, if the time intervals are expanded to an entire day (as in the left panels), it can be observed that in some instants, the values of ΔSTEC can be at the same level as or even larger than the values during the SFs. As shown in our paper, these results indicate the difficulty in establishing thresholds for unsupervised SF detections using this detector.

3 Regarding the claim about the novelty of the SF detectors

As mentioned in the introduction of the present answer, the goal of Curto et al. (2019), regarding the GNSS SF detectors, was not to present three new SF detectors but to analyse their

suitability for the automatic detection of SF. In this sense, the key results pertaining to this goal are the three complementary cumulative distribution functions presented in the three panels in Figure 9 in Curto et al. (2019). Indeed, from Figure 9, our conclusion was that ΔSTEC is not adequate for the automatic detection of SF. On the contrary, the two other detectors are more suitable for this automatic task.

We have not presented any of these SF detectors as a "new Solar Flare index", as HP&GR state in their comments. The only sentence that could be interpreted in this sense can be found at the end of *Section 2.2*: *Data and Thresholding*:

> "In conclusion, the value of ρ can be used as a measure of the confidence level for SF detection. This is a novelty with respect to previous SF detectors based on GNSS measurements, because it represents a self-consistent way for providing confidence to the SF detections".

When we compared ΔSTEC with the GNSS solar flare activity indicator (GSFLAI), we stated that they are "*similar*" (line 174) or "*equivalent*" (line 190) because, over the same events, the results obtained using our ΔSTEC detector are very similar, but not exactly the same, to those presented in Hernández-Pajares et al. (2012) (see, for instance, the aforementioned Fig. 2). There are several reasons that could explain these differences, some of which are the use of the slope (used in Hernández-Pajares et al., 2012) instead of ΔSTEC, the cadence of the data (1 s and 30 s) or the outlier exclusion strategies.

Moreover, note that the detector consists of more than just a model relating the angle between the IPP and solar zenith (χ) with each of $\Delta STEC_i^j$. For instance, Wan et al. (2005) proposed a proportional relationship of the sudden increase in total electron content (SITEC) with cos χ[1], while Hernández-Pajares et al. (2012) defined GSFLAI by means of a linear relationship between $\Delta STEC_i^j$ and cos χ. The detector, i.e., the parameters of the relationship, also depends on how these parameters are estimated: Kalman filter or least squares, constraint/smooth equations, etc. In our case, a linear relationship was assumed (as GSFLAI) instead of a proportional one (as SITEC). However, we realized that dropping the independent term of this linear relationship, the results were still worse than those presented in the left panel of Figure 9 in our paper. Therefore, we decided to constrain the value of the independent term to zero in such a way that our detector, ΔSTEC, can be close to the GSFLAI or SITEC depending on the constraint imposed on the independent term. For instance, using the case presented in the top-right panel of Figure 1 in this document, Figure 3 presents the ΔSTEC using different constraints on the independent term: a moderate constraint, as it is used in ΔSTEC (in red), a heavy constraint (in green), which should be equivalent to the SITEC in Wan et al. (2005), and no constraint on the independent term (in blue), which should be equivalent to the GSFLAI (assuming that the GSFLAI drops the independent term and considering the G2 definition for the GSFLAI that HP&GR mention in their document).

[1] Actually, the relationship shown in the paper is the inverse of the Chapman function, but, as the authors state in their paper, it can be approximated as a relationship with cos χ.

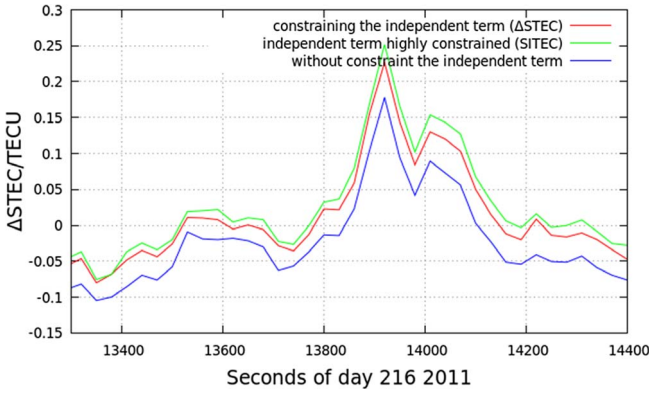

Fig. 3. ΔSTEC computed using three different constraints on the independent term of the linear fitting: without constraint (in blue), hard constraint (in green) and moderate constraint (in red).

As shown, a moderate constraint on the independent term causes ΔSTEC to behave within the GSFLAI and SITEC outputs. In this way, in this example, ΔSTEC is closer to the SITEC than to the GSFLAI.

In summary, there are some aspects of the implementation of the SF detectors that are not explicitly shown in the corresponding articles that describe the detector but that could affect their performance. This is the reason why we have compared only the results, concluding that they are similar, and for the same reason, we limited our conclusion to the poor performance of ΔSTEC as an automatic detector. However, in our opinion, this conclusion should be extended to detectors based on the sudden increase in the STEC at the SSP (not only ΔSTEC or the GSFLAI but others defined in previous works, such as the case of the SITEC). Consequently, coming back to the novelty, it would be a non-sense to present ΔSTEC as a new automatic detector (as HP&GR are claiming) and, after that, to conclude that it does not work as an automatic detector. Therefore, this is an irrelevant discussion because, in our paper, we are not using ΔSTEC or the GSFLAI for automatic detections.

Finally, HP&GR state that, in previous works, they have used the second difference in time of the VTEC at the SSP as an indicator of solar activity. Following the same line of thought as HP&GR, one could state that the first difference in time of the VTEC at the SSP was used in several works prior to Hernández-Pajares et al. (2012). Therefore, one should conclude that there is no novelty in the GSFLAI definition. However, we think that this is not the case and that, as we have commented before, in SF detection, it is important not only to determine which physical property should be used to characterize the SF occurrence but also to select the methodology necessary to obtain the corresponding parameters. Moreover, as we stated before, in our work, we did not claim that the detectors were novel, but simply discussed the best way to use them as automatic SF detectors, which, in the end, should be their goal.

For instance, HP&GR refer to Monte-Moreno & Hernández-Pajares (2014), where they used the "*subsolar Vertical Total Electron Content double difference in time*" as an indicator of solar activity. In fact, they used in this paper the difference in time (rate) of the GSFLAI (GSFLAIR) which, in our case,

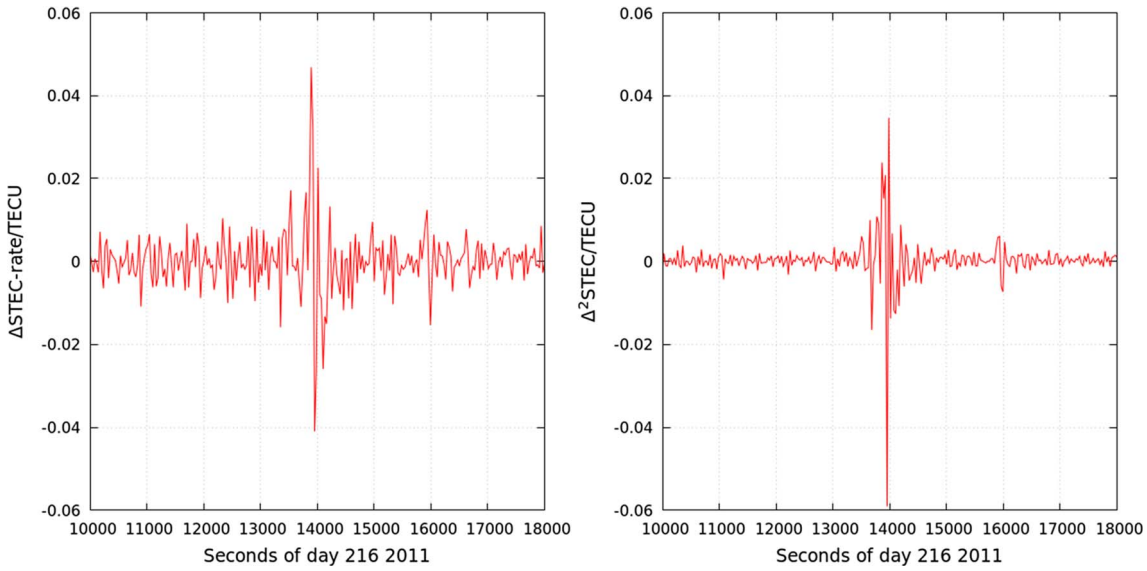

Fig. 4. Left panel: ΔSTEC rate for the example depicted Figure 3. Right panel: Δ^2STEC for the example depicted in Figure 3.

should be similar to the rate of ΔSTEC. However, Δ^2STEC is not equivalent to the ΔSTEC rate. Indeed, the first one is obtained by fitting a linear model to the satellite-receiver $\Delta^2\text{STEC}_i^j$, while the second one would be obtained by differencing in time ΔSTEC at the SSP. In this way, Δ^2STEC should be the rate of ΔSTEC* defined in our paper. In order to see the differences, Figure 4 depicts for the same example in Figure 3 the ΔSTEC rate in the left panel, and the Δ^2STEC in the right panel. It can be seen that both detectors have similar peaks when the SF occurs. However, the noise level of the ΔSTEC rate is several times larger than the noise in the Δ^2STEC detector. Probably, this is the reason why Monte-Moreno & Hernández-Pajares (2014) set a threshold of 0.025 TECU for the SF detection based on the "*experience of the authors comparing with other sources*". In our case, we set a threshold for Δ^2STEC to just 0.01 TECU based in our statistic results, which are shown in Figure 9 of our paper (middle panel). As it can be seen in this panel we are able to detect, in a confident way, much more SFs than putting the threshold in 0.025 TECU.

We have to recognize that we did not aware the work in Monte-Moreno & Hernández-Pajares (2014), otherwise we would remark in our work this improvement of Δ^2STEC with respect to GSFLAIR.

References

Curto JJ, Juan JM, Timoté CC. 2019. Confirming geomagnetic Sfe by means of a solar flare detector based on GNSS. *J Space Weather Space Clim* **9**: A42. https://doi.org/10.1051/swsc/2019040.

Hernández-Pajares M, García-Rigo A, Juan JM, Sanz J, Monte E, Aragón-Àngel A. 2012. GNSS measurement of EUV photons flux rate during strong and mid solar flares. *Space Weather* **10(12)**: doi: https://doi.org/10.1029/2012SW000826.

Monte-Moreno E, Hernández-Pajares M. 2014. Occurrence of solar flares viewed with GPS: Statistics and fractal nature. *J Geophys Res Space Phys* **119(11)**: 9216–9227. https://doi.org/10.1002/2014JA020206.

Rovira-Garcia A, Juan JM, Sanz J, González-Casado G, Ibáñez D. 2016. Accuracy of ionospheric models used in GNSS and SBAS: methodology and analysis. *J Geod* **90(3)**: 229–240. https://doi.org/10.1007/s00190-015-0868-3.

Rovira-Garcia A, Ibáñez-Segura D, Orús-Perez R, Juan JM, Sanz J, González-Casado G. 2019. Assessing the quality of ionospheric models through GNSS positioning error: methodology and results. *GPS Solu* **24(1)**: 4. https://doi.org/10.1007/s10291-019-0918-z.

Wan W, Liu L, Yuan H, et al. 2005. The GPS measured SITEC caused by the very intense solar flare on July 14, 2000. *Adv Space Res* **36**: 2465–2469. https://doi.org/10.1016/j.asr.2004.01.027.

Cite this article as: Curto JJ, Juan JM & Timoté CC 2020. Answer to the comments on "Confirming geomagnetic Sfe by means of a solar flare detector based on GNSS". *J. Space Weather Space Clim.* **10**, 16.

J. Space Weather Space Clim. 2020, **10**, 29

https://doi.org/10.1051/swsc/2020030

JSWSC

Available online at:
www.swsc-journal.org

Topical Issue - Scientific Advances from the European Commission H2020 projects on Space Weather

RESEARCH ARTICLE OPEN ACCESS

Impact of medium-scale traveling ionospheric disturbances on network real-time kinematic services: CATNET study case

Cristhian Camilo Timoté*, José Miguel Juan, Jaume Sanz, Guillermo González-Casado, Adrià Rovira-García, and Miquel Escudero

Research Group on Astronomy and Geomatics (gAGE), Universitat Politècnica de Catalunya (UPC), Jordi Girona 1–3, 08034 Barcelona, Spain

Received 2 December 2019 / Accepted 9 June 2020

Abstract – Medium-scale traveling ionospheric disturbances (MSTIDs) are fluctuations in the plasma density that propagate through the upper layer of the atmosphere at velocities of approximately 100 m/s and periods reaching some tens of minutes. Due to their wavelengths, MSTIDs can degrade the performance of differential positioning techniques, such as real-time kinematics (RTK) or network-RTK (NRTK). This paper defines a novel methodology as a tool for relating the errors in NRTK positioning based on an MSTIDs indicator using the second difference in time of the slant total electron content (STEC). The proposed methodology performs integer ambiguity resolution (IAR) on the undifferenced measurements instead of using double-differenced carrier-phase measurements, as it is usual in RTK and NRTK. Statistical tests are applied to evaluate the degradation in the position errors caused by the impacts of MSTIDs on RTK and NRTK positioning over a data set spanning one year gathered from the CATNET network; a dual-frequency network of fixed permanent GNSS receivers located at the mid-latitudes of northeastern Spain. With the development of the proposed methodology for measuring the position degradation, another results of the present research are the establishment of thresholds for the proposed MSTIDs index, which can be used to monitor the positioning solution and to warn users when the measurements are affected by MSTIDs events, relating the position error to MSTIDs that affect not only the user receivers but also of the reference receivers within the network.

Keywords: medium-scale TIDs / ionospheric disturbances / NRTK / integer ambiguity resolution

1 Introduction

Traveling ionospheric disturbances (TIDs) are plasma density fluctuations that propagate through the ionosphere with a broad range of velocities and frequencies. Depending on the TID characteristics, some authors (Jacobson et al., 1995) distinguish between large-scale TIDs (LSTIDs) with periods greater than 1 hour and moving faster than 0.3 km/s, and medium-scale TIDs (MSTIDs) with shorter periods (less than 1 h) and slower velocities (less than 0.3 km/s). Although the sources of MSTIDs are not unique, MSTIDs are linked to meteorological phenomena such as neutral winds, eclipses and the solar terminator (ST), which produces atmospheric gravity waves (AGW) and manifests them as TIDs at ionospheric heights (Hernández-Pajares et al., 2006).

The ionosphere represents one of the major signal error sources in positioning using Global Navigation Satellite Systems (GNSS). Without any modelling, the contributions of ionospheric errors to GNSS observables can reach up to tens of metres (Sanz et al., 2013). GNSS double-frequency receivers can eliminate up to 99.9% of the ionospheric refraction effect by implementing the ionosphere-free (IF) combination of code $\left(P_{\mathrm{IF}} = \frac{f_1^2 P_1 - f_2^2 P_2}{f_1^2 - f_2^2}\right)$ or carrier-phase $\left(L_{\mathrm{IF}} = \frac{f_1^2 L_1 - f_2^2 L_2}{f_1^2 - f_2^2}\right)$ measurements at frequencies f_1 and f_2. In contrast, single-frequency receivers must apply ionospheric models to account for the ionospheric refraction (Rovira-Garcia et al., 2019). The effects of the frequency-dependent terms (including the ionospheric refraction) can be estimated using the geometry-free (GF) combination of code ($P_{\mathrm{GF}} = P_2 - P_1$) or carrier-phase measurements ($L_{\mathrm{GF}} = L_1 - L_2$), which cancels out the geometric part of the measurements.

In the presence of MSTIDs, the total electron content (TEC) in the ionosphere increases by some TEC units (TECU), where 1 TECU represents an ionospheric delay of approximately 16 cm in the L1/E1 GNSS frequency (1575.42 MHz), which is less than the expected accuracy of the corrections provided by ionospheric models (Rovira-Garcia et al., 2016); this error has a minor impact on GNSS standard positioning services

*Corresponding author: cristhian.timote@upc.edu

based on code measurements. By contrast, high-accuracy positioning services (HAS) based on carrier-phase measurements, such as the precise point positioning (PPP), real-time kinematics (RTK), or network RTK (NRTK), require a precise modelling of the ionospheric effects. Indeed, fluctuations reaching several tenths of TECUs in the ionospheric corrections can affect the positioning accuracy of HAS when a precise ionospheric modelling is needed (Hernández-Pajares et al., 2000).

In the particular case of both RTK and NRTK, dual-frequency receivers can implement the L_{IF} combination to account for ionospheric refraction at the cost of enlarging the noise by a factor of three compared with the noise contributed by each individual signal. This is because the difference of squared frequencies dividing the measurements in the L_{IF} and P_{IF} definition (Sanz et al., 2013). For single-frequency receivers, the ionospheric delay of GNSS signals is corrected assuming that it is identical to the ionospheric delay experienced by the closest reference receiver (RTK) or to a linear combination of the ionospheric effects experienced by the network of reference receivers (NRTK). MSTIDs can degrade the ionospheric mitigation of single-frequency users because the baselines of RTK and NRTK are tens of kilometres, which are distances comparable to the typical wavelengths of MSTIDs (Alves et al., 2001; Lachapelle & Alves, 2002).

The present paper presents a new methodology for characterizing the impact of MSTIDs on NRTK positioning, and proposes an index as a tool to alert users about the MSTIDs effect on the GNSS user positioning. The manuscript is organized as follows: Section 1 is the current introduction. Section 2 presents the data set used and the network of NRTK stations to which the study is applied. Section 3 develops a novel methodology for creating the reference measurements from undifferenced measurements for which the carrier-phase ambiguities have been fixed. Section 4 presents the implementation of an ionosphere-free combination to obtain the reference navigation solution. Section 5 assesses the degradation of the positioning using a single frequency. Section 6 analyses the degradation of the positioning caused by MSTIDs, presents the implementation of a new index to warn RTK and NRTK users about the impacts of MSTIDs effects, and provides statistical results in order to assess the MSTIDs index performance. Finally, Section 7 summarizes the main conclusions of this work.

2 Data: the CATNET NRTK service

The methodology implemented in this study is developed using data from a network of sixteen permanent stations equipped with dual-frequency GNSS receivers. These stations are part of the CATNET NRTK service of the Cartographic and Geologic Institute of Catalonia (ICGC) in Spain (Talaya & Bosch, 1999). Nine stations are selected for the study in the following configuration: three of the stations are used as "service user" or "rover" receivers (*PLAN*, *MARE*, and *SBAR*, depicted in blue in Fig. 1), whereas the remaining six are treated as fixed reference receivers (*BEUD*, *BELL*, *SONA*, *GARR*, *LLIV*, and *CASE*, depicted in red in Fig. 1). Details about the implemented network are presented in Table 1 and Figure 1.

Additionally, in this study, the reference receiver *GARR* is used as the reference RTK receiver instead of implementing

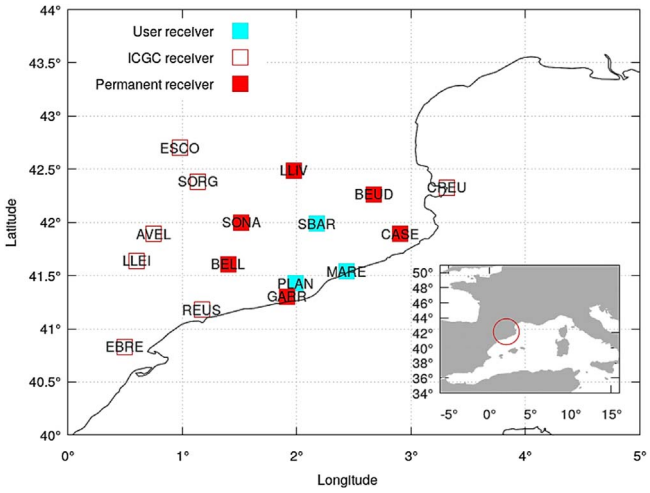

Fig. 1. CATNET NRTK network. Receivers in red: reference receivers; receivers in blue: user receivers.

the typical approach of dynamically selecting the closest reference receiver with respect to the user receiver. This approach is applied to represent the effect of the distance on the position solution for each of the three user receivers. The proposed network configuration does not represent the typical NRTK baselines between the user receiver and reference receivers, as we are implementing fixed stations as user receivers. The data set used in the present study comprises a full year of data from day of year (DoY) 200 in 2017 to DoY 200 in 2018.

3 Methodology for obtaining unambiguous measurements in the CATNET service

The accuracy of a HAS depends on factors such as the satellite geometry and/or the quality of the different HAS corrections (such as the ionospheric corrections). This dependency on several factors makes it difficult to separately attribute the degradation in the navigation solution to any of these factors. RTK and NRTK are based on fixing carrier phase ambiguities; therefore, one of the most relevant topics when computing the network correction is the ability to fix carrier-phase ambiguities at the network stations. To exclude this dependency, we have fixed all these carrier phase ambiguities offline. In this section, we explained how we process the data to obtain solutions with fixed carrier-phase ambiguities.

3.1 Fixing carrier-phase ambiguities

GNSS observables (consisting of the pseudorange P and carrier phase L) emitted by a satellite j and collected by a receiver i, at a frequency f_m can be modelled as (Sanz et al., 2013):

$$\begin{aligned} L^j_{m_i} &= \rho^j_i + c(T_i - T^j) + \mathrm{Trop}^j_i - I^j_{m_i} + \lambda_m\left(\delta_{mi} + \delta^j_m + N^j_{m_i}\right) \\ P^j_{m_i} &= \rho^j_i + c(T_i - T^j) + \mathrm{Trop}^j_i + I^j_{m_i} + D_{mi} + D^j_m \end{aligned} \quad (1)$$

where ρ^j_i stands for the geometric distance between the satellite and receiver, and c is the speed of light. T_i and T^j are the

Table 1. CATNET receivers' specifications.

Receiver	Latitude (degrees)	Longitude (degrees)	Type of receiver	Distances (km)								
				PLAN	*MARE*	*SBAR*	*BEUD*	*BELL*	*SONA*	*GARR*	*LLIV*	*CASE*
PLAN	41.23	1.99	User	–	39.3	64.3	109.1	52.8	74.7	15.2	117.7	92.2
MARE	41.34	2.43	User	39.3	–	54.6	83.2	86.5	92	50.7	112.2	55.5
SBAR	41.79	2.17	User	64.3	54.6	–	51.5	76.9	54.5	79.3	57.7	61.5
BEUD	42.06	2.67	Reference	109.1	83.2	51.5	–	128.4	100.2	124.3	62.9	45.5
BELL	41.41	1.40	Reference	52.8	86.5	76.9	128.4	–	44.6	54.7	108.4	128.9
SONA	41.80	1.52	Reference	74.7	92	54.5	100.2	44.6	–	84.4	65.8	115.7
GARR	41.10	1.91	Reference	15.2	50.7	79.3	124.3	54.7	84.4	–	131.7	105.4
LLIV	42.29	1.97	Reference	117.7	112.2	57.7	62.9	108.4	65.8	131.7	–	101.4
CASE	41.69	2.90	Reference	92.2	55.5	61.5	45.5	128.9	115.7	105.4	101.4	–

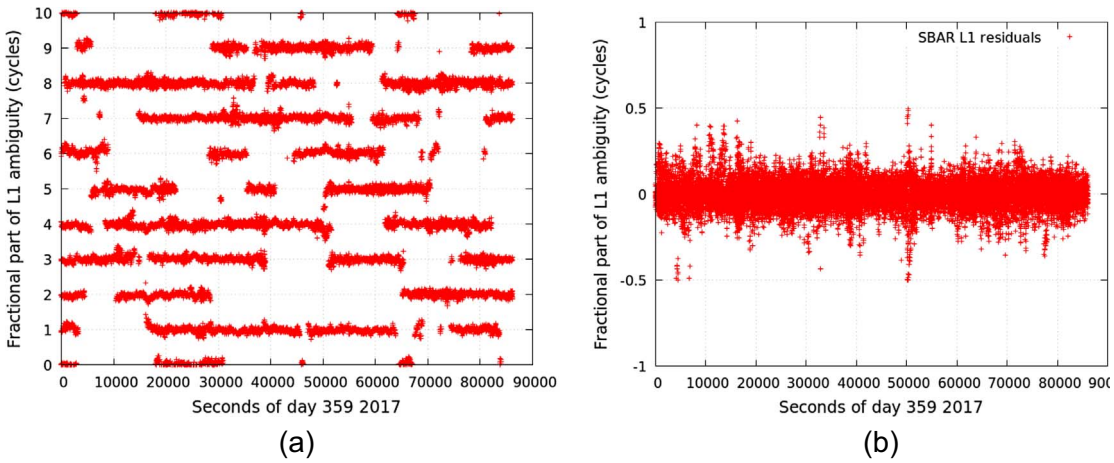

Fig. 2. Fractional part of the L1 carrier-phase ambiguities for all the satellites in view from the receivers *SBAR* on day 359 in 2017. The panels show the fixing-ambiguity process in which it is possible to fix the carrier-phase ambiguities with confidence.

receiver and satellite clock offsets, respectively. δ_{mi}, δ_m^j, D_{mi}, and D_m^j are the instrumental delays (floated numbers), at the frequency f_m, of each of the devices. Trop_i^j stands for the tropospheric effect on the GNSS signal. $I_{m_i}^j$ is the ionospheric delay (advance for the phase and delay for the code measurement) proportional to f_m^{-2}. Finally, for the carrier-phase measurement, λ_m represents the carrier-phase wavelength, and $N_{m_i}^j$ is the integer ambiguity. Although carrier-phase measurements $L_{m_i}^j$ are more precise than code measurements $P_{m_i}^j$, due to the unknown value of $N_{m_i}^j$, $L_{m_i}^j$ measurements are ambiguous.

In NRTK positioning, the expressions in equation (1) are simplified by forming double differences ($\Delta\nabla$) with respect to a reference receiver and a reference satellite. One of the advantages of this technique is that the parameters depending upon a single device (either a satellite or a receiver) are cancel out, producing the following observable (Seeber, 2008):

$$\Delta\nabla L_{m_i}^j = \Delta\nabla\rho_i^j + \Delta\nabla\mathrm{Trop}_i^j - \Delta\nabla I_{m_i}^j + \lambda_m\Delta\nabla N_{m_i}^j. \quad (2)$$

According to equation (2), computations in a NRTK network requires carrier-phase measurements with fixed ambiguities between the stations of the network. Estimation of the exact integer value of $\Delta\nabla N_{m_i}^j$ can be achieved by means of any of the well-known method for fixing such ambiguities, such as the LAMBDA method (Teunissen, 1995). Therefore, the accuracy of the position estimates depends upon the ability to fix carrier-phase ambiguities, more precisely, on how many ambiguities are present and how fast the ambiguities are fixed (Sanz et al., 2013).

To reduce the dependency on the ability to successfully resolve ambiguities (ambiguity-fixing success ratio), we fix the integer part of the carrier-phase ambiguities of all the measurements of the undifferenced mode (i.e. before Eq. (2)). To achieve this, we have taken advantage of knowing the precise coordinates of each receiver to solve the phase biases, the so-called fractional part of the carrier-phase ambiguities (Collins et al., 2008; Ge et al., 2008), to estimate the integer part of the carrier-phase ambiguities for all the measurements in the network.

Detailed information about the whole ambiguity-fixing process can be found in (Juan et al., 2020); here, we simply present some examples of this process. As a first example of the ambiguity-fixing capability, Figure 2a depicts the actual floating values of the ambiguities (modulo 10 of the floating values) for the receiver *SBAR* during the day 310 in 2017, illustrating that the real estimates of the ambiguities are close to the integer values (modulo 1 of the floating values). Figure 2b presents

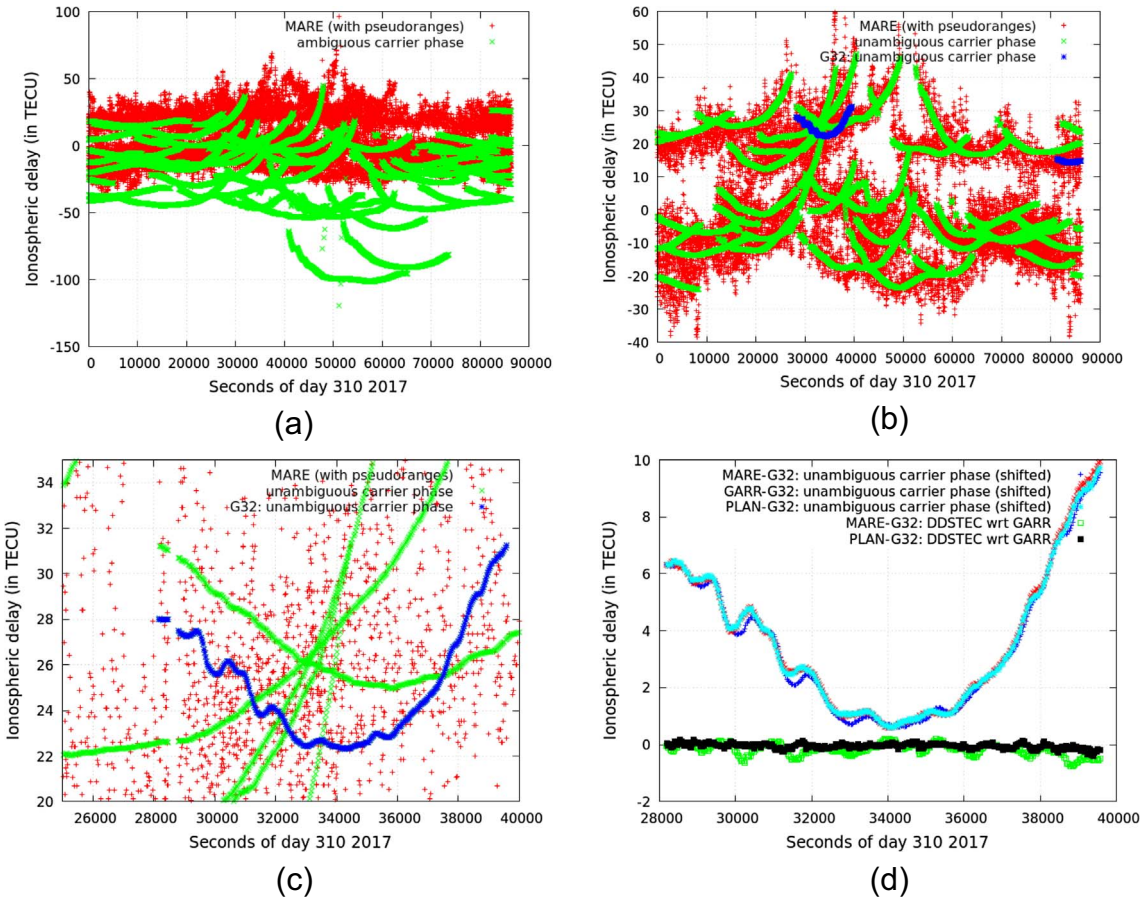

Fig. 3. Top panels: example of the ionospheric delays measured with the carrier phases (green) and pseudoranges (red) corresponding to the receiver *MARE* during DoY 310 in 2017. The top left panel (a) displays the raw measurements. The top right panel (b) corresponds to the measurements where the carrier-phase ambiguities have been fixed. The ionospheric delay for the satellite G32, affected by a MSTID, is highlighted in blue. The bottom left panel (c) presents a more detailed picture of the MSTID event highlighted in panel (b). The bottom right panel (d) depicts the undifferenced STEC for the satellite G32 measured by receivers *MARE* (blue), *GARR* (red), and *PLAN* (cyan). The double differences of the ionospheric delays with respect to *GARR* are also depicted in green (*MARE*) and black (*PLAN*).

how different the floating values of the carrier-phase ambiguities are from their closest integer values. The differences are typically less than 0.2 cycles, enabling the confident resolution of carrier-phase ambiguities to their integer values.

A second example showing the advantage of fixing undifferenced ambiguities can be found in Figure 3, which graphically presents a comparison between the GF combinations of the pseudoranges and carrier for the user receiver *MARE*. Figure 3a depicts the values without fixing the carrier-phase ambiguities, i.e. the raw measurements. Carrier-phase measurements are much more precise (less noisy) than pseudorange measurements. However, due to the presence of uncorrected ambiguities, the carrier phases present biases that make them less accurate than the pseudoranges. Figure 3b depicts the values after fixing the carrier-phases ambiguities; after this process, the ionospheric delays obtained from the carrier phases are precise and accurate. In this panel, we highlight the ionospheric delays experienced by the GPS satellite G32 in blue to demonstrate the effect produced by a MSTID. Figure 3c presents a magnified view of the Figure 3b, exposing the previously mentioned disturbance. Finally, Figure 3d shows the advantage of our approach (i.e., fixing the carrier-phase ambiguities in an undifferenced manner) with respect to the standard RTK method of fixing the carrier-phase ambiguities of the double-differenced (DD) measurements. Indeed, this panel depicts the ionospheric delays in the measurements from the satellite G32 and in those collected by the receivers *MARE*, *GARR*, and *PLAN* in blue, red and cyan, respectively. In all three arcs, the presence of the MSTID is clear, as is the propagation of the MSTID. This is not the case for the DD measurements from *MARE* (green) and *PLAN* (black) with respect to *GARR*. Indeed, only the differential effects can be seen, with the amplitude of the MSTID differential effect dependent on the baseline between the receivers.

4 Obtaining the reference navigation solution by means of the ionosphere-free combination

Following the methodology presented in the previous section, we fix the carrier-phase ambiguities for each of the nine receivers (the user and reference receivers) selected from

CATNET. We use these unambiguous data to compute all the navigation solutions. Note that these unambiguous measurements can be modelled as:

$$L^j_{m_i} = \rho^j_i + c(T_i - T^j) + \mathrm{Trop}^j_i - I^j_{m_i} + \lambda_m(\delta_{mi} + \delta^j_m) \quad (3)$$

which is mathematically equivalent to the pseudoranges $P^j_{m_i}$ model in equation (1), except for the sign of the ionospheric effect and the carrier-phase biases.

Equation (3) is the standard equation for the navigation problem, i.e. for obtaining the user position $\vec{r}_i$. After fixing carrier-phase ambiguities, there are several ways to proceed:

(i) To work with undifferenced measurements (as in Eq. (3)): in this case, one needs to know the satellite clock offsets (T^j) and the satellite phase biases (δ^j_m), which are usually provided by several centres, such as the International GNSS Service.
(ii) For a common satellite, to make differences between the user measurements and the measurements from a near-reference receiver: in this case, one does not need the satellite parameters.
(iii) To make double differences using a common reference satellite (as in Eq. (3)): in this case, one does not need to estimate the receiver clock (T_i).

Once ambiguities are fixed, these three techniques should provide similar results. For simplicity, let us assume we are using double differences: starting from an approximate position ($\vec{r}_o$) for the user, one can compute a value for the receiver-satellite vector ($\vec{\rho}^j_{oi}$). Therefore, equation (2) can be written as (Sanz et al., 2013):

$$\Delta\nabla\left(L^j_{m_i} - \rho_{oi}{}^j\right) = \frac{\vec{\rho}^j_{o_i}}{\rho^j_{o_i}}\Delta\vec{r}_i + \Delta\nabla\mathrm{Trop}^j_i - \Delta\nabla I^j_{m_i} \quad (4)$$

where obtaining the correction vector $\Delta\vec{r}_i = \vec{r}_i - \vec{r}_{oi}$ is the basic goal of the navigation problem. This is accomplished by solving equation (4) using techniques such as least squares or Kalman filter.

Differential tropospheric corrections, $\Delta\nabla\mathrm{Trop}^j_i$, are usually estimated alongside the correction vector using a simple tropospheric model. Therefore, the main unmodelled term in equation (4) is the differential ionospheric correction $\Delta\nabla I^j_{m_i}$, which cannot be solved in equation (4). In fact, the way that $\Delta\nabla I^j_{m_i}$ is treated determines the different types of navigation solutions that we present in this work:

- *Single frequency RTK solution*: For each satellite, the ionospheric delays for both user and reference receiver measurements are the same ($\Delta\nabla I^j_{m_i} = 0$).
- *Single frequency NRTK solution*: The differential ionospheric delays, $\Delta\nabla I^j_{m_i}$ at the user position can be estimated by linearly interpolating the delays in a set of permanent receivers surrounding the user receiver.
- *Ionosphere-free solution*: With a receiver having two frequencies, the user can build the L_{IF} combination, as defined in the introduction. This combination cancels out the ionospheric effect on the GNSS signals.

From their definitions, NRTK and RTK navigation solutions will be affected by the errors in the $\Delta\nabla I^j_{m_i}$ assumptions. These errors will become larger as the baseline between the user and the reference receiver increases. In contrast, ionosphere-free measurements are unaffected by the differential ionospheric corrections. Therefore, the corresponding navigation solution $\vec{r}_{\mathrm{IF}}$ will be independent of the baseline between the user and the reference receiver.

Figure 4 depicts an example of the navigation solution obtained with the unambiguous L_{IF} over 24 h for the receiver *PLAN*, the closest user receiver with respect to the reference receiver (15.2 km from the reference receiver *GARR*). As it can be seen, the 3D error in the navigation solution is usually below 10 cm, except during some epochs presenting poor satellite geometries, i.e., when the dilution of precision (DOP) is larger than 6 (red points). 3D positioning errors better than 10 cm constitute the nominal performance expected for NRTK positioning (see for instance Cannon et al., 2001; Lachapelle & Alves, 2002; Wielgosz et al., 2005).

A more general assessment of the 3D positioning error using L_{IF} is performed in Figure 5. This figure depicts the statistic for the three user receivers during the entire data period. This statistic is calculated by means of the complementary of the cumulative distribution function (CCDF, also represented as 1-CDF).

As depicted in Figure 5, 95% of the cases have an error smaller than 8 cm. This value can be established as the nominal reference value at the 95th percentile for the 3D positioning error with L_{IF}.

As expected, the three user receivers report similar statistics regardless of their distance to the reference station *GARR*. This is because, as mentioned above, L_{IF} measurements are not affected by differential ionospheric delays. Therefore, for each user receiver, this solution can be taken as the reference solution when one wants to assess the degradation in the positioning using the RTK or NRTK techniques, i.e., techniques affected by the correctness of the ionospheric assumptions.

5 Navigation solution using either the RTK or the NRTK techniques with a single-frequency receiver

When a user navigates solely with L1 measurements (single-frequency receivers), and therefore it is not able to build the IF combination, the navigation solutions are affected by the way in which the differential ionospheric delays are corrected.

And example of that can be seen in Figure 6, where the navigation solution using L_{IF}, RTK and NRTK are compared. This comparison is done using the CCDFs of the navigation solutions for the three user receivers and using the three HAS techniques defined in the previous section.

The shortest baseline length of 15.2 km is between *PLAN* and *GARR*. In this case, as shown in Figure 6a, up to 15 cm, the 3D position error using L1 (RTK or NRTK) is smaller than that using L_{IF}. This is because the differential ionospheric effects between *PLAN* and *GARR* are quite small (see the example in Fig. 3d) and, as mentioned in the introduction, the thermal error of L_{IF} is amplified by a factor of three with respect that of L1 and therefore it dominates the error. On the other hand, the RTK and NRTK single-frequency solutions are quite equivalent, and the degradation of the solution with respect to that using L_{IF} occurs with relatively low probability (less than 1%).

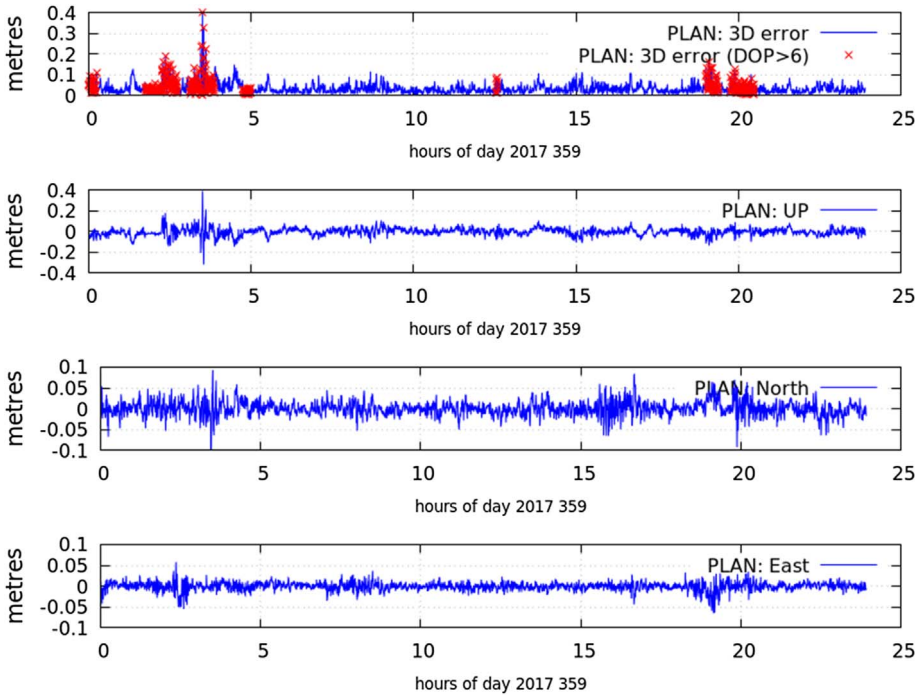

Fig. 4. Ionosphere-free combination for the navigation solution at the *PLAN* receiver. From top to bottom: 3D error, up, north, and east components.

Figure 6b presents the results for *MARE*, located at 50.7 km from *GARR*. The differential ionospheric term in equation (4) becomes greater than in the results for *PLAN*, and more than 10% of the cases using L1 with RTK positioning have positioning errors larger than 8 cm. However, if the ionospheric delay is corrected using the data from the network (NRTK), the probability of having an error larger than or equal to 8 cm is approximately 8%. This result is not exceedingly different from the percentage found in the case with L_{IF} (approximately 5%).

Finally, panel (c) of Figure 6 depicts the results for the user receiver *SBAR* (79.3 km from *GARR*). The degradation of the RTK solution increases considerably. Indeed, the probability of having an error larger than 8 cm in the 3D positioning reaches nearly 40%, while with NRTK positioning, the probability is approximately 10%, i.e., 5% more than the solution using L_{IF}.

Taking into account the previous results, we define the 3D positioning degradation, δ_{3D}, as the modulus of the difference between the single-frequency navigation (RTK or NRTK) solution $\vec{r}$ with respect to the reference solution $\vec{r}_{IF}$:

$$\delta_{3D} = \sqrt{||\vec{r}_{IF} - \vec{r}||^2}. \quad (4)$$

Figure 7 presents the statistical 3D degradation by means of the CCDF, for the three user receivers with the previously defined data set corresponding to the years 2017 and 2018. These plots confirm the results obtained and presented above. Indeed, for *SBAR*, as shown in Figure 7c, 10% of the RTK solutions present a degradation larger than 14 cm, while less than 1% of the NRTK cases present a degradation larger than 14 cm. However, if one compares the NRTK results for *SBAR* with those for *PLAN* (Fig. 7a), one can see that the 99th percentile is less than 9 cm for *PLAN* but 12 cm for *SBAR*. This represents a clear increase in the degradation in the NRTK solution, which is related with to the larger baseline.

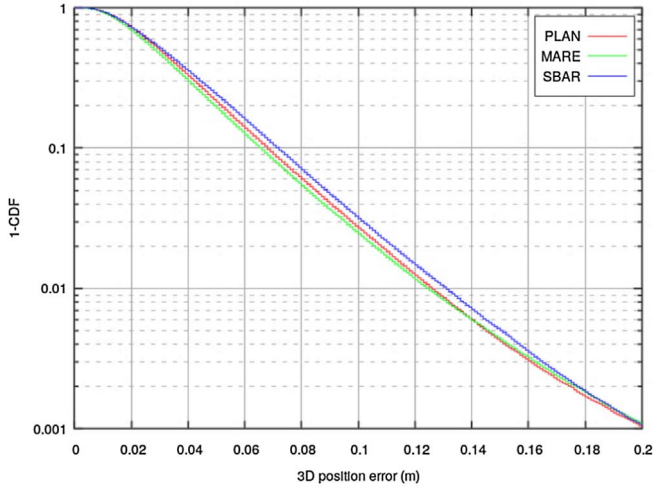

Fig. 5. Statistics for the 3D positioning error using the IF combination: the *Y*-axis depicts the probability of the 3D positioning error being greater than the value on the *X*-axis.

6 Effects of MSTIDs on position degradation: definition of an index linked to MSTIDs

We have shown that the NRTK solutions are closer than RTK solutions to the dual-frequency (L_{IF}) solution. However, as observed in Figure 7, there is some degradation in the

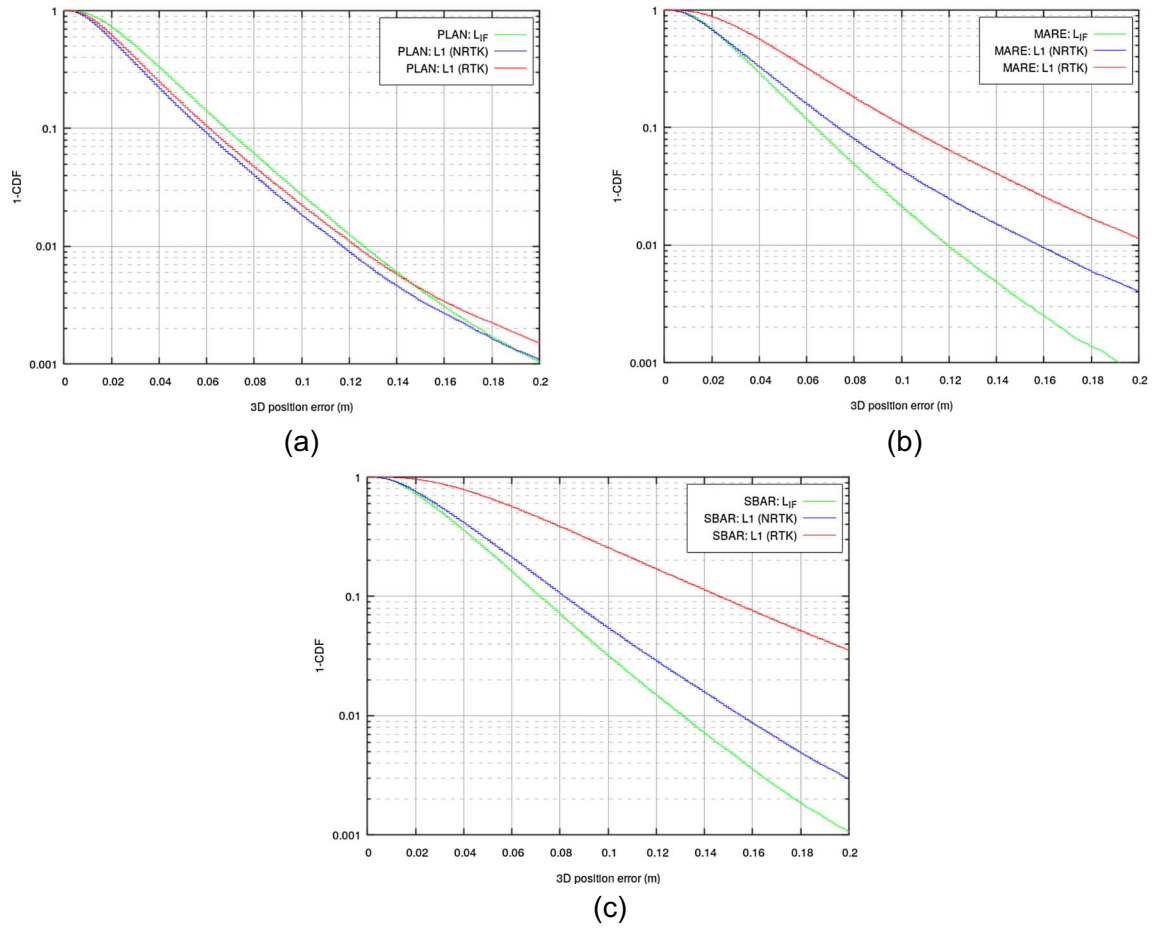

Fig. 6. Ionosphere-free (L_{IF}) solution in green, NRTK single-frequency (L1) solution in blue, and RTK single-frequency (L1) solution in red for three receivers: (a) *PLAN*, (b) *MARE*, and (c) *SBAR*.

positioning for the two receivers with the largest separation distance in the NRTK solution with respect to the IF solution. In this section, we analyse the part of the degradation in the NRTK solutions associated with the presence of MSTIDs. Indeed, NRTK positioning assumes that the differential ionospheric delays between receivers present a linear spatial behaviour. This linearity is broken by the presence of fluctuations with wavelengths (such as MSTIDs wavelengths) comparable to the network baselines. In the first subsection, we will show how MSTIDs can be detected and then propose the definition of an index linked to MSTIDs activity. In the second subsection, we will present some examples of the relationship between the position degradation and the presence of MSTIDs. Finally, in the third subsection, we will perform a statistical analysis of this relationship.

6.1 Detecting MSTIDs and defining a MSTIDs activity index

Hernández-Pajares et al. (2006) showed that the typical period of a MSTID is on the order of tens of minutes and further defined a method to detect such a fluctuations at this time scale by building the second difference in time (Δ^2) of the slant total electron content (STEC) at a given epoch t, defined as:

$$\Delta^2\mathrm{STEC}(t) = 0.5 \cdot (\mathrm{STEC}(t+\tau) + \mathrm{STEC}(t-\tau)) - \mathrm{STEC}(t) \quad (5)$$

where τ is set in such a way that it is optimal for detecting MSTIDs with a period of 10 min; i.e., when τ is equal to 5 min (Hernández-Pajares et al., 2006), there is sufficient sensitivity to detect the presence of MSTIDs with periods reaching tens of minutes. Additionally, by setting τ to 5 min, we are able to provide warnings about the presence of MSTIDs activity on a short time scale.

To quantify the activity of a MSTID, for each satellite-receiver pair, we define the MSTIDs index as the integrated amplitude over an interval 2τ (i.e., 10 min, which results in 20 samples when the measurements are sampled at a rate of 30 s):

$$\mathrm{MSTID}^2_{\mathrm{IDX}}(t) = \frac{1}{20}\sum_{i=t-2\tau}^{t}\left(M(\varepsilon)\cdot\Delta^2\mathrm{STEC}(i)\right)^2 \quad (6)$$

where M (e) is an obliquity factor for mitigating larger values of Δ^2 STEC (i) at low elevations.

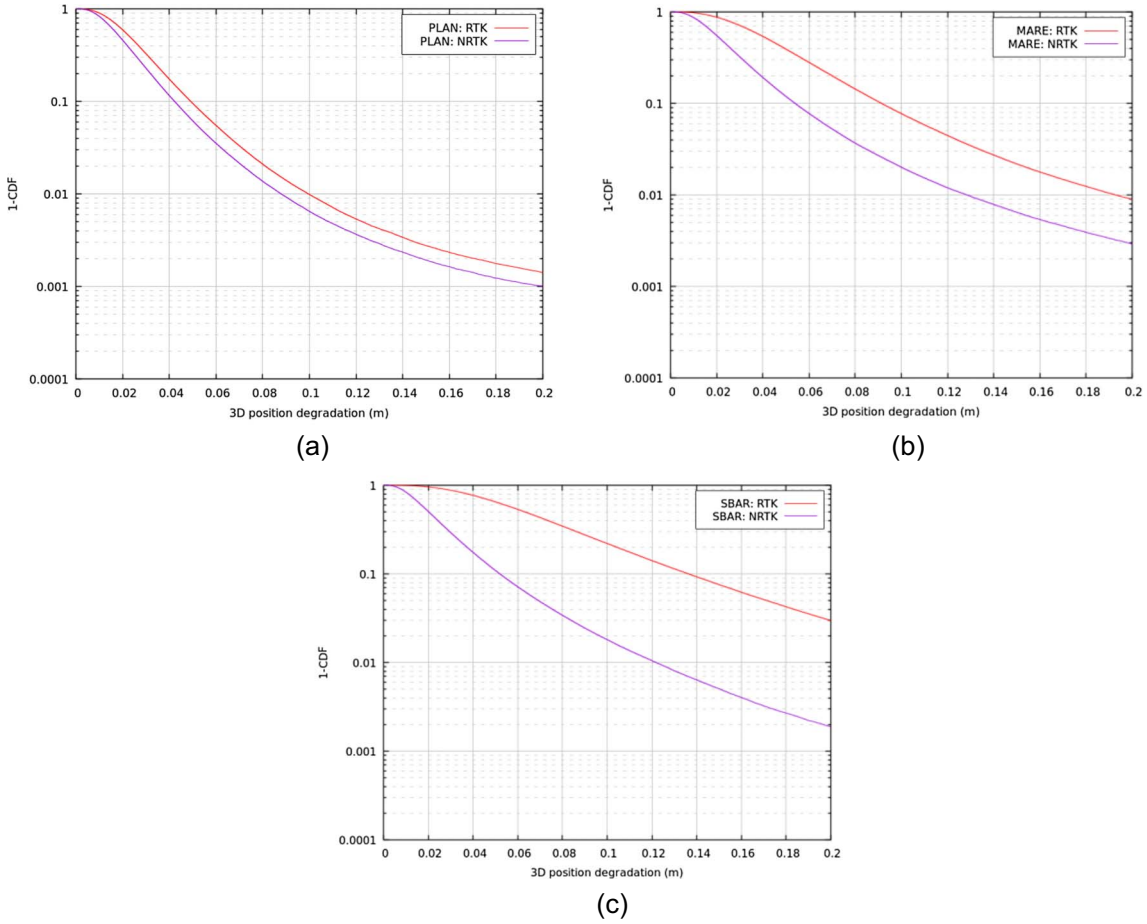

Fig. 7. CCDFs of the 3D degradation in the positioning error for the receivers (a) *PLAN*, (b) *MARE*, and (c) *SBAR* during the 1-year period of 2017–2018.

Figure 8 depicts the Δ^2 STEC, as defined in equation (5), for the receivers *GARR*, *SONA*, and *SBAR* tracking the same GPS satellite (G01). It is clear that the presence of a MSTID (with an amplitude close to 1 TECU and a period of approximately 1000 s) affects the three receivers. This STEC fluctuation clearly breaks the linearity assumption in NRTK positioning.

Figure 9 presents the results obtained after calculating $\text{MSTID}_{\text{IDX}}$ (defined in Eq. (6)) for the same satellite-receiver pairs as those in the example depicted in Figure 8. Certainly, it is possible to detect and isolate the MSTID event occurring at approximately 33,000 s of DoY 039, when $\text{MSTID}_{\text{IDX}}$ reaches a value of 0.5 TECU, which is 0.05 m for L_{GF} (1 TECU = 0.105 L_{GF} m).

6.2 Relationship of $\text{MSTID}_{\text{IDX}}$ with the error in the ionospheric corrections

Previous sections investigate the relation of the MSTID index with respect to the degradation in the ionospheric corrections and, consequently, in the position accuracy. Regarding the ionospheric corrections, note that this degradation is not influenced only by the MSTIDs activity during the user measurements period. Indeed, because the ionospheric delay is interpolated in NRTK positioning, any activity at any of the reference site contributes to the user positioning degradation. This can be seen in Figure 10, which corresponds to DoY 221 in 2017.

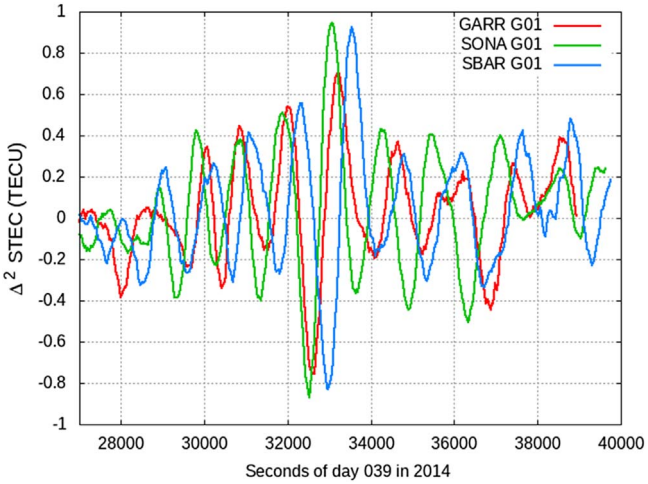

Fig. 8. MSTID effects on the second difference of the STEC for three receivers: *GARR*, *SONA*, and *SBAR*.

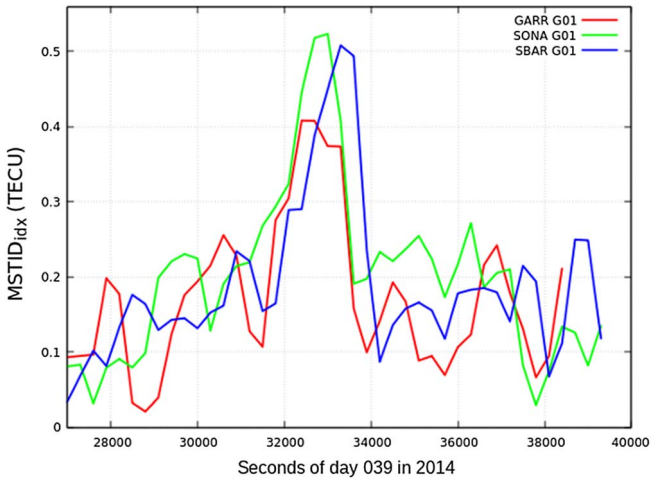

Fig. 9. MSTID index definition applied to three receivers on DoY 039 (February 6th) 2014: *GARR*, *SONA*, and *SBAR*.

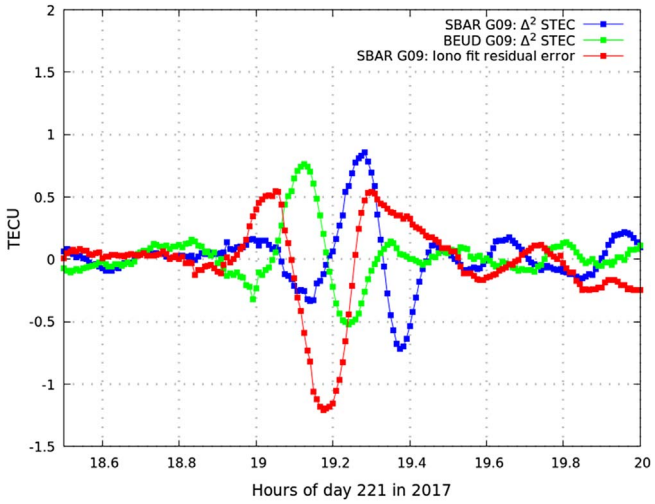

Fig. 10. Δ^2 STEC for the user receiver *SBAR* (blue) and reference receiver *BEUD* (green); the error in the ionospheric correction (red) is clearly correlated with the presence of a MSTID.

Figure 10 depicts the Δ^2 STEC experienced by measurements from the GPS satellite G09 for the user receiver *SBAR* and for the reference receiver *BEUD*. The resulting error in the ionospheric correction (which is obtained by fitting a linear model from the reference sites) at *SBAR* for the specific satellite G09 correlates with the presence of a MSTID that propagates towards the southwest. This results in a fluctuation of Δ^2 STEC observed first at *BEUD* and then at *SBAR*. Evidently, a MSTID affecting any of the reference receivers participating in the computation of the ionospheric correction in the network contributes to the error at the user receiver.

In light of previous results, one conservative approach is to define, for each satellite in view, an MSTID index associated with the whole NRTK network. This is accomplished by taking the maximum value of the $\text{MSTID}_{\text{IDX}}$ experienced by any reference receiver collecting data from that satellite. Taking into account this network of $\text{MSTID}_{\text{IDX}}$ values, users can be warned about large ionospheric errors in their corrections that could

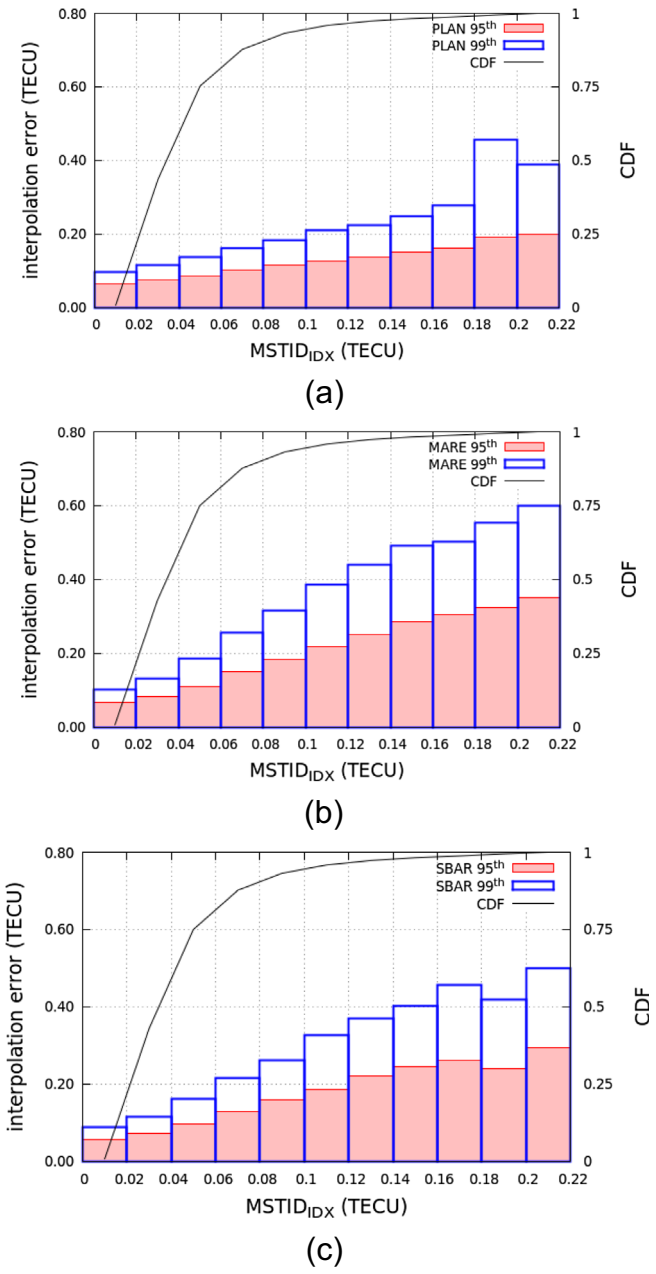

Fig. 11. Histogram of the error of the ionospheric corrections; 95th percentile (filled red boxes), 99th percentile (empty blue boxes). CDF of the ionospheric corrections (black line). The statistic is done for the three rover receivers: (a) *PLAN*, (b) *MARE*, and (c) *SBAR*.

affect their navigation solutions. However, the accuracy of the navigation solution depends on other factors in addition to the quality of the ionospheric corrections, such as the geometry of the observations. For that reason, we can take advantage of having undifferenced and unambiguous carrier-phase measurements to assess the errors in the ionospheric corrections at the user positions. Indeed, Figure 11 depicts the ionospheric errors during the studied period for the three user receivers. In this assessment, we consider only observations with elevation angles above 30°; in this way, we exclude large errors at low elevations that are not related to ionospheric activity. Each panel depicts,

for the three user receivers, histograms of the 95th and 99th percentiles of the ionospheric errors corresponding to specific values of the $MSTID_{IDX}$. As it can be seen, as the $MSTID_{IDX}$ increases the probability of having larger ionospheric errors also increases. Therefore, one could select some threshold value for $MSTID_{IDX}$ to exclude observations with large errors. For this purpose, we include the CDF of the overall cases in order to account for the percentage of the cases that will be filtered out with the $MSTID_{IDX}$ threshold. For instance, by setting the $MSTID_{IDX}$ to 0.1 TECU it is possible to guarantee that, for the three user receivers, the 95th percentile of the ionospheric corrections will be approximately less than 0.2 TECU, at the cost of excluding less than a 10% of the total measurements collected.

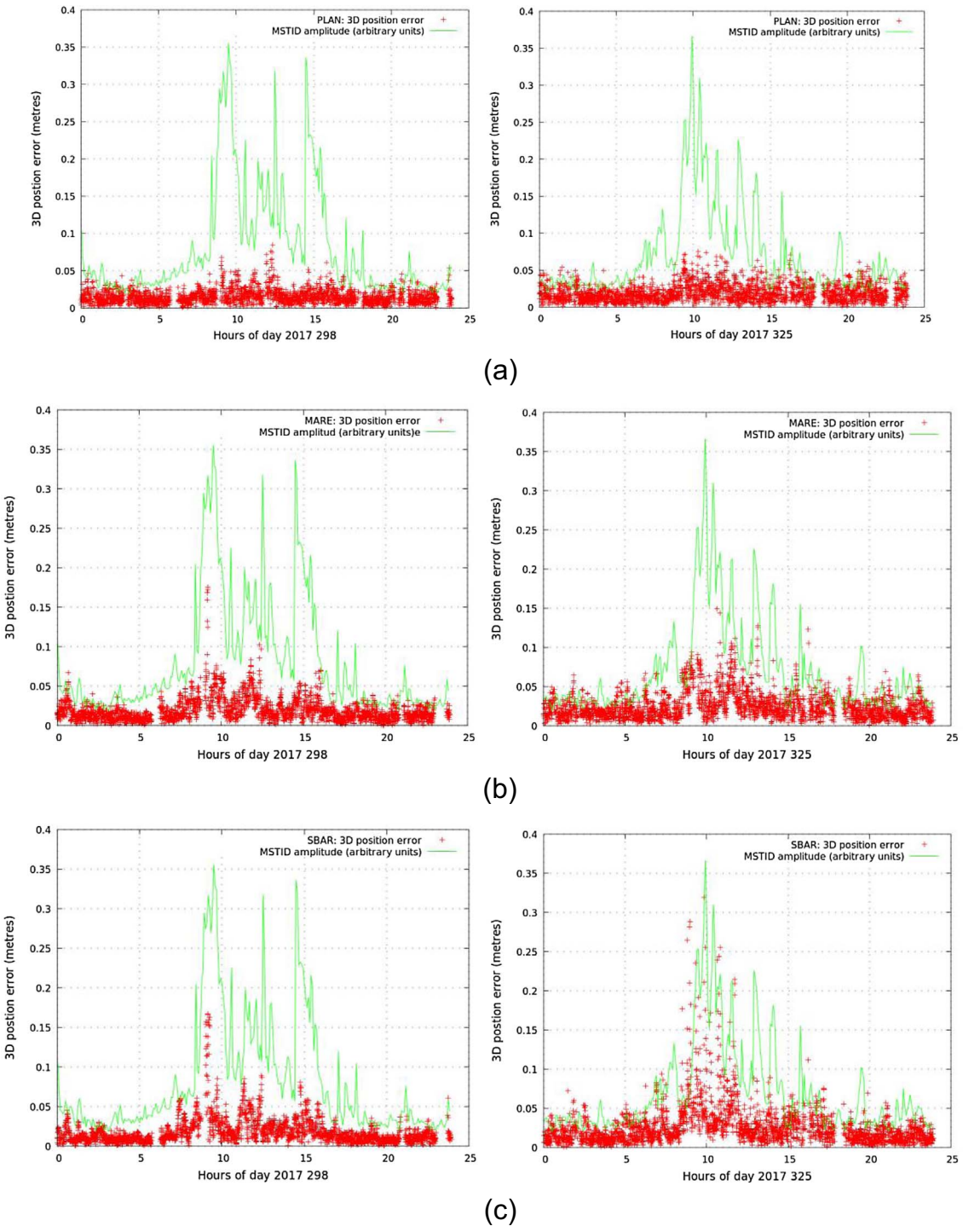

Fig. 12. 3D position errors and maximum MSTIDs amplitudes on days 298 and 325 of 2017 for the user receivers (a) *PLAN*, (b) *MARE*, and (c) *SBAR*.

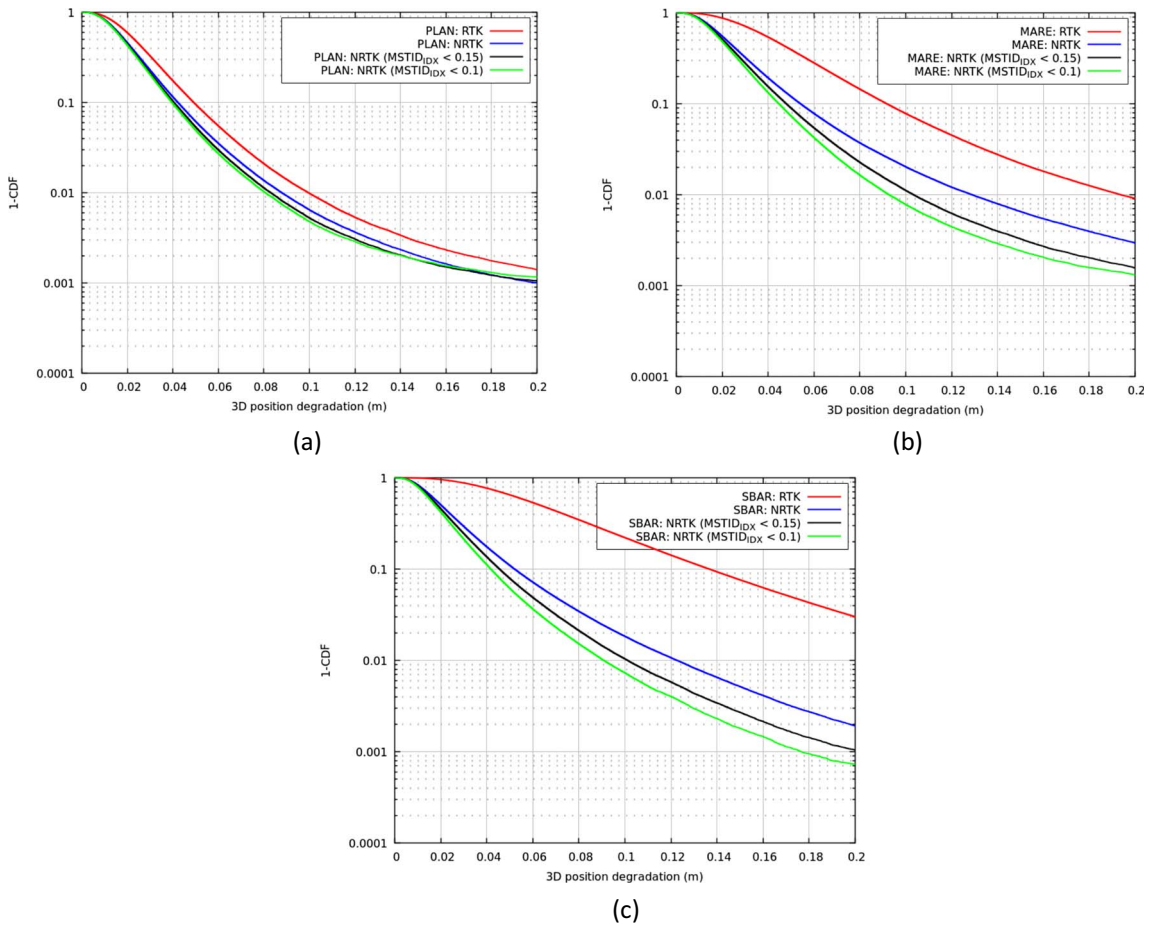

Fig. 13. 3D position degradation probabilities for user receivers: (a) *PLAN*, (b) *MARE*, and (c) *SBAR*. The solid lines represent the position solutions for RTK (red) and NRTK (blue) for all MSTIDs amplitudes. The NRTK solutions are also shown with MSTIDs amplitudes of less than 0.15 TECU (black) and with MSTIDs amplitudes of less than 0.10 TECU (green).

6.3 Relationship of MSTID$_{IDX}$ with the degradation in positioning

As mentioned in previous section, for a user that needs to correct for the ionospheric effects on their observations (i.e., users with single-frequency measurements), the errors in the ionospheric corrections are translated to the position accuracy. Figure 12 presents several examples of the degradation in the 3D position errors for three stations (from top to bottom *PLAN*, *MARE*, and *SBAR*) in contrast to the amplitude of the MSTID provided by the MSTID$_{IDX}$, on the left and on the right columns respectively. The examples correspond to days 298 and 325 of 2017. A noticeable relationship exists between the degradation in the position error of the receiver and the maximum detected MSTID amplitude in the NRTK network. For a better representation of this relationship, MSTID$_{IDX}$ has been amplified by an arbitrary scale factor from its original amplitude value (in metres). The user receiver *PLAN* shows less severe degradation of the position error than the two other receivers.

For results similar to those depicted in Figure 12 encompassing the whole period of time studied in this work, readers are referred to the following public website: http://147.83.47.222/TechTIDE_database/2017/DDD/NRTK_performance_CATNET/Plots/, where "DDD" is the three-digit DoY.

6.4 Statistical analysis

We performed a statistical analysis based on the CCDFs for the position results from DoY 200 in 2017 to DoY 200 in 2018. Figure 13 provides the probability of 3D position degradation for three user receivers (*PLAN*, *MARE*, and *SBAR*). Figure 13 also illustrates a comparison of the degradation using RTK and NRTK positioning. Moreover, to see the relationship between the 3D position degradation and MSTIDs, the NRTK solution is also computed when:

1. MSTID$_{IDX}$ is lower than 0.15 TECU, for which, in *SBAR*, 0.1% of the cases present a degradation larger than 10 cm in 3D coordinates.
2. MSTID$_{IDX}$, is lower than 0.10 TECU, for which, in *SBAR*, 0.2% of the cases present a degradation larger than 10 cm in 3D coordinates.

As shown in Figure 13, for the user receivers *SBAR* and *MARE*, which are located farther away than *PLAN*, there is a noticeable reduction in the degradation error when solutions are excluded from the statistics taking into account MSTID$_{IDX}$. In Tables 2–4, such a reduction in the degradation in the positioning error (by means of the 50th, 95th, and 99th percentiles)

Table 2. NRTK position degradation (in cm) for the user receiver *PLAN* with respect to MSTID index thresholds (in TECU) by means of the 50th, 90th, and 95th percentiles.

	50%	95%	99%
No threshold for MSTID	1.8	5.3	8.8
MSTID index less than 0.15	1.8	5.1	8.2
MSTID index less than 0.10	1.7	4.9	8.0

Table 3. NRTK position degradation (in cm) for the user receiver *MARE* with respect to MSTID index thresholds (in TECU) by means of the 50th, 90th, and 95th percentiles.

	50%	95%	99%
No threshold for MSTID	2.1	7.2	12.8
MSTID index less than 0.15	2.1	6.0	10.6
MSTID index less than 0.10	2.0	6.0	9.4

Table 4. NRTK position degradation (in cm) for the user receiver *SBAR* with respect to MSTID index thresholds (in TECU) by means of the 50th, 90th, and 95th percentiles.

	50%	95%	99%
No threshold for MSTID	2.0	6.7	12.2
MSTID index less than 0.15	1.9	5.8	10.2
MSTID index less than 0.10	1.8	5.7	9.3

is quantified for the same $MSTID_{IDX}$ thresholds presented in Figure 13.

From Figure 13 or the aforementioned tables, one can see that the reduction in the degradation is lower for the closest receiver, *PLAN* (approximately 10%), which is almost unaffected by MSTIDs: the degradation is maintained at approximately 5 cm in the 95th percentile and 8 cm in the 99th percentile.

This is not the case for the other two receivers, where the degradation is approximately 12 cm in the 99th percentile when $MSTID_{IDX}$ is not taken into account. However, if the $MSTID_{IDX}$ is considered, the degradation in the navigation solution is reduced up to 26% for *MARE* and 23% for *SBAR*. Furthermore, for the 95th percentile, *SBAR* and *MARE* reach levels of reduction similar to *PLAN* (the closest receiver). Therefore, $MSTID_{IDX}$ can be used as an indicator that warns users of degradation in the navigation solution.

7 Conclusions

The present contribution analyses the impacts of MSTIDs on a network of permanent geodetic receivers located at mid-latitudes. The methodology relies on three main steps: First, as detailed in Section 3, reference measurements are obtained by applying a novel method of fixing carrier-phase ambiguities in the undifferenced measurements, avoiding the classic use of double-differenced carrier-phase measurements, where only differential MSTIDs effects can be seen. In this way, we conduct this study independent of the ambiguity fixing success rate. Second, thanks to the previous carrier-phase ambiguity fixing, a reference navigation solution based on the ionosphere-free navigation combination (L_{IF}) is computed, making it possible to account for only the effects related to the ionosphere. Third, this reference navigation solution is compared with the navigation solution computed using either RTK or NRTK. In this way, we assess the impacts of the ionosphere effects on the 3D positioning.

The relationship between the positioning error and the MSTIDs is also shown, where the presence of an MSTID is a degrading factor for user positioning not only in RTK but also in NRTK. This degradation is related not only to the effect of the TID on the user measurements but also to the measurements of any of the reference receivers.

An MSTID index is defined and implemented as a tool to warn users about possible positioning degradation. The performance is tested with three stations located at 15, 50, and 79 km from the reference receiver. Using this index over a data set covering one year, we show that it is possible to obtain similar accuracies in the three baselines.

As a product related to this work, real-time estimates of $MSTID_{IDX}$, applied on more than one hundred of worldwide GNSS receivers, are computed and stored in the Warning and Mitigation Technologies for Travelling Ionospheric Disturbances Effects (TechTIDE) open repository, located at the following internet address: http://techtide.space.noa.gr/.

Acknowledgements. This work is sponsored by the European Union's Horizon 2020 research and innovation programme under grant agreement 776011 (TechTIDE project) and 797461 (NAVSCIN), and the Spanish Ministry of Science, Innovation and Universities RETOS RTI2018-094295-B-I00 (Programa Estatal de I + D + i Orientada a los Retos de la Sociedad). The authors acknowledge the use of data from the CATNET NRTK service from the Cartographic and Geologic Institute of Catalonia, Spain (*Institut Cartogràfic i Geològic de Catalunya* – ICGC), and data from the International GNSS Service (IGS). The editor thanks Yuichi Otsuka and an anonymous reviewer for their assistance in evaluating this paper.

References

Alves P, Lachapelle G, Cannon ME, Liu J, Townsend B. 2001. Evaluation of multiple-reference DGPS RTK using a large scale network. In: *Proceedings of the National Technical Meeting of the Institute of Navigation, ION NTM/2001 (January 2001, Long Beach, USA)*, pp. 665–671.

Cannon ME, Lachapelle G, Alves P, Fortes LP, Townsend B. 2001. GPS RTK Positioning using a regional reference network: Theory and results. In: *Proceedings of the Global Navigation Satellite Systems Conference (May 2001, Seville, Spain)*, Global Navigation Satellite Systems.

Collins P, Lahaye F, Héroux P, Bisnath S. 2008. Precise point positioning with ambiguity resolution using the decoupled clock model. In: *Proceedings of the 21st International Technical Meeting of the Satellite Division of The Institute of Navigation, ION GNSS 2008 (September 2008, Savannah, USA)*. pp. 1315–1322.

Ge M, Gendt G, Rothacher M, Shi C, Liu J. 2008. Resolution of GPS carrier-phase ambiguities in precise point positioning (PPP) with daily observations. *J Geodesy* **82(7)**: 389–399. https://doi.org/10.1007/s00190-007-0187-4.

Hernández-Pajares M, Juan JM, Sanz J, Colombo OL. 2000. Application of ionospheric tomography to real-time GPS carrier-phase ambiguities Resolution, at scales of 400–1000 km and with high geomagnetic activity. *Geophys Res Lett* **27(13)**: 2009–2012. https://doi.org/10.1029/1999GL011239.

Hernández-Pajares M, Juan JM, Sanz J. 2006. Medium-scale traveling ionospheric disturbances affecting GPS measurements: Spatial and temporal analysis. *J Geophys Res Space Phys* **111(A07S11)**. https://doi.org/10.1029/2005JA011474.

Jacobson AR, Carlos RC, Massey RS, Wu G. 1995. Observations of traveling ionospheric disturbances with a satellite-beacon radio interferometer: Seasonal and local time behavior. *J Geophys Res Space Phys* **100(A2)**: 1653–1665. https://doi.org/10.1029/94JA02663.

Juan JM, Sanz J, Rovira-Garcia A, González-Casado G, Ventura-Traveset J, Cacciapuoti L, Schoenemann E. 2020. A new approach to improve satellite clock estimates, removing the inter-day jumps. In: *Proceedings of the 51st Annual Precise Time and Time Interval Systems and Applications Meeting of the US Institute of Navigation*, pp. 279–301.

Lachapelle G, Alves P. 2002. Multiple reference station approach: Overview and current research. *J Glob Position Syst* **1(2)**: 133–136.

Rovira-Garcia A, Juan JM, Sanz J, González-Casado G, Ibáñez D. 2016. Accuracy of ionospheric models used in GNSS and SBAS: Methodology and analysis. *J Geodesy* **90(3)**: 229–240.

Rovira-Garcia A, Ibáñez-Segura D, Orús-Perez R, Juan JM, Sanz J, González-Casado G. 2019. Assessing the quality of ionospheric models through GNSS positioning error: Methodology and results. *GPS Solut* **24(1)**: 4. https://doi.org/10.1007/s10291-019-0918-z.

Sanz J, Juan Zornoza JM, Hernández-Pajares M. 2013. GNSS Data Processing. In: *Volume I: Fundamentals and algorithms*, ESA Communications, ESTEC, Noordwijk, The Netherlands, pp. 145–161.

Seeber G. 2008. *Satellite geodesy: Foundations, methods, and applications*, Walter de Gruyter, Berlin, Germany. https://doi.org/10.1515/9783110200089.

Talaya J, Bosch E. 1999. CATNET, a permanent GPS network with real-time capabilities. In: *Proc. ION GPS-99, 12th Int. Tech. Meeting of The Satellite Division of The US Institute of Navigation*, pp. 14–17.

Teunissen PJG. 1995. The least-squares ambiguity decorrelation adjustment: A method for fast GPS integer ambiguity estimation. *J Geodesy* **70**: 65–82.

Wielgosz P, Kashani I, Grejner-Brzezinska D. 2005. Analysis of long-range network RTK during a severe ionospheric storm. *J Geodesy* **79(9)**: 524–531. https://doi.org/10.1007/s00190-005-0003-y.

Cite this article as: Timoté CC, Juan JM, Sanz J, González-Casado G, Rovira-García A, et al. 2020. Impact of medium-scale traveling ionospheric disturbances on network real-time kinematic services: CATNET study case. *J. Space Weather Space Clim.* **10**, 29.

Journal of Geodesy (2021) 95:130
https://doi.org/10.1007/s00190-021-01581-x

ORIGINAL ARTICLE

Ionospheric corrections tailored to the Galileo High Accuracy Service

A. Rovira-Garcia[1] · C. C. Timoté[1] · J. M. Juan[1] · J. Sanz[1] · G. González-Casado[1] · I. Fernández-Hernández[2] · R. Orus-Perez[3] · D. Blonski[3]

Received: 19 May 2021 / Accepted: 14 October 2021 / Published online: 21 November 2021

Abstract
The Galileo High Accuracy Service (HAS) is a new capability of the European Global Navigation Satellite System that is currently under development. The Galileo HAS will start providing satellite orbit and clock corrections (i.e. non-dispersive effects) and soon it will also correct dispersive effects such as inter-frequency biases and, in its full capability, ionospheric delay. We analyse here an ionospheric correction system based on the fast precise point positioning (Fast-PPP) and its potential application to the Galileo HAS. The aim of this contribution is to present some recent upgrades to the Fast-PPP model, with the emphasis on the model geometry and the data used. The results show the benefits of integer ambiguity resolution to obtain unambiguous carrier phase measurements as input to compute the Fast-PPP model. Seven permanent stations are used to assess the errors of the Fast-PPP ionospheric corrections, with baseline distances ranging from 100 to 1000 km from the reference receivers used to compute the Fast-PPP corrections. The 99% of the GPS and Galileo errors in well-sounded areas and in mid-latitude stations are below one total electron content unit. In addition, large errors are bounded by the error prediction of the Fast-PPP model, in the form of the variance of the estimation of the ionospheric corrections. Therefore, we conclude that Fast-PPP is able to provide ionospheric corrections with the required ionospheric accuracy, and realistic confidence bounds, for the Galileo HAS.

Keywords Ionospheric modellings · High accuracy navigation · International GNSS service

1 Introduction

The Galileo High Accuracy Service (HAS) is a new capability of the European Global Navigation Satellite System (GNSS). The Galileo HAS will transmit differential corrections to the navigation message already being broadcast by Galileo and GPS satellites, to enable precise point positioning (PPP) on a global scale (Malys and Jensen 1990; Zumberge et al. 1997). The Galileo HAS will be free of charge, following the European Commission Implementing Decision 2018/321 (EC 2018). The Galileo program has defined and is currently testing the message standards on the E6 frequency band (Fernández-Hernández et al. 2020; Borio et al. 2020).

A. Rovira-Garcia
adria.rovira@upc.edu

[1] Universitat Politècnica de Catalunya (UPC), Jordi Girona, 1-3, 08034 Barcelona, Spain

[2] European Commission (EC), BREY, 1049 Brussels, Belgium

[3] European Space Agency (ESA), Keplerlaan, 1, 2201AZ Noordwijk ZH, The Netherlands

The approach selected for disseminating the HAS corrections is the state space representation (SSR), which separates dispersive and non-dispersive errors affecting the ranging signals. The Radio Technical Commission for Maritime Services (RTCM) has standardized the SSR correction format in its standard 10403.3 (RTCM 2016). The early testing phase ("phase 0") of the Galileo HAS only includes satellite orbit and clock corrections (i.e. non-dispersive effects), but its initial service ("phase 1") will include also inter-frequency biases (IFBs) and its full capability ("phase 2") will also include ionospheric delay corrections, at least in Europe. When in its full capability, the user performance requirements are 20 cm 95% horizontal accuracy, 40 cm 95% vertical accuracy, and a convergence time of 100 s (GSA 2020). This short convergence time will be achieved thanks to an accurate ionospheric model computed in real time, in such a way that any user could derive its ionospheric corrections within the service area (Rovira-Garcia et al. 2015).

Regarding the ionospheric corrections, two alternatives exist for broadcasting the total electron content (TEC) for GNSS applications. On the one hand, the Slant TEC

(STEC) corrections mechanism selected, for instance, by the Centimetre Level Augmentation Service (CLAS) that is broadcast by the Quasi Zenith Satellite System (QZSS) (MEC 2015). This STEC approach is closer to Network Real Time Kinematic (NRTK) Remondi (1985) than to PPP, and it is suitable to service a region such as the Japanese archipelago. Indeed, in a regional/local context it is affordable to transmit the STECs associated with the measurements of a dense network of receivers without requiring a huge bandwidth for the message. However, this approach is not possible in a continental/global context, which would require an unaffordable bandwidth for the message, especially in a multi-constellation scenario.

On the other hand, ionospheric corrections can be broadcast using vertical TEC (VTEC) values at a set of ionospheric grid points (IGPs). This VTEC approach is currently used by the Satellite-Based Augmentation System (SBAS) (RTCA 2016), as it is more suitable for covering a wide area such as an entire continent with only few tens of stations, regardless the number of operating satellites. The Galileo HAS foresees to use a VTEC correction system, and the fast precise point positioning (Fast-PPP) model described in (Rovira-Garcia et al. 2015; Rovira-Garcia et al. 2016a) can provide such corrections.

Provided that satellite orbits and clocks can be computed in real time with accuracies at the level of few centimetres in the so-called geodetic filter (Zhang et al. 2018), one should demand similar accuracies to the ionospheric corrections. In this sense, a value of one total electron content unit (TECU), where 1 TECU corresponds to 16.24 cm in the L1/E1 GNSS frequency band (1575.42 MHz), could be taken as a reference for the required accuracy for the ionospheric corrections in order to provide a HAS (Rovira-Garcia et al. 2015,2016b). Different users can benefit of having ionosphere corrections with an accuracy not much worse than the errors in the satellite orbits and clocks. Firstly, multi-frequency receivers shorten the time required to obtain a decimetre level of accuracy (i.e. the convergence time), as it is required in the phase 2 of Galileo HAS. This is because ionospheric corrections help the navigation filter to separate (i.e. decorrelate) the carrier phase ambiguities from the other parameters estimated: coordinates, time offsets and troposphere. Secondly, as it was shown in Rovira-Garcia et al. (2020), single-frequency receivers improve the navigation accuracy to the sub-metre level, because the ionospheric contribution to the navigation error, the largest error contribution besides receiver multipath and noise, is largely mitigated.

As it was shown in Rovira-Garcia et al. (2020), the accuracy of ionospheric models is not homogenous. In regions well-sounded by multiple reference stations, the ionospheric corrections present rather low variances, whereas the accuracy of ionospheric models degrades in poorly sounded regions as those far from the continents in open sea. In such cases, the ionospheric model should not degrade the accuracy or convergence time of the classical solution based on the ionospheric-free (IF) combination, which is usually taken as a reference. For that reason, the VTEC corrections of Fast-PPP are estimated together with its expected error, similarly to the grid ionospheric vertical error indicator (GIVEI) used in SBAS (RTCA 2016). That is, at each IGP, the value of the VTEC is distributed together with an indicator of the quality of the ionospheric correction, extracted from the co-variance matrix of the estimation of the Fast-PPP model. Far away from the reference stations, the GIVEIs of the ionospheric model should be high enough that the ionospheric correction does not help nor bias the navigation solution.

The aim of this contribution is to present some recent upgrades to the Fast-PPP ionospheric model tailored to the Galileo HAS (phase 2), which include the multi-constellation capability and to confirm the performance obtained in the past with GPS data [see Rovira-Garcia et al. (2016a) and Rovira-Garcia et al. (2020)]. In those works, the advantages of the Fast-PPP ionospheric model with respect to other models were shown focusing on the signal-in-space domain and in the position domain, respectively.

The manuscript is organized as follows: the next section details the data sets used for the present study. Then, we describe the geometry of the model that computes the VTECs, in particular the two-layer ionospheric grid, addressing some of the requirements to broadcast such ionospheric corrections. The methodology section presents the strategy used to compute the model, including the combinations of measurements and different strategies to solve the carrier-phase ambiguities. The results section show some examples obtained at seven permanent stations with different baseline distances from the reference receivers involved in the Fast-PPP corrections computation. While results use a global monitoring network and grid, three stations located in Europe may be representative of the future Galileo HAS ionospheric correction performance. The manuscript finalizes presenting a summary of the main findings and conclusions.

2 Data set

The Fast-PPP corrections are computed by a central processing facility (CPF), which retrieves data from permanent stations belonging to the networks of the International GNSS Service (IGS) (Beutler et al. 1999) and the Rede Brasileira de Monitoramento Continuo (RBMC), specifically code and carrier phase measurements at multiple frequencies and from multiple constellations. In addition to the so-called observables, Fast-PPP also requires accurate coordinates of the permanent receivers in the network and satellite orbits with enough accuracy.

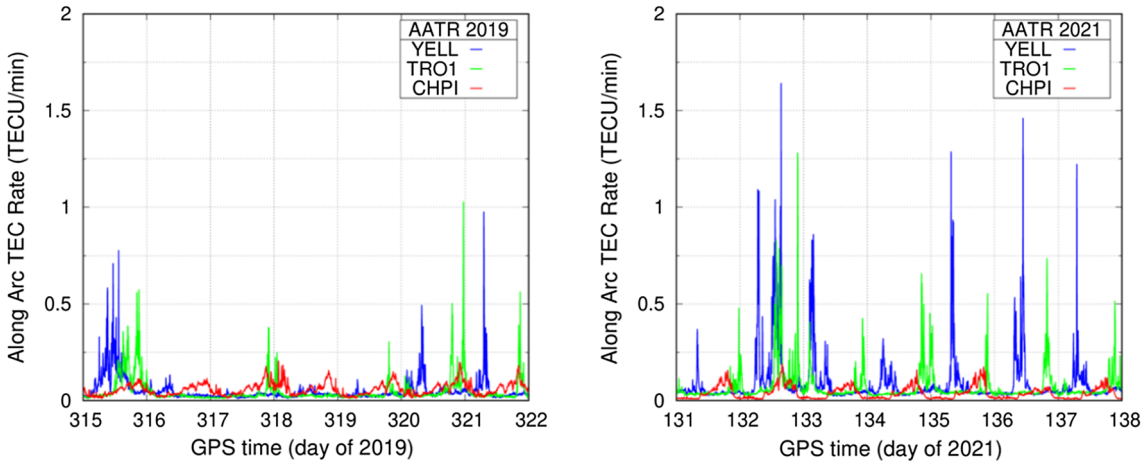

Fig. 1 Ionospheric activity every 300 s for three permanent stations, sampled by the Along Arc TEC Rate index for one week in 2019 (left plot) and for one week in 2021 (right plot)

We have run the Fast-PPP CPF for one week starting on day 315 in 2019 and for a week starting on day 131 in 2021. In order to evaluate the ionospheric activity, Fig. 1 depicts the values of the Along Arc TEC Rate (AATR) index (see Juan et al. 2018) every 300 s for two receivers at high latitudes, YELL (Canada) and TRO1 (Norway), and one receiver at a low latitude, CHPI (Brazil). According to Juan et al. (2018), AATRs larger than one TECU/min result from high ionospheric activity. Hence, there are only some hours of moderate activity during the week in 2019, whereas during the week in 2021, there are several periods with high ionospheric activity.

Figure 2 depicts around 180 permanent stations from the IGS that were collecting GPS, Galileo and GLONASS data to compute the Fast-PPP model. With this number of permanent receivers, it is possible to build a global ionospheric map (GIM) and, in some areas like Europe or Brazil, one has an enough density of permanent receivers which allows to provide accurate ionospheric corrections. In addition to these permanent stations, we have used also the data from other seven permanent receivers implemented as rover receivers (blue boxes). The data from these receivers are used just in the geodetic filter in order to fix their carrier phase ambiguities and, consequently, to have confident values that can be compared with the model predictions using the test defined in Rovira-Garcia et al. (2016a). Notice that three of these receivers are located in mid-latitude regions, including two in Europe and one in the USA, while the other three are located in Brazil, i.e. in a region where it is expected large ionospheric gradients and rates.

Table 1 depicts the rover coordinates and the distances to the nearest station used to compute the Fast-PPP ionospheric corrections. As it can be seen, these distances from the nearest reference receiver are around 100, 200 or 300 km, at mid, high and low latitudes, which are distances where it is expected

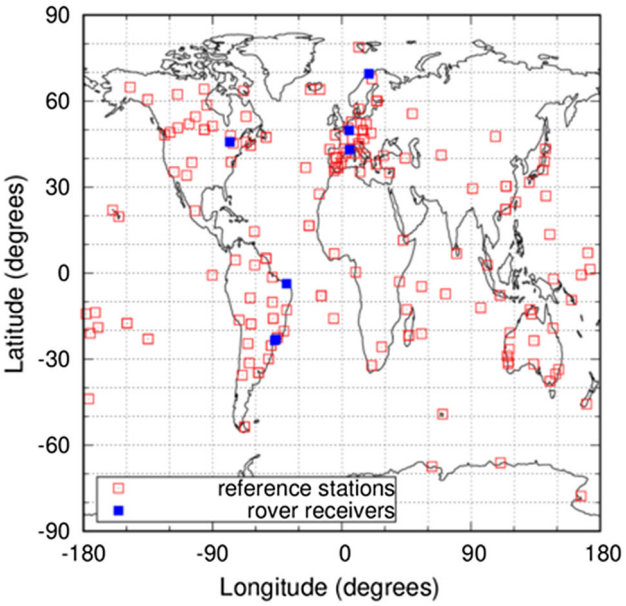

Fig. 2 Distribution of permanent stations from the IGS network. The red empty squares depict receivers used to compute the Fast-PPP ionospheric model, whereas the filled blue squares depict rover receivers that have not participated in the model calculus

that the ionospheric model would have the enough quality for providing HAS, i.e. an error of about one TECU (see, for instance, Rovira-Garcia et al. (2016b). In particular, one of the Brazilian receivers (named CEFT) is located more than 1,000 km to the East from the nearest permanent station. Therefore, this rover receiver can be considered as an extreme case where the ionospheric corrections would not help to improve the navigation solution.

In order to contextualize the performance of the Fast-PPP ionospheric model, we have applied the same test to the rapid combined GIM of the IGS, termed IGRG. The IGRG GIM is

Table 1 RMS of the post-fit residuals to Eq. (11) for seven rovers located at different distances from the nearest reference station used to compute the Fast-PPP ionospheric model. The residuals of GPS and Galileo are distinguished for Fast-PPP and IGRG ionospheric models and year

Station ID	Coordinates		Distance (km)	Residual errors (TECUs)							
	Lon (°)	Lat (°)		Day 315–322 in 2019				Day 131–138 in 2021			
				GPS		GAL		GPS		GAL	
				Fast-PPP	IGRG	Fast-PPP	IGRG	Fast-PPP	IGRG	Fast-PPP	IGRG
ALGO	− 78	45	198	0.3	0.8	0.3	1.0	0.3	1.2	0.3	1.4
CEFT	− 38	− 3	1019	2.0	2.2	1.9	2.3	2.3	4.0	2.0	3.8
MARS	5	43	315	0.2	0.8	0.2	0.7	0.3	1.1	0.3	0.8
POLI	− 46	− 23	201	0.7	1.7	0.6	1.9	0.5	2.2	0.5	2.0
REDU	5	49	104	0.3	0.7	0.3	0.7	0.2	0.8	0.2	0.8
SJSP	− 45	− 23	105	0.5	1.4	0.5	1.5	0.4	1.8	0.4	1.7
TRO1	18	69	217	0.7	0.8	0.6	0.9	0.6	0.9	0.5	0.9

a single-layer model that assumes the ionospheric delay to be concentrated in a thin shell at 450 km of altitude. Note that the IGRG GIM is obtained in post-process mode using forward and backward process, whereas Fast-PPP is computed in real time using only the forward mode. Finally, the IGRG GIM contains TEC maps every 2 h, whereas Fast-PPP every 5 min. In spite of the large refresh time, IGRG yields similar results to other IGS GIMs with shorter time updates and therefore is representative of the IGS GIMs.

3 Requirements for a HAS ionospheric model

Besides the accuracy of the ionospheric model, one of the key points of model tailored for HAS is the bandwidth of the message to be broadcast to the users, that is, the number of parameters to be computed and transmitted in real time and the required refresh time, in such a way that the optimum ionospheric model should be a trade-off between accuracy and message bandwidth.

Galileo satellites will transmit an ionospheric correction message over Europe when Galileo HAS reaches its full capability (i.e. the aforementioned "phase 2"). In order to transmit the ionospheric correction message swiftly, and also due to the possibly limited monitoring capability, the IGP grid can be reduced to the European continent. According to the current HAS SIS message structure and coding scheme (Fernández-Hernández et al. 2020), such ionospheric message could fit into 26 pages to cover the main European land. Therefore, a user could receive the ionospheric values in well under 100 s, most probably around 30 to 60 s depending on the final message specifications (e.g. elevation mask, service area and quantization).

The following subsections provide preparatory discussions of key aspects of the HAS ionospheric message, exploring possible solutions. In particular, we deal with some considerations on the geometric used to compute the Fast-PPP ionospheric model and how a user must take those into account in order to compute the ionospheric corrections for any receiver-satellite ray.

3.1 Geometry of the ionospheric model

Regarding the accuracy requirement, Fast-PPP uses a dual-layer model (see, for instance, Orús et al. 2021) to correct the ionospheric delay. The first layer contains 7176 IGPs at a height of 270 km and accounts for the main ionospheric content, whereas the second layer contains 1792 IGPs, i.e. about one-fourth of the IGPs in the first layer, at a height of 1600 km and accounts for the plasmaspheric content. In this manner, Fast-PPP overcomes the main simplification of the thin-shell models at a unique height, allowing some degree of vertical 3D representation of the TEC distribution. Notice

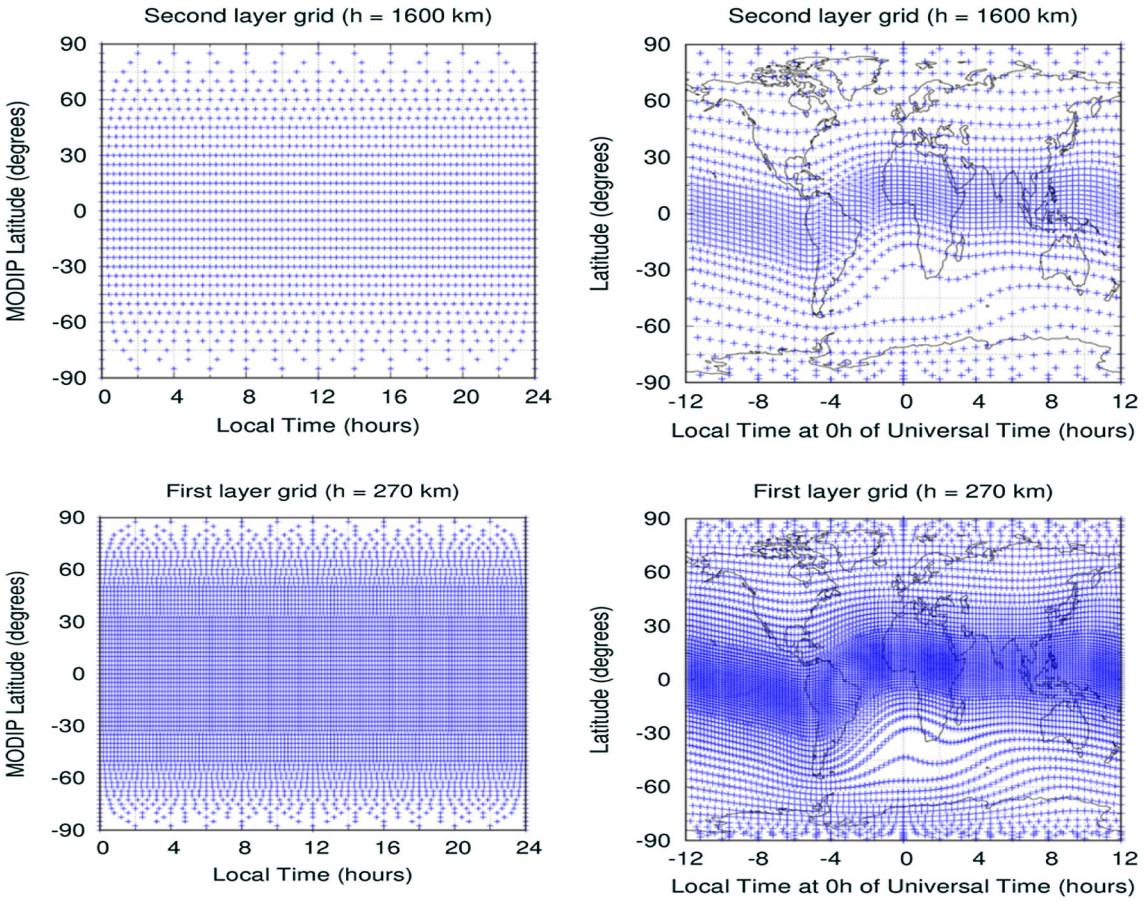

Fig. 3 Distribution of IGPs used in the Fast-PPP model for the top layer (top plot) and bottom layer (bottom plot). The right column represents the IGPs as a function of geographic latitude and local time at 0 h of Universal Time, whereas the left column represents the IGPs as a function of MODIP and local time

that, for any ground observation, these very different heights for the ionospheric layers will have a clear different obliquity factor on each layer. This will allow to distinguish an ionospheric delay occurring at the top layer from one occurring at the bottom layer. This capability represents a reduction of the mismodelling with respect to a single-layer assumption, which is a key factor to meet the accuracy requirement of one TECU for HAS (Rovira-Garcia et al. 2015,2016b).

Because the main drivers of the ionospheric state are the geomagnetic field and the Sun, the Fast-PPP ionospheric model defines the IGPs based on local time (LT). This allows enlarging the refresh time of the model. Moreover, in order to reduce the number of parameters to be transmitted, the IGPs are defined on a grid on LT and the MOdified DIP (MODIP) latitude (Rawer 1963). The VTEC grid is equally spaced over each MODIP band, which implies an irregular distribution of the IGPs in terms of longitude and latitude. Specifically, the IGPs of the bottom layer are equally spaced every 2.5 degrees in MODIP, whereas the IGPs of the top layer are equally spaced every 5 degrees of MODIP.

Regarding the LT spacing between IGPs, it decreases approximately with the cosine of MODIP:

$$\Delta \mathrm{LT}_{\mathrm{layer}} = \Delta \mathrm{MODIP}_{\mathrm{layer}} / \cos(\mathrm{MODIP}) \quad (1)$$

Figure 3 illustrates the Fast-PPP grid at each layer. The plots in the left column use the LT-MODIP coordinates, whereas the plots in the right column depict the irregular distribution of its geographic coordinates (longitude and latitude at 0 h of Universal Time). As it can be seen, this choice provides a high density of IGPs at low latitudes (i.e. low MODIP). Provided that enough coverage of permanent stations is available at such regions, this IGP distribution improves the accuracy of the Fast-PPP ionospheric model in regions around the geomagnetic equator, where great temporal and spatial gradients are experienced at the ionosphere. The irregular grid presents an additional benefit, which is the reduction in the number of IGPs to be estimated in comparison with a regular grid. As a numerical example considering the first layer with a regular resolution of $2.5° \times 2.5°$ in latitude and longitude, would require 10,500 IGPs instead of

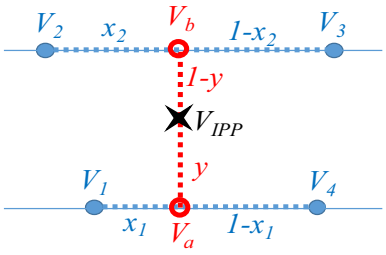

Fig. 4 Bi-linear interpolation of the VTEC at four IGPs surrounding the IPP

the 7179 IGPs of the irregular grid using Eq. (1). This corresponds to a reduction of 30% not only in the computational load in the CPF, but also in the message bandwidth.

3.2 Usage of ionospheric corrections

The proposed grid based on an irregular distribution of the IGPs requires a different interpolation scheme to the one used in SBAS (RTCA 2016) or in the IONosphere map EXchange format (IONEX) standard (Schaer et al. 1998), when Fast-PPP users need to compute the ionospheric corrections. The procedure is illustrated in Fig. 4, where the ray between the user receiver and the satellite intersects each ionospheric layer at the so-called ionospheric pierce point (IPP). Then, assuming that the IPP is surrounded by four IGPs located in the same layer at a given time, the user interpolates the VTEC at the four IGPs using the linear distances x and y:

$$V_{\mathrm{IPP}} = (1-y)V_a + yV_b \tag{2}$$

where V_a and V_b are computed as

$$\begin{aligned} V_a &= (1-x_1)V_1 + x_1V_4 \\ V_b &= (1-x_2)V_2 + x_2V_3 \end{aligned} \tag{3}$$

By simple algebraic manipulation, it follows that the algorithm is equivalent to the linear relationship:

$$\begin{aligned} V_{\mathrm{IPP}} = {} & (1-y)\cdot(1-x_1)\cdot V_1 + y\cdot(1-x_2) \\ & \cdot V_2 + (1-y)\cdot x_1 \cdot V_4 + y\cdot x_2 \cdot V_3 \end{aligned} \tag{4}$$

From Eqs. (2)–(4), it follows that in the case of a regular grid (i.e. $x_1 = x_2$) the algorithm corresponds to the interpolation method adopted in SBAS.

4 Methodology

During the last years, a trend has been consolidated in the GNSS parameter estimation consisting on the processing of the raw measurements in an undifferenced and uncombined manner (see, for instance, Odijk et al. 2016). This general approach includes also integer ambiguity resolution (IAR) and even the estimation of the parameters of an ionospheric model. Thanks to these estimation strategies, the different parameters can be determined with a high accuracy. However, in a worldwide context, this way of processing involves tens of thousands of parameters that should be estimated in real time in order to provide a HAS. For instance, for a global network with 200 receivers each one tracking the measurements of, let us assume, 30 satellites at three frequencies, this would require to estimate around $2\cdot10^4$ carrier phase ambiguities together with close to 10^4 parameters of the ionospheric model.

One of the main advantages of the data used to compute the Fast-PPP ionospheric model is that it does not have to directly deal with (i.e. estimate) the ambiguities of the carrier phase measurements at the same time as the ionospheric delays. In order to do so, a previous independent module called geodetic filter performs IAR, handling non-dispersive combinations of GNSS signals. Indeed, firstly, the ionosphere-free (IF) combination of carrier phases is used to determine the ambiguity in such combination, B_{IF}, using PPP models, the precise knowledge of station coordinates, and satellite orbits and clocks. The B_{IF} is estimated as a real number in what is known as a floated ambiguity. Notice that thanks to the knowledge of the receiver coordinates, the confidence (formal error) of the B_{IF} ambiguity, i.e. the square root of the diagonal elements in the covariance matrix of the estimates, is at the level of 1 cm since the beginning of the arc of data.

In parallel, the carrier phase ambiguity of the wide lane (WL) combination, B_{WL}, is calculated through the Hatch–Melbourne–Wübenna (HMW) combination (Hatch 1982), that is, the difference of the wide lane (WL) combination of carrier phases and the narrow lane (NL) combination of code pseudoranges. For a satellite j and a receiver i, B_{WL} (expressed in metres) can be written as:

$$B^j_{\mathrm{WL}i} = \lambda_{WL}\cdot\left(N^j_{\mathrm{WL}i} + \delta_{\mathrm{WL}i} + \delta^j_{\mathrm{WL}}\right) \tag{5}$$

Being λ_{WL} the wavelength of the WL combination $\lambda_{\mathrm{WL}} = \frac{c}{f_m - f_n}$, f_m and f_n are two different frequencies selected by the Fast-PPP operator, c is the speed of light, N_{WL} the integer part of the carrier phase ambiguity (expressed in cycles) and δ_{WL} the instrumental delay of the satellite or the receiver at the WL combination.

After few minutes of taking data, the double difference (DD) of N_{WL} between pairs of satellites and receivers can be fixed to an integer number. This can be done thanks to the wavelength of the WL combination (e.g. 86 cm using GPS frequencies L1 and L2 and 75 cm using Galileo frequencies E1 and E5a), which is large enough to allow DD IAR, despite the noise of the B_{WL} introduced by the NL combination of

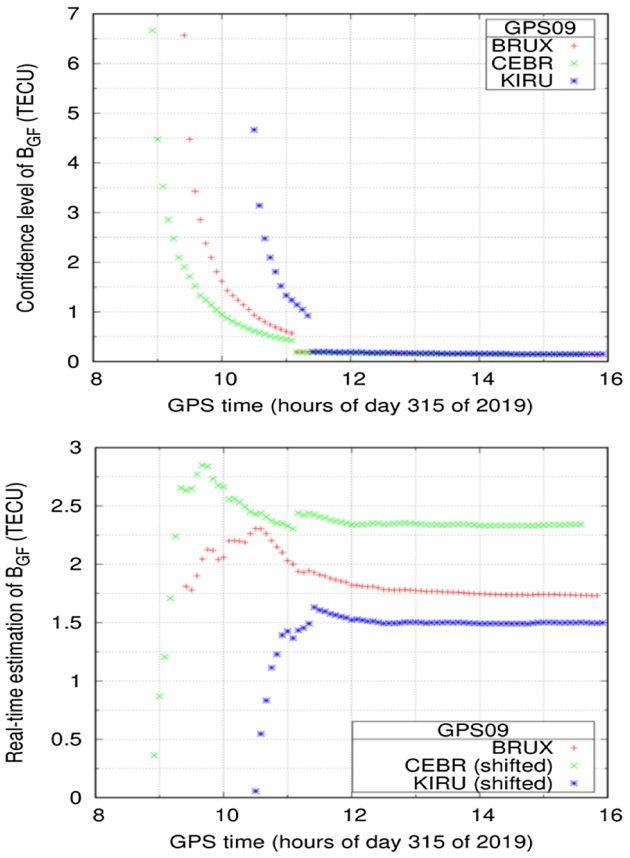

Fig. 5 B_{GF} estimates (bottom) and its estimated confidence level (top) for GPS satellite 9, performed by receivers BRUX (in Belgium), CEBR (in Spain) and KIRU (in Sweden)

pseudoranges. Once DD IAR is performed for B_{WL}, a link appears between the four WL ambiguities involved in the DDs, which reduces dramatically the formal error of each individual estimate of B_{WL}.

The final step of the geodetic filter consists in obtaining the ambiguity in the geometry-free (GF) combination, B_{GF}, for a receiver i and a satellite j, following (Sanz et al. 2013):

$$B^j_{\mathrm{GF}i} = \frac{f_m^2 - f_n^2}{f_m \cdot f_n} \cdot \left[B^j_{\mathrm{WL}i} - B^j_{\mathrm{IF}i} \right] \tag{6}$$

Figure 5 illustrates the IAR process for three stations and one GPS satellite. The top plot depicts the values of the confidence level of the estimates, whereas the bottom plot illustrates the estimated B_{GF} values. Once the confidence level is reduced, carrier phase ambiguities are fixed, which for this example occurs around 11 h. As a consequence of the IAR, the different B_{GF} values for different receivers or satellites remain linked in the estimation process. That is, they evolve in time in the same manner. This occurs because a constraint between them has been added to the Kalman filter, which increases the robustness of the overall ambiguity estimation.

The IAR performed before the Fast-PPP ionospheric model estimation represents a clear advantage with respect to other state-of-the-art approaches that solve the B_{GF} arc by arc in an independent (i.e. disconnected) manner. This is the case of the carrier phase to code levelling (CCL) process (Mannucci et al. 1998), which estimates B_{GF} averaging the difference between the GF combination of code pseudoranges P_{GF} and carrier phase measurements L_{GF} for each continuous arc of the samples:

$$B^j_{\mathrm{GF}i} = \left\langle L^j_{\mathrm{GF}i} - P^j_{\mathrm{GF}i} \right\rangle \tag{7}$$

Figure 6 illustrates the advantage of estimating B_{GF} with the geodetic filter over the CCL. For that purpose, we depict, for all arcs of data within day 315 of 2019, the difference of the two instantaneous estimations of B_{GF} with respect to their final estimate, $B_{GF}(t_{final})$, which is assumed the best estimate of the ambiguity because it involves all the data in the arc. Therefore, the figure compares the drift of the estimates ignoring possible final biases. As expected, during the first epochs in the instantaneous estimations, the errors of both methods are large. However, in almost all the arcs of the geodetic filter approach, the differences between the instantaneous and final estimates is below one TECU since the beginning. In contrast, the B_{GF} estimates with the CCL approach depict variations of several TECU, i.e. larger than the required accuracy for a HAS. Because the input data of the ionospheric model are the unambiguous STEC (STEC $=$ $L_{GF} - B_{GF}$), the more accurate the B_{GF} are, the more accurate the ionospheric estimates will be.

Besides the improvement of the unambiguous STEC precision, performing IAR at the CPF facilitates the IAR process at the user side. Indeed, once IAR is done inside the geodetic filter, it is easy to compute receiver and satellite phase biases (Rovira-Garcia et al. 2021). These satellite biases can be broadcast every few minutes by a HAS in order to enable IAR on the user side.

Figure 7 depicts, for two GPS and two Galileo satellites, the real-time estimates of the phase biases of the WL combination (left) and the L1 (right). As it can be seen, the noise in the phase bias estimates is usually well below a tenth of one cycle, which guarantees the IAR. Only the phase bias of L1 can present some problems in the epochs when the satellite is poorly tracked (e.g. orbiting over the oceans). In any case, the noise remains well-below half a cycle.

5 Testing the ionospheric model

The assessment of the accuracy of any ionospheric model is a key, and difficult, point that has been addressed using several methods. The difficulty of such assessments relies on the procedure to obtain confident ionospheric values with

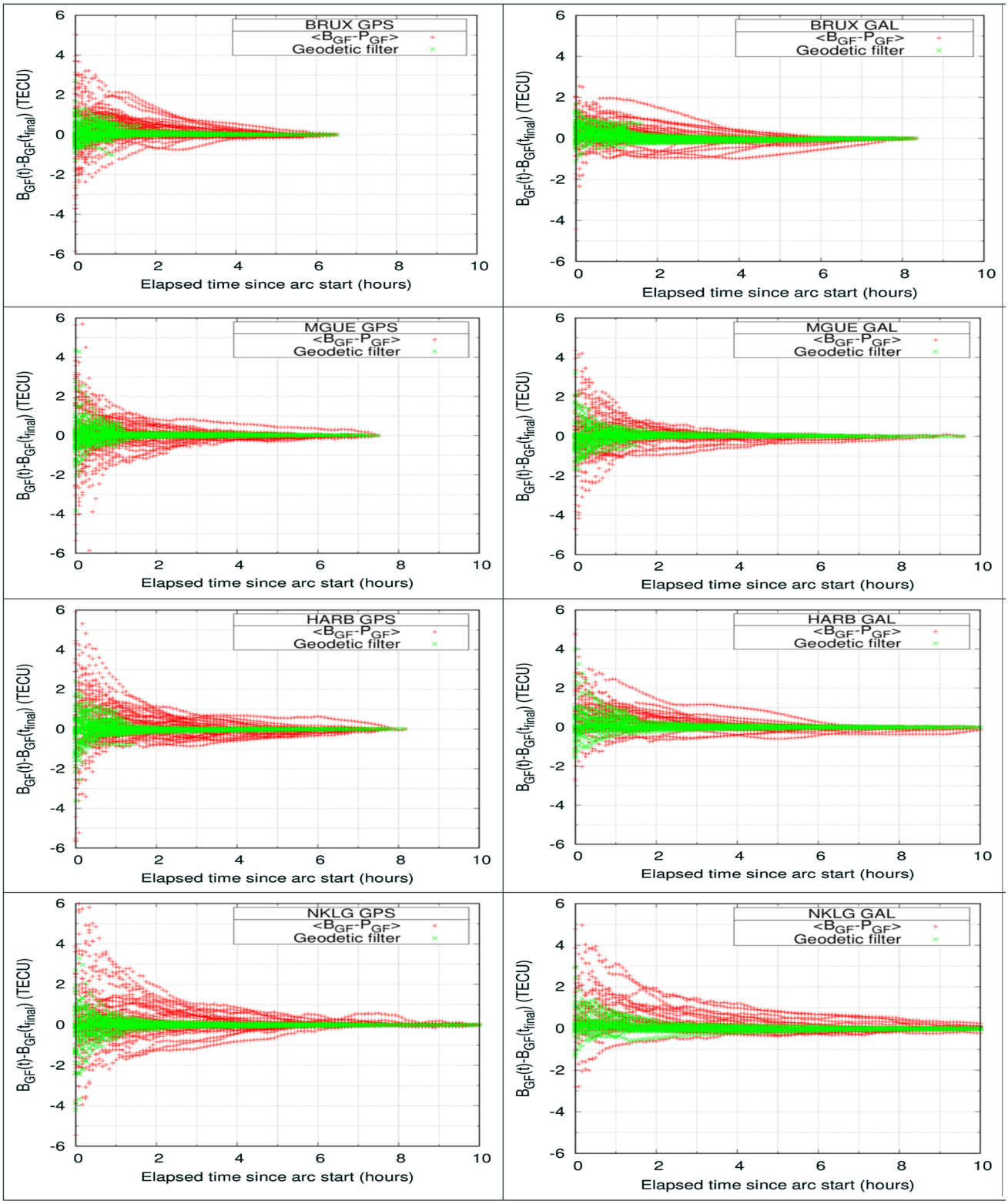

Fig. 6 Difference of instantaneous estimates of B_{GF} with respect to the final estimated value using geodetic filter (green) or CCL (red) approaches for different permanent stations, separating GPS (left column) from Galileo (right column) satellites

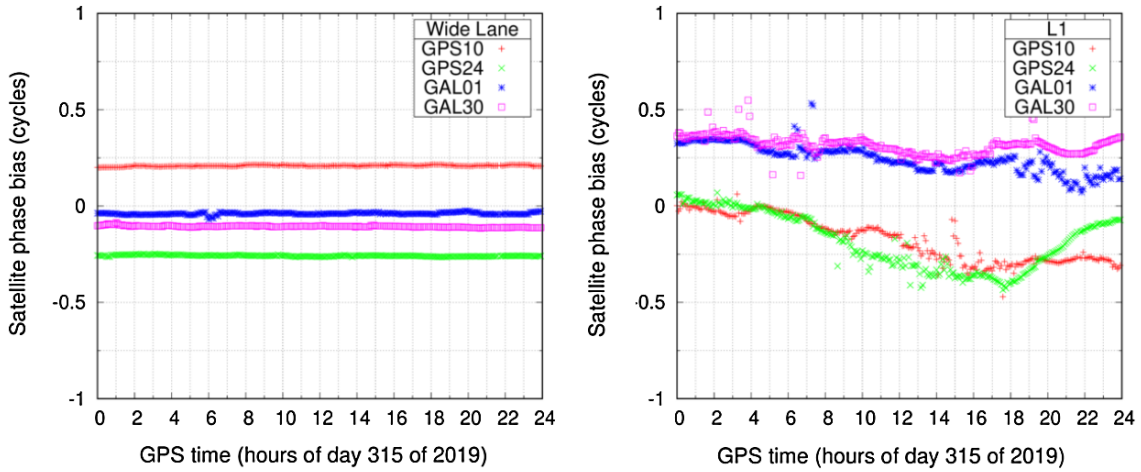

Fig. 7 Phase biases in the WL combination (left) and L1 (right) for different GPS and Galileo satellites

enough accuracy to be used as a reference. Indeed, direct ionospheric measurements, using different techniques, are affected by unknown biases that shall be removed before using such measurements as the reference. For instance, Orús et al. (2021) used simulated data in order to discard the problem with the biases, focusing the assessment on the different geometry of the ionospheric model. However, unlike simulated data, actual ionosphere has irregularities at different spatial and temporal scales that can affect the estimation of the ionospheric parameters such as hardware biases.

In order to assess ionospheric models with actual data, Orús et al. (2005) introduced the self-consistency test (SCT), which nowadays is widely used. SCT is based on the variation of L_{GF} with respect to a L_{GF} measurement done at a reference time (t_{ref}), that is, $L_{\mathrm{GF}}(t) - L_{\mathrm{GF}}(t_{\mathrm{ref}})$. Note that such differentiation cancels the carrier phase ambiguity B_{GF} present in the carrier phase measurements, because all the measurements belong to the same continuous arc of data that share the same ambiguity value. Then, the SCT consists on comparing the variation of L_{GF}, in metres, with the variation of the ionospheric model predictions for these measurements, $I(t) - I(t_{\mathrm{ref}})$, in TECU, defining the variation of the STEC prediction error as:

$$\begin{aligned}\Delta\mathrm{STEC}_i^j &= \frac{1}{\alpha_n - \alpha_m} \\ &\cdot \left[\left(L_{\mathrm{GF}i}^j(t) - L_{\mathrm{GF}i}^j(t_{\mathrm{ref}})\right) - \left(I_i^j(t) - I_i^j(t_{\mathrm{ref}})\right)\right]\end{aligned} \tag{8}$$

where i corresponds to a receiver and j to a satellite, the factor $\alpha_m = 40.3 \cdot 10^{16}/f_m^2$ converts an ionospheric delay from TECU to metres of delay at the frequency f_m.

Once the carrier phase ambiguity B_{GF} is removed, the variation of L_{GF} along the arc has an error at the level of 1 cm (at the level of a tenth of one TECU); this error level should be enough for assessing ionospheric models tailored for HAS. In this way, the metric to quantify the SCT results could be the RMS of $\Delta\mathrm{STEC}_i^j$ or any other statistic like percentiles. There are different choices to select t_{ref} for performing the comparison in Eq. (8). In Orús et al. (2005), the SCT was defined using the comparison between two epochs with the same satellite elevation, whereas Hernández-Pajares et al. (2017) selected t_{ref} as the epoch with the maximum satellite elevation in the dSTEC tests, which is based on the same idea. It is easy to see that both the SCT and the dSTEC tests, based on the STEC variation along the arc, are equivalent to estimate, per each continuous arc, a carrier phase ambiguity (B_{GF}) as:

$$L_{\mathrm{GF}i}^j(t) - (\alpha_n - \alpha_m) \cdot I_i^j(t) = B_{\mathrm{GF}i}^j \tag{9}$$

where the metric for the test is the residual of this fitting, e.g. the RMS of the post-fit residual. Note that for a worldwide network of about one hundred stations and one hundred of satellites (in a multi-constellation scenario), Eq. (9) involves estimating tens of thousands ambiguities (whose exact number depends on how many arcs occur per receiver-satellite pair). This huge number of ambiguities to be estimated implies that the assessment is done just in a local/regional scale (what the IPP sweeps during the length of the arc of data), in such a way that any regional bias of the ionospheric model could be absorbed by the B_{GF} estimates. Therefore, because the bias values are arbitrary (or the selection of t_{ref}), only the standard deviation of the fitting of Eq. (9), arc by arc, makes sense for the assessment.

In contrast, we can take advantage from IAR, which allows us to determine the integer values of the carrier phase ambiguities at each frequency, N_{mi}^j and N_{ni}^j. Then, Eq. (9) becomes:

$$\begin{aligned}&L_{\mathrm{GF}i}^j(t) - (\alpha_n - \alpha_m) \cdot I_i^j(t) - \lambda_m N_{mi}^j + \lambda_n N_{ni}^j \\ &\quad = \lambda_m\left(\delta_{mi} + \delta_m^j\right) - \lambda_n\left(\delta_{ni} + \delta_n^j\right)\end{aligned} \tag{10}$$

where the IAR values of the ambiguities have been subtracted in the left-hand side. The δ_{ki} and δ_k^j are instrumental delays (i.e. the phase biases) for the receiver i and the satellite j at each frequency k. Note that the right-hand side of Eq. (8) are constant values, which can be estimated for instance once per day, as it was proposed in Rovira-Garcia et al. (2016a):

$$L^j_{\mathrm{GF}i}(t) - (\alpha_n - \alpha_m) \cdot I_i^j(t) - \lambda_m N^j_{mi} + \lambda_n N^j_{ni} = k_i + k^j \tag{11}$$

where the constant values k include the instrumental delays of each receiver and each satellite. Note that in this last test, the fitting involves only the sum of the number of receivers and the number of the satellites considered (some hundreds). In this way, the post-fit residual of the global fit over the whole network becomes a confident measure of the self-consistency of the ionospheric delay estimates. That is, for the same previous case of a network of one hundred receivers and one hundred satellites, the test using Eq. (11) would estimate less than two hundred parameters, two orders of magnitude less than in the SCT or dSTEC test involving Eq. (9). This is the reason why the test proposed in Rovira-Garcia et al. (2016a) is one of the assessments routinely used by the Fast-PPP ionospheric model.

Figure 8 illustrates, for two rover receivers, the residuals of the estimation of the daily constant k values in the right-hand side of Eq. (11), after subtracting two different ionospheric models I to the unambiguous GF combination of carrier phase measurements. The black dots depict the performance of the Fast-PPP ionospheric model obtained in real time, whereas the red squares depict the results obtained by the IGRG GIM. The results, extended in Table 1 for the seven rovers and for every week in each period, confirm those presented in Rovira-Garcia et al. (2016a). That is, in well-sounded areas, the root mean square (RMS) of the residuals of Fast-PPP is two or three times lower than the RMS of the IGS GIM. As expected, there is less improvement when the station is located in poorly sounded areas.

In Table 1, we have split the performance into Galileo and GPS measurements, in order to see differences between the two constellations (notice that IGRG is computed using only GPS data). However, the resulting residuals are quite similar for the two constellations. Note that stations REDU (Redu, Belgium), MARS (Marseille, France) or TRO1 (Tromso, Norway) may be representative of future ionospheric corrections of Galileo HAS over central Europe, assuming a monitoring network with a similar density over Europe and surroundings as that used in our test.

As it can be seen in Table 1, except for the farthest receiver CEFT (at more than 1000 km from the nearest reference receiver), the RMS of the error of the ionospheric corrections using the Fast-PPP ionospheric model is clearly smaller than one TECU and is several times smaller than those using the IGRG ionospheric model. This confirms the results presented, for instance, in Rovira-Garcia et al. (2020) using just GPS data. In the case of CEFT, these large ionospheric errors would not help to improve the navigation solution. However, these errors are still clearly smaller than those using the IGRG GIM.

We now turn our attention to the assessment of the actual errors (Fig. 9) and the predicted errors (Fig. 10) for both the IGRG GIM (top rows) and the Fast-PPP model (bottom rows) for the two analysed periods in 2019 (left columns) and 2021 (right columns). The chosen metric that is depicted in every plot is the complementary cumulative distribution function (CCDF), to allow assessing the percentiles of actual and predicted errors of both ionospheric models. In every plot of Fig. 9, the 5% value in the CCDF is indicated with a dashed line in order to identify the 95th percentile of each error distribution.

As it can be seen in the bottom plots of Fig. 9, 99% of the Fast-PPP ionospheric corrections have actual errors below one TECU in well-sounded areas and in mid-latitude stations. We can observe that the 95% error percentiles, which can be identified thanks to the dashed line, do not degrade between the right and left column plots, despite the fact that some rovers experience an ionospheric activity substantially higher in the 2021 period. Therefore, one can conclude that Fast-PPP is able to provide the required accuracy for HAS in such conditions. The performance is degraded for stations at low latitude or at the highest latitude, where in these regions the Fast-PPP model uses a higher process noise for computing the VTECs, in order to account for the larger ionospheric activity expected in this area. However, for these receivers and during the two periods, the 95% error remains under 2 TECU. In contrast, the top row plots depict the errors for the IGRG GIM, where, in the best conditions (REDU station in mid-latitude), more than the 10% of the ionospheric corrections have an error larger than one TECU.

Looking the RMS of Table 1 or the percentiles inferred from Fig. 9, it is worth noting that the ionospheric errors in the present work are significantly lower than those in Rovira-Garcia et al. (2020). This is because the results on that paper were obtained during year 2014, close to Solar Cycle maximum. Consequently, using the ionospheric corrections of this work for navigation purposes would produce even better positioning results than those presented in Rovira-Garcia et al. (2020).

Figure 10 depicts the predicted errors of the ionospheric corrections, which are derived from the covariance matrix of the estimates. It is interesting to see that in the case of the Fast-PPP model, these formal errors provide some kind of guarantee to the quality of the ionospheric corrections, i.e. larger predicted errors are linked to larger actual errors in the ionospheric corrections depicted in Fig. 9. This is not the case for the IGRG GIM, where the larger actual errors in the

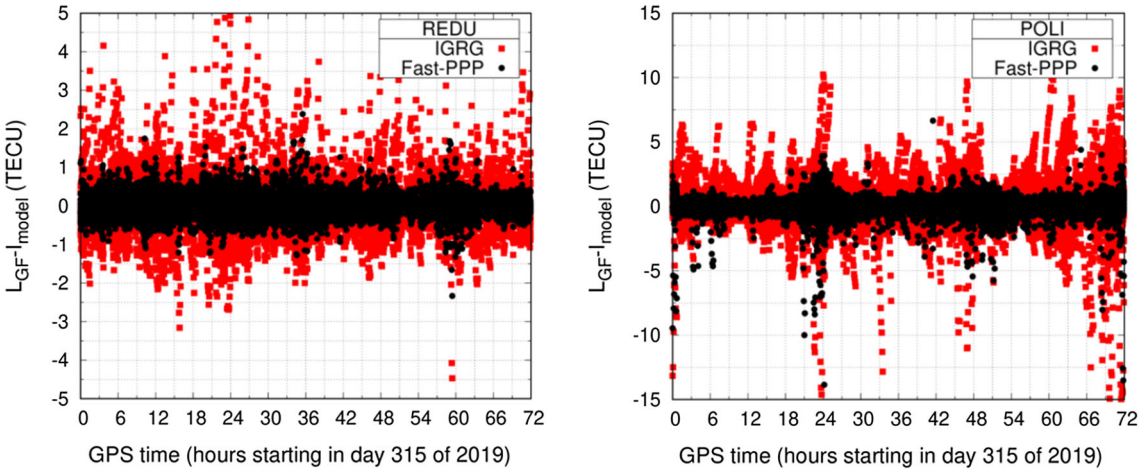

Fig. 8 Post-fit residuals to Eq. (11) for Fast-PPP (black) and the rapid IGS GIM (red) for permanent receivers REDU (left) and POLI (right)

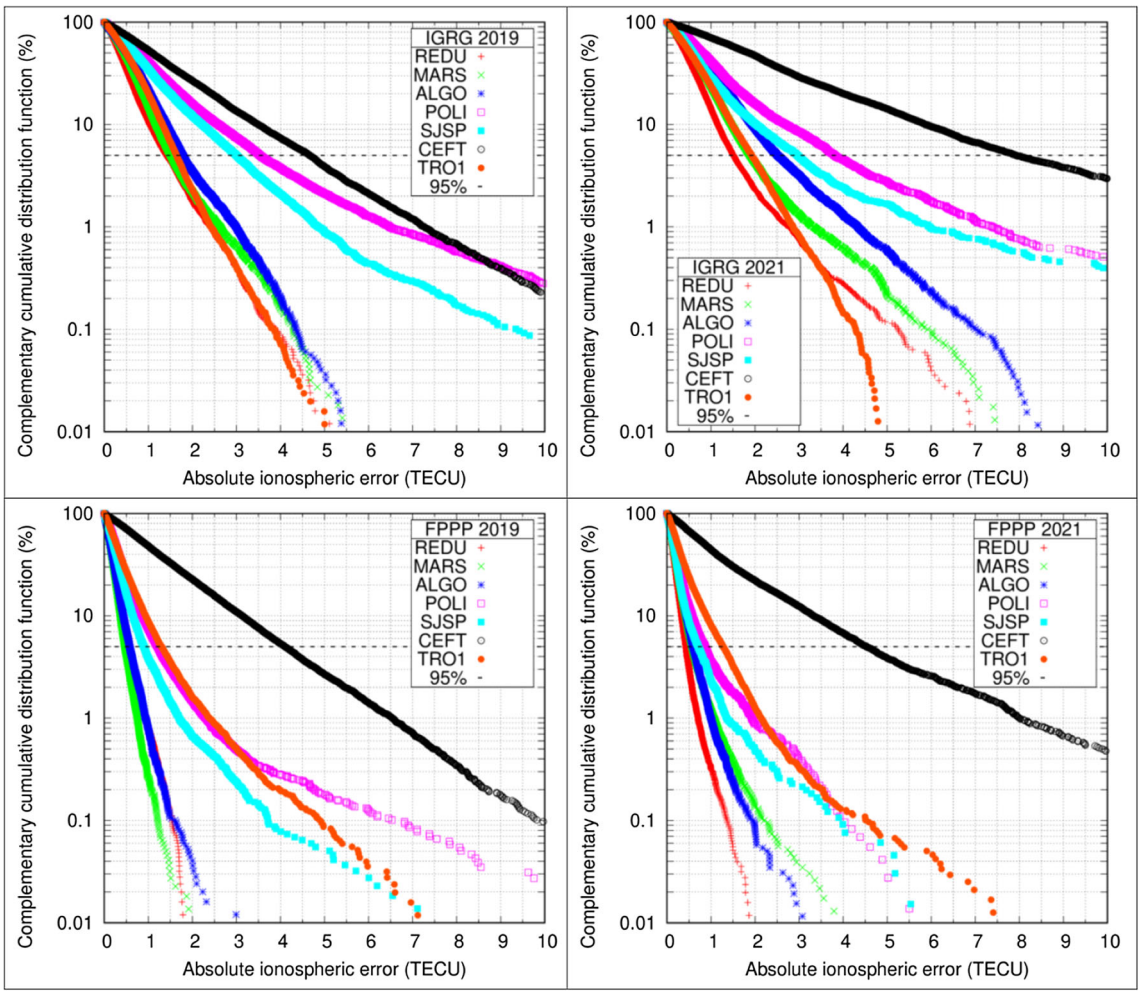

Fig. 9 Actual errors of the IGRG GIM (top row) and Fast-PPP model (bottom row) for the seven rovers depicted in Fig. 2 and for one week starting on day 315 of 2019 (left column) and one week starting on day 131 in 2021 (right column). The dashed line indicates the 95% percentile

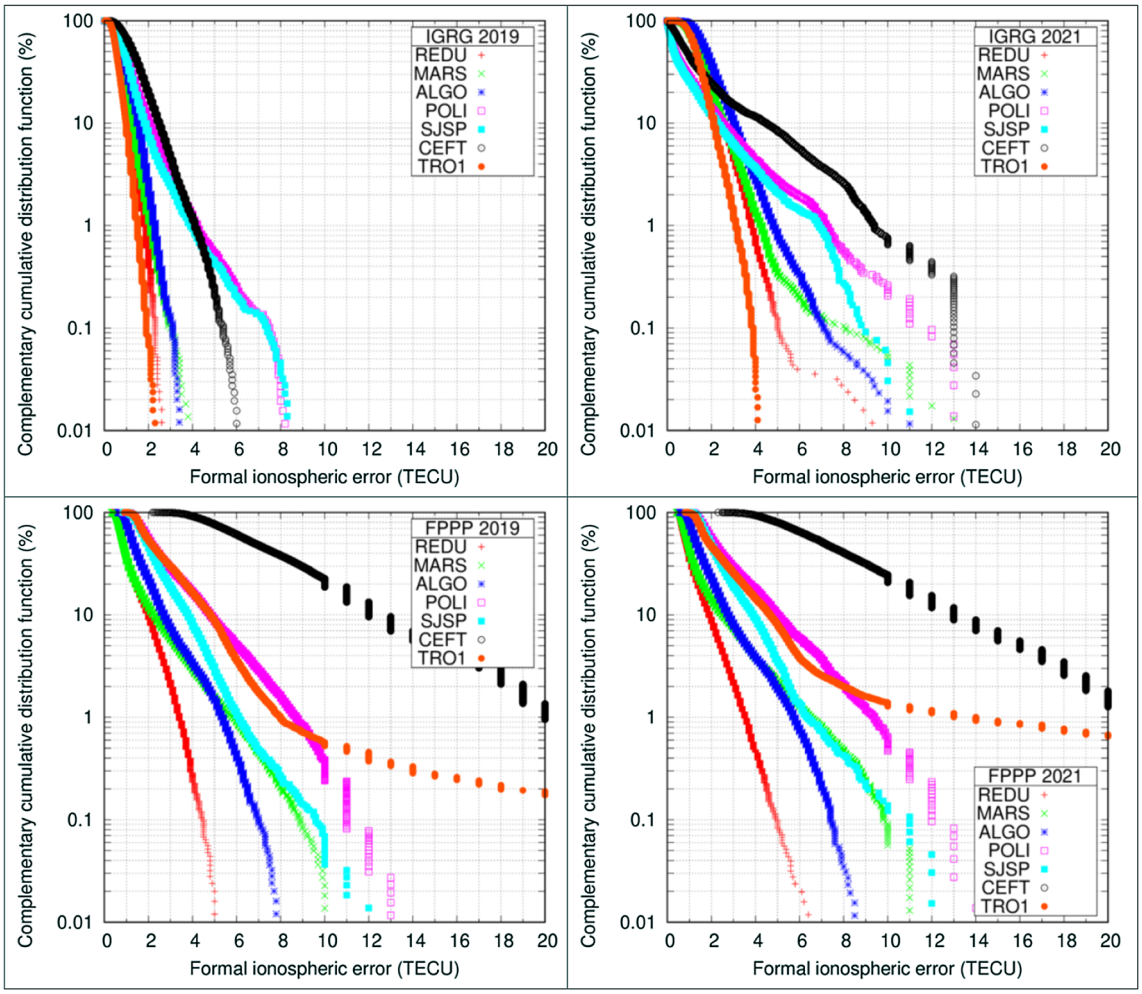

Fig. 10 Predicted errors of the IGRG GIM (top row) and Fast-PPP model (bottom row) for the seven rovers depicted in Fig. 2 and for one week starting on day 315 of 2019 (left column) and one week starting on day 131 in 2021 (right column)

ionospheric corrections are not necessarily those with larger formal errors.

6 Conclusions

Ionospheric models with an accuracy at the level of one TECU can be useful for high-accuracy applications, such as the Galileo HAS. The present work has described some novel characteristics of the Fast-PPP ionospheric model that contributes to provide such accuracy. The first one is related to the geometry of the model, which, as it was shown in previous works, uses a dual-layer description of the ionospheric and plasmaspheric delays and the use of the MODIP latitude and LT to distribute the IGPs. The regular distribution based on MODIP increases the resolution at equatorial latitudes. Unlike other ionospheric models, the IGP distribution in LT is not regular. This choice reduces 30% of the IGPs needed to be computed and broadcast.

Based on this model, some aspects concerning the requirements and usage of ionospheric corrections for Galileo HAS have been discussed. A second novel characteristic is related to the quality of the measurement data used as input to compute the Fast-PPP model, which uses IAR instead of CCL to obtain unambiguous carrier phase measurements feeding the ionospheric model.

The accuracy of the Fast-PPP ionospheric model has been examined using rover receivers that have not participated into the computation of the model, confirming accuracies at the level of one TECU in well-sounded regions. In addition, the Fast-PPP model provides a realistic prediction of the error through the formal errors, so that HAS users can decide whether to apply such ionospheric corrections.

Acknowledgements The authors would like to thank J. de Blas from GSA and the respective ESA/GSA teams involved in the Galileo HAS.

Author contributions IFH proposed the general idea of this contribution and initiated the work. JMJ and JS designed and developed the Fast-PPP

CPF used in the study. GGC performed the data gathering and processing. ARG and CCT analysed the results and wrote the manuscript. IFH, RO and DB contributed to the technical discussion and organization of the manuscript. All authors provided advice and critically reviewed the manuscript.

Funding Open Access funding provided thanks to the CRUE-CSIC agreement with Springer Nature. The present work was supported in part by the European Space Agency contract IONO4HAS 4000128823/19/NL/AS, by the project RTI2018-094295-B-I00 funded by the MCIN/AEI 10.13039/501100011033 which is co-founded by the FEDER programme and by the Horizon 2020 Marie Skłodowska-Curie Individual Global Fellowship 797461 NAVSCIN.

Data availability The authors acknowledge the use of data and products provided by the International GNSS Service and the Rede Brasileira de Monitoramento Continuo, as detailed in the section Data set. All the data and products are publicly available through the respective organizations' websites.

References

Beutler G, Rothacher M, Schaer S, Springer T, Kouba J, Neilan R (1999) The International GPS Service (IGS): an interdisciplinary service in support of Earth sciences. Adv Space Res 23(4):631–653. https://doi.org/10.1016/S0273-1177(99)00160-X

Borio D, Senni T, Fernandez-Hernandez I (2020) Experimental Analysis of a candidate Galileo E6-B data dissemination scheme. In: Proceedings of the 2020 international technical meeting of the institute of navigation, San Diego, California, January 21–24, pp 509–520. https://doi.org/10.33012/2020.17159

European Commission (2018) Commission Implementing Decision (EU) 2018/321. Off J Eur Union 62:34–35. https://eur-lex.europa.eu/legal-content/EN/TXT/PDF/?uri=CELEX:32018D0321&from=EN

European GNSS Agency (2020) Galileo high accuracy service (HAS) info note. ISBN 978-92-9206-050-3. https://doi.org/10.2878/581340. https://www.gsc-europa.eu/sites/default/files/sites/all/files/Galileo_HAS_Info_Note.pdf

Fernández-Hernández I, Senni T, Borio D, Vecchione G (2020) High-parity vertical Reed-Solomon codes for long GNSS high-accuracy messages. NAVIGATION J Inst Navig 67(2):365–378. https://doi.org/10.1002/navi.357

Hatch R (1982) The synergism of GPS code and carrier measurements. In: Proceedings of the 3rd international geodetic symposium on satellite Doppler positioning. Las Cruces, USA. February 8–12, vol 2, pp 1213–1231

Hernández-Pajares M, Roma-Dollase D, Krankowski A, García-Rigo A, Orús-Pérez R (2017) Methodology and consistency of slant and vertical assessments for ionospheric electron content models. J Geod 91(12):1405–1414. https://doi.org/10.1007/s00190-017-1032-z

Juan JM, Sanz J, Rovira-Garcia A, González-Casado G, Ibáñez D, Orús-Pérez R (2018) AATR an ionospheric activity indicator specifically based on GNSS measurements. J Space Weather Space Clim 8(A14):5. https://doi.org/10.1051/swsc/2017044

Malys S, Jensen PA (1990) Geodetic point positioning with GPS carrier beat phase data from the CAS UNO experiment. Geophys Res Lett 17(5):651–654. https://doi.org/10.1029/GL017i005p00651

Mannucci AJ, Wilson BD, Yuan DN, Ho CH, Lindqwister UJ, Runge TF (1998) A global mapping technique for GPS-derived ionospheric total electron content measurements. Radio Sci 33(3):565–582. https://doi.org/10.1029/97RS02707

Mitsubishi Electric Corporation (2015) Specification of compact SSR messages for satellite based augmentation service—RTCM paper 164-2015-SC104-904

Odijk D, Zhang B, Khodabandeh A, Odolinski R, Teunissen PJG (2016) On the estimability of parameters in undifferenced, uncombined GNSS network and PPP-RTK user models by means of S-system theory. J Geod 90(1):15–44. https://doi.org/10.1007/s00190-015-0854-9

Orús R, Hernández-Pajares M, Juan JM, Sanz J (2005) Improvement of global ionospheric VTEC maps by using kriging interpolation technique. J Atmos Solar Terr Phys 67(16):1598–1609. https://doi.org/10.1016/j.jastp.2005.07.017

Orús R, Nava B, Parro J, Kashcheyev A (2021) ESA UGI (Unified-GNSS-Ionosphere): an open-source software to compute precise ionosphere estimates. Adv Space Res 67(1):56–65. https://doi.org/10.1016/j.asr.2020.09.011

Radio Technical Commission for Aeronautics (2016) Minimum operational performance standards for global positioning system/wide area augmentation system airborne equipment—RTCA DO-229D

Rawer K (1963) Propagation of decameter waves (HF-band) in meteorological and astronomical influences on radio wave propagation. Pergamon Press, New York

Remondi BW (1985) Performing centimeter-level surveys in seconds with GPS carrier phase: initial results. Navigation 32(4):386–400. https://doi.org/10.1002/j.2161-4296.1985.tb00918.x

Rovira-Garcia A, Juan JM, Sanz J, González-Casado G (2015) A worldwide ionospheric model for fast precise point positioning. IEEE Trans Geosci Remote Sens 53(8):4596–4604. https://doi.org/10.1109/TGRS.2015.2402598

Rovira-Garcia A, Juan JM, Sanz J, González-Casado G, Ibáñez D (2016a) Accuracy of ionospheric models used in GNSS and SBAS: methodology and analysis. J Geodesy 90(3):229–240. https://doi.org/10.1007/s00190-015-0868-3

Rovira-Garcia A, Juan JM, Sanz J, González-Casado G, Bertran E (2016b) Fast precise point positioning: a system to provide corrections for single and multi-frequency navigation. NAVIGATION J Inst Navig 63(3):231–247. https://doi.org/10.1002/navi.148

Rovira-Garcia A, Ibáñez-Segura D, Orús-Perez R, Juan JM, Sanz J, González-Casado G (2020) Assessing the quality of ionospheric models through GNSS positioning error: methodology and results. GPS Solut 24(1):4. https://doi.org/10.1007/s10291-019-0918-z

Rovira-Garcia A, Juan JM, Sanz J, González-Casado G, Ventura-Traveset J, Cacciapuoti L, Schoenemann E (2021) Removing day-boundary discontinuities on GNSS clock estimates: methodology and results. GPS Solut 25(2):35. https://doi.org/10.1007/s10291-021-01085-3

Radio Technical Commission for Maritime Services Special Comitte 104 (2016) RTCM standard 10403.3 differential GNSS services—version 3. http://www.rtcm.org/differential-global-navigation-satellite–dgnss–standards.html

Sanz J, Juan JM, Hernández-Pajares M (2013) GNSS data processing, vol I: fundamentals and algorithms. ESA communications, ESTEC TM-23/1, ISBN 9292218867. Noordwijk, The Netherlands

Schaer S, Gurtner W, Feltens J (1998) IONEX: the IONosphere map exchange format version 1. In: Proceedings of the IGS AC workshop, Darmstadt, Germany, February 9–11, pp 233–247

Zhang L, Yang H, Gao Y, Yao Y, Xu C (2018) Evaluation and analysis of real-time precise orbits and clocks products from different IGS analysis centers. Adv Space Res 61(12):2942–2954. https://doi.org/10.1016/j.asr.2018.03.029

Zumberge JF, Heflin MB, Jefferson DC, Watkins MM, Webb FH (1997) Precise Point Positioning for the efficient and robust analysis of GPS data from large networks. J Geophys Res Solid Earth 102(B3):5005–5017. https://doi.org/10.1029/96JB03860

J. Space Weather Space Clim. 2020, **10**, 42

https://doi.org/10.1051/swsc/2020043

JSWSC

Available online at:
www.swsc-journal.org

Topical Issue - Scientific Advances from the European Commission H2020 projects on Space Weather

RESEARCH ARTICLE OPEN ACCESS

An overview of methodologies for real-time detection, characterisation and tracking of traveling ionospheric disturbances developed in the TechTIDE project

Anna Belehaki[1,*] Ioanna Tsagouri[1], David Altadill[2], Estefania Blanch[2,3], Claudia Borries[4], Dalia Buresova[5], Jaroslav Chum[5], Ivan Galkin[6], José Miguel Juan[7], Antoni Segarra[2], Cristhian Camilo Timoté[7], Kostas Tziotziou[1], Tobias G. W. Verhulst[8], and Jurgen Watermann[9]

[1] National Observatory of Athens, IAASARS, 152 36 Palaia Penteli, Greece
[2] Observatori de l'Ebre (OE), CSIC – Universitat Ramon Llull, 43520 Roquetes, Spain
[3] Departament de Física-EPSEB, UPC Barcelona Tech, 08028 Barcelona, Spain
[4] German Aerospace Center, Institute for Solar-Terrestrial Physics, 17235 Neustrelitz, Germany
[5] Institute of Atmospheric Physics, Czech Academy of Sciences, 14100 Prague, Czech Republic
[6] Borealis Designs Ltd., 9000 Varna, Bulgaria
[7] gAGE, Universitat Politecnica de Catalunya, 08034 Barcelona, Spain
[8] Royal Meteorological Institute, 1180 Dourbes, Belgium
[9] jfwConsult, La Tetrade, 443 Chemin de Pichot, Tourrettes, 83440 Var, France

Received 8 April 2020 / Accepted 4 August 2020

Abstract – The main objective of the TechTIDE project (warning and mitigation technologies for travelling ionospheric disturbances effects) is the development of an identification and tracking system for travelling ionospheric disturbances (TIDs) which will issue warnings of electron density perturbations over large world regions. The TechTIDE project has put in operation a real-time warning system that provides the results of complementary TID detection methodologies and many potential drivers to help users assess the risks and develop mitigation techniques tailored to their applications. The TechTIDE methodologies are able to detect in real time activity caused by both large-scale and medium-scale TIDs and characterize background conditions and external drivers, as an additional information required by the users to assess the criticality of the ongoing disturbances in real time. TechTIDE methodologies are based on the exploitation of data collected in real time from Digisondes, Global Navigation Satellite System (GNSS) receivers and Continuous Doppler Sounding System (CDSS) networks. The results are obtained and provided to users in real time. The paper presents the achievements of the project and discusses the challenges faced in the development of the final TechTIDE warning system.

1 Introduction

The Earth's upper atmosphere is directly affected by the solar variability, by the near-Earth space dynamics and lower atmosphere phenomena. This results in a complex and dynamic environment influenced by solar radiation, energy transfer, winds, waves, tides, electric, and magnetic fields, and plasma processes. Travelling ionospheric disturbances (TIDs) constitute an important Space Weather effect in the upper atmosphere driven by this complexity. TIDs are plasma density fluctuations that propagate as waves through the ionosphere at a wide range of velocities and frequencies and play an important role in the exchange of momentum and energy between various regions of the upper atmosphere. TIDs are the ionospheric manifestation of internal atmospheric gravity waves (AGW) in the thermosphere (e.g., Hunsucker, 1982; Hocke & Schlegel, 1996). The vast majority of observations suggests that gravity waves transport momentum and energy from auroral latitudes to middle latitudes (Hocke & Schlegel, 1996) and can also transfer momentum and energy from the lower to the upper atmosphere. Francis (1975) concluded in his classic review on atmospheric gravity waves that theory and observations imply that "the only natural sources of large-scale TIDs are in the auroral zones". However, some cases of large-scale TIDs (LSTIDs) being launched in the vicinity of the magnetic equator were recently reported (Habarulema et al., 2015, 2016, 2018) although such cases appear to be rare. AGW and consequently TIDs are

*Corresponding author: belehaki@noa.gr, abeleha@otenet.gr

classified according to their wave velocity and period. LSTIDs have horizontal propagation velocities between 300 m/s and 1000 m/s, horizontal wavelengths greater than 1000 km (1000–3000 km) and periods in the range of 30 min to 3 h. Medium-scale TIDs (MSTIDs) have horizontal propagation velocities between 100 m/s and 300 m/s, horizontal wavelengths of several hundreds of km and periods between 15 min and 60 min. Besides, small-scale TIDs that have wavelengths of less than 300 km have also been observed. They are not considered here.

According to the literature, LSTIDs are mostly associated with auroral and geomagnetic activity (e.g., Tsugawa & Saito, 2004; Figueiredo et al., 2017, and references therein). MSTIDs are mostly associated with ionospheric coupling with the lower atmosphere, as comprehensively explained by Hunsucker (1982) and further demonstrated with experimental observations during ionosphere–troposphere coupling events such as tsunami events (e.g., Savastano et al., 2017) and convective storms (e.g., Azeem et al., 2015). Long wavelength gravity waves propagate quasi-horizontally in the thermosphere. These waves are ducted by the temperature gradient in the lower thermosphere and dominate at great distances from the source. In the mid-latitude ionosphere, these gravity waves can be observed as typical LSTIDs propagating equatorward. The second gravity wave mode, of a shorter wavelength, is a wave from the lower to the upper thermosphere that propagates near the source. In the lower atmosphere, ducted waves dominate at large distances away from the source, and Earth-reflected gravity waves propagate after reflection at the Earth's surface back into the thermosphere, where they are rapidly dissipated because of their short wavelength. However, simulation models for the generation and propagation of gravity waves, suggest a more complex mode spectrum (Balthazor & Moffet, 1997).

Numerical simulations show that wave amplitudes are not necessarily directly related to the strength of excitation and that the source geometry is extremely important. A large enhancement of energy deposition into the ionosphere is often not accompanied by a large increase of gravity wave excitation. On the other hand, excitation of large-scale gravity waves occurs even under quiet geomagnetic conditions with relatively low energy depositions but optimal source properties (Mayr et al., 1990). These results indicate that perturbations detected in the ionospheric characteristics due to TIDs and the source of their excitation do not have a one-to-one correspondence. This is the reason why, the tracking and even the nowcasting of TIDs is very challenging.

The following requirements have to be fulfilled for the development of a comprehensive TID selection system:

Monitoring the TID drivers: TIDs constitute a specific type of space weather phenomenon that can be solar-driven or be driven by other processes acting below the ionosphere. LSTID drivers are physical characteristics that provide information on the level of solar-wind magnetosphere coupling during isolated substorms and on the impact of coronal mass ejections (CME) and corotating interaction region/solar wind high-speed streams (CIR/HSS) on the Earth environment. They are represented by the magnetosphere coupling functions, the Auroral Electrojet intensity, and the polar cap electron and proton fluxes, as summarized by Buresova et al. (2018). Recently Zhang et al. (2019), based on the analysis of GNSS differential TEC observations, suggested X-class solar flares, can be also considered to drive LSTIDs.

MSTID drivers are described by physical characteristics that specify the level of ionosphere–lower atmosphere coupling and specifically, the coupling of processes on the Earth's surface or in the lower-lying layers of the atmosphere with electric and electromagnetic phenomena in the ionosphere (Lastovicka, 2006). Upward propagating waves in the neutral atmosphere triggered by seismic activity, the occurrence of strong meteorological phenomena (large convective storms, passages of strong cold fronts, tornados, typhoons), the passage of solar terminator and solar flares are the main physical drivers of MSTIDs (Buresova et al., 2018), which in turn generates ionospheric irregularities such as spread F, N-shaped pulse disturbances or irregular variation of ionospheric parameters (Jayachandran et al., 1987; Sauli & Boska, 2001; Xiao et al., 2007). Regarding MSTIDs, their identification and tracking contain large uncertainty, since they are associated with gravity waves propagation and plasma instability that can impact the ionospheric electrodynamics. Wide and dense networks of observing systems that include ground-based and space-borne sensors are required to monitor simultaneously disturbances in the lower atmosphere, in the ionosphere, in the magnetosphere and in the solar wind; such a network is required to draw a global picture of the solar wind – magnetosphere – ionosphere – lower atmosphere coupled system, which is necessary for monitoring of the TID drivers in real time and evaluate the criticality of the TID triggering conditions in order to issue warnings.

Detection of conditions for LSTID triggering at high latitudes: Since LSTIDs are triggered by auroral activity, it is expected that the detection of LSTIDs at high latitudes could help warning for TID activity in lower latitudes. Observational networks of Global Navigation Satellite Systems (GNSS) receivers can provide estimates of the total electron content (TEC). The perturbation in TEC at high latitudes is indicative of TID activity initiation at regions close to the gravity wave excitation source. These results can be used as an early warning for forthcoming TID activity at middle and low latitudes (Borries et al., 2017).

Development of dense networks of in situ measurements for the detection of perturbations imposed by TIDs in the bottomside ionosphere: Direct TIDs effects are primarily observed in the bottomside ionosphere (e.g., Beley et al., 1995). Specific observations must be collected from this region using dense networks of ionospheric sounders, which are able to operate in synchronised mode as transmitter–receiver pairs. These are the oblique Digisonde-to-Digisonde (D2D) "skymap" observations which were introduced by Reinisch et al. (2018). They are required to identify the disturbance in the radio wave propagation characteristics due to TIDs. Such a network exists in Europe mainly due to developments in the Net-TIDE project (Belehaki et al., 2015; Reinisch et al., 2018). This special operation mode requires continuous adjustment of the transmitting frequency to reach optimum communication conditions.

Develop methods to detect TIDs at any altitude in the bottomside and topside ionosphere: TEC parameters provide an indication of a TID without specification of the height of the maximum disturbance. Electron density reconstruction models can fulfil this need. As an example, the 3D version of the Topside

Sounder Model (TSM)-assisted Digisonde (TaD) model is able to track the TID triggered disturbances in the electron density at various heights in the F layer and in the topside ionosphere (Kutiev et al., 2016).

Establishment of permanent networks to detect TIDs excited in the lower atmosphere: To identify TIDs triggered by mechanisms acting below the ionosphere altitudes, i.e. MSTIDs, specific methodologies are employed. These include the Continuous Doppler Sounding System (CDSS) and the GNSS detrending. The CDSS method detects MSTIDs, because of the topology of the network and its sensitivity to fast changes. CDSS networks operate in Europe and South Africa. The GNSS detrending method relies on the analysis of data from clusters of GNSS receivers to verify TID propagation characteristics with wavelength of the scales of the GNSS stations distances.

Define regional ionosphere background conditions: The amplitude of TID perturbation is directly proportional to the background electron density (Hooke, 1968). Ionospheric storms are large scale disturbances resulting in electron density enhancements or depletions depending on local time, storm time, geomagnetic location and season. Neutral winds and strong dawn-to dusk electric field can cause large uplifts or downdrafts of the ionospheric plasma leading to large-scale local time dependent enhancements or decreases of the ionospheric electron content at all latitudes. In depleted ionospheric plasma, the TIDs are faint (Reinisch et al., 2018). However, for users requesting accurate ionospheric characteristics in real time, even under ionospheric storm conditions the electron density modulation triggered by TIDs must be identifiable.

The main objective of the TechTIDE project (warning and mitigation technologies for travelling ionospheric disturbances effects) is the development of an identification and tracking system for TIDs considering all the requirements listed above. For the first time such a system operates in realtime. TechTIDE will issue the results of various detection methodologies and warnings of electron density perturbations over wide world areas. TechTIDE methodologies are based on the exploitation of data collected in real time from Digisondes, GNSS receivers, and CDSS networks.

In this paper we report on the main activities carried out in the frame of the TechTIDE project. In Section 2 we summarize the key specifications of a real-time TID warning system and the main data required to be collected and retrieved in real time; in Section 3 we present the main methodologies that are exploited in TechTIDE to detect TIDs and their detection capabilities; in Section 4 we discuss the challenges that need to be addressed for the reliable operation of a real-time TID warning system.

2 Specifications of a real-time TID warning system and required data

Specification of TID activity over large world regions is a key requirement from the operators of systems using or affected by ionospheric conditions; TIDs severely affect all operational systems using predictable ionospheric characteristics as they can impose disturbances with amplitudes of up to ~20% of the ambient electron density, and Doppler frequency shifts of the order of 0.5 Hz on HF signals (Reinisch et al., 2018).

The accuracy of ground-based single-site-location (SSL) HF radio wave direction finding is severely compromised by the passage of TIDs through the ionospheric reflection area (Nickisch et al., 2016). Small amplitude TIDs, occurring virtually all the time with varying amplitudes, similar to cloud occurrence in the troposphere, can tilt the reflecting isodensity contours by as much as 3°–5°. These time-varying tilts cause variances in the measured bearings of about 1° for emitter distances of 1000 km to about 100° for 100 km, the "short-range catastrophe" (Ross, 1947). TIDs of larger amplitudes affect the performance of GNSS, and in particular, the Satellite Based Augmentation Systems (SBAS), such as the European Geostationary Navigation Overlay System (EGNOS, Pintor & Roldán, 2015), as they can produce variations in TEC of several total electron content units (TECUs). These variations cannot be completely detected and corrected by these systems. This, results in a decrease of the observation accuracy and a limitation of the availability of these navigation systems for the different types of applications that they support (mainly aviation). Furthermore, it was shown by Hernández-Pajares et al. (2006) that TIDs of medium scale can affect the performance of the high accuracy navigation systems, like network real-time kinematic (N-RTK). Because N-RTK services are based on interpolating the ionospheric delays, the effect of TIDs can be quite significant. The radio astronomy community reports phase errors in low frequency radio telescope images due to small variations in TEC caused by MSTIDs (Mevius et al., 2016). Overall TIDs are a nuisance for any system using transionospheric radio wave propagation.

Basic users' requirements that need to be fulfilled by a real-time identification and tracking TIDs system, are collected by the TechTIDE consortium and summarized by Altadill et al. (2019):

- Detection of MSTIDs and LSTIDs occurrence in real time over large geographical regions.
- Estimation of the period, phase velocity, propagation direction, wavelength, and amplitude for both LSTIDs and MSTIDs.
- Estimation of the Doppler frequency, angle of arrival, and signal time-of-flight from transmitter to receiver for HF communications.
- Estimation of de-trended ionospheric characteristics and spectral energy contribution for specific measuring stations.
- Indication of the altitude of the maximum disturbance in the electron density over a region.
- Calculation of TEC gradients in real-time over wide regions in the globe.
- 3D electron density distribution maps over large geographical regions, for the bottomside and the topside ionosphere.
- Scaling of TID activity and characterization of the criticality of the induced disturbances in the systems concerned.
- Indication for the initiation of TIDs at high latitudes.
- Monitoring of the TID activity drivers, including the interhemispheric circulation.
- Specification of ionospheric background conditions, including the mapping of critical ionospheric characteristics foF2 and hmF2.

To meet these requirements the TechTIDE consortium deploys several independent and complementary detection techniques which are presented in the next section. A variety of data are exploited to operate the TID detection algorithms and to calculate the indicators and monitor the drivers:

- Digisonde vertical sounding measurements and oblique Digisonde-to-Digisonde observations from the European and South African networks.
- Data from ground-based GNSS receivers.
- Data from Doppler sounders.
- Additional auxiliary data from Spacecraft missions at L1 vintage point, magnetospheric, solar and geomagnetic indices, retrieved from World and Regional Data Centers.

Digisonde vertical incidence ionospheric measurements are openly accessible through the GIRO web site. Oblique Digisonde-to-Digisonde measurements and CDSS data are owned by the TechTIDE partners: the Royal Meteorological Institute of Belgium (RMI), the Institute of Atmospheric Physics of the Czech Republic (IAP), the Leibniz Institute of Atmospheric Physics of Germany (L-IAP), the National Observatory of Athens in Greece (NOA), and the Ebro Observatory in Spain (OE). The GNSS-RINEX data files are obtained from IGS and EUREF GNSS stations and are processed in real-time by the Deutsches Zentrum für Luft- und Raumfahrt (DLR) and the Universitat Politecnica de Catalunya (UPC).

3 TechTIDE methodologies for the real-time detection of TIDs

In the upper atmosphere, gravity waves are observed either directly as density and velocity fluctuations of the neutral gas, or indirectly as fluctuations of the ionospheric plasma, which is in principle a passive tracer of the neutral gas motions. The ionospheric fluctuations are measured using different radio techniques employing ionosondes, HF Doppler systems, GNSS receivers, and their networks. TechTIDE warning services are based on the implementation of several methodologies that are able to detect and analyze signatures of TIDs in real time. These methodologies include the Digisonde-to-Digisonde TID detection method (HF-TID), the HF Interferometry method (HF-INT), the Doppler Sounder detection method (CDSS-MSTID), the electron density perturbation at any ionospheric altitude calculated with the TaD ionospheric profiler model to estimate the LSTID index (LSTIDx), the Spatial and Temporal GNSS analysis that provides the MSTID index ($MSTID_{idx}$), the GNSS TEC gradients method (TECgrad) and the Along the Arc TEC Rate (AATR) indicator method. Among them, the HF-TID and HF-INT methods are based on Digisonde observed characteristics, the CDSS-MSTID results are inferred from CDSS measurements, the LSTIDx method is based on the TaD model which combines input from ground-based Digisonde data and GNSS-TEC estimates, while other methods exploit exclusively GNSS data. The detection capabilities of the aforementioned

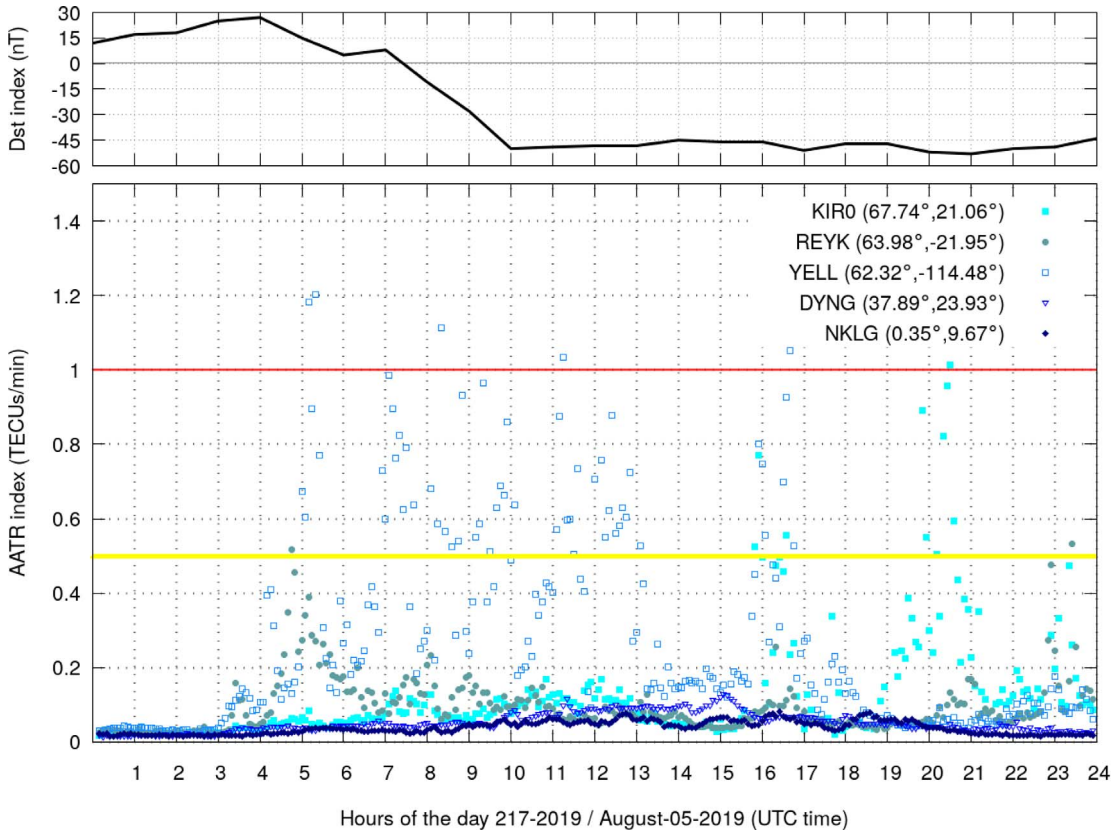

Fig. 1. Top panel: The Dst-index during 5 August 2019, the day when the initial and main phase of the moderate geomagnetic storm occurred. Bottom panel: the AATR indicator for 5 GNSS receivers at high, middle and low latitudes.

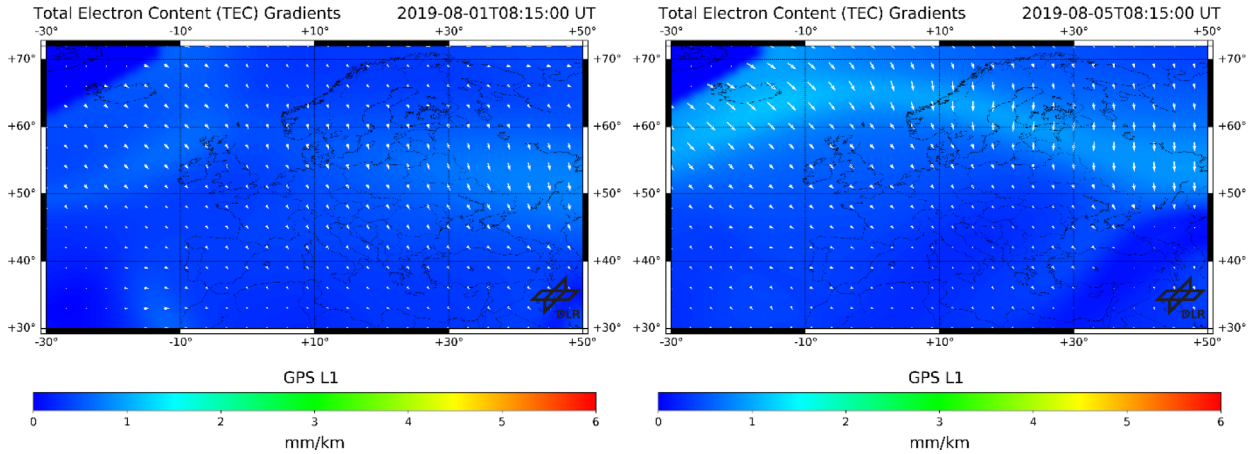

Fig. 2. Results from the gradient TEC method on the quiet day 1st August 2019 at 08:15 UT (left) and at the same time but for the disturbed day 5 August 2019 (right) when a moderate geomagnetic storm was in its main phase.

methodologies may depend on their intrinsic features but also on the configuration and the specifications of the observations' programmes. Consequently, the HF-TID, HF-INT and LSTIDx methods support the detection of LSTIDs, while the CDSS-MSTID and $\text{MSTID}_{\text{idx}}$ help detection of MSTIDs. The TECgrad and AATR methods results provide indicators of TIDs occurrence as both can be interpreted as proxies of the ionospheric activity at auroral latitudes. Finally, the TechTIDE warning services are supported by the specification of the ionospheric background conditions to help the users assess the criticality of any ongoing disturbances. In the following paragraphs indicative results obtained by the TechTIDE methodologies are presented. The detection efficiency of LSTIDs is demonstrated for the period 5–9 August 2019 that is characterized by the occurrence of a geomagnetic storm of moderate intensity (min Dst = −53 nT). The MSTID detection results are presented for a quiet day (20 January 2020) when no activity was recorded in the auroral electrojets.

3.1 Indicators of initiation of TID activity at high latitudes

During geomagnetic storms the high-latitude ionosphere is prone to heating and convection processes which tend to produce strong spatially and temporally variable plasma density gradients. Such gradients form the source of LSTIDs which then propagate equatorward.

The **AATR indicator** is a method that provides a metric for TID activity at high latitudes. The AATR indicator (Sanz et al., 2014) was developed in the context of ionospheric studies for EGNOS.

As developed in Juan et al. (2018), the AATR indicator is based on the rate of the slant TEC (STEC) variation and implements the rates of all satellites in view at a single site. The basic AATR input is the geometry-free combination of carrier-phase measurements, i.e., LI = L1–L2. The STEC (ΔSTEC) variation between two consecutive observations separated Δt, for a receiver i and a satellite j, can be computed for a given epoch, t, as:

$$\Delta\text{STEC}_i^j(t) = \text{LI}_i^j(t) - \text{LI}_i^j(t - \Delta t).$$

The definition of the instantaneous AATR index is then given by the following equation:

$$\text{AATR}_i^j(t) = \frac{1}{(M(\epsilon))^2}\frac{\Delta\text{STEC}_i^j(t)}{\Delta t}$$

where, Δt is the sampling rate of the carrier-phase measurements and $M(\epsilon)$ is an obliquity factor defined as the secant of the zenith angle at the mean ionospheric height. Finally, the RMS of the instantaneous $\text{AATR}_i^j(t)$ is computed for a predefined period for all "j" satellites in view from a particular station, resulting into the AATR index per a given "i" receiver as:

$$\text{AATR}_i(T) = \sqrt{\frac{1}{N}\sum_{t=T}^{T+\Delta T}\sum_{j=1}^{n_{\text{sat}}(t)}\left(\text{AATR}_i^j(t)\right)^2}$$

where N is total number of observations during the selected interval ΔT.

Juan et al. (2018) showed that AATR can be used for specifying ionospheric activity which causes performance degradation of the EGNOS network. They established a threshold of around 0.5 TECUs/min for moderate and around 1.0 TECUs/min for large ionospheric perturbations. The TechTIDE warning system provides routinely the values of the AATR indicator at approximately 150 locations of permanent GNSS receivers worldwide in the form of a color-coded global map, as ASCII values and in daily plots that are dynamically refreshed every 5 min. Figure 1 presents the variation of the AATR indicator on 5 August 2019, during the main and recovery phase of a moderate geomagnetic storm as indicated by the Dst index variation (top panel of figure). The results from five stations are presented, REYK, KIR0, YELL in the auroral zone, DYNG at middle latitudes and NKLG at low latitudes. The yellow line is the threshold for the EGNOS system to receive warnings about moderate ionospheric disturbances, whereas the red line is the threshold for high ionospheric activity warnings. In the event shown in Figure 1, only the auroral zone stations provide AATR estimates that are higher than 0.5 TECU/min, while the middle and lower latitude stations record quiet conditions.

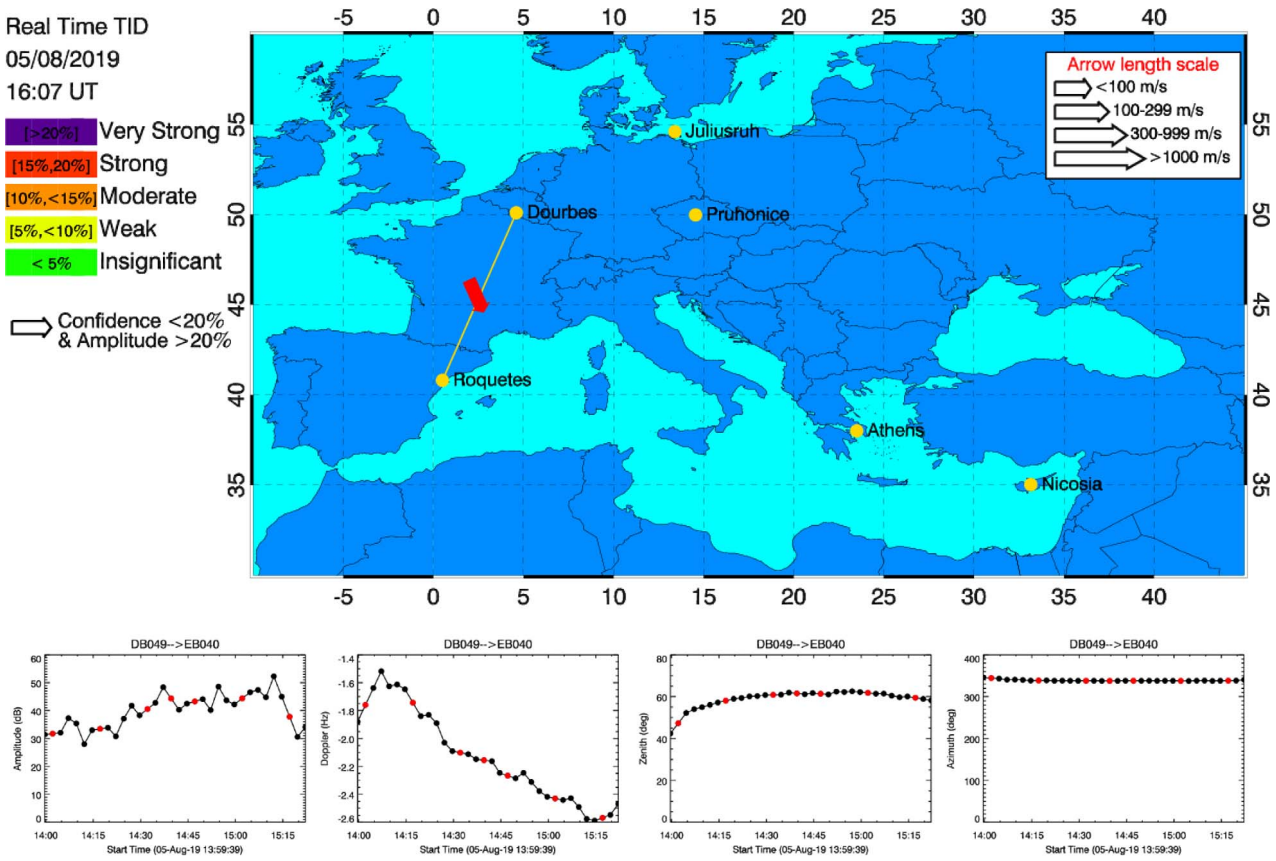

Fig. 3. Graphical representation of the HF-TID results in the TechTIDE warning system during the geomagnetic disturbed period of 5 August 2019.

The **GNSS TEC gradient** method has been proposed by Borries et al. (2017). The method calculates temporal and spatial TEC gradients based on TEC maps. TEC gradients are not a direct signature of TIDs. Therefore, TID occurrence cannot be directly inferred from TEC gradients. Instead, TEC gradients are considered to be precursors of LSTID activity. Significant TEC gradients at high latitudes are indicative of strong ionosphere–thermosphere perturbations, which are in turn considered to be sources of LSTIDs. Such TEC gradients are typically observed in the auroral oval. For operational purposes, the estimation of TEC gradients is based on TEC maps. Since the generation of TEC maps averages out steep TEC gradients, rather low thresholds must be assumed for the indication of the probability of LSTID generation. The statistical analysis of TEC gradients shows, that the average TEC gradient has an amplitude of about 0.2 mm/km. Alert thresholds can be based on the 90%, 95%, and 99% quantile, derived from the complementary of the cumulative distribution function of the high-latitude region. TEC gradients are considered low with amplitudes below 1.2 mm/km, moderate with amplitudes between 1.2 mm/km and 2 mm/km and strong above 2 mm/km.

Figure 2 presents the results of this method derived from DLR TEC maps at 15° E. The TEC gradient map for the geomagnetically quiet day 01 August 2019 at 08:15 UT is presented on the left side. The results for 5 August 2019, at 08:15 UT when a geomagnetic storm is in its main phase, is presented on the right. Maps of large-scale TEC gradients are routinely produced by the DLR and the results are disseminated to the users through the TechTIDE warning system.

3.2 Large scale TID detection methodologies

The **HF-TID method** (Huang et al., 2016; Reinisch et al., 2018) is based on the exploitation of DPS4D ionosonde data and is implemented to directly identify TIDs in real-time. For the real-time detection and evaluation of TIDs Digisonde-to-Digisonde (D2D) data from synchronized HF sounding between pairs of DPS4D ionosondes are analysed.

The method is based on the assumption that the ionosphere is represented by a moving undulated mirror, to relate HF signal parameters to TID characteristics, using the Doppler-Frequency-Angular-Sounding (FAS) technique (Paznukhov et al., 2012). Measurement of all signal properties (Doppler frequency, angle of arrival, and time-of-flight from transmitter to receiver) proved to be instrumental in detecting the TID and deducing the TID parameters: amplitude of the detected perturbation with respect to the ambient electron density (AMP%), propagation velocity and azimuth. The signal processing technique applied to HF data is capable of consistently extracting different signals that have propagated along different ionospheric paths. An intelligent system for "signal tracking" has been developed to handle the multi-path signal, based on a neural network model of

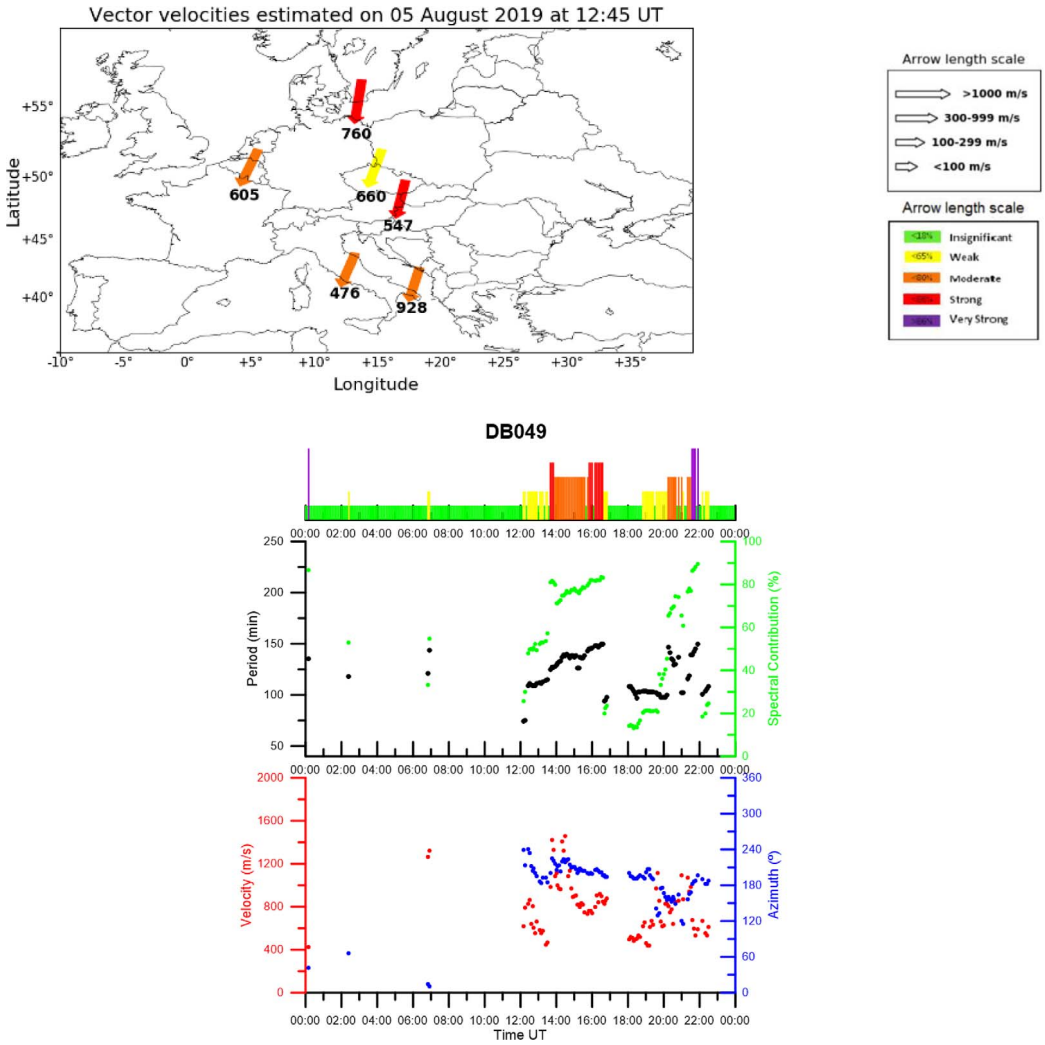

Fig. 4. Graphical representation of the HF-INT method results in the TechTIDE warning system. The European map with the TID velocities over stations are given in a colour scale which indicated the speed magnitude (top panel). Specific TID characteristics, i.e., period, spectral contribution, velocity and azimuth are presented in a daily real-time updated plot for the Dourbes Digisonde (center and bottom panels). The graphs refer to results extracted from observations collected on 5 August 2019.

a pre-attentive vision capable of extracting continuous signal tracks from the multi-path signal ensemble.

HF-TID is sensitive to the quasi-periodic variations of the HF radio signal recorded on oblique D2D links. Once such quasi-periodic signal behavior is detected, HF-TID uses the observed signal to infer properties of the TID wave responsible for the variation. The TID wave amplitude A_N is one of such HF-TID derived properties, readily available for categorization and presentation to the user. While HF-TID has been proven to be sensitive even to minute undulations caused by the traveling disturbance, that determination is pertinent to a very particular area in the ionosphere. This makes estimation of the impact on the end user operations even more difficult, as these systems exhibit different sensitivity to plasma disturbances of different extent in space, both in the vertical and horizontal dimensions. Unfortunately, this means that there is no universal TID activity metric definition that would suit all systems. The perturbation amplitude $A_N(z_0)$ is an excellent candidate for a consistent and objective characterization of the TID phenomenon as evaluated by the HF-TID technique. It has a clear physical meaning and well-defined minimum and maximum values. A_N is defined formally under assumption of a simple TID model in which, for any particular fixed altitude z_0 in the ionosphere, TID is a sinusoidal perturbation of the ambient electron density. For an easier interpretation, $A_N(z_0)$ is given in %, thus ranging from 0 to 100%. The HF-TID version presented here defines five levels of LSTID activity in relation to the detected amplitude; Insignificant activity for events with AMP < 5%, weak for events with 5% $\leq$ AMP < 10%, moderate for events with 10% $\leq$ AMP < 15%, strong for events with 15% $\leq$ AMP < 20%, and very strong activity for events with AMP $\geq$ 20%.

The performance of the method has been demonstrated with oblique D2D "skymap" observations from European Digisondes (Reinisch et al., 2018). The method can detect

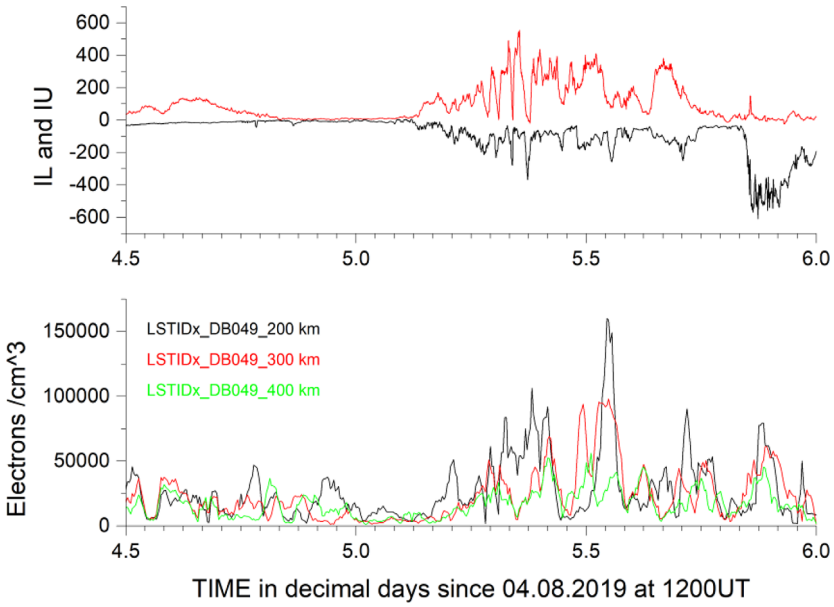

Fig. 5. Bottom panel: The LSTIDx calculated with the TaD model for three heights at 200 km, 300 km and 400 km, during the moderate geomagnetic storm on 5 August 2019. The TaD model results are calculated using data from Dourbes Digisonde (DB049). Top panel: The auroral electrojet indices IU and IL provided by the IMAGE magnetometer network in Finland.

electron density perturbations from 5% to 20% of the ambient electron density making possible the identification of both LSTIDs and MSTIDs. The method is implemented in real time in TechTIDE and provides the signatures of TID activity detected by any active pair of Digisondes performing D2D measurements in bistatic link mode. For the 5 August 2019 storm, only the link between the Ebro (EB040, Rx) and Dourbes (DB049, Tx) Digisondes was operated systematically. Figure 3 presents the map at 16:07 UT with the TID propagation direction and the visualization of the amplitude, Doppler, zenith, and azimuth of the detected TID.

The **HF-Interferometry (HF-INT) method** identifies LSTIDs for the monostatic measurements of a given network of HF sensors (i.e. ionosondes). The spatial distribution of the network should be dense enough to detect LSTID i.e., distance between measuring sites no larger than 1000 km. The method detects quasi-periodic oscillations of ionospheric characteristics, identifies coherent oscillation activity at different measuring sites of the network and sets bounds on time intervals for which such activity occurs in a given region. The disturbance potentially associated to TID in the last 6-h interval can be related to the de-trended ionospheric characteristics after removing the main daily harmonics. The dominant period of oscillation and amplitude of the LSTID are obtained by spectral analysis. This allows for identification of TID activity from Digisonde networks. The vector velocity of propagation is estimated by the measured time delays of the disturbance of a given ionospheric characteristic at different sensor sites and assuming a plane wave propagation. Classification of the TID activity for the HF-INT method is related to the *spectral energy contribution* (SEC) of the detected TID. Altadill et al. (2019, 2020a) have shown that the SEC of a given LSTID to the total spectral energy is equivalent to the contribution of the LSTIDs to the total variability for a given time series. Thus, the larger the SEC of a LSTID, the larger the impact of the LSTID to the variability. Altadill et al. (2020b) have performed a statistical analysis for all events detected during 2018 in the European region. As a result, they have defined different levels of activity from the distribution of the cumulative number of events for a given SEC or lower (Fig. 4 in Altadill et al., 2020b). The first decile of the distribution defines the threshold between Insignificant and Weak activity. The second quartile of the distribution defines the threshold between weak and moderate. The third quartile defines the threshold between moderate and strong, and the ninth decile defines the threshold between strong and very strong activity. Thus, we define Insignificant activity for events with SEC < 18%, weak for events with 18% $\leq$ SEC < 65%, moderate for events with 65% $\leq$ SEC < 80%, strong for events with 80% $\leq$ SEC < 86%, and very strong activity for events with SEC $\geq$ 86.

In TechTIDE, the method is implemented in real time based on typical ionospheric characteristics measured with Digisondes in the European and South African Digisonde Networks (Altadill et al., 2020a). Representative products released by TechTIDE for the disturbed day 5 August 2019, based on the HF INT method are shown in Figure 4. LSTID activity is detected after 12:00 UT in the lower panel with the method's characteristics variation over Dourbes Digisonde during that day. The European map which corresponds to 12:45 UT shows coherent activity at all locations providing data at that specific time.

The **TID-induced perturbations in electron density predicted with the TaD model**. The Topside Sounder Model (TSM)-assisted Digisonde (TaD) profiler provides vertical electron density profiles (EDP) above Digisonde sounding stations operating in Europe, from the bottom of the ionosphere up to the GNSS orbit altitude (Kutiev et al., 2016). This model is based on the Topside Sounder Model (TSM) proposed by Kutiev et al. (2006). The TSM model provides with empirical

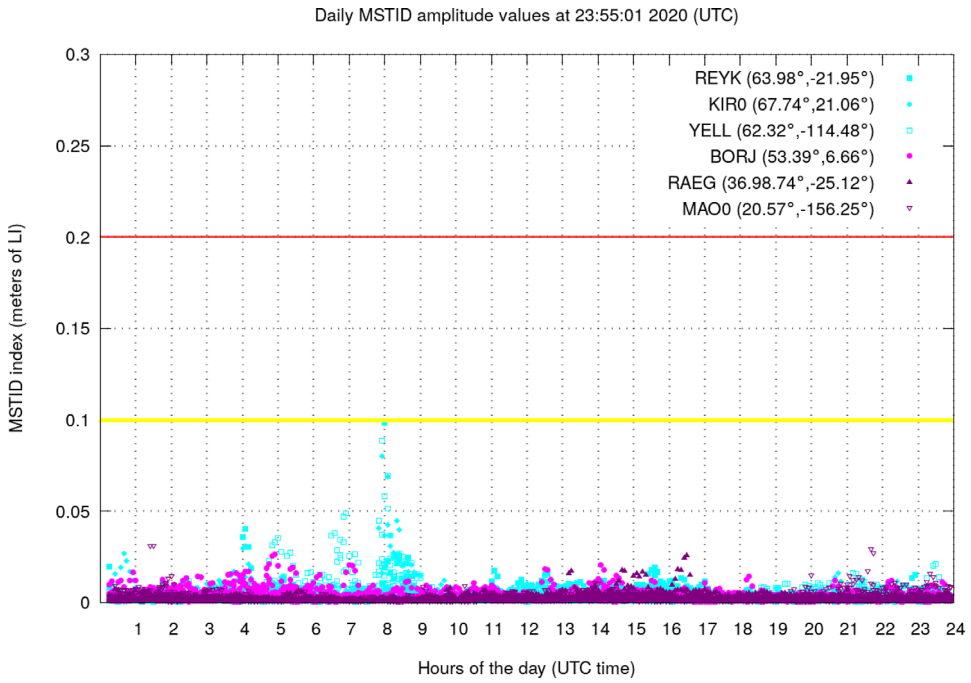

Fig. 6. The daily plot for the MSTID index for 20 January 2020, with the results from six GNSS receivers at high, middle and low latitudes, as indicated in the color coded legend.

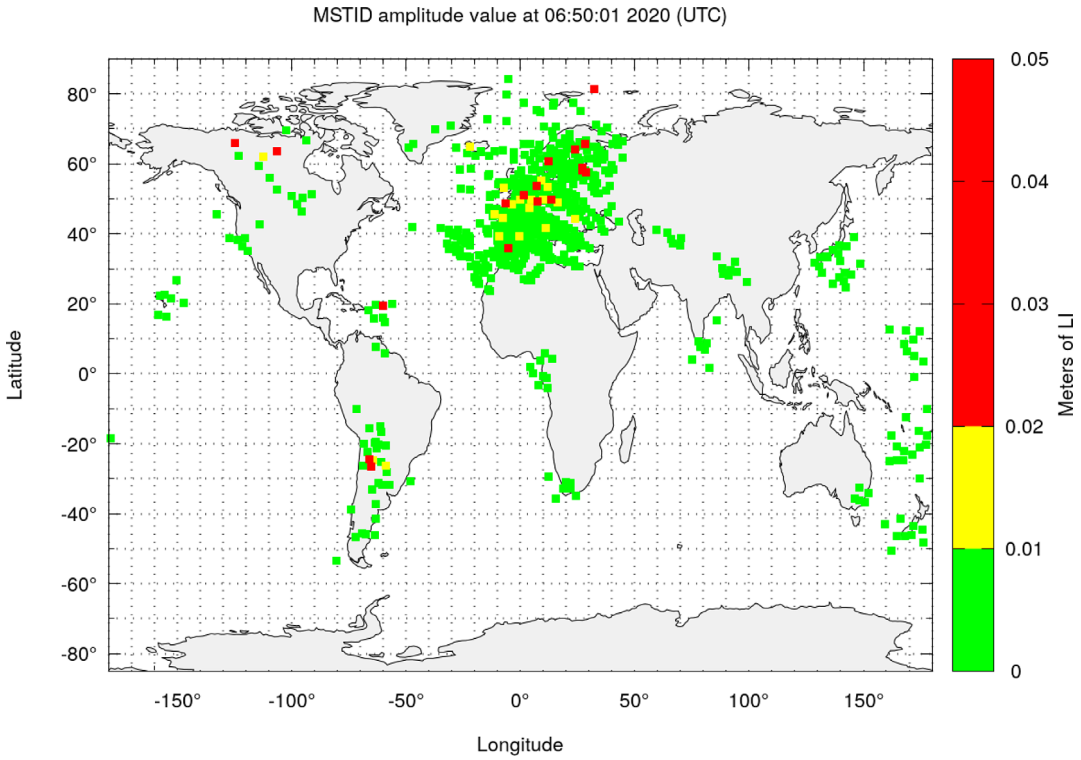

Fig. 7. The global map of the MSTID activity index at 06:40 UT on 20 January 2020.

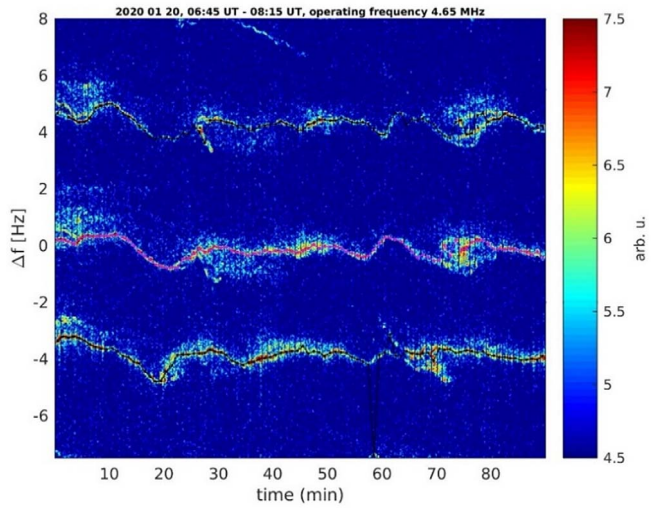

Fig. 8. The CDSS system which is located in Czech Republic detected significant activity on 20 January 2020 in the morning sector simultaneously with the intensification of MSTID index in Europe shown in Figure 6.

equations the scale height and transition height in the topside ionosphere from the Alouette/ISIS topside sounders data. The results are updated for the actual ionospheric and geospace conditions with the ionospheric characteristics at hmF2 (the critical frequency foF2, the true height hmF2 and scale height Hm of the F2 layer) obtained from an ionospheric sounder and with the TEC parameter at the location of the ionospheric sounder.

The electron density predicted by the model at various heights is detrended with 1-h running averages. At each different height, the LSTID index (LSTIDx) is derived as the absolute values of the residuals of the current detrended values from the 30-days running median detrended values. For this methodology to be effective, the time resolution of the source vertical sounding ionospheric parameters must be at least 5 min. Some representative LSTIDx results are shown in Figure 5 for three heights at 200 km, 300 km and 400 km, during the moderate geomagnetic storm of 5 August 2019. The results are calculated using Digisonde data from the Dourbes ionospheric station. The auroral electrojet indicators IU and IL provided by the IMAGE magnetometer network in Finland are presented in the top panel of Figure 5, to give a measure of the auroral activity in the European longitude sector. The strongest values of the LSTIDx are detected at 200 km. LSTIDx decreases quickly towards higher altitudes. At 400 km the perturbation marginally exceeds the background levels. These results are in agreement with earlier studies reporting that TID amplitudes maximize near or below the background electron density maximum hmF2 (e.g., Morgan & Ballard, 1978).

In the current version of the TechTIDE warning system the LSTIDx is computed with autoscaled data. The autoscaled data include very often outliers and gaps. The large number of outliers produces noise in any statistical analysis attempted to define activity levels. Unless an intelligent method is applied to overcome this issue, the LSTIDx must be evaluated in correlation with a relevant driver, which for the middle European latitudes, is the IL and IU indicator from the IMAGE magnetometer network, as shown in the case presented in Figure 5.

3.3 Medium scale TID detection methodologies

The detection of MSTIDs is based on data collected from ground-based GNSS receivers and from Continuous Doppler Sounding Systems.

The **Spatial and Temporal GNSS analysis** procedure detects and characterises TIDs, including velocity and period, based on GNSS measurements (Hernández-Pajares et al., 2006). This procedure allows the study of any ionospheric perturbation and can be used for detecting a TID (with a single receiver) and estimating the propagation parameters (from a network of receivers). The basic GNSS measurement used is the geometry-free combination of carrier phases, with measurement noise at the level of few millimetres. The first step for the TID detection is to detrend the data in order to remove the well-known dependences, such as diurnal and elevation angle variations, which have larger time scales than the TID. This detrending can be applied in realtime and for a single receiver to calculate the MSTID index ($MSTID_{idx}$) for each transmitter–receiver pair or for a RTK network. Therefore, information about the TID occurrence can be obtained for the monitored region around the receiver. In the case of small networks, as it is shown in Hernández-Pajares et al. (2006), it is possible to estimate the MSTIDs propagation parameters (velocity and direction) from the differential effects experienced by different receivers on the network.

Users with a single frequency receiver can achieve confidence on their positioning solution by using just observations with $MSTID_{idx} < 0.01$ LI meters (LI is the geometry free combination of carrier phases, i.e. LI = L1–L2). $MSTID_{idx}$ is a representative index for ionospheric perturbations with time scales from some minutes to tens of minutes, which are the typical periods of MSTIDs. According to its definition, $MSTID_{idx}$ varies largely depending on the receiver location. To specify this effect, a statistical study was performed with $MSTID_{idx}$ results for the years 2018 and 2019, for a receiver at high latitude (KIRU) and a receiver at mid latitude (EBRE), using the complementary of the cumulative distribution function (1-CDF), i.e. the probability of being the $MSTID_{idx}$ larger than a specific value. The results indicate that the activity at high latitude is much more pronounced than at mid latitude, with the high-latitude $MSTID_{idx}$ larger than 0.01 LI meters in around 10% of the cases. On the other hand, ionospheric activity at these time scales is, in general, very low at mid latitude. However, the N-RTK service, with single frequency receivers, requires high accuracy in the ionospheric corrections, thus it can be affected by perturbations with only some tenths of a TECU of amplitude. In this sense, observations with $MSTID_{idx} > 0.01$ LI meters (i.e. around 0.1 TECUs) cause a non-negligible positioning error.

An example of the $MSTID_{idx}$ as presented in the TechTIDE warning system is shown in Figure 6. Here, the daily plot for 20 January 2020 is presented, with the results from six GNSS receivers at high, middle and low latitudes, as indicated in the color

coded legend. Figure 7 shows the global map the same day at 06:40 UT.

The **CDSS-MSTID detection method** is based on the analysis of multipoint CDSS operating at three frequencies (f = 3.59, 4.65, and 7.04 MHz) in the Czech Republic, at 3.59 MHz in South Africa, at 4.63 MHz in Northern Argentina and at 4.66 MHz in Taiwan. There are at least three sounding paths (transmitter – receiver pairs) at each frequency at each location. The CDSS method is suitable for the monitoring of MSTIDs but not of LSTIDs. There are two reasons. First, the triangle of measuring points has a horizontal expansion of the order of 100 km, which is suitable for the monitoring of MSTIDs. Second, temporal changes at LSTIDs are slower, i.e. CDSS is less sensitive to them.

The basic principles of the Doppler sounding and phenomena that can be analysed were reviewed by Lastovicka & Chum (2017). For the automatic detection and analysis of MSTIDs in real-time only CDSS operating at 4.65 MHz in the Czech Republic is used.

The recorded data are automatically processed in several steps. The complete computation is repeated every 15 min. First, Doppler shift spectrograms are computed for the last 90-min record (e.g., Fig. 8). Then maxima of spectral intensities are searched in three frequency bands that correspond to the frequency bands of signals from the individual transmitter to receiver pairs. The frequencies f_{Di} corresponding to the maxima of spectral intensities for each transmitter–receiver pair are stored together with powers p_{pi} calculated in the narrow frequency band around these maxima (bandwidth on the order of ~0.1 Hz). In addition, powers p_{Ti} in the whole frequency bands in which the maxima are searched are evaluated (frequency band of about 4 Hz). In addition to the values of f_{Di} and p_{pi} the power ratios $r_i = p_{pi}/p_{Ti}$ are also stored to a file with 1-min step (the stored values are 1 min averages). High values of r_i approaching 1 indicate clear signals suitable for further analysis, whereas low values of r_i indicate signals with insignificant spectral maxima that occur e.g. under spread F conditions. Such signals are inconvenient for further analysis.

In the next step, the stored values of f_{Di}, p_{pi} and r_i are analyzed. First, the offsets are removed to obtain $f_{DCi} = f_{Di} - \langle f_{Di} \rangle$ where $\langle f_{Di} \rangle$ is the mean value calculated over the 90-min intervals. Next the validity of criterion (1) is tested,

$$\left(p_{pi} > \mathrm{Th}_1\right) \quad \text{and} \quad \left(r_i \geq \mathrm{Th}_2\right). \tag{1}$$

The requirement ($p_{pi} > \mathrm{Th}_1$) ensures that sufficient signal power was received (Th_1 is an experimentally found threshold). Insufficient power is received, e.g., if the critical frequency is lower than sounding frequency f = 4.65 MHz and the signals do not reflect from the ionosphere. The second requirement ($r_i > \mathrm{Th}_2$; $\mathrm{Th}_2 \sim 0.5$) ensures that the spectral maxima are significant (e.g., no spread F occurred). TIDs are only analyzed if condition (1) is fulfilled for more than 80% of data points in the last 90 min. The observed horizontal velocity and azimuth of propagation are then computed from the observed time (phase) delays between signals recorded for different sounding paths (transmitter–receiver pairs) using three different calculation methods described by Chum & Podolská (2018): (i) slowness search; (ii) least squares fitting to the time delays obtained from cross-correlation of the f_{DCi} series; (iii) weighted least squares fitting to the time delays obtained from cross-correlation of the f_{DCi} series; the weights are the maxima of the cross-correlation functions. The values of v_H and azimuth AZ that are finally reported are the mean values of v_H and AZ quantities obtained by the three different methods; their uncertainties are estimated as corresponding standard deviations. Specifically, 2-D versions of the described methods are used. In addition, root mean square (RMS) value of Doppler shift and dominant periods are evaluated. It should also be noted that the f_{DCi} series are first filtered to keep only signals with periods from 4 to 50 min. The aim is to remove a possible high frequency noise and to remove long-period fluctuations (large-scale TIDs) that cannot be reliably analyzed with respect to 90-min intervals and with respect to the relatively small spatial scale (tens of km) of the measuring array defined by the reflection points.

Figure 8 shows the Doppler shift spectrogram recorded in Czech Republic on 20 January 2020 from 06:45 UT to 08:15 UT at the operating frequency 4.65 MHz. Figure 8 also demonstrates an example of a relatively complex Doppler shift spectrogram with ambiguous spectral peaks during several subintervals (e.g., around 75 min elapsed time) and an outlier in the automatic determination of a spectral peak in the bottom trace (around 60 min elapsed time). The results of automatic MSTID propagation analysis for the time interval in Figure 8 are as follows: observed horizontal velocity $v_{\mathrm{obs}} \sim 230$ m/s, azimuth AZ ~ 200°; the results after manual corrections are: $v_{\mathrm{obs}} \sim 190$ m/s, AZ ~ 135°. The RMS value of Doppler shift is about 0.25 Hz. Within the same period, the MSTID shows an intensification in the stations located in central Europe as seen in the map presented in Figure 7. The auroral electrojets during that day were extremely weak, as documented by the AE indices (not shown here), and this is an indication that the disturbances seen with the two methods do not have a magnetospheric origin and must be related to other drivers, which probably are disturbances in the lower atmosphere. Moreover, the propagation analysis of MSTIDs by CDSS often shows roughly poleward propagation, especially during the summer season (Lastovicka & Chum, 2017; Chum & Podolská, 2018, and references therein).

The characterization of the TID activity scales based on the CDSS Doppler shift is under continuous development as new results are accumulated in the TechTIDE database.

3.4 Specification of ionospheric background conditions

Ionospheric background conditions provide the first indication to the user about the overall disturbances in the ionosphere over a region of interest and about the probability for TID detection given that for TIDs produced by gravity waves, the amplitude of the TID perturbation is directly proportional to the background electron density (Hooke, 1968). Ionospheric background conditions are defined by the normal ionospheric variability and by large scale ionospheric storm effects. The key characteristic among the ionospheric conditions is the electron density. To obtain the electron density distribution in the bottomside and topside ionosphere over an extended region such as Europe, we apply the 3D version of the TaD model. The 3D

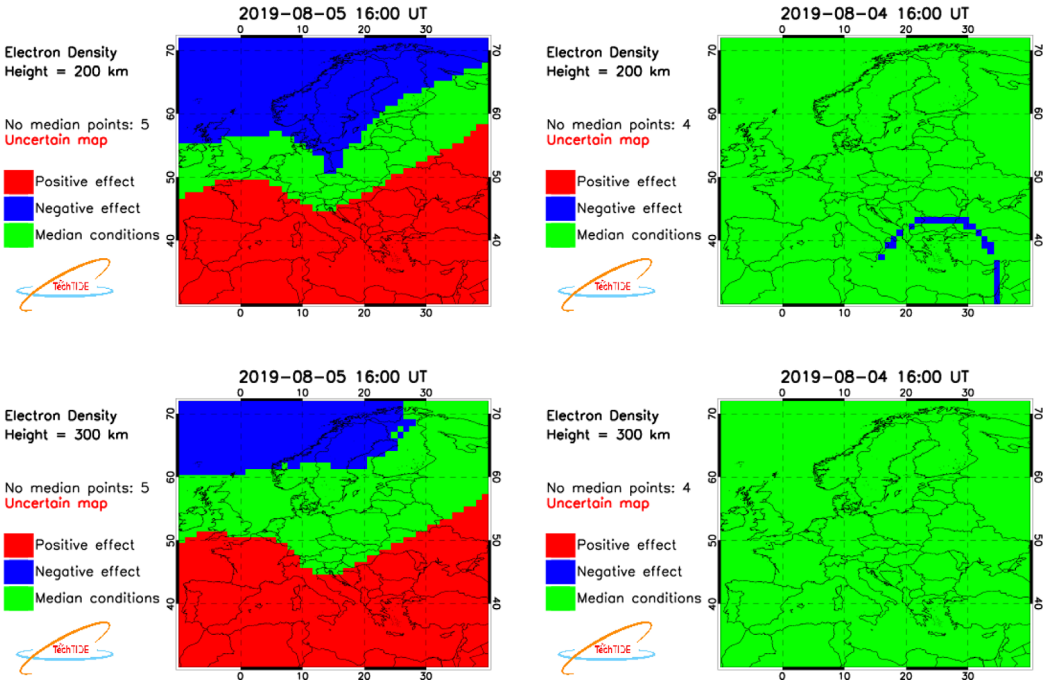

Fig. 9. Ionospheric background activity maps calculated during the main phase of a moderate storm (left) and during a quiet day (right), using the relative standard deviation of the electron density at each ionospheric altitude, taken into account for the estimation of the median values. Here the maps at 200 km (top row) and at 300 km (bottom row) are presented.

mapping technique is described in Kutiev et al. (2016). The TaD profiler first computes electron density profiles (EDP) over the European Digisonde locations. For the implementation of the method in TechTIDE, ionospheric data of foF2 and hmF2 are used from the European Digisondes of Athens, Rome, Ebro, Dourbes, Pruhonice, Juliusruh and Chilton. Using the Poly-weight interpolation method the 2D maps of the basic ionospheric plasma parameters at the height of maximum electron density concentration, are derived. The TaD profiler calculates EDPs at each node and adjusts them to the GNSS-TEC values extracted from the GNSS TEC maps (Belehaki et al., 2012; Kutiev et al., 2012). Electron density at any arbitrary point within the 3D space is calculated by a linear interpolation from their respective values at the neighbouring grid nodes. The electron density distribution (EDD) between any two points in the space is then obtained by calculating successive ED values with a defined step along the ray path. The model error based on the comparison of 3D EDD model values with vertical TEC (vTEC) and slant TEC (STEC), calculated from individual GNSS receivers, is 10% for STEC and 6% for vTEC (Kutiev et al., 2016). Belehaki et al. (2017) showed the sensitivity of the TaD EDD to disturbances in the electron density due to LSTIDs and the model capability to detect the altitude of the maximum perturbation.

In TechTIDE, the 3D electron-density maps Ne(i, j, k) (where i denotes the latitude, j the longitude and k the height) produced by the TaD model are used for the derivation of the near-real time ionospheric condition maps in Europe for the heights of 200, 300, 400, and 500 km. The respective median MED(i, j, k) and the standard deviation STD(i, j, k) maps are produced using the electron density maps corresponding to the same UT over the previous 30 days and two quantities a, b are derived as follows:

$$a(i,j,k) = 100 \times \frac{[\mathrm{Ne}(i,j,k) - \mathrm{MED}(i,j,k)]}{\mathrm{MED}(i,j,k)}$$

$$b(i,j,k) = 100 \times \frac{\mathrm{STD}(i,j,k)}{\mathrm{MED}(i,j,k)}.$$

In practice, the STD map reflects the standard deviations of the values taken into account in the calculation of the corresponding medians at each point of the grid. In this respect, b that represents the relative STD (%) aims to delimit the normal ionospheric variability (Tsagouri et al., 2018b, 2018c). Ionospheric effects at each pixel of the map (i, j, k) are characterised as "median" when $|a| \leq |b|$, as "positive" when $|a| > |b|$ and $a > 0$ and as "negative" when $|a| > |b|$ and $a < 0$. A map is considered as "uncertain" if less than 17 maps are used for the derivation of the median and standard deviation maps. When a specific effect characterizes more than 80% of the ionospheric effect map then this effect is considered as dominating, otherwise if the sum of pixels with positive and negative effects exceeds the number of pixels with median effects, conditions tend to be disturbed while conditions tend to be median in the reverse case. Note that the area covered by Digisonde observations is delimited in latitude and longitude by the four stations at its edges, Chilton, Ebro, Athens, and Juliusruh. This area includes the 80% of the mapped region. That is why the 80% percentage is critical to characterize conditions over Europe.

Table 1. TechTIDE detection methodologies for TIDs.

Detection method and main characteristics	Products
Methods specific to the detection of LSTIDs	
HF-TID *Input*: Signal properties from Digisonde synchronized operation. *Output*: TID velocity, amplitude, propagation direction at the signal reflection point between the stations. The method is fully described in the paper by Reinisch et al. (2018).	1. European map indicating the velocity, amplitude and propagation direction at the reflection points between Digisondes operated in bistatic mode. 2. Report of TID characteristics extracted from the analysis of the raw data from the D2D operations, i.e TID propagation Doppler frequency, angle of arrival, and time-of-flight from Tx to Rx, both OI and VI sounding. 3. Plots of amplitude, Doppler, azimuth within the last 45 min from the TID detection.
HF interferometry *Input*: Ionospheric characteristics from VI and OI soundings. *Output*: 2D TID vector velocity, amplitude, period and spectral energy contribution. The method is described in the paper by Altadill et al. (2020a) while the calculation of the corresponding activity levels is given in the TechTIDE project report by Altadill et al. (2020b).	Dominant period, amplitude and horizontal vector velocity of detected LSTID over the region of interest and over each Digisonde location.
1D version of TaD-EDD model – LSTID index *Input*: Ionospheric characteristics at the hmF2 altitude and TEC maps. *Output*: Analytical function of the electron density distribution with altitude from 90 km to 22,000 km. The method is first proposed by Belehaki et al. (2017).	LSTID index: The residuals of the detrended electron density from the median values, calculated with the TaD model for heights ranging from 150 up to 900 km with 50 km step. The results are provided over specific European Digisondes performing VI sounding at least every 5 min.
Methods specific to the detection of MSTIDs	
CDSS-MSTID *Input*: CDSS reflected signals, ionospheric characteristics and irregularities. *Output*: Doppler shift, Doppler shift. Fluctuations associated to the TIDs and estimation of the propagation parameters (direction, velocity, and amplitude). The method is fully described in the paper by Chum & Podolská (2018).	Period, amplitude of Doppler measurements, observed horizontal velocities and azimuths of MSTIDs.
Spatial & temporal GNSS analysis *Input*: GNSS TEC from single receivers over a region. *Output*: Fluctuations associated to the TIDs and estimation of the propagation parameters (direction, velocity, and amplitude). The method is first proposed by Hernández-Pajares et al. (2006).	MSTID index calculated at each GNSS contributing receiver.
Indicators	
GNSS TEC gradient *Input*: Grids of TEC maps over a region. *Output*: Latitude-time maps of TEC gradients and indication of significant gradients. The method is described in the paper by Borries et al. (2017).	Maps of TEC gradients for the European region
AATR indicator *Input*: Slant TEC parameters. *Output*: The along Arc STEC Rate, metric to characterize the ionosphere operational conditions of EGNOS. The method is described in the paper by Juan et al. (2018).	Along Arc TEC Rate (AATR) calculated at each contributing GNSS receiver.
Ionospheric background conditions *Input*: Ionogram derived characteristics in the F2 layer from ionosondes; GNSS TEC at the ionosonde location; geomagnetic, and solar flux indices. *Output*: Maps of the electron density at any height in the bottomside and topside ionosphere. The methodologies that define ionospheric background conditions are described in the TechTIDE project report by Tsagouri et al. (2018a).	Maps of relative standard deviation of the electron density at each ionospheric altitude with an indication of the probability for LSTIDs detection.

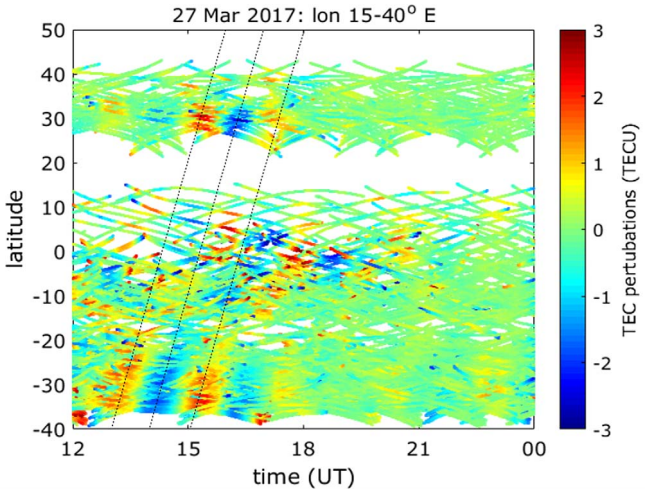

Fig. 10. Northward propagating LSTID (dotted lines) starting in the southern hemisphere, crossing the equator and propagating into the northern hemisphere. Shown is the difference between observed TEC and an unperturbed TEC background. Latitude is geographic. The geomagnetic equator is located about 10° north of the geographic equator. Figure kindly provided by Zama Katamzi-Joseph, South African National Space Agency.

Table 2. Interhemispheric characteristics of LSTID observed during geomagnetic storms. The total number of events analysed is 26. The first three-row group shows the distribution according to the LSTID geographic origin, the second according to interhemispheric appearance. Each group sums up to 26.

LSTID observed during geomagnetic storm periods	26
LSTID of high latitude origin propagating equatorward	14
LSTID of equatorial origin propagating poleward	3
LSTID of both high latitude and equatorial origin	9
LSTID observed in both hemispheres without interhemispheric circulation	16
LSTID with observed interhemispheric circulation	4
No conclusive results due to insufficient data in one hemisphere	6

The time resolution of the maps is 15 min which is required to monitor the evolution of large-scale disturbances. An example is shown in Figure 9 for a disturbed day (left) and for the day before which is a quiet day (right). The disturbed day is the 5th August 2019 and at the selected timestamp 16:00 UT the main phase of the geomagnetic storm is ongoing. These maps indicate conditions favorable for TID identification since the sum of pixels with positive and negative effects exceeds the number of pixels with median effects. The maps for the day before, show clearly that quiet conditions dominate in the selected ionospheric heights.

4 Discussion

TIDs are propagating waves altering an a priori variable ambient ionospheric electron density distribution. The TechTIDE project provides for the first time a real-time identification and tracking system for TIDs. The TechTIDE warning system provides the results of complementary TID detection methodologies and many potential drivers to help the users assess the risks and develop mitigation strategies tailored to their applications.

The TID detection methodologies deployed in the TechTIDE project rely on data retrieved from ionosonde and GNSS observations. Both types of observations have advantages and disadvantages with respect to TID detection capabilities. The known disadvantage of the TEC measurements is the integration of the electron density over the entire satellite-ground signal path. Considering that the most significant contribution to the TEC value comes from the topside ionosphere (e.g., Belehaki & Tsagouri, 2002), there are concerns about the sensitivity of the GNSS TEC measurements to the smaller scale ionospheric disturbances which may not affect the entire volume of the ionosphere. Data obtained from HF sounding can have higher sensitivity to smaller scale disturbances since the HF waves are reflected in the lower part of the ionosphere at the heights where the local plasma gyrofrequency is equal to the sounding frequency. On the other hand, certain gaps exist in the data which are associated with small signal-to-noise ratios and signal degradation through electromagnetic interference and sporadic E layers. They are most frequent at middle latitudes where TIDs also occur. The opportunity and challenge for the TechTIDE research community is to demonstrate that combined analysis of results from different TID detection methodologies based either on HF soundings or GNSS TEC data or on both can lead to improvements in the calculation of TID characteristics confidence levels, for both medium and large scale TIDs, under various different geophysical conditions. The ultimate goal is to effectively support the requirements of the users. TechTIDE has set the frame and the work progresses as more results are stored in the system archive.

The TechTIDE methodologies are able to detect in realtime activity caused by both large-scale and medium-scale TIDs and characterize background conditions and external drivers, as an additional information required by the users to assess in real time the criticality of the ongoing disturbances. These methodologies are based on the exploitation of data collected in real time from Digisondes, GNSS receivers and CDSS networks. The results of the data analysis are obtained and distributed in real time. The calculated TID characteristics and the products available and distributed by the TechTIDE warning system are summarized in Table 1.

Further improvements are expected from the simultaneous application of the TID detection methodologies in Europe and South Africa and collection of simultaneous results for TID activity, to better estimate the probability for TID interhemispheric circulation and its effects. Case studies of past events performed within the TechTIDE project (Watermann, 2020) indicate that during geomagnetic storms, even if of moderate magnitude, one may expect with rather high likeliness TIDs to be launched at auroral latitudes in both hemispheres which propagate equatorward. If LSTIDs are launched in one hemisphere during the main or early recovery phases of a geomagnetic storm it is almost certain that LSTIDs are simultaneously launched in the other hemisphere. Interhemispheric circulation of TIDs (i.e. propagation across the equator from one hemisphere into the other) was also observed in a few cases,

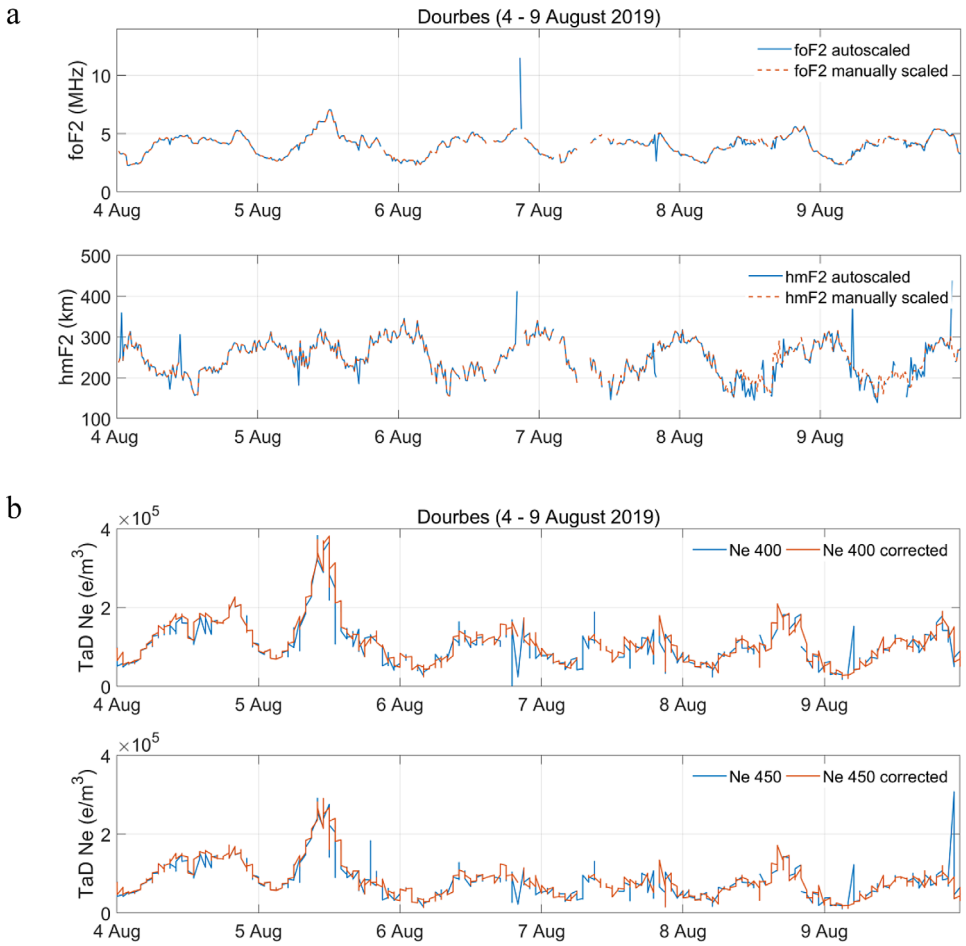

Fig. 11. (a) The autoscaled values of the foF2 and hmF2 ionospheric characteristics (blue line) obtained over Dourbes in comparison to manually scaled ones (red dashed line) for the time interval 4–9 August 2019. (b) Results of the TaD algorithm in the topside ionosphere (400 and 450 km) with autoscaled (blue line) and manually scaled (red line) foF2 and hmF2 values as input.

but such events constituted a minority. Balthazor & Moffett (1997) employed the CTIP (Coupled Thermosphere–Ionosphere–Plasmasphere) model (Millward et al., 1996) to simulate propagation of TIDs on a global scale. According to their numerical results all TID modes interfere constructively at the magnetic equator and continue their propagation into the opposite hemisphere. However, only few actual observations of AGW or TID crossing the equator and subsequently propagating into the other hemisphere were reported in the literature (Ding et al., 2008; Bowman & Mortimer, 2011; Guo et al., 2014, 2015; Pradipta et al., 2016).

We investigated 26 event periods lasting between 4 h and 15 h each, the majority of which took place during geomagnetic storms. The analysis revealed that during the main and early recovery phases of strong storms with Dst < −90 nT LSTID are almost always launched in both hemispheres. But very few of them were observed to cross the geomagnetic equator and continue their way into the opposite hemisphere. An example is shown in Figure 10.

The data coverage is, unfortunately, poor in the vicinity of the geomagnetic equator and up to 25° geographic north. This latitude band corresponds to Central and sub-Sahara Africa and suffers from the low density of reliable and accessible research quality GNSS receivers. Table 2 shows the results in a quantitative manner. Observations, method and results are described in more detail in the TechTIDE report D3.4 an updated version of which is publicly available (Watermann, 2020).

Additional enhancements are expected with the integration of results from supplementary methods to further support specification of TID activity with better confidence. In this framework, the height-time-reflection intensity (HTI) method is considered, first proposed by Haldoupis et al. (2006). The application of this method in the frames of the project will enable the identification and tracking of the TID activity over each Digisonde station by using the actual ionograms produced over each station. This technique considers an ionogram a "snapshot" of intensity and height as a function of Digisonde frequency, and uses a sequence of ionograms to compute an average HTI plot, (for a given frequency bin) that is essentially a 3-D plot of reflected signal-to-noise ratio as a function of height within a given time interval.

Following the implementation of the TechTIDE methodologies, the key challenges for the development of a reliable real-time TID warning system are: (a) the quality of ingested data, and (b) a better specification of the activity levels in correlation with performance degradation data from operations systems concerned.

(a) The quality of the data ingested into TechTIDE algorithms strongly affects the accuracy and reliability of the results. Note that the results shall be driven by real-time input that in several cases suffers from occasional errors, as for instance data spikes or outliers. These errors may be attributed to measurement errors or raw data processing errors. As an indicative example of relevant cases one may consider the Digisonde-derived ionospheric characteristics that serve as input to some of the methodologies (e.g., LSTIDx and HF-INT). The real-time implementation of the algorithms is based on the exploitation of the automatically scaled ionograms. Although previous studies of the quality of specific autoscaling algorithms suggest their excellent overall compatibility with the manual scaling at selected ionosonde stations (Galkin et al., 2008), the autoscaled values may still occasionally be dramatically wrong, thus contributing errors to the algorithms' output. Figure 11a presents the autoscaled values of the foF2 and hmF2 ionospheric characteristics obtained over Dourbes in comparison to manually scaled ones for the time interval 4–9 August 2019 to indicate the occurrence of data outliers in the autoscaled characteristics. The respective effect of the data errors in TaD's performance that is related to LSTIDx performance is investigated in Figure 11b. It is clear, that data quality control should be anticipated in any future upgrade of the TechTIDE warning services to ensure reliability of the results in all possible cases. Since any operational implementation cannot rely on manually scaled data, the development of data filtering algorithms may be envisaged, which apart from data outliers, will partially address data gaps issues.

(b) The next big challenge in future developments is the scaling of TID activity and characterization of the criticality of the induced disturbances in the systems concerned. Significant progress has been made in TechTIDE, especially for the correlation of the AATR and $MSTID_{idx}$ indices with performance degradation data from the EGNOS and N-RTK system respectively (Juan et al., 2019). Indicatively, a preliminary AATR analysis has shown inverse correlation between the AATR values and the EGNOS availability. This correlation was also observed between AATR and the horizontal protection level (HPL) and vertical protection level (VPL) values as an increase of the AATR values leads to an increase of the protection levels (xPL). However, the AATR tends to present different distributions for different locations, so for the use of AATR as an indicator of ionospheric activity, different AATR values should be defined at different latitudinal zones. Moreover, the results show that the presence of MSTIDs degrades the user positioning in both RTK and NRTK services. This degradation is not only related to the effect of the TID on the user measurements but in the measurements of any of the reference receivers. The analysis has shown that it is possible to implement the MSTID index as a tool to mitigate positioning degradation (Juan et al., 2019). It has been clearly demonstrated that TIDs can have multiple effects in the operation of aerospatial and ground-based infrastructures and especially in EGNOS and N-RTK services, in high frequency (HF) communications, in radio reconnaissance operations and in very high frequency – ultra high frequency (VHF–UHF) radiowave propagation. The real-time identification of perturbations induced in the ionospheric characteristics is a strong requirement from all operation sectors concerned.

Promising developments could also be envisaged through the exploitation of TechTIDE detection algorithms to develop new methodologies able to provide a probability of TID occurrence well in advance. This task should include also the analysis of TID drivers that are physical mechanisms corresponding to solar X rays, solar protons, solar wind, interplanetary magnetic field structures at L1, high-latitude ionospheric electric fields, auroral electron precipitation, the ring current the magnetospheric electron fluxes and the ionospheric convection pattern. Furthermore, the TechTIDE results also indicate that CMEs, as well as CIR/CH HSS are very efficient sources of TIDs. Although further research is needed on using empirical methods (e.g. time delay in ionospheric response, season and latitudinal dependence, interhemispheric circulation) and gather more data for statistical analysis (e.g., amplitudes and periods vs. solar wind speed, duration of TID activity), it may be expected that ionospheric models which depend on solar wind and magnetospheric conditions, such as the SWIF model (Tsagouri et al., 2009), can be considered to provide short-term forecasted conditions for the next 24 h including TID occurrence.

Finally, we note that the source code of all TID detection methods is available for downloading from the TechTIDE repository (at http://tech-tide.eu) under the Creative Commons Attribution License.

Acknowledgements. The TechTIDE project has received funding from the European Union's Horizon 2020 research and innovation programme under grant agreement no. 776011. AB acknowledges financial support provided by the AFRL grant award FA9550-19-1-7019. IT and KT acknowledge support of this work by the project "PROTEAS II" (MIS 5002515), which is implemented under the Action "Reinforcement of the Research and Innovation Infrastructure", funded by the Operational Programme "Competitiveness, Entrepreneurship and Innovation" (NSRF 2014–2020) and co-financed by Greece and the European Union (European Regional Development Fund). The IL and IU indicators are retrieved from the IMAGE web site of FMI. JW owes special thanks to Zama Katamzi-Joseph, South African Space Agency SANSA, for processing a substantial amount of GNSS data and producing DTEC maps to support the LSTID analysis which led to Table 2. The editor thanks Paulo Fagundes and an anonymous reviewer for their assistance in evaluating this paper.

References

Altadill D, Belehaki A, Blanch E, Borries C, Buresova D, Chum J, Galkin I, Haralambous H, Juan Zornoza JM, Kutiev I, Oikonomou C, Sanz Subirana J, Segarra A, Tsagouri I. 2019. *Report on the design and specifications of the TID algorithms and products*. https://doi.org/10.5281/zenodo.2590419.

Altadill D, Segarra A, Blanch E, Juan JM, Paznukhov VV, Buresova D, Galkin I, Reinisch BW, Belehaki A. 2020a. A method for real-time identification and tracking of traveling ionospheric disturbances using ionosonde data: First results. *J Space Weather Space Clim* **10**: 2. https://doi.org/10.1051/swsc/2019042.

Altadill D, Belehaki A, Blanch E, Buresova D, Tsagouri I, Juan Zornoza JM, Timoté C, Borries C, Galkin I, Haralambous H, Mielich J. 2020b. *Report on TID activity metrics*. https://doi.org/10.5281/zenodo.3837357

Azeem I, Yue J, Hoffmann L, Miller SD, Straka WC III, Crowley G. 2015. Multisensor profiling of a concentric gravity wave event propagating from the troposphere to the ionosphere. *Geophys Res Lett* **42**: 7874–7880. https://doi.org/10.1002/2015GL065903.

Balthazor RL, Moffett RJ. 1997. A study of atmospheric gravity waves and travelling ionospheric disturbances at equatorial latitudes. *Ann. Geophys* **15**: 1048–1056. https://doi.org/10.1007/s00585-997-1048-4.

Belehaki A, Kutiev I, Marinov P, Tsagouri I, Koutroumbas K, Elias P. 2017. Ionospheric electron density perturbations during the 7–10 March 2012 geomagnetic storm period. *Adv Space Res* **59(4)**: 1041–1056. https://doi.org/10.1016/j.asr.2016.11.031.

Belehaki A, Reinisch B, Galkin I, Altadill D, Buresova D, Francis M, Mielich J, Paznukhov V, Stankov S. 2015. Pilot network for identification of travelling ionospheric disturbances. In: *Proceedings of the 14th International Ionospheric Effects Symposium*, pp. 284–291. http://ies2015.bc.edu/wp-content/uploads/2015/08/IES2015-Proceedings.pdf.

Belehaki A, Tsagouri I. 2002. Investigation of the relative bottomside/topside contribution to the total electron content estimates. *Ann Geophys* **45(1)**: 73–86. https://doi.org/10.4401/ag-3498.

Belehaki A, Tsagouri I, Kutiev I, Marinov P, Fidanova S. 2012. Upgrades to the topside sounders model assisted by Digisonde (TaD) and its validation at the topside ionosphere. *J Space Weather Space Clim* **2**: A20. https://doi.org/10.1051/swsc/2012020.

Beley VS, Galushko VG, Yampolski YM. 1995. Traveling ionospheric disturbance diagnostics using HF signal trajectory parameter variations. *Radio Sci* **30(6)**: 1739–1752. https://doi.org/10.1029/95RS01992.

Borries C, Jakowski N, Kauristie K, Amm O, Mielich J, Kouba D. 2017. On the dynamics of large-scale travelling ionospheric disturbances over Europe on 20th November 2003. *J Geophys Res* **122**: 1199–1211. https://doi.org/10.1002/2016JA023050.

Bowman GG, Mortimer IK. 2011. Some aspects of large-scale travelling ionospheric disturbances which originate at conjugate locations in auroral zones, cross the equator and sometimes encircle the Earth. *Ann Geophys* **29**: 2203–2210. https://doi.org/10.5194/angeo-29-2203-2011.

Buresova D, Belehaki A, Tsagouri I, Watermann J, Galkin I, Altadill D, Blanch E, Chum J, Sindelarova T, Kouba D, Borries C, Habarulema JB, Katamzi Z, Haralambous H, Verhulst T, Mielich J. 2018. *Report on methodology for the specification of additional parameters*. https://doi.org/10.5281/zenodo.2555119.

Chum J, Podolská K. 2018. 3D analysis of GW propagation in the ionosphere. *Geophys Res Lett* **45**: 11562–11571. https://doi.org/10.1029/2018GL079695.

Ding F, Wam W, Liu L, Afraimovich EL, Voeykov SV, Perevalova NP. 2008. A statistical study of large-scale traveling ionospheric disturbances observed by GPS TEC during major magnetic storms over the years 2003–2005. *J Geophys Res* **113**: A00A01. https://doi.org/10.1029/2008JA013037.

Figueiredo CAOB, Wrasse CM, Takahashi H, Otsuka Y, Shiokawa K, Barros D. 2017. Large-scale traveling ionospheric disturbances observed by GPS dTEC maps over North and South America on Saint Patrick's Day storm in 2015. *J Geophys Res Space Phys* **122**: 4755–4763. https://doi.org/10.1002/2016JA023417.

Francis SH. 1975. Global propagation of atmospheric gravity waves: A review. *J Atmos Sol-Terr Phys* **37(6–7)**: 1011–1054. https://doi.org/10.1016/0021-9169(75)90012-4.

Galkin IA, Reinisch BW, Huang X, Paznukhov VV. 2008. Uncertainty and Confidence of Ionospheric Specifications with the Digisonde ARTIST-5 Ionogram Autoscaler. In: *Proc. IES-2008, Alexandria, VA, May 13–15, 2008*, pp. 450–457

Guo J, Forbes JM, Wei F, Feng X, Liu H, Wan W, Yang Z, Liu C, Emery BA, Deng Y. 2015. Observations of a large-scale gravity wave propagating over an extremely large horizontal distance in the thermosphere. *Geophys Res Lett* **42**: 6560–6565. https://doi.org/10.1002/2015GL065671.

Guo J, Liu H, Feng X, Wan W, Deng Y, Liu C. 2014. Constructive interference of large-scale gravity waves excited by interplanetary shock on 29 October 2003: CHAMP observation. *J Geophys Res* **119**: 6846–6851. https://doi.org/10.1002/2014JA020255.

Habarulema JB, Katamzi ZT, Yizengaw E. 2015. First observations of poleward large-scale traveling ionospheric disturbances over the African sector during geomagnetic storm conditions. *J Geophys Res* **120**: 6914–6929. https://doi.org/10.1002/2015JA021066.

Habarulema JB, Katamzi ZT, Yizengaw E, Yamazaki Y, Seemala G. 2016. Simultaneous stormtime equatorward and poleward large-scale TIDs on a global scale. *Geophys Res Lett* **43**: 6678–6686. https://doi.org/10.1002/2016GL069740.

Habarulema JB, Yizengaw E, Katamzi-Joseph ZT, Moldwin MB, Buchert S. 2018. Storm time global observations of large-scale TIDs from ground-based and in situ satellite measurements. *J Geophys Res* **123**: 711–724. https://doi.org/10.1002/2017JA024510.

Haldoupis C, Meek C, Christakis N, Pancheva D, Bourdillon A. 2006. Ionogram height–time–intensity observations of descending sporadic E layers at mid-latitude. *J Atmos Sol-Terr Phys* **68**: 539–557. https://doi.org/10.1016/j.jastp.2005.03.020.

Hernández-Pajares M, Juan JM, Sanz J. 2006. Medium scale traveling disturbances affecting GPS measurements: Spatial and temporal analysis. *JGR* **111**: A07–S11. https://doi.org/10.1029/2005JA011474.

Hocke K, Schlegel K. 1996. A review of atmospheric gravity waves and travelling ionospheric disturbances. *Ann Geophys* **14(917)**: 1996. https://doi.org/10.1007/s00585-996-0917-6.

Hooke WH. 1968. Ionospheric irregularities produced by internal atmospheric gravity waves. *J Atmos Sol-Terr Phys* **30**: 795–823. https://doi.org/10.1016/S0021-9169(68)80033-9.

Huang X, Reinisch BW, Sales GS, Paznukhov VV, Galkin IA. 2016. Comparing TID simulations using 3-D ray tracing and mirror reflection. *Radio Sci* **51**: 337–343. https://doi.org/10.1002/2015RS005872.

Hunsucker RD. 1982. Atmospheric gravity waves generated in the high-latitude ionoshpere: A review. *Rev Geophys Space Phys* **20 (2)**: 293–315. https://doi.org/10.1029/RG020i002p00293.

Jayachandran B, Balan N, Nampoothiri SP, Rao PB. 1987. HF Doppler observations of vertical plasma drifts in the evening F region at the equator. *J Geophys Res* **92(A10)**: 11253–11256. https://doi.org/10.1029/JA092iA10p11253.

Juan JM, Sanz J, González-Casado G, Timoté C, Tölle J, Magdaleno S, Rupiewicz J, Mielich J. 2019. Statistical analysis of the results: Assessment of the impact on aerospace and ground systems. https://doi.org/10.5281/zenodo.3453687.

Juan JM, Sanz J, Rovira-Garcia A, González-Casado G, Ibáñez D, Orus Perez R. 2018. AATR an ionospheric activity indicator specifically based on GNSS measurements. *J Space Weather Space Clim* **8(2018)**: A14. https://doi.org/10.1051/swsc/2017044.

Kutiev I, Marinov P, Belehaki A. 2016. Real time 3-D electron density reconstruction over Europe by using TaD profiler. *Radio Sci* **51**: 1176–1187. https://doi.org/10.1002/2015RS005932.

Kutiev I, Marinov P, Fidanova S, Belehaki A, Tsagouri I. 2012. Adjustments of the TaD electron density reconstruction model with GNSS TEC parameters for operational application purposes. *J Space Weather Space Clim* **2**: A21. https://doi.org/10.1051/swsc/2012021.

Kutiev I, Marinov P, Watanabe S. 2006. Model of topside ionosphere scale height based on topside sounder data. *Adv Space Res* **37(5)**: 943–950. https://doi.org/10.1016/j.asr.2005.11.021.

Lastovicka J. 2006. Forcing of the ionosphere by waves from below. *J Atmos Sol-Terr Phys* **68**: 479–497. https://doi.org/10.1016/j.jastp.2005.01.018.

Lastovicka J, Chum J. 2017. A review of results of the international ionospheric Doppler sounder network. *Adv Space Res* **60(8)**: 1629–1643. https://doi.org/10.1016/j.asr.2017.01.032.

Mayr HG, Harris I, Herrero FA, Spencer NW, Varosi F, Pesnell WD. 1990. Thermospheric gravity waves - Observations and interpretation using the transfer function model (TFM). *Space Sci Rev* **54**: 297–375. https://doi.org/10.1007/BF00177800.

Mevius M, van der Tol S, Pandey VN, Vedantham HK, Brentjens MA, et al. 2016. Probing ionospheric structures using the LOFAR radio telescope. *Radio Sci.* **51**: 927–941. https://doi.org/10.1002/2016RS006028.

Millward GH, Moffett RJ, Quegan S, Fuller-Rowell TJ. 1996. A coupled thermosphere-ionosphere-plasmasphere model CTIP. In: *STEP handbook on ionospheric models*, Schunk RW (Ed.), Utah State University, Logan, UT, p. 239.

Morgan MG, Ballard KA. 1978. The height dependence of wave-normal depression and disturbance amplitude in TID's. *J Geophys Res* **83(A12)**: 5741–5744. https://doi.org/10.1029/JA083iA12p05741.

Nickisch LJ, Fridman S, Hausman M, San Antonio GS. 2016. Feasibility study for reconstructing the spatial temporal structure of TIDs from high resolution backscatter ionograms. *Radio Sci* **51**: 443–453. https://doi.org/10.1002/2015RS005906.

Paznukhov VV, Galushko VG, Reinisch BW. 2012. Digisonde observations of AGWs/TIDs with frequency and angular sounding technique. *Adv Space Res* **49(4)**: 700–710. https://doi.org/10.1016/j.asr.2011.11.012.

Pintor P, Roldán R, Gomez J, de La Casa C, Fidalgo RM. 2015. The impact of the high ionospheric activity in the EGNOS performance. *Coord Mag* **XI(3)**, 20–28.

Pradipta R, Valladares CE, Carter BA, Doherty PH. 2016. Interhemispheric propagation and interactions of auroral traveling ionospheric disturbances near the equator. *J Geophys Res Space Phys* **121**: 2462–2474. https://doi.org/10.1002/2015JA022043.

Reinisch B, Galkin I, Belehaki A, Paznukhov V, Huang X, et al. 2018. Pilot ionosonde network for identification of traveling ionospheric disturbances. *Radio Sci* **53**: 365–378. https://doi.org/10.1002/2017RS006263.

Ross W. 1947. The estimation of the probable accuracy of high frequency radio direction-finding bearings. *J IEE* **94(Part III)**: 722–726. https://doi.org/10.1049/ji-3a-2.1947.0092.

Sanz J, Juan JM, González-Casado G, Prieto-Cerdeira R, Schlueter S, Orús R. 2014. Novel ionospheric activity indicator specifically tailored for GNSS users. In: *Proceedings of ION GNSS+ 2014. Tampa, Florida (USA)*, pp. 1173–1182. http://www.ion.org/publications/abstract.cfm?jp=p&articleID=12269.

Sauli P, Boska J. 2001. Tropospheric events and possible related gravity wave activity effects on the ionosphere. *J Atmos Sol-Terr Phys* **63**: 945–950.

Savastano G, Komjathy A, Verkhoglyadova O, Mazzoni A, Crespi M, Wei Y, Mannucci AJ. 2017. Real-time detection of tsunami ionospheric disturbances with a stand-alone GNSS receiver: A preliminary feasibility demonstration. *Sci Rep* **7**: 46607. https://doi.org/10.1038/srep46607.

Tsagouri I, Belehaki A, Koutroumbas K. 2018a. *Models for the specification of ionospheric background*, Zenodo. https://doi.org/10.5281/zenodo.3929555.

Tsagouri I, Goncharenko L, Shim JS, Belehaki A, Buresova D, Kuznetsova MM. 2018b. Assessment of current capabilities in modeling the ionospheric climatology for space weather applications: foF2 and hmF2. *Space Weather* **16**: 1930–1945. https://doi.org/10.1029/2018SW002035.

Tsagouri I, Koutroumbas K, Belehaki A. 2009. Ionospheric foF2 forecast over Europe based on an autoregressive modeling technique driven by solar wind parameters. *Radio Sci* **44**: RS0A35. https://doi.org/10.1029/2008RS004112.

Tsagouri I, Koutroumbas K, Elias P. 2018c. A new short-term forecasting model for the total electron content storm time disturbances. *J Space Weather Space Clim* **8**: A33. https://doi.org/10.1051/swsc/2018019.

Tsugawa T, Saito A. 2004. A statistical study of large-scale traveling ionospheric disturbances using the GPS network in Japan. *J Geophys Res* **109**: A06302. https://doi.org/10.1029/2003JA010302.

Watermann J. 2020. *Methodology for the identification of the interhemispheric circulation (version 1.2)*. TechTIDE Project Report. https://doi.org/10.5281/zenodo.4019014.

Xiao Z, Xiao SG, Hao YQ, Zhang DH. 2007. Morphological features of ionospheric response to typhoon. *J Geophys Res* **112**: A04304. https://doi.org/10.1029/2006JA011671.

Zhang S-R, Coster AJ, Erickson PJ, Goncharenko LP, Rideout W, Vierinen J. 2019. Traveling ionospheric disturbances and ionospheric perturbations associated with solar flares in September 2017. *J Geophys Res Space Phys* **124**: 5894–5917. https://doi.org/10.1029/2019JA026585.

Cite this article as: Belehaki A, Tsagouri I, Altadill D, Blanch E, Borries C, et al. 2020. An overview of methodologies for real-time detection, characterisation and tracking of traveling ionospheric disturbances developed in the TechTIDE project. *J. Space Weather Space Clim.* **10**, 42. https://doi.org/10.1051/swsc/2020043.

Acronyms

AATR Along Arc TEC Ratio. 18, 24

APC Antenna Phase Center. 13

BEIDOU BeiDou. xi, 2–4

BNC BKG Ntrip Client. 10

CPF Central Processing Facility. iv, vi, 20

DCB Diferential Code Bias. 19

EGNOS European Geostationary Navigation Overlay System. 18

ESA European Space Agency. 17, 21

FDMA Frequency Division Multiple Access. 4

FOC Full Operation Capability. 2

FPPP Fast Precise Point Positioning. iii, iv, vi, 17, 18, 26

GF geometry-free combination. 9, 16, 19

GLONASS Global'naya Navigatsionnaya Sputnikovaya Sistema. xi, 2, 4

GNSS Global Navigation Satellite System. iii, v, xi, 1–5, 7–12, 14, 15, 17, 20, 21, 24–27, 97

GPS Global Positioning System. iii, iv, xi, 2–4, 7

HAS high-accuracy positioning services. iii, iv, vi, 5, 13, 17, 20, 21

ICAO International Civil Aviation Organization. 18

IF ionosphere-free combination. 15, 21

IGP Ionospheric Grid Point. 18–20

IGS International GNSS Service. 18

IONO4HAS Ionpsheric Corrections for High-Accuracy positioning Services. ix, 17, 21

IPP Ionospheric Pierce Point. 9, 13, 14, 19

MSTID Medium Scale Travelling Ionospheric Disturbance. iii, v, 15–18, 24–26

NRTK Network-Real-Time Kinematics. iii, v, 5, 15–17, 25–27

NTRIP Networked Transport of RTCM via Internet Protocol. 10

PPP Precise Point Positioning. 5, 17, 19

PRN Pseudo Random Noise. 3

RINEX Receiver INdependent EXchange Format. 10, 17, 18

RTK Real-Time Kinematics. 5, 15

SBAS Satellite-Based Augmentation System. 18

SF Solar Flare. iii, 13, 14, 18

Sfe Solar Flares Effects. 13

SPP Standard Point Positioning. 5

SSP Sub Solar Point. 13, 14

SSR Space State Representation. 17

STEC Slant Total Electron Content. iii, v, 8, 9, 13, 19

TEC Total Electron Content. 8, 14, 15

TechTIDE Warning and Mitigation Technologies for Travelling Ionospheric Disturbances Effects. 17

TECU Total Electron Content Units. 8, 14, 16, 17, 20, 21, 26

VTEC Vertical Total Electron Content. 8, 19

Appendix 1
Implemented GNSS stations

The selection of GNSS stations from different networks has been done taking into consideration three main characteristics: first, ensuring a spread worldwide distribution. Second, defining a dense area of GNSS receivers broadcasting in real-time concentrated in Europe. Finally, a selection dense enough to define sub-networks of GNSS stations broadcasting in real-time, in order to simulate positioning scenarios using GNSS receivers as users of the products. This additional chapter provides the full list of GNSS stations used in real-time during the development of this thesis, indicating for each GNSS station its 4 alphanumeric identification, the country in which the station is located and its geographic coordinates (in degrees).

Station name	Country	Longitude (°)	Latitude (°)
ABMF	GLP	-61.5	16.15
ACOR	ESP	-8.39	43.17
ADH1	ARE	54.51	24.23
AJAC	FRA	8.762	41.73
ALBA	ESP	-1.85	38.78
ALBY	AUS	117.8	-34.7
ALGO	CAN	-78	45.76
ALIC	AUS	133.8	-23.5
ALME	ESP	-2.45	36.66
AREG	PER	-71.4	-16.3
ARUB	AUS	125.9	-31.6
ASCG	SHN	-14.3	-7.86
AUT1	GRC	23	40.37
BAKO	IDN	106.8	-6.44
BIK0	KGZ	74.53	42.66
BORJ	DEU	6.666	53.39
BRAZ	BRA	-47.8	-15.8
BRMF	FRA	4.938	45.53
BRST	FRA	-4.49	48.18
BRUX	BEL	4.358	50.6
BUCU	ROU	26.12	44.27
BUTE	HUN	19.05	47.28
CACE	ESP	-6.34	39.29
CARG	ESP	-0.97	37.41
CAS1	ATA	110.5	-66.1
CASC	PRT	-9.41	38.5
CCJ2	JPN	142.1	26.91
CEU1	ESP	-5.3	35.7
CFRM	CZE	18.35	49.49
CHOF	JPN	139.5	35.49
CHUR	CAN	-94	58.58
CKIS	CKI	-159	-21
CLIB	CZE	15.05	50.58
COBA	ESP	-4.72	37.72
COSO	USA	-117	35.79
CPAR	CZE	15.78	49.84
CPVG	CPV	-22.9	16.62
CREU	ESP	3.315	42.12
CTAB	CZE	14.68	49.21
CTWN	ZAF	18.46	-33.7
CUT0	AUS	115.8	-31.8
CUUT	THA	100.5	13.64
CZTG	ATF	51.85	-46.2
DARW	AUS	131.1	-12.7
DAV1	ATA	77.97	-68.4
DENT	BEL	3.399	50.74

Station name	Country	Longitude (°)	Latitude (°)
DJIG	DJI	42.84	11.45
DLF1	NLD	4.387	51.79
DOUR	BEL	4.594	49.9
DRAO	CAN	-119	49.13
DUMG	ATA	140	-66.5
EBRE	ESP	0.492	40.63
EIJS	NLD	5.683	50.56
FLRS	PRT	-31.1	39.26
FTNA	WLF	-178	-14.2
GAIA	PRT	-8.58	40.91
GAMB	PYF	-134	-22.9
GAMG	KOR	127.9	35.4
GANP	SVK	20.32	48.84
GOP6	CZE	14.78	49.72
GRAC	FRA	6.92	43.56
HOFN	ISL	-15.1	64.11
HRAG	ZAF	27.68	-25.7
IGEO	MDA	28.84	46.83
IJMU	NLD	4.556	52.27
IQAL	CAN	-68.5	63.6
ISTA	TUR	29.01	40.91
IZAN	ESP	-16.4	28.14
JFNG	CHN	114.4	30.34
JOG2	IDN	110.3	-7.71
KIR8	SWE	21.06	67.74
KIRU	SWE	20.96	67.72
KITG	UZB	66.88	38.94
KOS1	NLD	5.818	51.98
KOUC	NCL	164.2	-20.4
KOUG	GUF	-52.6	5.064
KRA1	POL	19.92	49.87
KRAW	POL	19.92	49.87
KRGG	ATF	70.25	-49.1
LAMA	POL	20.66	53.7
LAMP	ITA	12.6	35.31
LAUT	FJI	177.4	-17.4
LHAZ	CHN	91.1	29.49
LMMF	MTQ	-60.9	14.5
LPAL	ESP	-17.8	28.6
M0SE	ITA	12.49	41.7
MAC1	AUS	158.9	-54.3
MAJU	MHL	171.3	7.071
MALL	ESP	2.624	39.36
MAO0	USA	-156	20.57
MAS1	ESP	-15.6	27.6
MATG	ITA	16.7	40.45

Station name	Country	Longitude (°)	Latitude (°)
MAW1	ATA	62.87	-67.4
MAYG	MYT	45.25	-12.6
MET3	FIN	24.39	60.05
METG	FIN	24.38	60.07
METS	FIN	24.39	60.05
MGUE	ARG	-69.3	-35.5
MIK3	FIN	27.1	61.41
MIZU	JPN	141.1	38.94
MSSA	IGS	138.3	35.95
NICO	CYP	33.39	34.96
NKLG	GAB	9.672	0.351
NOT1	ITA	14.98	36.69
NRC1	CAN	-75.6	45.26
NRMG	NCL	166.4	-22
NYA2	NOR	11.85	78.85
OBE4	DEU	11.27	47.89
OHI3	ATA	-57.9	-63.1
OLK2	FIN	21.5	61.02
ONS1	SWE	11.92	57.22
ORID	MKD	20.79	40.93
ORIV	FIN	24.21	61.45
OUS2	NZL	170.5	-45.6
OWMG	NZL	-176	-43.8
PASA	ESP	-1.93	43.12
PAT0	GRC	21.78	38.09
PERC	BRA	-34.9	-8
PNGM	PNG	147.3	-2.02
POAL	BRA	-51.1	-29.9
POTS	DEU	13.06	52.19
PRDS	CAN	-114	50.68
PTGG	PHL	121	14.44
RDSD	DOM	-69.9	18.34
REUN	REU	55.57	-21
REYK	ISL	-21.9	63.98
RGDG	ARG	-67.7	-53.6
RIGA	LVA	24.05	56.77
RIO1	ESP	-2.42	42.27
RIO2	ARG	-67.7	-53.6
SASK	CAN	-106	52
SAVO	BRA	-38.4	-12.8
SCTB	ATA	166.7	-77.7
SEYG	SYC	55.53	-4.64
SGOC	LKA	79.87	6.846
SGPO	USA	-97.4	36.42
SIN1	SGP	103.6	1.333
SOFI	BGR	23.39	42.36
SONS	ESP	-3.96	39.48
SRJV	BIH	18.41	43.67
SSIA	SLV	-89.1	13.6
STFU	USA	-122	37.24
STJO	CAN	-52.6	47.4
SULP	UKR	24.01	49.64
SUR4	EST	24.38	59.29
SUTM	ZAF	20.81	-32.2
TASH	UZB	69.29	41.13
TBOB	AUS	142	-29.2
TERS	NLD	5.219	53.17
TERU	ESP	-1.12	40.16
THTG	PYF	-149	-17.4
TIT2	DEU	6.431	50.84
TLSE	FRA	1.48	43.36
TOIL	EST	27.53	59.25
TONG	TON	-175	-21
TRDS	NOR	10.31	63.21
TUO2	FIN	22.44	60.25
UCAG	ITA	9.11	39.03
ULAB	MNG	107	47.67
URUM	CHN	87.6	43.61
VALA	ESP	-4.7	41.51
VARS	NOR	31.03	70.21
VEN1	ITA	12.35	45.23
VFCH	FRA	1.719	47.1
VIR2	FIN	27.55	60.37
VIS0	SWE	18.36	57.47
VIS6	SWE	18.36	57.47
VLIS	NLD	3.597	51.25
WARE	BEL	5.245	50.5
WARN	DEU	12.1	53.98
WHIT	CAN	-135	60.58
WSRT	NLD	6.604	52.72
WUH2	CHN	114.3	30.36
YEBE	ESP	-3.08	40.33
YELL	CAN	-114	62.32
ZARA	ESP	-0.88	41.44
SJSP	BRA	-45.8	-23
MGRP	BRA	-46.1	-19
ALMA	BRA	-35.7	-9.49

Station name	Country	Longitude (°)	Latitude (°)
EACH	BRA	-46.4	-23.3
MGMC	BRA	-43.8	-16.6
PEAF	BRA	-37.6	-7.71
AMCR	BRA	-63.1	-4.05
POLI	BRA	-46.7	-23.4
RNNA	BRA	-35.2	-5.79
RJCG	BRA	-41.3	-21.6
ARD2	AUS	151.6	-30.3
RJNI	BRA	-43.1	-22.7
PRMA	BRA	-51.9	-23.2
EESC	BRA	-47.8	-21.8
SPFE	BRA	-50.2	-20.1
SPS1	BRA	-47.4	-23.3
ANDA	AUS	137.1	-30.2
BATF	BRA	-39.7	-17.4
ROJI	BRA	-61.9	-10.7
ALAR	BRA	-36.6	-9.68
UBA1	BRA	-45.1	-23.3
CESB	BRA	-40.3	-3.65
RSPE	BRA	-52.4	-31.6
PEPE	BRA	-40.5	-9.32
MSDR	BRA	-54.9	-22
MTLA	BRA	-59.3	-15.1
KZN2	RUS	49.11	55.61
CRUZ	BRA	-72.6	-7.56
SPBO	BRA	-48.4	-22.7
GOJA	BRA	-51.7	-17.7
WIND	NAM	17.08	-22.4
SICO	ARG	-67.7	-40.3
ARD2	AUS	151.6	-30.3
CN55	PAN	-80.5	8.188
P195	USA	-122	38.47
DYNG	GRC	23.93	37.89
UTQI	USA	-156	71.2
IITK	IND	80.23	26.36
IND1	CRI	-85.5	9.799
MOM0	NIC	-86.5	12.32
EPEC	ECU	-78.4	-0.31

Bibliography

[IEE, 2003] (2003). Ieee standard letter designations for radar-frequency bands. *IEEE Std 521-2002 (Revision of IEEE Std 521-1984)*, pages 1–10.

[Cla, 2021] (2021). 2021 journal impact factor, journal citation reports (clarivate analytics). https://jcr.clarivate.com/jcr/home. Accessed: February 27, 2023.

[Afraimovich et al., 2001] Afraimovich, E., Altynsev, A., Grechnev, V., and Leonovich, L. (2001). Ionospheric effects of the solar flares as deduced from global gps network data. *Advances in Space Research*, 27(6-7):1333–1338.

[Afraimovich et al., 1998] Afraimovich, E., Palamartchouk, K., and Perevalova, N. (1998). Gps radio interferometry of travelling ionospheric disturbances. *Journal of Atmospheric and Solar-Terrestrial Physics*, 60(12):1205–1223.

[Afraimovich, 2000] Afraimovich, E. L. (2000). Gps global detection of the ionospheric response to solar flares. *Radio Science*, 35(6):1417–1424.

[Agency, 2021] Agency, E. G. (2021). *Galileo High Accuracy Service (HAS): info note*. Publications Office.

[Belehaki, Anna et al., 2020] Belehaki, Anna, Tsagouri, Ioanna, Altadill, David, Blanch, Estefania, Borries, Claudia, Buresova, Dalia, Chum, Jaroslav, Galkin, Ivan, Juan, José Miguel, Segarra, Antoni, Timoté, Cristhian Camilo, Tziotziou, Kostas, Verhulst, Tobias G. W., and Watermann, Jurgen (2020). An overview of methodologies for real-time detection, characterisation and tracking of traveling ionospheric disturbances developed in the techtide project. *J. Space Weather Space Clim.*, 10:42.

[Bilitza, 2001] Bilitza, D. (2001). International reference ionosphere 2000. *Radio Science*, 36(2):261–275.

[Bilitza et al., 2022] Bilitza, D., Pezzopane, M., Truhlik, V., Altadill, D., Reinisch, B. W., and Pignalberi, A. (2022). The international reference ionosphere model: A review and description of an ionospheric benchmark. *Reviews of Geophysics*, 60(4):e2022RG000792. e2022RG000792 2022RG000792.

[Buonsanto, 1999] Buonsanto, M. J. (1999). Ionospheric storms—a review. *Space Science Reviews*, 88(3):563–601.

[Calais et al., 2003] Calais, E., Haase, J., and Minster, J. (2003). Detection of ionospheric perturbations using a dense gps array in southern california. *Geophysical research letters*, 30(12).

[Cherniak et al., 2018] Cherniak, I., Krankowski, A., and Zakharenkova, I. (2018). Roti maps: A new igs ionospheric product characterizing the ionospheric irregularities occurrence. *Gps Solutions*, 22:1–12.

[Coster et al., 1992] Coster, A. J., Gaposchkin, E. M., and Thornton, L. E. (1992). Real-time ionospheric monitoring system using gps. *Navigation*, 39(2):191–204.

[Curto et al., 2019] Curto, J. J., Juan, J. M., and Timoté, C. C. (2019). Confirming geomagnetic sfe by means of a solar flare detector based on gnss. *Journal of Space Weather Space Climate*, 9.

[Curto, Juan José et al., 2020] Curto, Juan José, Juan, Jose Miguel, and Timoté, Cristhian Camilo (2020). Answer to the comments on "confirming geomagnetic sfe by means of a solar flare detector based on gnss". *J. Space Weather Space Clim.*, 10:16.

[García-Rigo et al., 2007] García-Rigo, A., Hernández-Pajares, M., Juan, J., and Sanz, J. (2007). Solar flare detection system based on global positioning system data: First results. *Advances in Space Research*, 39(5):889–895.

[Gulyaeva and Stanislawska, 2008] Gulyaeva, T. and Stanislawska, I. (2008). Derivation of a planetary ionospheric storm index. In *Annales Geophysicae*, volume 26, pages 2645–2648. Copernicus Publications Göttingen, Germany.

[Gurtner and Estey, 2007] Gurtner, W. and Estey, L. (2007). Rinex-the receiver independent exchange format-version 3.00. *Astronomical Institute, University of Bern and UNAVCO, Bolulder, Colorado.*

[Hernández-Pajares et al., 2012] Hernández-Pajares, M., García-Rigo, A., Juan, J. M., Sanz, J., Monte, E., and Aragón-Àngel, A. (2012). Gnss measurement of euv photons flux rate during strong and mid solar flares. *Space Weather*, 10.

[Hernández-Pajares et al., 2006] Hernández-Pajares, M., Juan, J. M., and Sanz, J. (2006). Medium-scale traveling ionospheric disturbances affecting gps measurements: Spatial and temporal analysis. *Journal of Geophysical Research: Space Physics*, 111.

[Jakowski et al., 2006] Jakowski, N., Stankov, S., Schlueter, S., and Klaehn, D. (2006). On developing a new ionospheric perturbation index for space weather operations. *Advances in Space Research*, 38(11):2596–2600.

[Juan et al., 2012] Juan, J. M., Hernández-Pajares, M., Sanz, J., Ramos-Bosch, P., Aragon-Angel, A., Orus, R., Ochieng, W., Feng, S., Jofre, M., Coutinho, P., et al. (2012). Enhanced precise point positioning for gnss users. *IEEE transactions on geoscience and remote sensing*, 50:4213–4222.

[Juan et al., 2018] Juan, J. M., Sanz, J., Rovira-Garcia, A., González-Casado, G., Ibáñez, D., and Perez, R. O. (2018). Aatr an ionospheric activity indicator specifically based on gnss measurements. *Journal of Space Weather and Space Climate*, 8:A14.

[Jursa, 1985] Jursa, A. S. (1985). Handbook of geophysics and the space environment. 4th edition (final).

[Klobuchar, 1987a] Klobuchar, J. A. (1987a). Ionospheric time-delay algorithm for single-frequency gps users. *IEEE Transactions on Aerospace and Electronic Systems*, AES-23(3):325–331.

[Klobuchar, 1987b] Klobuchar, J. A. (1987b). Ionospheric time-delay algorithm for single-frequency gps users. *IEEE Transactions on aerospace and electronic systems*, pages 325–331.

[Liu et al., 2004] Liu, J., Lin, C., Tsai, H., and Liou, Y. (2004). Ionospheric solar flare effects monitored by the ground-based gps receivers: Theory and observation. *Journal of Geophysical Research: Space Physics*, 109(A1).

[Misra and Enge, 2006] Misra, P. and Enge, P. (2006). *Global positioning system: Signals, measurements, and performance*. Ingram.

[Nie et al., 2019] Nie, Z., Yang, H., Zhou, P., Gao, Y., and Wang, Z. (2019). Quality assessment of cnes real-time ionospheric products. *GPS Solutions*, 23:1–15.

[Pi et al., 1997] Pi, X., Mannucci, A., Lindqwister, U., and Ho, C. (1997). Monitoring of global ionospheric irregularities using the worldwide gps network. *Geophysical Research Letters*, 24(18):2283–2286.

[Radicella, 2009] Radicella, S. M. (2009). The nequick model genesis, uses and evolution. *Annals of geophysics*, 52(3-4):417–422.

[Roma-Dollase et al., 2018] Roma-Dollase, D., Hernández-Pajares, M., Krankowski, A., Kotulak, K., Ghoddousi-Fard, R., Yuan, Y., Li, Z., Zhang, H., Shi, C., Wang, C., et al. (2018). Consistency of seven different gnss global ionospheric mapping techniques during one solar cycle. *Journal of Geodesy*, 92:691–706.

[Rovira-Garcia et al., 2019] Rovira-Garcia, A., Ibáñez-Segura, D., Orús-Perez, R., Juan, J. M., Sanz, J., and González-Casado, G. (2019). Assessing the quality of ionospheric models through gnss positioning error: methodology and results. *GPS Solutions*, 24:4.

[Rovira-Garcia et al., 2016a] Rovira-Garcia, A., Juan, J., Sanz, J., González-Casado, G., and Bertran, E. (2016a). Fast precise point positioning: A system to provide corrections for single and multi-frequency navigation. *Navigation*, 63(3):231–247.

[Rovira-Garcia et al., 2015] Rovira-Garcia, A., Juan, J. M., Sanz, J., and Gonzalez-Casado, G. (2015). A worldwide ionospheric model for fast precise point positioning. *IEEE Transactions on Geoscience and Remote Sensing*, 53(8):4596–4604.

[Rovira-Garcia et al., 2021] Rovira-Garcia, A., Juan, J. M., Sanz, J., González-Casado, G., Ventura-Traveset, J., Cacciapuoti, L., and Schoenemann, E. (2021). Removing day-boundary discontinuities on GNSS clock estimates: methodology and results. *GPS Solutions*, 25(2).

[Rovira-Garcia et al., 2016b] Rovira-Garcia, A., Juan, J. M., Sanz, J., González-Casado, G., and Ibáñez, D. (2016b). Accuracy of ionospheric models used in gnss and sbas: methodology and analysis. *Journal of geodesy*, 90:229–240.

[Saito et al., 1998] Saito, A., Fukao, S., and Miyazaki, S. (1998). High resolution mapping of tec perturbations with the gsi gps network over japan. *Geophysical research letters*, 25(16):3079–3082.

[Sanz et al., 2013] Sanz, J., Zornoza, J. M. J., and Hernández-Pajares, M. (2013). *GNSS Data Processing, Volume I: Fundamentals and Algorithms*.

[Seeber, 2008] Seeber, G. (2008). *Satellite geodesy: foundations, methods, and applications*. Walter de gruyter.

[TechTIDE, 2022] TechTIDE (2022). Warning and mitigation technologies for travelling ionospheric disturbances effects. http://techtide.space.noa.gr, visited on February 27, 2023.

[Teunissen and Kleusberg, 2012] Teunissen, P. J. and Kleusberg, A. (2012). *GPS for Geodesy*.

[Timoté et al., 2020] Timoté, C. C., Juan, J. M., Sanz, J., González-Casado, G., Rovira-García, A., and Escudero, M. (2020). Impact of medium-scale traveling ionospheric disturbances on network real-time kinematic services: Catnet study case. *Journal of Space Weather Space Climate*, 10.

[Tsugawa et al., 2007] Tsugawa, T., Otsuka, Y., Coster, A., and Saito, A. (2007). Medium-scale traveling ionospheric disturbances detected with dense and wide tec maps over north america. *Geophysical Research Letters*, 34(22).

[Wan et al., 2002] Wan, W., Yuan, H., Liu, L., and Ning, B. (2002). The sudden increase in ionospheric total electron content caused by the very intense solar flare on july 14, 2000. *Science in China Series A: Mathematics*, 45:142.

[Weber and Mervart, 2007] Weber, G. and Mervart, L. (2007). The bkg ntrip client (bnc). In *Report on EUREF symposium*.

[Wilken, Volker et al., 2018] Wilken, Volker, Kriegel, Martin, Jakowski, Norbert, and Berdermann, Jens (2018). An ionospheric index suitable for estimating the degree of ionospheric perturbations. *J. Space Weather Space Clim.*, 8:A19.

[Zhang et al., 2018] Zhang, L., Yang, H., Gao, Y., Yao, Y., and Xu, C. (2018). Evaluation and analysis of real-time precise orbits and clocks products from different IGS analysis centers. *Advances in Space Research*, 61(12):2942–2954.